

# **Nanomaterials for Ammonia Decomposition**

vorgelegt von  
M.Sc. Chemiker  
Weiqing Zheng  
aus Dalian (V.R. China)

Von der Fakultät II - Mathematik und Naturwissenschaften  
der Technischen Universität Berlin  
zur Erlangung des akademischen Grades  
Doktor der Naturwissenschaften  
Dr.rer.nat.

genehmigte Dissertation

Promotionsausschuss:

Vorsitzender: Prof. Dr. Arne Thomas

Berichter/Gutachter: Prof. Dr. R. Schlögl (FHI der MPG, Berlin)

Berichter/Gutachter: Prof. Dr. R. Schomäcker

Berichter/Gutachter: Prof. Dr. K. Rademann (HU Berlin)

Berichter/Gutachter: Prof. Dr. T. Ressler

Tag der wissenschaftlichen Aussprache: 16.12.2011

Berlin 2012

D 83



Weiqing Zheng

## **Abstract**

With the aim of developing a high efficient catalyst for CO<sub>x</sub>-free hydrogen production from ammonia, a series of well define nanostructured materials were synthesized, characterized and evaluated for the catalytic decomposition of ammonia.

The ruthenium nanoparticles were deposited on carbon nanotubes (CNTs) and graphite with different local geometry and functionalities in order to vary the metal-support interaction. The work starts with surface modification of carbon by chemical functionalization, exfoliation and thermal annealing. The characterization results reveal that the pretreatments can efficiently remove the pyrolytic carbon and vary the oxygen functional groups on the surface of carbon. Post characterization of Ru/carbon catalysts supports the notion that high reactivity of Ru particles benefits from the high graphitization of carbon support leading to a weaker metal-carbon interaction and hence to form larger particles. According to the high-resolution TEM images, the local disorder of the support induces the local disorder to the Ru particle immobilized on it, and further influence the desorption of nitrogen from catalyst surface, which is the most difficult step for ammonia decomposition. The direct observation of reaction intermediate (adsorbed dinitrogen) from *in situ* XPS measurement operating at 400 °C and relative high pressure of ammonia, efficiently supports the conclusions from the post characterization of the Ru particles on carbon materials.

Considering the sintering and nitridation of Fe at working conditions, Fe catalyst was modified by alloying Co or Ni and supported on CNTs. The homogeneous distributions of Fe and Co in the isolated nanoparticles were evidenced by the bulk and surface structural and compositional characterization. The stability of iron was significantly improved by alloying with cobalt or nickel, and by encapsulated inside the tubular channel of CNTs.

About 30 mmol/(g<sub>cat</sub>·min) constant H<sub>2</sub> production rate could be achieved over a high surface area molybdenum carbide catalyst in 100 hours. Observed deactivation (in the first 15 hours) of the molybdenum carbide during reaction was ascribed to considerable reduction of specific surface area due to the nitridation of carbide under reaction condition. The relatively high rate of reaction is ascribed to the highly energetic sites (twin-boundaries, stacking faults, steps and defects) which are observed in both the molybdenum carbide and nitride samples. The prevalence of such sites in the as-synthesised material results in a much higher H<sub>2</sub> production rate in comparison with previously reported Mo-based catalysts. Homogeneous molybdenum nitride nanoparticles dispersed in carbon were prepared by using hydrothermal carbonization and ammolytic with proper Mo:C mole ratio. With the help of carbon, the individual MoN particles could survive throughout the long-term catalytic reaction and offer a constant H<sub>2</sub> formation rate (23 mmol/(g<sub>cat</sub>·min)). We herein show that the transition metal carbide and nitride materials have great potential to replace Ru as the catalyst for ammonia decomposition.

The last part of this work is the reaction kinetic study over the three catalytic systems by varying the partial pressures of NH<sub>3</sub>, N<sub>2</sub> and H<sub>2</sub> at different temperatures. The kinetic results from applying the power-law model show that the reaction behaviors were controlled by the domain crystalline size of molybdenum nitride. Lower activation energy and strong inhibitive effect of hydrogen were observed on nanostructured molybdenum nitride, close to those for supported ruthenium nanoparticles indicates the similar properties between nitride and noble metal for the reaction of ammonia decomposition.



## **Zusammenfassung**

Mit dem Ziel der Entwicklung hocheffizienter Katalysatoren zur CO<sub>x</sub>-freien Wasserstoff-Synthese aus Ammoniak wurden eine Reihe wohldefinierter, nanostrukturierter Materialien auf Basis von Ruthenium, Eisen und Molybdän dargestellt, charakterisiert und hinsichtlich ihrer Eigenschaften für die katalytische Zersetzung von Ammoniak untersucht.

Ru-Nanopartikel wurden auf Kohlenstoffnanoröhren („CNTs“) und Graphit abgeschieden, wobei durch die Verwendung unterschiedlicher Geometrien und Funktionalisierungen am Träger eine breite Variation der Metall-Träger-Wechselwirkung erreicht wurde. Ex situ Untersuchungen an diesen Katalysatoren deuten darauf hin, dass hohe Aktivitäten des Metalls durch größere Partikel erreicht werden, welche bei hoher Graphitisierung des Kohlenstoffs und damit schwächeren Metall-Träger-Wechselwirkungen entstehen. Hochauflösende TEM-Aufnahmen zeigen, dass lokale Fehlorderungen am Träger die Ausbildung lokale Defekte am Metallpartikel bewirken. Diese beeinflussen maßgeblich die Desorption von Stickstoff von der Oberfläche als geschwindigkeitsbestimmenden Schritt. Die direkte Beobachtung von adsorbiertem Distickstoff an der Metalloberfläche gelang mit Hilfe von in situ XPS-Experimenten, welche die Schlussfolgerungen der vorrangegangenen ex situ Untersuchungen weiter bekräftigen.

Fe/CNT-Katalysatoren konnten hinsichtlich ihrer Stabilität gegenüber Sintern und Nitridierung unter Reaktionsbedingungen durch Legieren mit Co und Ni wesentlich verbessert werden, wobei die hierbei notwendige Homogenität der Legierungspartikel durch verschiedene bulk- und oberflächensensitive Methoden sichergestellt wurde. Die Stabilität wird zusätzlich durch die gezielte Immobilisierung der Partikel im Innenraum der Kohlenstoffnanoröhren erhöht.

Mittels eines Molybdäncarbids mit hoher Oberfläche konnten konstante H<sub>2</sub>-Bildungsraten von ca. 30 mmol/(gKat·min) nach 100 Stunden erzielt werden. Eine dabei beobachtete 15 Stunden andauernde Deaktivierungsphase zu Beginn der Reaktion wird mit der Umsetzung des Metallcarbids zum Metallnitrid und einhergehender deutlicher Verringerung der spezifischen Oberfläche begründet. Die dennoch, verglichen mit literaturbekannten Mo-Katalysatoren, hohe Reaktionsrate lässt sich auf das präparationsbedingte vermehrte Auftreten hochenergetischer Zentren in Form von Zwillingsgrenzen, Stufen und Stapelfehlern zurückführen. Desweiteren wurden in Kohlenstoff dispergierte Molybdännitrid-Partikel durch Hydrothermalsynthese dargestellt. Durch die Anwesenheit des Kohlenstoffs unterliegen die Molybdännitrid-Partikel keinen Sintervorgängen unter Reaktionsbedingungen und zeigen eine stabile H<sub>2</sub>-Bildungsgeschwindigkeit von 23 mmol/(gKat·min). Diese Ergebnisse verdeutlichen das hohe Potential von Metallcarbiden und –nitriden als Katalysatoren für die Zersetzung von Ammoniak.

Schließlich wurden kinetische Untersuchungen an den beschriebenen Katalysatorsystemen durch Änderung der Partialdrücke von NH<sub>3</sub>, N<sub>2</sub> und H<sub>2</sub> bei verschiedenen Temperaturen vorgenommen. Durch Anwendung des „Power-Law“-Modells lässt sich zeigen, dass die katalytischen Eigenschaften des Molybdännitrides durch dessen Kristallitgröße bestimmt werden. Die niedrigen Aktivierungsenergien und Inhibierungseffekte des H<sub>2</sub> des nanostrukturierten Molybdännitrides sind vergleichbar mit denen der geträgerten Ru-Nanopartikel und zeugen von den sehr ähnlichen Eigenschaften eines Edelmetalls und eines Nitrids als Katalysatoren für die Zersetzung von Ammoniak.



# Table of Content

<b>Abstract_English</b> .....	i
<b>Zusammenfassung_Deutsch</b> .....	iii

## **Chapter 1. Introduction**

1.1 Research background .....	1
1.1.1 Hydrogen production .....	1
1.1.2 Ammonia as hydrogen carrier .....	2
1.2 Aims of this work and thesis structure .....	3
1.3 Ammonia decomposition .....	5
1.3.1 The reaction .....	5
1.3.2 The catalysts .....	6
1.3.2.1 Ruthenium .....	7
1.3.2.2 Iron, cobalt and nickel .....	11
1.3.2.3 Carbide and nitride .....	12
1.3.3 The supports (carbon) .....	15
1.4 Publication declaration .....	18
<b>References</b> .....	19

## **Chapter 2. Experimental and characterization methods**

2.1 Catalytic performance measurements .....	25
2.1.1 Reactivity evaluations .....	25
2.1.2 kinetic measurements .....	26
2.2 The synthesis of nanostructured materials .....	27
2.2.1 the synthesis Ru-based catalysts supported on carbon .....	27
2.2.1.1 Surface modification of CNTs .....	27
2.2.1.2 Preparation of exfoliated graphite .....	29
2.2.1.3 Selective deposition of Ru nanoparticles on CNTs .....	29

2.2.1.4 Impregnation of Ru on graphite .....	31
2.2.2 The synthesis of metal alloy catalysts supported on CNTs .....	31
2.2.2.1 Pre-treatment of CNT/CNFs .....	31
2.2.2.2 Selective deposition of metal alloy on CNTs .....	31
2.2.3 The synthesis of molybdenum carbide and nitride .....	32
2.2.3.1 The synthesis of high-surface-area molybdenum carbide .....	32
2.2.3.2 The synthesis of nanostructured Mo nitride by HTC method .....	33
2.3. Characterization techniques .....	33
2.3.1. Textural properties .....	33
2.3.2. Raman spectroscopy .....	34
2.3.3. Powder X-ray diffraction .....	35
2.3.4. Electron Microscopy techniques .....	35
2.3.5. X-ray photoelectron spectroscopy .....	38
2.4. Density functional theory calculations .....	38
<b>References</b> .....	39

### **Chapter 3. Ruthenium nanoparticles on carbon**

3.1. Structure-function correlations for Ru/CNT .....	41
3.1.1. Surface modification of CNTs .....	42
3.1.1.1 Textural properties of CNTs .....	43
3.1.1.2 Graphitization characterization of CNTs .....	45
3.1.1.3 Surface characterization of CNTs .....	47
3.1.2 Selective deposition of Ru nanoparticles on CNTs .....	49
3.1.3 Catalytic NH <sub>3</sub> decomposition .....	54
3.2 Structure-function correlations for Ru/graphite .....	56
3.2.1 Characterization of the supports .....	57
3.2.1.1 Textural properties of graphite samples .....	57
3.2.1.2 Graphitization characterization of graphite samples .....	59
3.2.1.3 Surface analysis of graphite samples .....	60
3.2.2 Catalytic performance of ruthenium samples .....	62
3.2.3 Morphology of Ru nanoparticles on graphite .....	63

3.2.4 <i>In-situ</i> XPS measurements of working system .....	67
3.3 Chapter conclusions.....	70
3.3.1 Ru- CNTs .....	70
3.3.2 Ru-graphite .....	70
<b>References</b> .....	72
<b>Chapter 4. Alloying transition metal nanoparticles on CNT/CNFs</b>	
4.1 Textural property of support CNTs/CNFs.....	78
4.2 Characterizations of metal alloy nanoparticles on CNTs/CNFs.....	80
4.3 Catalytic decomposition of NH <sub>3</sub> .....	85
4.4 Selective deposition of metal alloy nanoparticles on CNTs/CNFs.....	87
4.5 Chapter conclusions.....	89
<b>References</b> .....	90
<b>Chapter 5. Molybdenum carbides and nitrides</b>	
5.1 Bulk system of Mo carbides and nitrides .....	94
5.1.1 Catalytic performance of high-surface-area Mo carbide.....	94
5.1.2 Textural properties of fresh and used Mo carbide.....	95
5.1.3 Phase identifications of fresh and used Mo carbide.....	99
5.1.4 Electronic properties of fresh and used Mo carbide .....	102
5.1.5 Density functional theory calculations.....	104
5.1.6 Carbon coating on high-surface-area Mo carbide .....	107
5.2 Nanosizing Mo carbides and nitrides.....	110
5.2.1 CNTs/CNFs supported Mo carbide .....	110
5.2.2 Hydrothermal carbonization preparation of Mo nitride .....	115
5.2.2.1 Characterizations of nanosizing Mo-based catalysts .....	115
5.2.2.2 Catalytic performance of Mo-based catalysts .....	121
5.3 Chapter conclusions.....	124
5.3.1 Bulk system of Mo carbide and nitride .....	124
5.3.2 Nanosizing Mo carbide and nitride catalysts .....	125
<b>References</b> .....	126

**Chapter 6. Preliminary kinetic study of molybdenum nitrides and metal nanoparticles**

6.1 Kinetic results of molybdenum nitrides .....	133
6.1.1 Kinetic results of MoN- $Mo_2C$ .....	133
6.1.2 Kinetic results of MoN- $MoO_3$ and MoN- <i>HTC</i> .....	137
6.2 Kinetic results of ruthenium and iron-cobalt alloy catalysts .....	139
6.2.1 Kinetic results of FeCo-CNTs .....	139
6.2.2 Kinetic results of Ru-graphite .....	141
6.3 Comparison of kinetic measurements .....	144
6.4 Chapter conclusions and outlook .....	146
6.4.1 Chapter conclusions .....	146
6.4.2 Outlook .....	146
<b>References</b> .....	149
<b>Curriculum Vitae</b> .....	a
<b>Acknowledgements</b> .....	c

# Chapter 1: Introduction

## 1.1 Research background

### 1.1.1 Hydrogen production

Energy shortage and pollution have led global efforts of science and technology researches towards clean and efficient energy system. One scenario is hydrogen as the ultra-clean energy carrier.<sup>[1]</sup> The advantages of using H<sub>2</sub> as energy are summarized below:

- Caloric energy of H<sub>2</sub> is 1.4E5 kJ/kg, larger than fossil, chemical and biology energy sources.
- There is no pollution in this energy circle, that the only product of this reaction is water. Furthermore, water could be dissociated to form hydrogen and oxygen.<sup>[2]</sup>
- It could be used not only as heat energy by reacting with oxygen, but also as electronic energy by reacting with oxygen atoms, which is well known as Fuel cell application.<sup>[3]</sup>

Currently the dominant technology for direct production of hydrogen is steam reforming from hydrocarbons. Hydrogen can be also produced from many other methods known including electrolysis and thermolysis. On the other hand, the high reactivity with oxygen makes the transfer, delivery and storage of hydrogen much more difficult.<sup>[4]</sup> Nowadays, the exploration of the most efficient, economical, and secure procedures and sources to produce hydrogen for fuel cell application is still one of the hot topics in this field. There are three technical routes to produce hydrogen in fuel cell application:

- Large scale H<sub>2</sub> production based on conventional reaction of fossil fuels or biomass. Although it has high efficiency of H<sub>2</sub> production, the cost of storage and transfer of hydrogen obstruct the development of this technique
- On-board H<sub>2</sub> production. The development of this technical route was restricted by the complicated operating system.
- On-site H<sub>2</sub> production at fueling stations. This route will decrease the cost of delivery and storage of hydrogen and predigest the fuel cell system.

### ***1.1.2 Ammonia as hydrogen carrier***

Compared with the conventional chemical processes for hydrogen production (steam reforming, partial oxidation, auto-thermal reforming, coal gasification, biomass process, electronic process and so on.), ammonia decomposition has several outstanding advantages <sup>[5-8]</sup>:

- Ammonia could be easily liquefied and storage.
- The technique of ammonia synthesis is well established infrastructure, which is well known as Haber-Bosch process.<sup>[9]</sup>
- CO<sub>x</sub> is absent in the reaction of ammonia decomposition, in which would be beneficent for the lifetime of catalyst in fuel cell. Ppm level of CO<sub>x</sub> can poison the catalysts in proton exchange membrane fuel cell.<sup>[3]</sup>
- The reaction process is convenient, since the thermodynamic equilibrium conversion could achieve more than 99% at 400 °C, 1 atm.

It has been reported that, the group VIII metals (Ru, Fe, Co, Ni, Ir and Rh) and metal carbides/nitrides (MoC<sub>x</sub>/MoN<sub>x</sub>, VC<sub>x</sub>/VN<sub>x</sub>, WC<sub>x</sub>, etc.) could catalyze the decomposition of ammonia to form H<sub>2</sub> and N<sub>2</sub>. Supported ruthenium clusters (especially on carbon nanotubes) have been proven to be the most active catalyst.<sup>[10]</sup> However, the limited availability of nobel metal (ruthenium) and the low catalytic activities of non-precious metals (Fe, Co and Ni) make it

necessary to optimize the catalytic system offering a better performance at low temperature over the non-precious metals catalysts.

## **1.2 Aims of this work and thesis structure**

The overall goal of this work is to develop a high performance catalyst for hydrogen production from ammonia decomposition. Three catalytic systems (ruthenium, iron/cobalt/nickel and molybdenum carbide/nitride) were selected as probe catalyst to understand the structural and functional correlations of nanostructured catalytic units in ammonia decomposition. To simplify this target it will be broken down into the following parts:

- To synthesize a series of well-defined nanostructured catalysts via selective deposition of ruthenium nanoparticles on modified carbon surfaces, alloying early transition metals on modified carbon nanotubes, and nanosized molybdenum nitrides in carbon
- To test the catalytic properties of the series of nanostructured catalysts and gain insight into the nature and influence of the structure and function
- To characterize the fresh and post catalysts including in-situ technique to gain the intrinsic understanding of the catalytic properties with the relation to those observed for the structural-functional properties of ruthenium nanoparticles
- To investigate the reaction kinetic behaviors of representative catalysts

In this thesis, the realization of the above goals is described over four chapters as follows:

Chapter Three – Ruthenium nanoparticles on carbon presents the investigation of metal-support interaction of ruthenium and carbons. In-situ and post characterizations were carried out over the ruthenium catalysts in order to find out the correlation between the chemico-physical properties of component and the catalytic performance in ammonia decomposition.

Chapter Four – Alloying transition metals on CNTs/CNFs presents the experimental results on the binary alloy of group metals (iron, cobalt and nickel) for ammonia decomposition. The role of carbon nanotubes as support will be also addressed in this chapter.

Chapter Five – Molybdenum carbides and nitrides presents the investigations of molybdenum carbide and nitride as catalysts for ammonia decomposition. This chapter also contains the synthesis of nanostructured molybdenum nitride with the aim to study the size effect towards the catalytic performance.

Chapter Six – Preliminary kinetic study of molybdenum nitride and metal nanoparticles presents the kinetic results of the representative catalysts investigated in previous chapters. This final chapter is trying to find the links between noble metal (ruthenium), non-precious metal (iron/cobalt) and nitride (molybdenum nitride) with the respect of the reaction mechanism.

Before presenting all the experimental data including characterizations, catalytic measurements, results and discussions in the main chapters, this thesis starts with:

Chapter One – Introduction contains research background, literature review and explains why those three catalytic components (ruthenium, iron/cobalt/nickel alloy and carbide/nitride) were selected for the reaction of ammonia decomposition.

Chapter Two – Experimental and characterization methods presents the details of catalytic measurement apparatuses (reactivity evaluation and kinetic measurement), synthesis of catalysts and the characterization techniques used in this work.

### 1.3 Ammonia decomposition

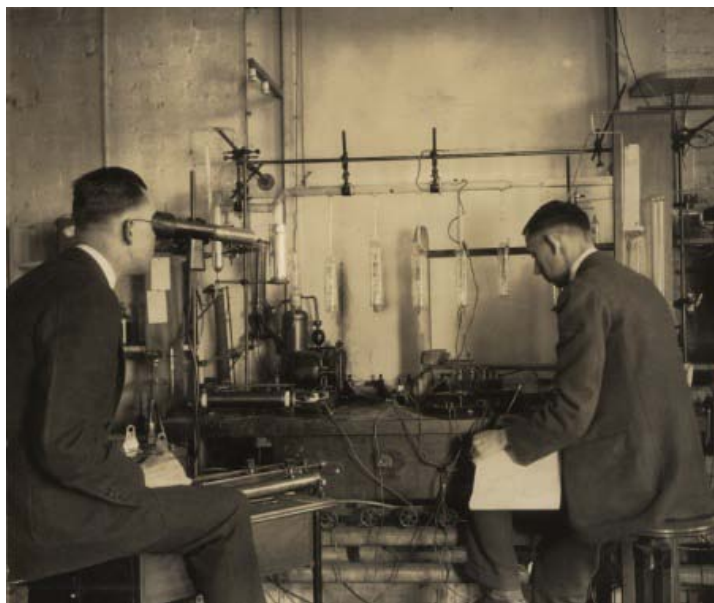


Figure 1-1. R. A. Nelson and C. H. Kunsman with apparatus used for the study of the decomposition of ammonia on catalyst surfaces in April 1926.

#### 1.3.1 The reaction

<b>Table 1-1. Thermodynamic equilibrium conversion of NH<sub>3</sub> decomposition</b>						
<b>Temperature (K)</b>	<b>Reaction pressure (atm)</b>					
	<b>1</b>	<b>2</b>	<b>3</b>	<b>4</b>	<b>5</b>	<b>6</b>
<b>473</b>	52.24	29.68	15.57	5.81	~0	~0
<b>523</b>	80.93	67.08	56.09	47.20	39.82	33.59
<b>573</b>	92.39	85.81	79.84	74.45	69.56	65.10
<b>623</b>	96.69	93.64	90.70	87.89	85.23	82.67
<b>673</b>	99.16	98.34	97.54	96.76	96.02	91.16
<b>723</b>	99.59	99.13	98.70	98.27	97.86	95.24
<b>773</b>	99.75	99.50	99.26	99.02	98.78	97.27
<b>823</b>	99.85	99.70	99.55	99.41	99.26	98.35
<b>873</b>	99.90	99.81	99.72	99.62	99.53	98.94
<b>923</b>	99.94	99.87	99.81	99.75	99.68	99.30

The ammonia decomposition reaction is endothermic:



The Gibbs free energy  $\Delta G^0$  for the reaction is  $+16.4 \text{ kJ mol}^{-1}$ . With these data including the data of its reversal reaction, the equilibrium for the “reforming” of ammonia can be estimated, which were summarized in Table 1-1. The equilibrium conversions in Table 1-1. show the drastic effects of both temperature and pressure. The beneficial low pressure effect means that a change in molar volume shifts the equilibrium into the direction of a lower total molar volume. Thus, the equilibrium conversion of ammonia decomposition benefits from the high temperature and low pressure. These data indicates the possibility of completed conversion of ammonia at relative low temperature (400 °C), which imply the large improvement might be needed for the existing catalysts systems, even for the Ru-based catalysts.

### 1.3.2 The catalysts

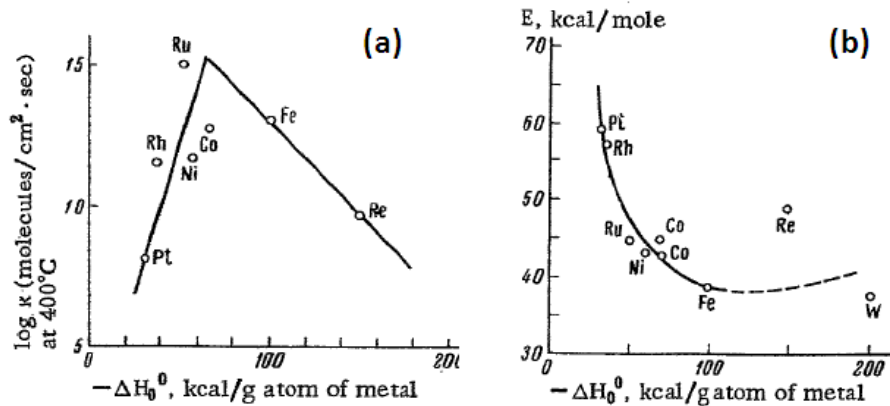


Figure 1-2. a Activity of metals in the decomposition of ammonia as function of  $-\Delta H_0^0$ ; b Activation energy of the decomposition of ammonia on various metals as a function of  $-\Delta H_0^0$ . (Figures were taken from Ref. [11]).

In the literature of ammonia decomposition, a large number of catalysts systems have been tested, which are Fe [12-21], Ni [6, 13, 22-28], Pt [10, 29-32], Ir [6, 32-34], Rh [10, 32, 35-38], Pd [10, 32, 35], Ru [6, 10, 27, 35, 39-60], Ni-Pt [7], W [61, 62], Mo [63], carbides (  $MoC_x$  [64],  $VC_x$  [65],  $WC_x$  [66],  $FeC_x$  [67]), nitrides ( $MoN_x$  [68],  $VN_x$  [69, 70],  $WN_x$  [61]), and  $ZrON$  [71, 72]. Although many proved to be active systems,

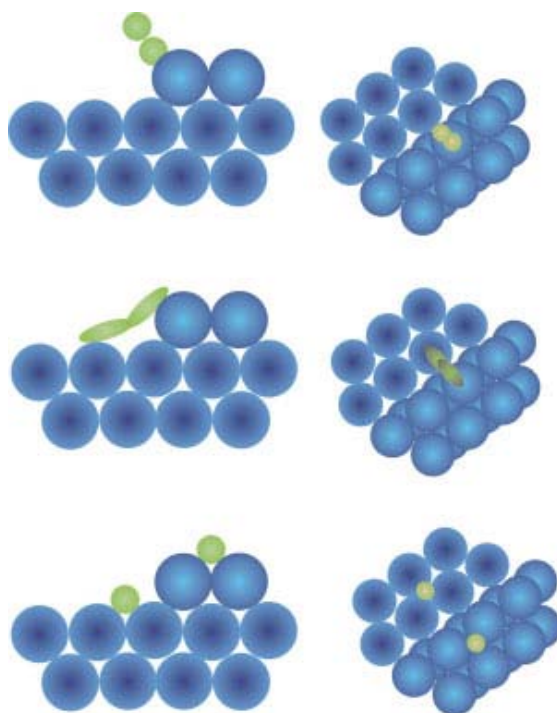
only iron and ruthenium have been intensively studied with the aims of studying the reverse reaction of ammonia synthesis more than 50 years ago and hydrogen production for the hot project of fuel cell at the end of last century. Some works from Papapolymerou et al. [32], Choudhary et al. [6] and Yin et al. [10] gave the comparisons of the ammonia decomposition reactivity among different metals, normally ranking in the order of: Ru > Ir > Rh > Ni > Pt > Pd > Fe, which were also reported by Tanaka and Tamaru [11] some 40 years ago (as shown in Fig. 1-2).

### ***1.3.2.1 Ruthenium***

The early studies on ruthenium catalysts for the ammonia decomposition were focused on the investigation of ammonia synthesis. Amano and Taylor reported the higher catalytic activity of ruthenium than rhodium and palladium supported on alumina for ammonia decomposition.[35] Tsai and Weinberg investigated the steady-state decomposition kinetics of ammonia on Ru(001).[40] Their results showed the temperature dependence of the reaction limiting step, that is desorption of NH<sub>3</sub> and dissociation of N-H bond at high temperatures, and only desorption of NH<sub>3</sub> at low temperature. This reaction was further investigated on stepped Ru(1110) and flat Ru(001) surfaces by Egawa et al.[39] They found that the rate of N<sub>2</sub> formation on Ru(1110) is one order of magnitude faster than that on Ru(001) for which edge effects have been eliminated. A much more open structure of Ru(11 $\bar{2}$ 1) surface was also proved to be much more reactive than Ru(0001) surface, which were reported by Dietrich et al.[41]

Those successful works on the single-crystal approach could give us a proposed general concept that the steps should be the active sites, and not the low-indexed flat terraces. This suggests that the abundance of steps [73] is much larger in morphologically “rough” particles rather than in equilibrated flat forms of bulk or well-structured particulate preparations.[9] Of course much more precise works were conducted in ammonia synthesis, which focused on the dissociative activation of N<sub>2</sub>, that is the energy barrier should be identical between single crystal and nanostructured systems.[5, 73-78] The central step in ammonia synthesis, which is the dissociative activation of N<sub>2</sub> on a Ru surface was elucidated by Schlögl [9] (in scheme 1-1), that N<sub>2</sub> molecule adsorbed at an edge site is followed by activation requiring a maximum electron density from the

catalyst to populate the anti-bonding states of the di-nitrogen molecules. According to this impression, the reverse reaction, ammonia decomposition, should require two neighboring stepped sites to recombinative desorption of one  $N_2$  molecule. This might be the main reason differs the mechanism in the synthesis and decomposition of ammonia, which will be presented in Chapter 3.



Scheme 1-1. An artist's impression of an active site in nitrogen dissociation. (Image was taken from Ref. [9]).

At the beginning of this century, due to the requirement of high purity hydrogen for fuel cell applications, there was a renewed interest of nanostructured ruthenium catalysts for ammonia decomposition.<sup>[6]</sup> Numerous supports were selected for deposition of nanostructured Ru particles, such as  $SiO_2$  <sup>[6]</sup>,  $Al_2O_3$  <sup>[6, 10, 48, 49, 57, 59]</sup>,  $ZrO_2$  <sup>[10, 48, 52]</sup>,  $TiO_2$  <sup>[10, 49]</sup>, titanates <sup>[60]</sup>,  $MgO$  <sup>[10, 48, 49, 53]</sup>,  $MgAl_2O_4$  <sup>[46]</sup>, carbon materials (active carbon <sup>[10, 43, 44, 48, 49, 55, 58]</sup>, ordered mesoporous carbon <sup>[54, 55]</sup>, carbon black <sup>[55]</sup>, graphite <sup>[51, 55]</sup>, CNTs <sup>[10, 47-49, 55]</sup>), and industrial solid waste <sup>[56]</sup>. Most of these researches were trying to correlate the high activity of Ru to the structural and size of Ru nanoparticles following the idea that the activity benefited from the abundance of the particular step sites allowing the fivefold coordination of nitrogen (B-5 site as shown in Fig. 1-

3).<sup>[79]</sup> As shown in Fig.1-3-D, the density of active sites (B-5 site) of Ru particles calculated by Wulff construction shows the maximum abundance at about 2.5 nm, which is favorable compared to the experimental particle size distribution of practical Ru-based catalyst for ammonia synthesis. Garcí'a-Garcí'a et al.<sup>[58]</sup>, Zhang et al.<sup>[53]</sup> and Zheng et al.<sup>[57]</sup> reported the similar result that the optimum Ru particle size for ammonia decomposition is between 3 and 5 nm, which are in agreement with the maximum concentration of B-5 site on the Ru particle.

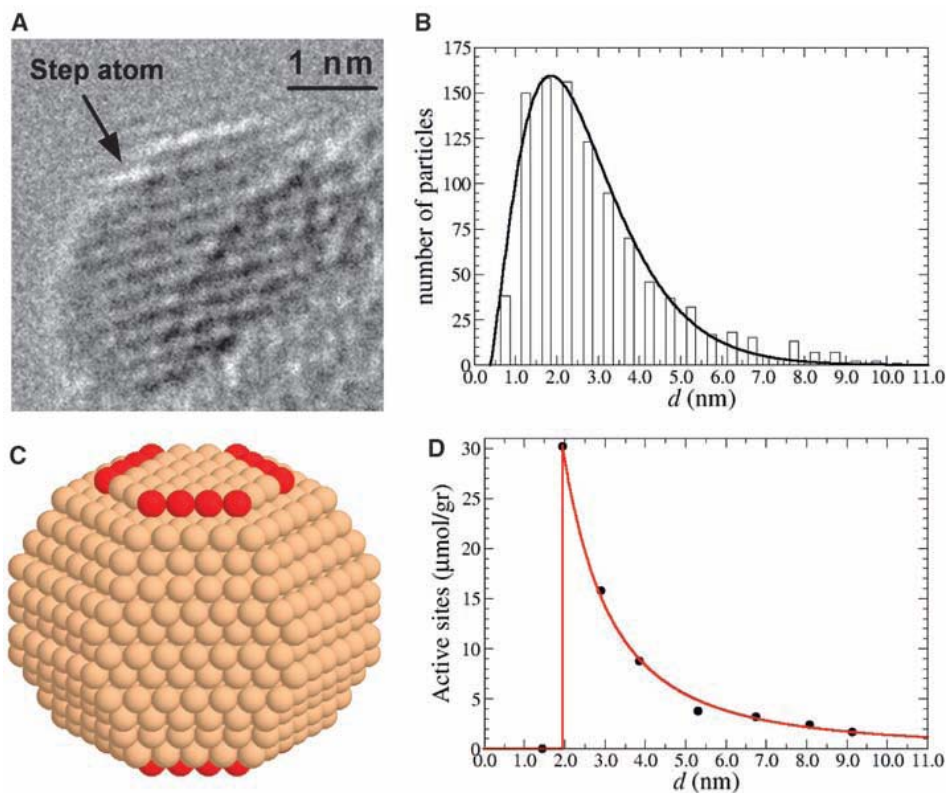


Figure 1-3. (A) TEM image of a supported Ru particle with a step. (B) Particle size distribution function obtained from the TEM experiments.  $d$ , diameter. (C) A typical calculated Ru particle, with an average diameter of 2.9 nm. Atoms that belong to active B5 sites are shown in red. (D) Density of active sites as a function of particle diameter, as calculated through analysis of the atomistic Wulff construction. (Figures were taken from Ref. [79])

It was further argued that larger particles are more active in this reaction.<sup>[59]</sup> Karim et al.<sup>[59]</sup> attributed the high activity on large Ru particle (about 7 nm) to elongated planar structure compared to the small Ru particle (1.8-3 nm) with hemispherical morphology. Unfortunately, the HRTEM image (Fig. 1-4-a) is difficult to confirm the elongated structure owing to the distortion of observing Ru particles, and the morphologies of Ru are not in line with the HADDF-STEM

image (Fig. 1-4-b), although the pretreatment of these two samples were different. The metal-support interaction effect and hydrogen inhibition effect were ignored by authors.

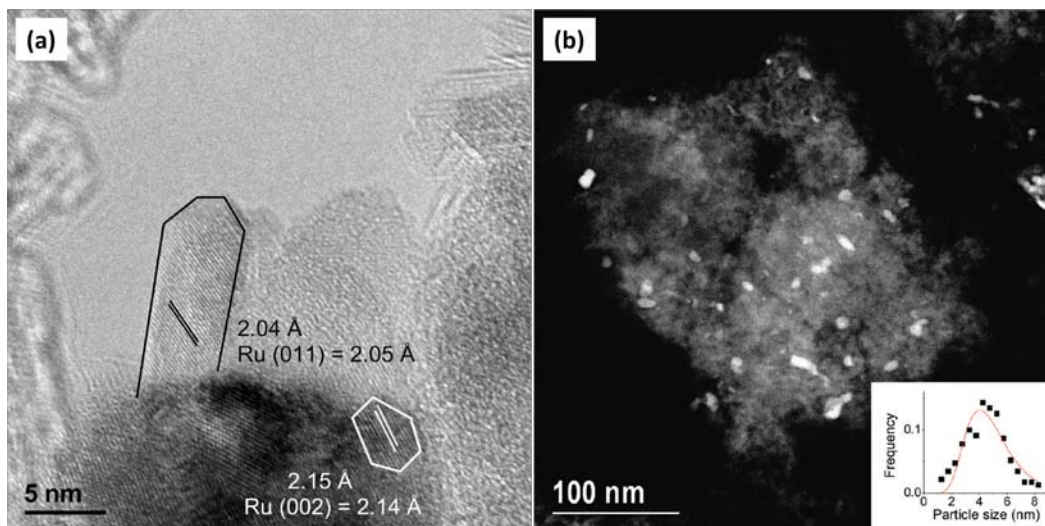


Figure 1-4. (a) HRTEM image of 4wt% Ru/Al<sub>2</sub>O<sub>3</sub> catalyst calcined at 500 °C and reduced at 450 °C; (b) HADDF-STEM image of 4wt% Ru/Al<sub>2</sub>O<sub>3</sub> catalyst reduced at 450 °C, calcined at 250 °C and reduced again at 450 °C. Both of them were collected after ammonia decomposition below 450 °C. (Figures were taken from Ref. [59]).

It is well known that the metal-support interaction could influence the particle size and shape of deposited metals. In ammonia decomposition, Raróg-Pilecka et al. [44] reported their results of Ru supported on active carbons modified with different pretreatments of supports; Li et al. summarized Ru supported on different ordered mesoporous carbons (OMC) [54] and different carbons [55]. Unfortunately, the correlations of structures and functions were still missing in the study of Ru-carbon system in ammonia decomposition reaction. It should be noticed that, among the numerous Ru-based catalyst, the one supported on CNTs seems to be the most active catalyst [8, 10, 47-49], which were ascribed to the basicity and conductivity of CNTs as support by authors. We believed that the key points of Ru-carbon system in ammonia decomposition are still missing, that are:

- How does carbon anchor ruthenium particles? How does the local structure of carbon influence the structure of ruthenium particles?
- Direct characterization information of practical Ru particles with different morphologies offering different catalytic performances.

In Chapter 3, we summarized the results on Ru-carbon system in efforts to answer the above questions. It is well known that ruthenium system is so sensitive to promotion, both electronically and structurally.<sup>[5, 9]</sup> The promotion effects on ruthenium for ammonia decomposition were not mainly discussed in this thesis, due to the complicated interactions between Ru, carbon and promoters.

### ***1.3.2.2 Iron, cobalt and nickel***

The early transition metals (Fe, Co and Ni) were also investigated in ammonia decomposition with the aim of a better understanding of ammonia synthesis during the early study.<sup>[12, 14, 16, 80-82]</sup> Unlike ruthenium catalysts, the few studies of iron catalysts in ammonia decomposition to hydrogen for fuel cell application is due to the poor catalytic performance (activity and stability) of iron catalyst, which should be related to the much stronger interaction of Fe-N compared to Ru-N.<sup>[9]</sup> This strong interaction between iron and nitrogen could lead to the formation of subnitrides, or even bulk nitrides, which were believed to be the inhibitors for the decomposition of ammonia described in earlier studies.<sup>[83, 84]</sup> In order to achieve high activity of iron catalyst, high energy is needed to overcome the large energy barrier of nitrogen desorption, which leads much higher reaction temperature on iron catalyst compared to ruthenium one. The consequence of high reaction temperature is the sintering of iron particles, leading to the deactivation of reactivity owing to the lost of active surface.

At the beginning of this century, both experimental<sup>[85-88]</sup> and theoretical<sup>[89-91]</sup> works reported a similar non-ruthenium catalyst, that is binary catalytic components following the quite old idea to optimize the performance of those elements on the slope of the curve (Fig. 1-2, or the re-plotted curve in Ref. [92]) which react either too little or too vigorously with nitrogen. The volcano curve in figure 1-5 (similar tendency can be found in earlier study<sup>[92]</sup>) shows the

correlation between computed TOFs and calculated relative heats of chemisorptions of activated nitrogen. In general, the idea is combining two metals: one with too high adsorption energy and one with too low adsorption energy of nitrogen interaction, which could achieve the optimum electronic structure for activation of di-nitrogen.

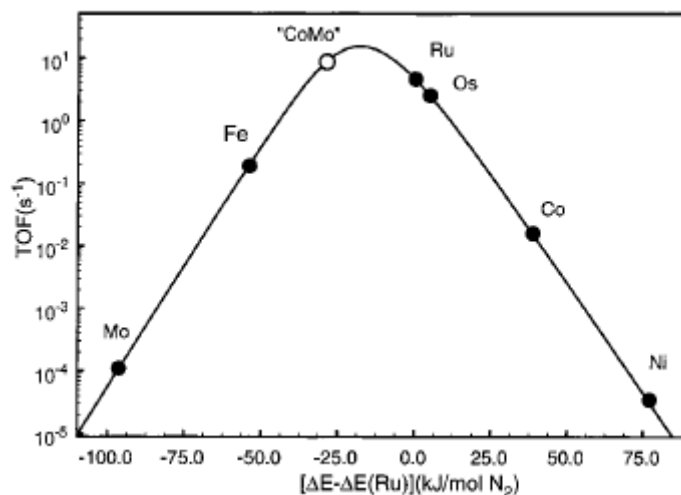


Figure 1-5. Calculated turnover frequencies for ammonia synthesis as a function of the adsorption energy of nitrogen. (Figure were taken from Ref. [89]).

We believe that, following the mentioned idea of combining two metallic elements should also work in the reverse reaction, ammonia decomposition. It should be additionally noticed that, the interaction between H and iron metal is much weaker compared to ruthenium, which could not lead to such a strong effect of hydrogen inhibition as Ru catalyst. In chapter 4, the modification of electronic structure of iron by cobalt and nickel will be investigated.

### 1.3.2.3 Carbide and nitride

It is well known that transition metal carbide and nitride exhibit similar electronic properties as noble metals, which was mainly inspired by the pioneer work of Levy and Boudart,<sup>[93]</sup> that the tungsten carbide showed the similar behavior as platinum in hydrogenolysis and isomerization of 2,2-dimethylpropane. Along the history of ammonia, one of the important issues is the formation

of nitride, like iron catalyst, which was named “ammonia iron” by Schlögl,<sup>[94]</sup> who drew an intensively roadmap of catalytic iron for ammonia synthesis.<sup>[9]</sup> Nitrides of group IVB and VIIB, and of Fe, Co and Ni are interstitial compounds. Those of Fe, Co and Ni are only formed from  $\text{NH}_3$  and not  $\text{N}_2$ .

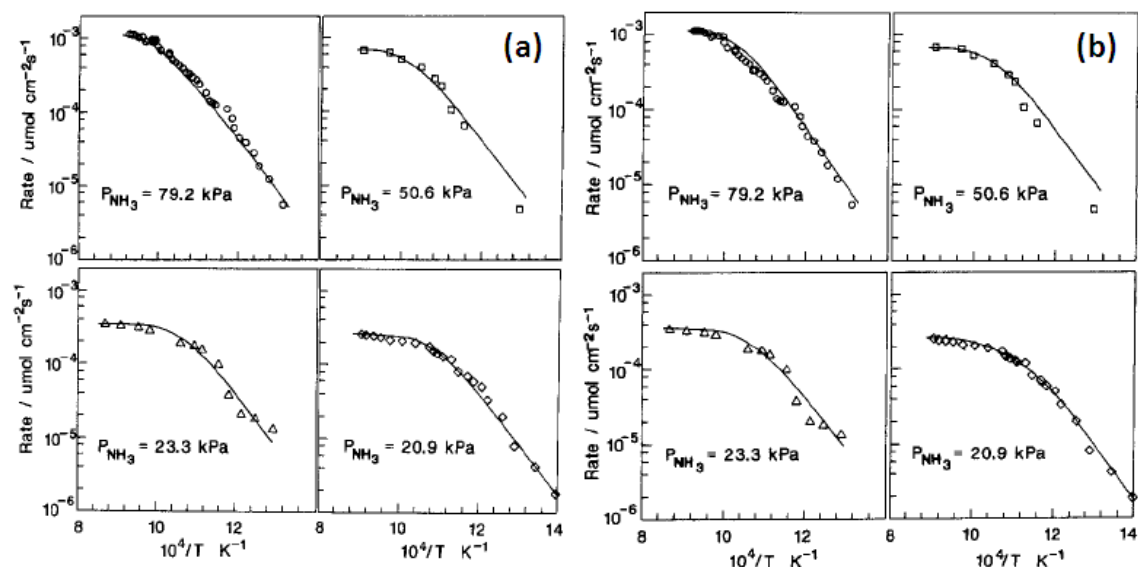


Figure 1-6. Ammonia decomposition reaction rates over vanadium nitride as function of temperature with different ammonia partial pressures. (a) ammonia first-order model, (b) ammonia second-order model. (Figures were taken from Ref. [70]).

On the other hand, considering the catalytic efficiency of the elements for synthesis and decomposition ammonia was correlated with the chemisorption energy of nitrogen, carbides and nitrides have been introduced in both synthesis and decomposition of  $\text{NH}_3$ .<sup>[95]</sup> Oyama showed a number of interstitial alloys (molybdenum carbide and nitride), that were more active than ruthenium but less active than the doubly-promoted iron catalyst for ammonia synthesis.<sup>[96]</sup> He also reported similar rate parameters of vanadium nitride to those of iron and platinum in ammonia decomposition.<sup>[70]</sup> He found that on vanadium nitride system at high temperature, the rate of ammonia decomposition was independent of nitrogen and hydrogen partial pressures, and was first order in ammonia partial pressures at low temperatures and zero order at high temperatures (as shown in Figure 1-6). The observation suggests that the reaction could follow

the Tamaru mechanism, that is the irreversible steps of ammonia decomposition are the adsorption of ammonia and desorption of dinitrogen.<sup>[97]</sup> This finding differs from the earlier reported work on ammonia decomposition over vanadium nitride,<sup>[69]</sup> in which the Temkin-Pyzhev mechanism was observed, that is nitrogen desorption is the only rate-determining step.<sup>[98]</sup>

The preparations of the two mentioned vanadium nitrides are slight different, one was pretreated with ammonia at above 1000 °C over V<sub>2</sub>O<sub>5</sub> and the other was with ammonium vanadate. This might lead to a different structure of nitrides, which could influence the reaction behavior as consequence. With this consideration, a primary comparison of kinetic reaction behaviors was investigated over three types of molybdenum nitrides, which are prepared *in-situ* from high surface area molybdenum carbide, molybdenum trioxide and nanosized molybdenum nitride. Results will be shown in chapter 6.

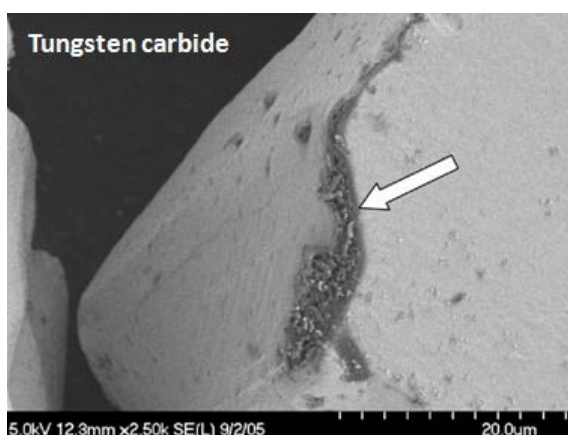


Figure 1-7. SEM image of WC catalyst after pretreatment in the presence of a H<sub>2</sub>-CO mixture. (Image was taken from Ref. [66]).

Another aim to develop those three types of nitride/carbide is related to the low performance of metal carbides/nitrides for ammonia decomposition in the existing literature. Choi investigated vanadium carbide<sup>[65]</sup> and molybdenum carbide,<sup>[64]</sup> and Pansare et al. studied tungsten carbide<sup>[66]</sup> for ammonia decomposition. Those materials reported in the literature showed interesting performance for ammonia decomposition, unfortunately, none of the catalysts could achieve more than 4 mmol/(g<sub>cat</sub>·min) H<sub>2</sub> formation rate, which is likely due to the low surface area of the reported materials (representative morphology of those kind of materials was shown in figure 1-

7.). Recently, a mesoporous  $\text{Fe}_3\text{C}$  was synthesized by Kraupner et al.<sup>[67]</sup> using a hard-templating approach with carbothermal reduction. Although, a 16-hour constant  $\text{H}_2$  formation rate of about 9 could be achieved over this catalyst, the reactivity is still not comparable with Ru-based catalyst. In Chapter 5 of this thesis, we will report a high active molybdenum carbide catalyst showing a stable performance in 100 hours.

### ***1.3.3 The supports (carbon)***

As mentioned in last section, numerous support materials have been utilized for the catalysts in ammonia decomposition. The application of carbon materials as supports has been widely reported in catalysis, especially in ammonia synthesis,<sup>[9, 94]</sup> mostly on activated carbon (AC) owing to its high thermal stability, high surface area and cheap and easy recovery of the metal catalyst by simple combustion.

Carbon is a versatile material which, depending on its hybridization and assembly in one-, two- or three-dimensional networks, exhibits important electronic and chemical properties with countless practical applications. For example, it is found in printer inks, pencils, water purification systems, thermal isolation and antistatic materials. More elaborate carbon materials such as carbon nanotubes are also employed in nanotechnology, with applications in sensing or field emission. Black carbon is cheap, easy to synthesize and to modify. Thus, it is also particularly suited as a support for heterogeneous catalysis as both the structure (macroscopic shape, porosity) and the surface chemistry can be tailored depending on the target application. The most important reason to use carbon as support to deposit metals is related to the structural variability and tunable chemical environment of carbon surface given by its tendency to form homonuclear bonds in essentially two hybridizations. The inter-nuclear bond length of different hybridizations will be different which will have chemical and physical consequences. The basal plane of graphite is inert and as strong as diamond, whereas the interplanar bonds are very weak which gives graphite the soft and lubricant properties. Chemical reactivity is also profoundly different for the basal and the prismatic edge planes in graphite. Combustion in perfect graphite for example will preferably start from the prismatic edges. These anisotropies in graphite of physical and chemical characters are the result of the trigonal geometry. Thus geometrical

change of homonuclear carbon materials eg; vacancies, defects, bending, the presence of pentagon- or heptagon- ring within the hexagonal network in graphite will altered these properties. In addition the broad possibilities of hetero elements present in carbon materials due to the moderate electronegativity of carbon are able to modify the electronic properties.

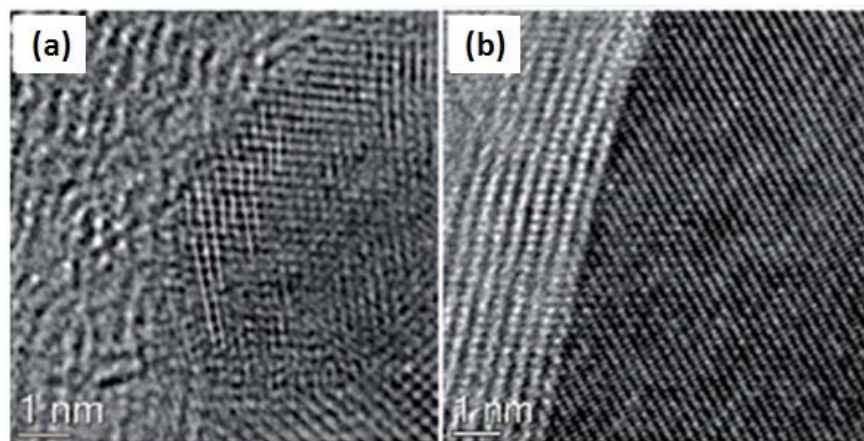


Figure 1-8. High resolution TEM images of nickel particles deposited on defective carbon (a) and graphitic carbon (b). (Images were taken from Ref. [99]).

It is of crucial importance to study how the graphitic character influences the anchoring of the nanoparticles and eventually modifies the catalytic activity of the metal. Varying the graphitic order might offer new and fascinating possibilities for catalyst design. The direct observation of different morphology of metal nanoparticle on different CNTs surface was reported by Rinaldi et al.<sup>[99]</sup> As shown in Figure 1-8-a, the nickel nanoparticles supported on defective carbon are polycrystalline, which is in contrast that nickel on graphitic carbon support is well ordered (fig. 1-8-b). This different morphology of nickel nanoparticles could lead to the different carbon filament grown by deposition of  $C_2H_4$ . It should be noted that, the direct evidence from in-situ XPS reveals the carbon incorporation that changes the catalytic performance of the nickel catalyst, which is a powerful tool to understand the heterogeneous catalytic process.

Recently, Shao et al. reported a high activity and stable nanocrystalline  $Pd_2Ga$  intermetallics catalyst for selective hydrogenation of alkyne, due to the oxidized vacancies and local double bonds on CNTs inhibiting sintering and loss of the  $Pd_2Ga$  nanoparticles during reactions.<sup>[100]</sup>

Figure 1-9 shows the representative HRTEM image of Pd<sub>2</sub>Ga nanoparticles supported on CNTs surface.

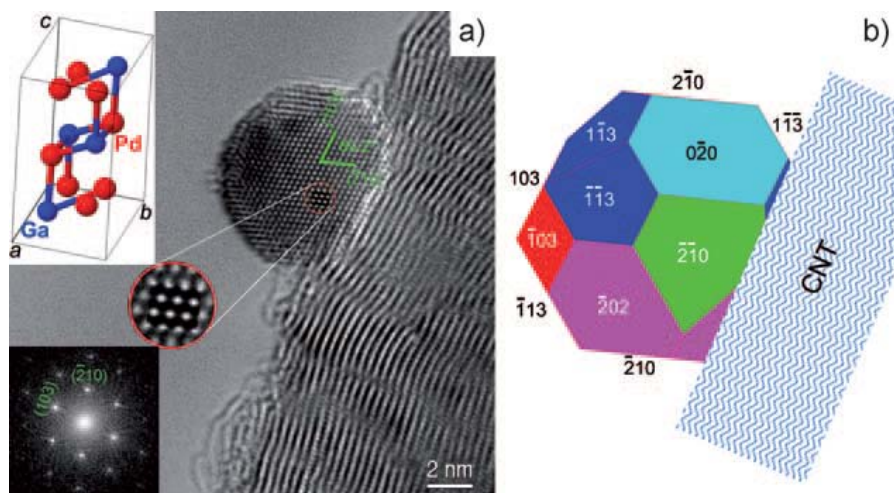


Figure 1-9. Microstructure characterizations of Pd<sub>2</sub>Ga/CNT. (a) HRTEM image, with crystallographic model of Pd<sub>2</sub>Ga and fast Fourier transform of the local HRTEM image; (b) the Wulff constructions of the corresponding Pd<sub>2</sub>Ga nanoparticle in (a). (Figure was taken from Ref. [100]).

Thus, modified graphite and CNTs have been chosen as supports for metallic nanoparticles and metal carbide in this study in order to investigate the metal-carbon interaction influence on the catalytic decomposition of ammonia. When using CNTs as support, selective deposition of catalytic component was also investigated, as it was reported that a “confinement effect” originates from the tubular graphitic structure of CNT support.<sup>[101-106]</sup> Considering the average diameter of multi-wall CNTs, which is normally large than 5-10 nm, the catalytic differences might directly relate to the local morphology of nanoparticles owing to the bending of graphene sheets, but not to the electronic density differences on the walls of CNTs.

## 1.4 Publication declaration

Parts of this work were published and will be submitted as articles, details as follows:

1. “Structure-Function Correlation for Ru/CNT in the Catalytic Decomposition of Ammonia”

W. Zheng, J. Zhang, B. Zhu, R. Blume, Y. Zhang, K. Schlichte, R. Schlögl, F. Schüth, D. S. Su, *ChemSusChem*, 2010, 3(2): p. 226-230.

2. “Revealing Catalytic Activity of Ru/graphite for NH<sub>3</sub> Decomposition: Metal Support Interaction and Reaction Intermediates”

W. Zheng, J. Zhang, L. Yao, R. Blume, D. S. Su, K. Schlichte, F. Schüth, R. Schlögl, in preparation.

3. “Individual Fe-Co Alloy Nanoparticles on Carbon Nanotubes: Structural and Catalytic Properties”

J. Zhang, J. Müller, W. Zheng, D. Wang, D. S. Su, R. Schlögl, *Nano Lett.*, 2008, 8(9): p. 2738-2743.

4. “High Surface Area Molybdenum Carbide for Ammonia Decomposition”

W. Zheng, T. Cotter, P. Kaghazchi, T. Jacob, W. Zhang, D. S. Su, K. Schlichte, F. Schüth, R. Schlögl, in preparation.

5. “Stabilizing Molybdenum Nitride Nanoparticles by Carbon from Hydrothermal Carbonization”

W. Zheng, D. S. Su, B. Zhang, K. Schlichte, F. Schüth, R. Schlögl, in preparation.

6. “Kinetic study of Nanostructured Materials for Ammonia Decomposition”

W. Zheng, T. Otremba, B. Frank, D. S. Su, R. Schomäcker, R. Schlögl, in preparation.

## References

1. McCarthy, J. (1995-12-31) *Hydrogen*.
2. Osterloh, F.E., *Inorganic Materials as Catalysts for Photochemical Splitting of Water*. Chemistry of Materials, 2007. **20**(1): p. 35-54.
3. in *Handbook of Fuel Cells: Fundamentals, Technology, Applications, 4-Volume Set*, W. Vielstich, A. Lamm, and H.A. Gasteiger, Editors. March 2003, Wiley. p. 3826.
4. Schlögl, R. and A. Züttel, *Hydrogen-Storage Materials for Mobile Applications*. Nature, 2001. **414**(6861): p. 353-358.
5. Schlögl, R., *Catalytic Synthesis of Ammonia—A “Never-Ending Story”?* Angewandte Chemie International Edition, 2003. **42**(18): p. 2004-2008.
6. Choudhary, T.V., C. Sivadinarayana, and D.W. Goodman, *Catalytic Ammonia Decomposition: CO<sub>x</sub>-free Hydrogen Production for Fuel Cell Applications*. Catalysis Letters, 2001. **72**(3-4): p. 197-201.
7. Chellappa, A.S., C.M. Fischer, and W.J. Thomson, *Ammonia Decomposition Kinetics over Ni-Pt/Al<sub>2</sub>O<sub>3</sub> for PEM Fuel Cell Applications*. Applied Catalysis A: General, 2002. **227**(1-2): p. 231-240.
8. Yin, S.F., et al., *A Mini-Review on Ammonia Decomposition Catalysts for On-Site Generation of Hydrogen for Fuel Cell Applications*. Applied Catalysis a-General, 2004. **277**(1-2): p. 1-9.
9. Schlögl, R., *Ammonia Synthesis*, in *Handbook of Heterogeneous Catalysis*, G. Ertl, et al., Editors. 2008, Wiley-VCH Verlag GmbH & Co. KGaA.
10. Yin, S.F., et al., *Investigation on the Catalysis of CO<sub>x</sub>-free Hydrogen Generation from Ammonia*. Journal of Catalysis, 2004. **224**(2): p. 384-396.
11. Tanaka, K.-I. and K. Tamaru, *On One General Principle of the Catalytic Activity of Metals*. Kinetika i Kataliz, 1966. **7**(2): p. 242-247.
12. Love, K.S. and P.H. Emmett, *The Catalytic Decomposition of Ammonia over Iron Synthetic Ammonia Catalysts*. Journal of the American Chemical Society, 1941. **63**(12): p. 3297-3308.
13. Logan, S.R. and C. Kemball, *The Catalytic Decomposition of Ammonia on Evaporated Metal Films*. Transactions of the Faraday Society, 1960. **56**: p. 144-153.
14. Takezawa, N. and I. Toyoshima, *The Change of the Rate-Determining Step of the Ammonia Decomposition over an Ammonia Synthetic Iron Catalyst*. The Journal of Physical Chemistry, 1966. **70**(2): p. 594-595.
15. Lu, A.-H., et al., *Spatially and Size Selective Synthesis of Fe-Based Nanoparticles on Ordered Mesoporous Supports as Highly Active and Stable Catalysts for Ammonia Decomposition*. Journal of the American Chemical Society, 2010. **132**(40): p. 14152-14162.
16. Löffler, D.G. and L.D. Schmidt, *Kinetics of NH<sub>3</sub> Decomposition on Iron at High Temperatures*. Journal of Catalysis, 1976. **44**(2): p. 244-258.
17. Jedynek, A., et al., *Ammonia Decomposition over the Carbon-Based Iron Catalyst Promoted with Potassium*. Applied Catalysis A: General, 2002. **237**(1-2): p. 223-226.
18. Ohtsuka, Y., *Decomposition of Ammonia with Iron and Calcium Catalysts Supported on Coal Chars*. Fuel, 2004. **83**(6): p. 685-692.
19. Zhang, J., et al., *Commercial Fe- or Co-containing Carbon Nanotubes as Catalysts for NH<sub>3</sub> Decomposition*. Chemical Communications, 2007(19): p. 1916.

20. Kielbasa, K., R. Pelka, and W. Arabczyk, *Studies of the Kinetics of Ammonia Decomposition on Promoted Nanocrystalline Iron Using Gas Phases of Different Nitriding Degree*. The Journal of Physical Chemistry A, 2010. **114**(13): p. 4531-4534.
21. Arabczyk, W. and J. Zamlynny, *Study of the Ammonia Decomposition over Iron Catalysts*. Catalysis Letters, 1999. **60**(3): p. 167-171.
22. Ertl, G. and J. Rüstig, *Decomposition of NH<sub>3</sub> on Nickel: Absence of a Magneto-Catalytic Effect*. Surface Science, 1982. **119**(1): p. L314-L318.
23. Abashar, M.E.E., Y.S. Al-Sughair, and I.S. Al-Mutaz, *Investigation of Low Temperature Decomposition of Ammonia Using Spatially Patterned Catalytic Membrane Reactors*. Applied Catalysis A: General, 2002. **236**(1-2): p. 35-53.
24. Zhang, J., et al., *Characterizations and Activities of the Nano-sized Ni/Al<sub>2</sub>O<sub>3</sub> and Ni/La-Al<sub>2</sub>O<sub>3</sub> Catalysts for NH<sub>3</sub> decomposition*. Applied Catalysis A: General, 2005. **290**(1-2): p. 87-96.
25. Zhang, J., H. Xu, and W. Li, *Kinetic study of NH<sub>3</sub> Decomposition over Ni nanoparticles: The Role of La Promoter, Structure Sensitivity and Compensation effect*. Applied Catalysis A: General, 2005. **296**(2): p. 257-267.
26. Zheng, W., et al., *Effects of CeO<sub>2</sub> Addition on Ni/Al<sub>2</sub>O<sub>3</sub> Catalysts for the Reaction of Ammonia Decomposition to Hydrogen*. Applied Catalysis B: Environmental, 2008. **80**(1-2): p. 98-105.
27. Li, X., et al., *Ammonia Decomposition over Ru and Ni Catalysts Supported on Fumed SiO<sub>2</sub>, MCM-41, and SBA-15*. Journal of Catalysis, 2005. **236**(2): p. 181-189.
28. Liu, H., et al., *Preparation, Characterization and Activities of the Nano-sized Ni/SBA-15 Catalyst for Producing CO<sub>x</sub>-free Hydrogen from Ammonia*. Applied Catalysis A: General, 2008. **337**(2): p. 138-147.
29. Löffler, D.G. and L.D. Schmidt, *Kinetics of NH<sub>3</sub> Decomposition on Polycrystalline Pt*. Journal of Catalysis, 1976. **41**(3): p. 440-454.
30. Tsai, W., J.J. Vajo, and W.H. Weinberg, *Inhibition by Hydrogen of the Heterogeneous Decomposition of Ammonia on Platinum*. The Journal of Physical Chemistry, 1985. **89**(23): p. 4926-4932.
31. Guthrie, W.L., J.D. Sokol, and G.A. Somorjai, *The Decomposition of Ammonia on the Flat (111) and Stepped (557) Platinum Crystal Surfaces*. Surface Science, 1981. **109**(2): p. 390-418.
32. Papapolymerou, G. and V. Bontozoglou, *Decomposition of NH<sub>3</sub> on Pd and Ir Comparison with Pt and Rh*. Journal of Molecular Catalysis A: Chemical, 1997. **120**(1-3): p. 165-171.
33. Santra, A.K., et al., *Decomposition of NH<sub>3</sub> on Ir(100): A Temperature Programmed Desorption Study*. The Journal of Physical Chemistry B, 2001. **106**(2): p. 340-344.
34. Chen, W.H., I. Ermanoski, and T.E. Madey, *Decomposition of Ammonia and Hydrogen on Ir Surfaces: Structure Sensitivity and Nanometer-Scale Size Effects*. Journal of the American Chemical Society, 2005. **127**(14): p. 5014-5015.
35. Amano, A. and H. Taylor, *The Decomposition of Ammonia on Ruthenium, Rhodium and Palladium Catalysts Supported on Alumina*. Journal of the American Chemical Society, 1954. **76**(16): p. 4201-4204.
36. Leewis, C., et al., *Ammonia Adsorption and Decomposition on Silica Supported Rh Nanoparticles Observed by in situ Attenuated Total Reflection Infrared Spectroscopy*. Applied Surface Science, 2006. **253**(2): p. 572-580.

37. Gasser, R.P.H. and D.P. Green, *The Decomposition of Ammonia at Low Pressures by Ruthenium*. Surface Science, 1979. **82**(2): p. L582-L584.
38. Vavere, A. and R.S. Hansen, *Decomposition of Ammonia on Rhodium Crystals*. Journal of Catalysis, 1981. **69**(1): p. 158-171.
39. Egawa, C., et al., *Ammonia Decomposition on (1 1 10) and (0 0 1) Surfaces of Ruthenium*. Journal of the Chemical Society, Faraday Transactions 1: Physical Chemistry in Condensed Phases, 1984. **80**(6): p. 1595-1604.
40. Tsai, W. and W.H. Weinberg, *Steady-State Decomposition of Ammonia on the Ruthenium(001) Surface*. The Journal of Physical Chemistry, 1987. **91**(20): p. 5302-5307.
41. Dietrich, H., K. Jacobi, and G. Ertl, *Decomposition of NH<sub>3</sub> on Ru(111)*. Surface Science, 1996. **352-354**: p. 138-141.
42. Bradford, M.C.J., P.E. Fanning, and M.A. Vannice, *Kinetics of NH<sub>3</sub> Decomposition Over Well Dispersed Ru*. Journal of Catalysis, 1997. **172**(2): p. 479-484.
43. Raróg-Pilecka, W., *Ammonia Decomposition over the Carbon-based Ruthenium Catalyst Promoted with Barium or Cesium*. Journal of Catalysis, 2003. **218**(2): p. 465-469.
44. Raróg-Pilecka, W., et al., *Catalytic Properties of Small Ruthenium Particles Deposited on Carbon: Ammonia Decomposition Studies*. Carbon, 2003. **41**(3): p. 589-591.
45. Deshmukh, S.R., A.B. Mhadeshwar, and D.G. Vlachos, *Microreactor Modeling for Hydrogen Production from Ammonia Decomposition on Ruthenium*. Industrial & Engineering Chemistry Research, 2004. **43**(12): p. 2986-2999.
46. Szmigielski, D., *Ammonia Decomposition over the Ruthenium Catalysts Deposited on Magnesium-Aluminum Spinel*. Applied Catalysis A: General, 2004. **264**(1): p. 59-63.
47. Wang, S., *Investigation on Modification of Ru/CNTs Catalyst for the Generation of CO<sub>x</sub>-free Hydrogen from Ammonia*. Applied Catalysis B: Environmental, 2004. **52**(4): p. 287-299.
48. Yin, S., *Nano Ru/CNTs: a Highly Active and Stable Catalyst for the Generation of CO<sub>x</sub>-free Hydrogen in Ammonia Decomposition*. Applied Catalysis B: Environmental, 2004. **48**(4): p. 237-241.
49. Yin, S.F., et al., *Carbon Nanotubes-Supported Ru Catalyst for the Generation of CO<sub>x</sub>-free Hydrogen from Ammonia*. Catalysis Today, 2004. **93-95**: p. 27-38.
50. Sorensen, R., et al., *Catalytic Ammonia Decomposition: Miniaturized Production of CO<sub>x</sub>-free Hydrogen for Fuel Cells*. Catalysis Communications, 2005. **6**(3): p. 229-232.
51. Sørensen, R.Z., et al., *Promoted Ru on High-Surface Area Graphite for Efficient Miniaturized Production of Hydrogen from Ammonia*. Catalysis Letters, 2006. **112**(1-2): p. 77-81.
52. Yin, S., et al., *Nanosized Ru on High-Surface-Area Superbasic ZrO<sub>2</sub>-KOH for Efficient Generation of Hydrogen via Ammonia Decomposition*. Applied Catalysis A: General, 2006. **301**(2): p. 202-210.
53. Zhang, J., et al., *Highly Efficient Ru/MgO Catalysts for NH<sub>3</sub> Decomposition: Synthesis, Characterization and Promoter Effect*. Catalysis Communications, 2006. **7**(3): p. 148-152.
54. Li, L., et al., *Catalytic Ammonia Decomposition over CMK-3 Supported Ru Catalysts: Effects of Surface Treatments of Supports*. Carbon, 2007. **45**(1): p. 11-20.

55. Li, L., et al., *Catalytic Ammonia Decomposition over Ru/carbon Catalysts: The Importance of the Structure of Carbon Support*. Applied Catalysis A: General, 2007. **320**: p. 166-172.
56. Ng, P.F., et al., *Catalytic Ammonia Decomposition over Industrial-Waste-Supported Ru Catalysts*. Environmental Science & Technology, 2007. **41**(10): p. 3758-3762.
57. Zheng, W., et al., *NH<sub>3</sub> Decomposition Kinetics on Supported Ru Clusters: Morphology and Particle Size Effect*. Catalysis Letters, 2007. **119**(3-4): p. 311-318.
58. García-García, F., A. Guerrero-Ruiz, and I. Rodríguez-Ramos, *Role of B5-Type Sites in Ru Catalysts Used for the NH<sub>3</sub> Decomposition Reaction*. Topics in Catalysis, 2009. **52**(6): p. 758-764.
59. Karim, A.M., et al., *Correlating Particle Size and Shape of Supported Ru/ $\gamma$ -Al<sub>2</sub>O<sub>3</sub> Catalysts with NH<sub>3</sub> Decomposition Activity*. Journal of the American Chemical Society, 2009. **131**(34): p. 12230-12239.
60. Klerke, A., S.K. Klitgaard, and R. Fehrmann, *Catalytic Ammonia Decomposition Over Ruthenium Nanoparticles Supported on Nano-Titanates*. Catalysis Letters, 2009. **130**(3-4): p. 541-546.
61. Shindo, H., et al., *Reaction Mechanism of Ammonia Decomposition on Tungsten*. Journal of the Chemical Society, Faraday Transactions 1: Physical Chemistry in Condensed Phases, 1980. **76**: p. 280-290.
62. Egawa, C., S. Naito, and K. Tamaru, *Adsorption and Decomposition of Ammonia on W(100); XPS and UPS Studies*. Surface Science, 1983. **131**(1): p. 49-60.
63. Boudart, M., et al., *Nitrogen Adsorption and Ammonia Decomposition on Polycrystalline Molybdenum*. Journal de Chimie Physique et de Physico-Chimie Biologique, 1981. **78**(11-12).
64. Choi, J.-G., *Ammonia Decomposition over Mo Carbides*. Journal of Industrial and Engineering Chemistry, 2004. **10**(6): p. 967-971.
65. Choi, J.-G., *Ammonia Decomposition over Vanadium Carbide Catalysts*. Journal of Catalysis, 1999. **182**(1): p. 104-116.
66. Pansare, S., W. Torres, and J. Goodwinjr, *Ammonia Decomposition on Tungsten Carbide*. Catalysis Communications, 2007. **8**(4): p. 649-654.
67. Kraupner, A., et al., *Mesoporous Fe<sub>3</sub>C Sponges as Magnetic Supports and as Heterogeneous Catalyst*. Journal of Materials Chemistry, 2010. **20**(29): p. 6019-6022.
68. Liang, C., et al., *Catalytic Decomposition of Ammonia over Nitrated MoN<sub>x</sub>/ $\alpha$ -Al<sub>2</sub>O<sub>3</sub> and NiMoNy/ $\alpha$ -Al<sub>2</sub>O<sub>3</sub> Catalysts*. Industrial & Engineering Chemistry Research, 2000. **39**(10): p. 3694-3697.
69. McGill, W.J. and F. Sebba, *The Kinetics of Ammonia Decomposition over Vanadium Nitride*. Journal of Catalysis, 1963. **2**(2): p. 104-108.
70. Oyama, S.T., *Kinetics of Ammonia Decomposition on Vanadium Nitride*. Journal of Catalysis, 1992. **133**(2): p. 358-369.
71. Soerijanto, H., et al., *The Impact of Nitrogen Mobility on the Activity of Zirconium Oxynitride Catalysts for Ammonia Decomposition*. Journal of Catalysis, 2007. **250**(1): p. 19-24.
72. Otremba, T., et al., *Kinetic Studies on Ammonia Decomposition over Zirconium Oxynitride*. Applied Catalysis A: General, 2011. **392**(1-2): p. 103-110.

73. Dahl, S., E. Törnqvist, and I. Chorkendorff, *Dissociative Adsorption of N<sub>2</sub> on ru(0001): A Surface Reaction Totally Dominated by Steps*. Journal of Catalysis, 2000. **192**(2): p. 381-390.
74. Hinrichsen, O., et al., *The Kinetics of Ammonia Synthesis over Ru-Based Catalysts: 1. The Dissociative Chemisorption and Associative Desorption of N<sub>2</sub>*. Journal of Catalysis, 1997. **165**(1): p. 33-44.
75. Rosowski, F., et al., *Ruthenium Catalysts for Ammonia Synthesis at High Pressures: Preparation, Characterization, and Power-Law Kinetics*. Applied Catalysis A: General, 1997. **151**(2): p. 443-460.
76. Dahl, S., et al., *Surface Science Based Microkinetic Analysis of Ammonia Synthesis over Ruthenium Catalysts*. Journal of Catalysis, 2000. **192**(2): p. 391-399.
77. Dahl, S., et al., *Role of Steps in N<sub>2</sub> Activation on Ru(0001)*. Physical Review Letters, 1999. **83**(9): p. 1814.
78. Dahl, S., et al., *The Synthesis of Ammonia over a Ruthenium Single Crystal*. Journal of Catalysis, 1998. **178**(2): p. 679-686.
79. Honkala, K., *Ammonia Synthesis from First-Principles Calculations*. Science, 2005. **307**(5709): p. 555-558.
80. Kunsman, C.H., *The Decomposition of Ammonia on Iron Catalysts*. Science, 1927. **65**(1691): p. 527-528.
81. Winter, E., *Der Katalytische Ammoniakzerfall an Eisen*. Z. physikal. Chem. , 1931. **B13**: p. 401-424.
82. Brunauer, S., K.S. Love, and R.G. Keenan, *Adsorption of Nitrogen and the Mechanism of Ammonia Decomposition Over Iron Catalysts*. Journal of the American Chemical Society, 1942. **64**(4): p. 751-758.
83. Mittasch, A. and W. Frankenburg, *Early Studies of Multicomponent Catalysts*, in *Advances in Catalysis*, V.I.K. W.G. Frankenburg and E.K. Rideal, Editors. 1950, Academic Press. p. 81-104.
84. Wagner, C., *Die Stabilität von Metallen und Metalloxiden als Katalysatoren in H<sub>2</sub>—O<sub>2</sub>-Gemischen und anderen reagierenden Gemischen*. Berichte der Bunsengesellschaft für physikalische Chemie, 1970. **74**(4): p. 401-409.
85. Kojima, R. and K.-i. Aika, *Cobalt Molybdenum Bimetallic Nitride Catalysts for Ammonia Synthesis: Part 1. Preparation and Characterization*. Applied Catalysis A: General, 2001. **215**(1-2): p. 149-160.
86. Kojima, R. and K.-i. Aika, *Cobalt Molybdenum Bimetallic Nitride Catalysts for Ammonia Synthesis: Part 3. Reactant Gas Treatment*. Applied Catalysis A: General, 2001. **219**(1-2): p. 157-170.
87. Kojima, R. and K.-i. Aika, *Cobalt Molybdenum Bimetallic Nitride Catalysts for Ammonia Synthesis: Part 2. Kinetic Study*. Applied Catalysis A: General, 2001. **218**(1-2): p. 121-128.
88. Kojima, R. and K.-i. Aika, *Rhenium Containing Binary Catalysts for Ammonia Synthesis*. Applied Catalysis A: General, 2001. **209**(1-2): p. 317-325.
89. Jacobsen, C.J.H., et al., *Catalyst Design by Interpolation in the Periodic Table: Bimetallic Ammonia Synthesis Catalysts*. Journal of the American Chemical Society, 2001. **123**(34): p. 8404-8405.
90. Bligaard, T., et al., *The Brønsted-Evans-Polanyi Relation and the Volcano Curve in Heterogeneous Catalysis*. Journal of Catalysis, 2004. **224**(1): p. 206-217.

91. Jacobsen, C.J.H., et al., *Optimal Catalyst Curves: Connecting Density Functional Theory Calculations with Industrial Reactor Design and Catalyst Selection*. Journal of Catalysis, 2002. **205**(2): p. 382-387.
92. Ozaki, A. and K. Aika, *Catalytic Activation of Dinitrogen*, in *Catalysis: Science and Technology*. 1981, Springer-Verlag: Berlin Heidelberg New York. p. 87-158.
93. Levy, R.B. and M. Boudart, *Platinum-Like Behavior of Tungsten Carbide in Surface Catalysis*. Science, 1973. **181**(4099): p. 547-549.
94. Schlögl, R., *Preparation and Activation of the Technical Ammonia Synthesis Catalyst*, in *Catalytic Ammonia Synthesis, Fundamental and Applied Catalysis*, J.R. Jennings, Editor. 1991, Springer: New York. p. 19.
95. Kojima, R. and K.-i. Aika, *Molybdenum Nitride and Carbide Catalysts for Ammonia Synthesis*. Applied Catalysis A: General, 2001. **219**(1-2): p. 141-147.
96. Oyama, S.T., *Preparation and Catalytic Properties of Transition Metal Carbides and Nitrides*. Catalysis Today, 1992. **15**(2): p. 179-200.
97. Tamaru, K., *A "New" General Mechanism of Ammonia Synthesis and Decomposition on Transition Metals*. Accounts of Chemical Research, 1988. **21**(2): p. 88-94.
98. Temkin, M. and V. Pyzhev, *Kinetics of Ammonia Synthesis on Promoted Iron Catalysts*. Acta Physicochimica Urss, 1940. **12**(3): p. 327-356.
99. Rinaldi, A., et al., *Dissolved Carbon Controls the Initial Stages of Nanocarbon Growth*. Angewandte Chemie International Edition, 2011. **50**(14): p. 3313-3317.
100. Shao, L., et al., *Nanosizing Intermetallic Compounds Onto Carbon Nanotubes: Active and Selective Hydrogenation Catalysts*. Angewandte Chemie International Edition, 2011: p. n/a-n/a.
101. Castillejos, E., et al., *An Efficient Strategy to Drive Nanoparticles into Carbon Nanotubes and the Remarkable Effect of Confinement on Their Catalytic Performance*. Angewandte Chemie International Edition, 2009. **48**(14): p. 2529-2533.
102. Ma, H., et al., *Pt nanoparticles Deposited over Carbon Nanotubes for Selective Hydrogenation of Cinnamaldehyde*. Catalysis Communications, 2007. **8**(3): p. 452-456.
103. Chen, W., et al., *Effect of Confinement in Carbon Nanotubes on the Activity of Fischer-Tropsch Iron Catalyst*. Journal of the American Chemical Society, 2008. **130**(29): p. 9414-9419.
104. Chen, W., X. Pan, and X. Bao, *Tuning of Redox Properties of Iron and Iron Oxides via Encapsulation within Carbon Nanotubes*. Journal of the American Chemical Society, 2007. **129**(23): p. 7421-7426.
105. Chen, W., et al., *Facile Autoredution of Iron Oxide/Carbon Nanotube Encapsulates*. Journal of the American Chemical Society, 2006. **128**(10): p. 3136-3137.
106. Pan, X., et al., *Enhanced Ethanol Production Inside Carbon-Nanotube Reactors Containing Catalytic Particles*. Nature Materials, 2007. **6**(7): p. 507-511.

# Chapter 2:

## Experimental and Characterization Methods

### 2.1 Catalytic performance measurements

#### 2.1.1 Reactivity evaluations

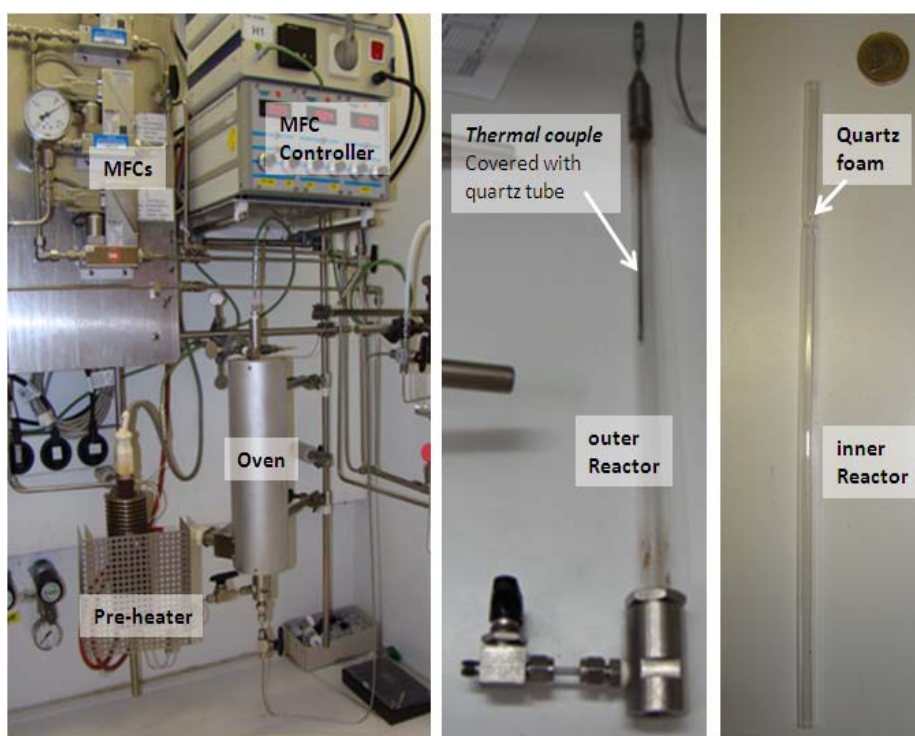


Figure 2-1. Overview photograph of the fixed bed reactor setup for reactivity evaluation.

The catalytic performance measurements were done at the Department of Heterogeneous catalysis at the Max-Planck-Institut für Kohlenforschung, on a tubular fixed bed reactor. The

effluent gas was analyzed by an online gas chromatograph (3000A MicroGC, Agilent), equipped with two lines, a PLOTU pre-column/Molsieve column combination with Ar as carrier gas for N<sub>2</sub>, H<sub>2</sub> and CH<sub>4</sub>, and a PLOTU column with He as carrier gas for NH<sub>3</sub> and CH<sub>4</sub>. Both lines were equipped with TCD detectors.

### 2.1.2 Kinetic measurements

The catalytic performance measurements were performed at the Institute for Technical Chemistry at Technische Universität Berlin, on a fixed-bed reactor made of silica, shown in Fig. 2-2, which is known to have no significant influence on the reaction in the examined temperature range of 475-630 °C. The catalyst bed consisted of 100 mg catalyst and 500 mg quartz beads with the diameter of 200-500 μm, which separated the catalyst from the frit. The carrier gas was chosen to be He. NH<sub>3</sub>, H<sub>2</sub>, and H<sub>2</sub> concentration were varied in order to investigate the reaction behaviour.

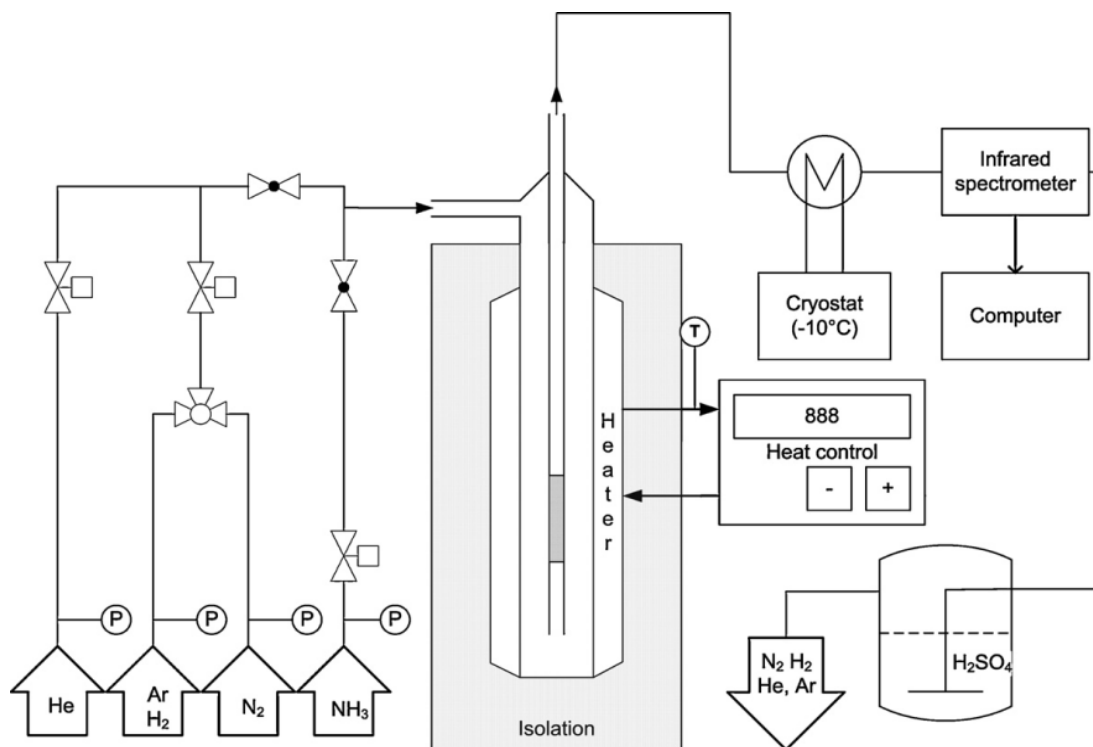


Figure 2-2. Schematic diagram of the gas lines of the setup for kinetic measurements.

## 2.2 The synthesis of nanostructured materials

### 2.2.1 The synthesis of Ru-based catalysts supported on carbon

#### 2.2.1.1 Surface modification of CNTs

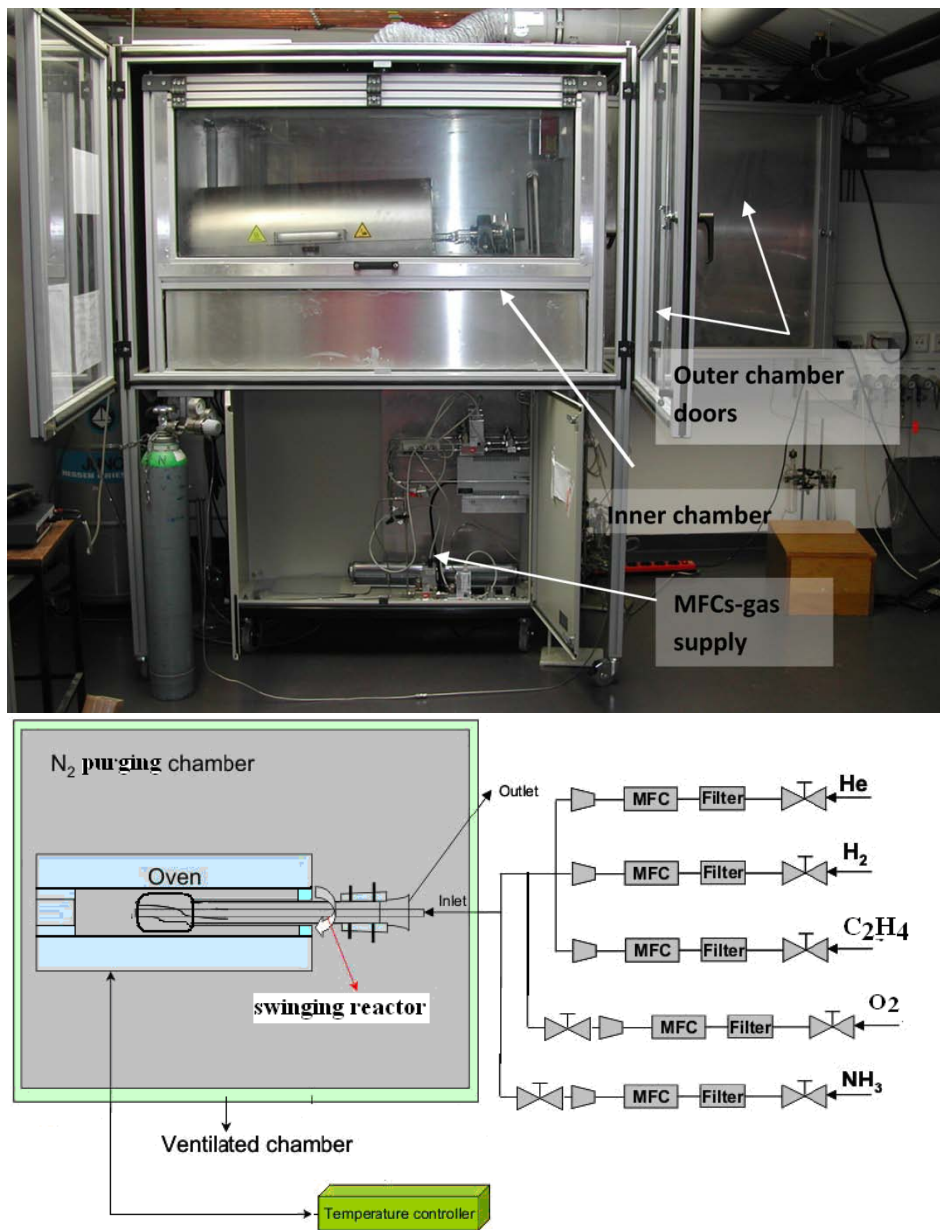


Figure 2-3. Overview photograph of the UTP furnace (up) and the schematic diagram of the gas lines (down). The N<sub>2</sub> purging chamber is a security measure to avoid O<sub>2</sub> from the atmosphere to diffuse into the hot zone and the reactor.

Commercial multi-wall CNTs (Baytubes, Bayer Material Science C150P) were treated with concentrated HNO<sub>3</sub> (70%, Sigma Aldrich) at 130°C for 2h to eliminate inorganic impurities. The functionalized CNTs were then washed with deionized water and further dried overnight at 60 °C. The obtained CNTs were ground and annealed in graphite oven (Fig. 2-3 shows the photograph of the lab-constructed UTP furnace for thermal pretreatment of samples in inert gas atmosphere) with inert gas (He/N<sub>2</sub>) at 450, 900 and 1500 °C respectively. The HNO<sub>3</sub>-treated and high temperature annealed supports samples are referred as C450, C900 and C1500 (described in Table 2-1) (representative TEM images are shown in Fig. 2-4).

Table 2-1. Sample information		
Sample	Database number	Details
Raw CNTs	3832#	Commercial CNTs from Bayer Material Science
C450	5959#	Annealed in He at 450 °C
C900	5960#	Annealed in He at 900 °C
C1500	5937#	Annealed in N <sub>2</sub> at 1500 °C

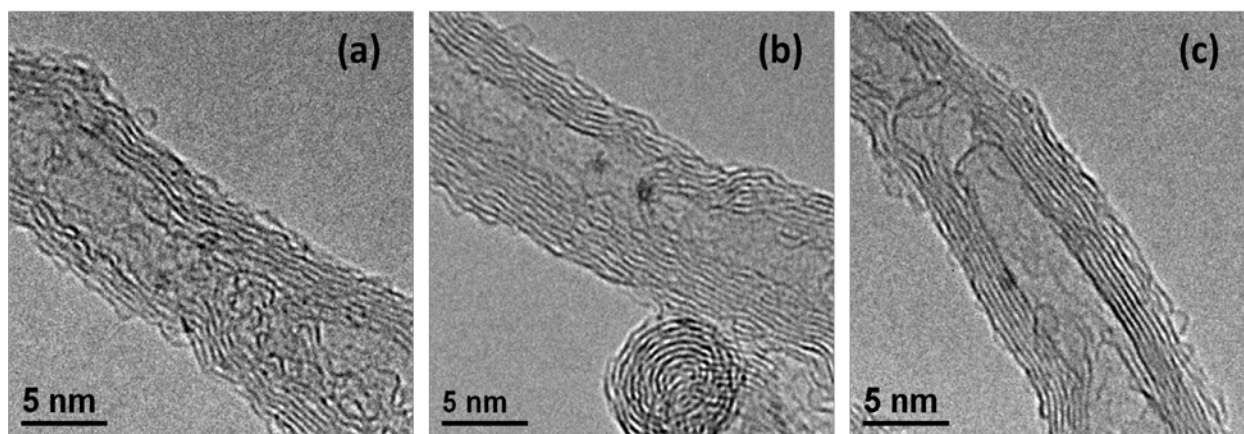


Figure 2-4. Representative TEM images of C450 (a), C900 (b) and C1500 (c) after HNO<sub>3</sub> functionalization and thermal pretreatment in inert gas.

### 2.2.1.2 Preparation of exfoliated graphite

Commercial graphite (Graphite-AF, Graphit Kropfmühl AG) was intercalated with a 3:1 mixture of concentrated  $\text{H}_2\text{SO}_4$  and  $\text{HNO}_3$  for 24h with magnetic stirring in an ice-bath. The intercalated graphite was transferred into a pre-heated oven at  $800^\circ\text{C}$  for 1 minute. The obtained sample was annealed in He at  $450^\circ\text{C}$  for 4 hrs and labeled as EG for the further applications. In Fig. 2-5, the SEM images of Graphite-AF (denoted as G) and exfoliated graphite (EG) were attached.

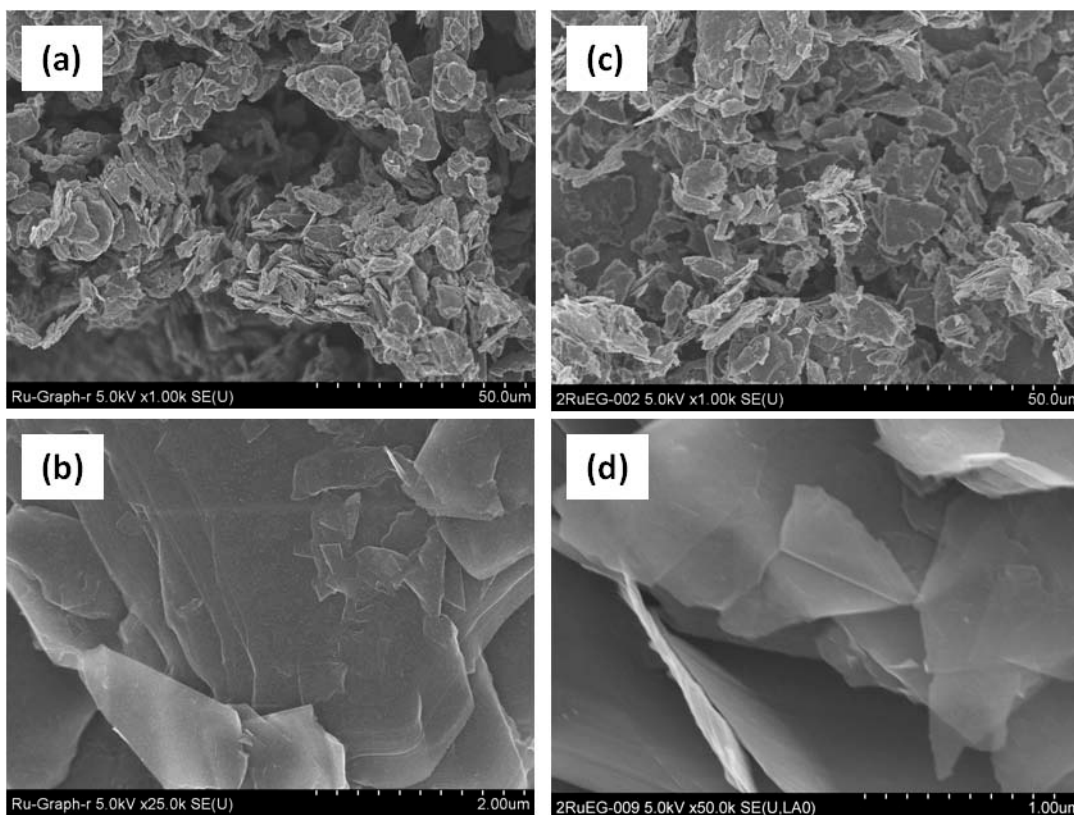


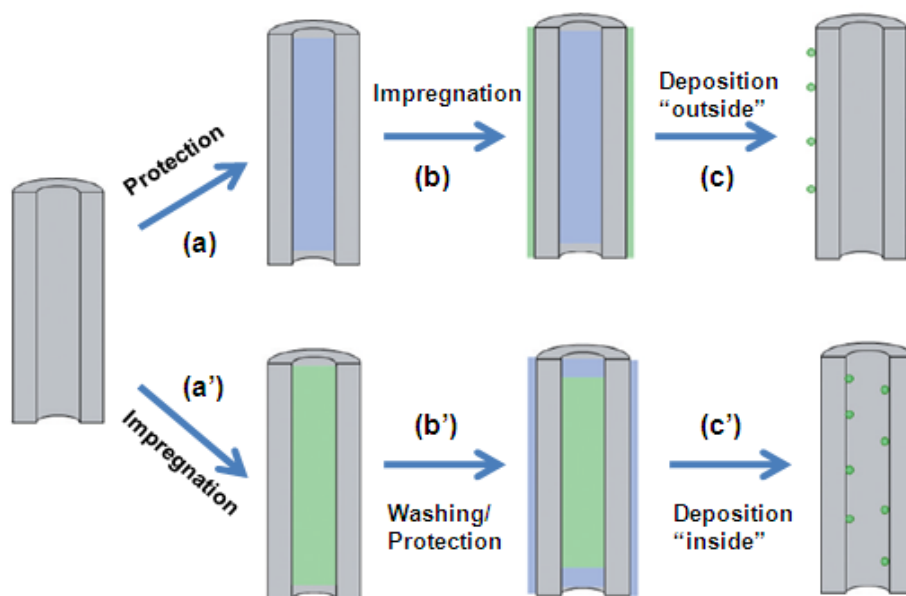
Figure 2-5. Representative SEM images of graphite-AF (a-b) and Exfoliated graphite (c-d).

### 2.2.1.3 Selective deposition of Ru nanoparticles on CNTs

The process of selective deposition of ruthenium nanoparticles on CNTs was elaborated in the previous work of our group.<sup>[1]</sup>

The inside supported Ru-based catalysts were prepared by a two-step synthesis (Scheme 2-1, a'-c'): CNTs were first impregnated with an ethanol solution containing the ruthenium

nitrosyl nitrate (Alfa Aesar). The volume of the solution was set to be lower than the porous volume of the CNTs. Because of its low surface tension ( $22 \text{ mN}\cdot\text{m}^{-1}$ ), the ethanolic solution wets the CNT surface and fills the inner channel, as described by the Young-Laplace equation.<sup>[2]</sup> Pure distilled water was then added in a second step. The intrinsic lipophilicity of the CNTs leads to lower liquid/solid interface energies for organic solvents than aqueous ones. Therefore the aqueous phase is expected to remain outside of CNTs and to displace the thin film of ethanolic solution located on the outer surface to the inner channel. The samples were dried at room temperature for 10 hrs and at  $110^\circ\text{C}$  overnight and denoted as Ru-in and Ru-out respectively (in Table 2-2)



Scheme 2-1. Schematic view of a longitudinal cross section of a carbon nanotube during the different steps for the selective deposition of Ru nanoparticles inside/outside CNTs. (Figure was taken from Ref. [1]).

Table 2-2. Sample information			
Sample	Database number	Sample	Database number
<b>Ru-in-C450</b>	6064#	<b>Ru-out-C450</b>	6535#
<b>Ru-in-C900</b>	6065#	<b>Ru-out-C900</b>	6542#
<b>Ru-in-C1500</b>	6066#	<b>Ru-out-C450</b>	6536#

#### ***2.2.1.4 Impregnation of Ru on graphites***

Commercial graphite (Graphite-AF, Graphit Kropfmühl AG), as-prepared exfoliated graphite (EG) and commercial graphite (High-surface-area graphite, HSAG-300, TIMCAL) were selected as supports for 2wt% Ru catalyst. The supports, impregnated with ethanol solution containing the ruthenium nitrosyl nitrate (Alfa Aesar), were dried at room temperature for 10h, and at 100 °C in air overnight consecutively. The samples were labeled as Ru-G, Ru-EG and Ru-HSAG respectively.

<b>Table 2-3. Sample information</b>			
<b>Support</b>	<b>Database number</b>	<b>Catalyst</b>	<b>Database number</b>
<b>Graphite</b>	4680#	<b>Ru-G</b>	4748#
<b>Exfoliated graphite</b>	6765#	<b>Ru-EG</b>	6993#
<b>High surface area graphite</b>	5441#	<b>Ru-HSAG</b>	7197#

### ***2.2.2 The synthesis of metal alloy nanoparticles supported on CNTs***

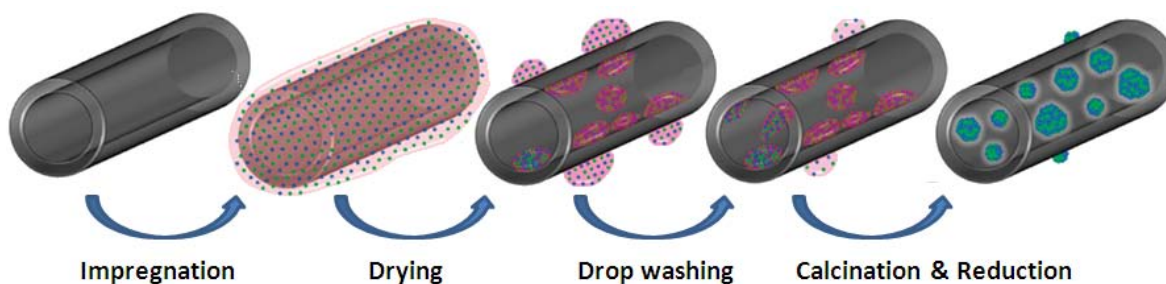
#### ***2.2.2.1 Pretreatment of CNTs/CNFs***

Commercial multi-wall CNTs/CNFs (Applied Science PR24-HHT, Applied Science Inc.) were treated with concentrated HNO<sub>3</sub> (70%, Sigma Aldrich) at 130°C for 2h. The functionalized CNTs were washed with deionized water and further dried overnight at 60 °C. The obtained CNTs were ground and annealed in a tubular oven with inert gas (He) at 450°C denoted as HHT-F for the further applications.

#### ***2.2.2.2 Selective deposition of metal alloy nanoparticles on CNTs***

5wt% Fe-Co and Fe-Ni bimetallic nanoparticles with different Fe/Co and Fe/Ni ratios were supported on functionalized CNTs respectively. The mixture of Fe-Co and Fe-Ni nitrates (Iron(III) nitrate nonahydrate, Merck; Cobalt(II) nitrate hexahydrate, Merck; Nickel(II) nitrate hexahydrate, Sigma-Aldrich) solution was dropped on CNTs under continuous stirring, during

which metal precursors are distributed on both inner and outer surfaces. Then, less amounts of solvent were dropped over the sample in the same way, and most of the residual metal ions adsorbed on the external walls were pulled inside of CNTs channel by the capillary force under the assistance of ultrasonic treatment. Finally, the obtained sample was dried at room temperature for 10h and 110 °C overnight. After calcinations and H<sub>2</sub> reduction, most of the metal particles were deposited on the inner walls of CNTs as the procedure shown in Scheme 2-2. A representative FeCo outside supported sample was prepared by the same procedure and it is described in section 2.2.1.3.



Scheme 2-2. Scheme of synthesis route to CNTs-supported FeCo/FeNi alloy nanoparticles.

## 2.2.3 The synthesis of molybdenum carbide and nitride

### 2.2.3.1 The synthesis of high surface area molybdenum carbide

Table 2-4. Sample information		
Sample	Database number	Details
Mo <sub>2</sub> C	7484#	fresh sample
Mo <sub>2</sub> C-NH <sub>3</sub> -4h	7825#	sample collected after reaction for 4h
Mo <sub>2</sub> C-NH <sub>3</sub> -100h	7824#	sample collected after reaction for 100h

The high surface area molybdenum carbide was prepared by a colleague, Dr. Thomas Cotter at the Department of Inorganic Chemistry at the Fritz-Haber-Institut der Max-Planck-Gesellschaft. A

temperature programmed reduction-carburization method was used to prepare the desired material from a lab-prepared  $h\text{-MoO}_3$  in a flowing mixture of Ar/H<sub>2</sub>/CH<sub>4</sub> under temperature ramps to a final hold temperature of 675 °C for two hours.<sup>[3]</sup> Samples were labeled as described in Table 2-4.

### ***2.2.3.2 The synthesis of nanostructured molybdenum nitride by HTC method***

To synthesize the desired samples, a hydrothermal carbonization synthesis and amination were adapted to transform the water solution of ammonium heptamolybdate (AHM, Merck) and glucose (Sigma) with Mo:C (2:15 and 1:15) ratios. The mixture solution of AHM and glucose was added into an autoclave equipped with Teflon inner reactor. The hydrothermal carbonization was operated at 200 °C for 2h. The obtained black powder was washed and dried at 110 °C for 10h. The sample was further ground and annealed in a UTP furnace (described in Fig. 2-3) in NH<sub>3</sub> at 650 °C for 3h. The prepared samples were labeled as MoN-HTC-I (10477# in AC database) and MoN-HTC-II (106754# in AC database) respectively.

## **2.3 Characterization Techniques**

### ***2.3.1 Textural properties***

The analytical methods for the determination of the textural properties, i.e. specific surface area and porosity of materials, are based on the physical adsorption/desorption of N<sub>2</sub> at the condensation temperature (77K). The surface area was calculated from the Brunauer, Emmet and Teller method (BET),<sup>[4]</sup> an extension of Langmuir model applied to multilayer adsorption, could obtain the surface area by measuring the amount of monolayer adsorbed gas. Pore size distribution was calculated from the desorption branch of N<sub>2</sub> isotherm by the Barrett-Joyner-Halenda method (BJH).<sup>[5]</sup> The sample was out-gas at 200 °C for 2 hrs in vacuum prior to the physical adsorption/desorption of N<sub>2</sub> measurement, on a Quantachrome Autosorb-6B KR sorptometer.

### 2.3.2 Raman spectroscopy

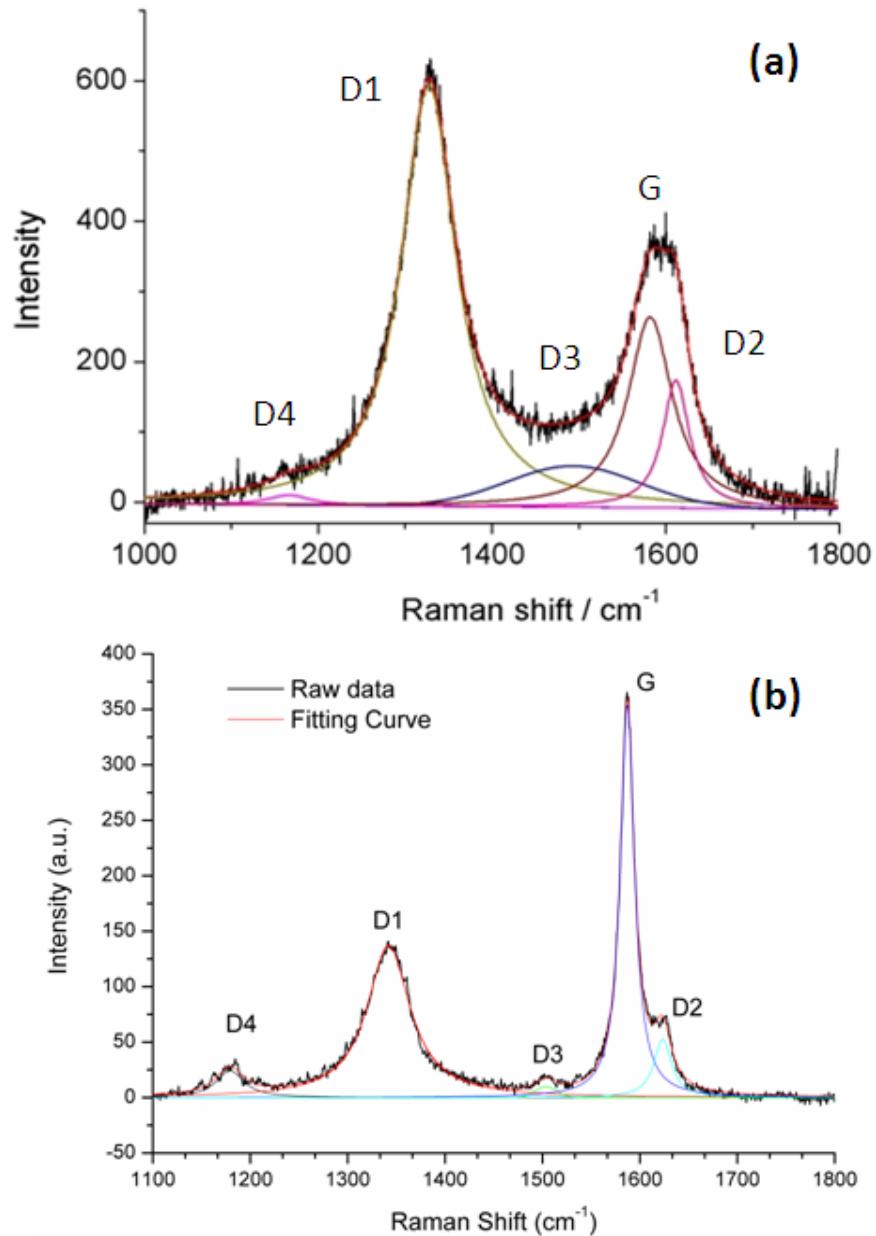


Figure 2-6. Fitting procedure of Raman spectrum from commercial CNTs (Baytube) and exfoliated graphite.

Raman spectroscopy is a sensitive method to study the properties of carbon materials with different structure, including crystalline, nanocrystalline and disordering carbons.<sup>[6, 7]</sup> Fig. 2-6 shows the typical Raman spectrum of CNTs (Baytube) inserting a representative fitting

procedure by using the method in literature.<sup>[8]</sup> The G-band peak at  $1580\text{ cm}^{-1}$  is assigned to in-plane vibrations of graphite (sp<sup>2</sup>-bonded carbon, E<sub>2g</sub> symmetry); D-band peak at around  $1350\text{ cm}^{-1}$  is attributed to the disorder-induced band of graphitic carbon (graphene layer deges, A<sub>1g</sub> symmetry). In addition a feature near  $1620\text{ cm}^{-1}$  is seen in most samples, which is assigned to disordered graphitic lattice (surface graphene layers, E<sub>2g</sub> symmetry). The Gaussian peak at  $1500\text{ cm}^{-1}$  is assigned to amorphous carbon. In particular, the commercial CNTs (Bayertube) used in this thesis, the contribution of the D1 and D2 peaks are quite appreciable suggesting that the CNT sample very likely contains other carbonaceous materials such as amorphous carbon and polyene like material originating from the pyrolysis of hydrocarbons (Fig. 2-6).

Raman spectroscopy was done on HORIBA Jobin Yvon spectrometer with an excitation line 633 nm 10x objectives. The spectra were collected at acquisition time of 120 sec. From the fitting procedure <sup>[8]</sup> the ratio of the D and G intensity ( $I_D/I_G$ ) was extracted for a semi-quantitative analysis of the presence of defective (D1) and graphitic carbon (G) in the sample.

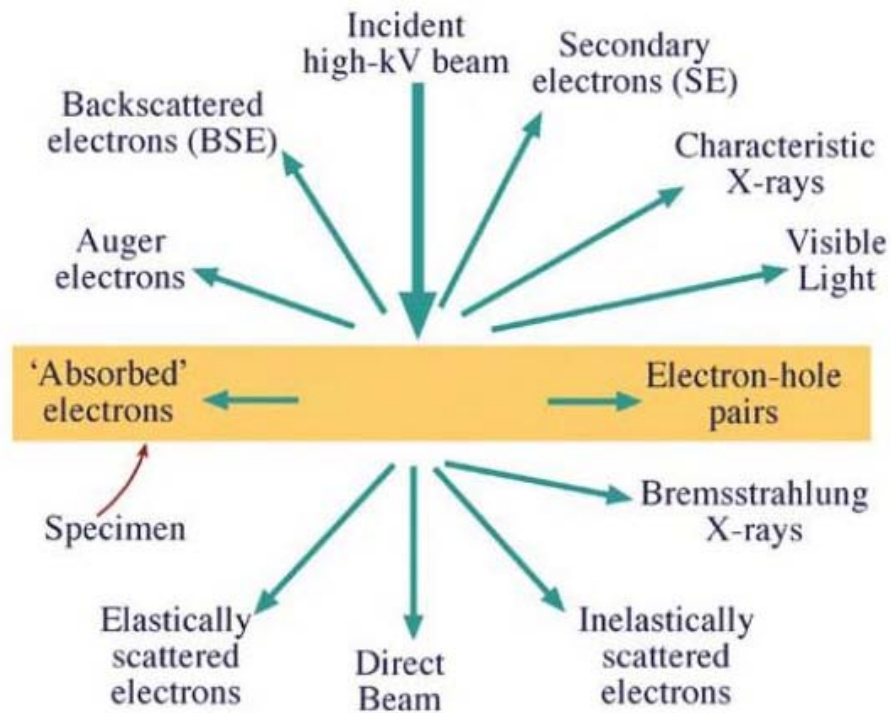
### ***2.3.3 X-ray diffraction***

Powder X-ray diffraction was carried out over all samples using a STOE STADI P diffractometer in transmission geometry (primary focusing Ge monochromator, Cu K $\alpha$ 1 radiation ( $\lambda = 1.5406\text{ \AA}$ ), linear position sensitive detector).

### ***2.3.4 Electron Microscopy techniques***

Electron microscopy techniques are powerful tools for the local information of morphology, nanostructure, dispersion, size distribution and electronic properties of solid materials. The information is derived from the detection of the signal generated by physical processes occurring as consequence of the interaction of the electron beam with observing sample. The elastically scattered electrons can be forwarded through the sample or backscattered; the inelastically scattered electrons transfer the energy to secondary processes such as Auger electron and x-ray emission. Those processes are summarized in Scheme 2-3.

In the Scanning Electron Microscope (SEM), the images are formed by the detection of secondary electrons and elastically backscattered electrons. The secondary electrons have low energy so that they are emerging from the sample with a probing depth of few nanometers, depending on the acceleration voltage, that means secondary electrons can provide information about the surface morphology. The probability of back scattered electron (BSE) is proportional to the atomic mass of the elements, thus images in BSE mode provide information about the elemental composition of a samples. Standard SEM instruments are always equipped with EDX detector, which gives information about elemental composition by analyzing x-rays emitted in the relaxation process that follow the generation of the hole in the core shell due to the interaction with electron beam.



Scheme 2-3. Schematic representation of the interaction between electron beam and observing specimen. (Image taken from Ref. [9]).

Transmission Electron Microscope (TEM) operates in diffraction mode or in image mode. The diffraction mode produces the diffraction pattern of the sample when the electron beam is in Bragg condition. The transmitted electron beam forms an image, which is a two-dimensional

projection of a three-dimensional object in the direction of the beam. Images formed by the large angle elastically scattered electrons are characterized by a contrast which is indicative of mass/thickness. The cross section of high angle scattering is proportional to the thickness of the sample and the atomic mass of the elements composing the specimen. Thus, assuming the thickness constant, the HAADF gives information about the element composition. A TEM can be equipped with Electron Energy Loss Spectroscopy (EELS) detector. The EELS is based on the detection of the inelastically scattered electrons. The inelastic scattering of the primary electron beam originates from interaction in which a part of the energy of the incident electron beam is transferred to the process of the ejection of an electron from the ground state to the valence band. Thus, the measure of the energy loss of the primary beam gives information about the electronic structure of the atoms and bonding states of the elements in the specimen. The possibility of coupling all this information output in one instrument makes the electron microscopy techniques very powerful and established characterization techniques in catalysis. It should be however emphasized that due to the high resolution of the instrument they give only a local view of the system under investigation.

The electron microscopes used throughout the work of this thesis are as follows:

1. A Hitachi S-5200 Scanning Electron Microscope (SEM) coupled with EDX detector for elemental analysis was used to investigate the surface morphologies of the studying materials. The samples under investigation have been deposited on conduction carbon tape. All images were acquired using an acceleration voltage of 3 kV for better resolution of surface features, and 15 kV to investigate the inner cavity of the samples.
2. A TEM equipped with a LaB<sub>6</sub> emitter (Philips CM200) operated at 200 kV was used to perform overview investigations of particle size and carbon nanofilament (MWCNT) microstructure. HRTEM investigations have been performed with a Philips CM200 TEM equipped a FEG emitter and a GATAN tridiem for EEL spectroscopy.
3. For high resolution images were obtained from a Cs-corrected transmission electron microscope operated at 80-300 kV (FEI Titan).

### 2.3.5 X-ray photoelectron spectroscopy

The high-pressure XPS experiments were performed at the ISIS beamline located at the BESSY II synchrotron facility in the end station of the FHI-MPG. The as-prepared samples were pelletized and transferred into the reaction cell,  $\sim 2$  mm away from an aperture to the differentially pumped stages of the lens system of the hemispherical analyser Phoibos 150 (SPECS). The probe size is  $\sim 100 \mu\text{m} \times 1$  mm. The in-situ measurements were operated at  $400^\circ\text{C}$  under 0.5 mbar of  $\text{NH}_3$ . All spectra are collected in normal emission geometry at photon energies of 585 eV for the C1s and Ru3d, 700 eV for the N1s and 830 eV for the O1s region, respectively, with a spectral resolution of  $\sim 0,3$  eV. For these photon energies, the electron mean free path is 9 Å.<sup>[10]</sup> Background correction is performed by using a Shirley background. The spectra are fitted following the Levenberg-Marquardt algorithm to minimize the  $\chi^2$ . Peak shapes are modeled by using asymmetric Doniach-Sunjic functions convoluted with Gaussian profiles. The accuracy of the peak position for different fits is  $\sim 0.05$  eV.

### 2.4 Density functional theory calculations

The DFT calculations were done by Dr. Payam kaghazchi and Dr. Timo Jacob at the Institut für Elektrochemie, Universität Ulm. The calculations were performed using CASTEP<sup>[11]</sup> with Vanderbilt-type ultrasoft pseudopotentials<sup>[12]</sup> and the generalized gradient approximation (GGA) exchange-correlation functional proposed by Perdew, Burke, and Ernzerhof (PBE)<sup>[13]</sup>. A plane-wave basis set with an energy cutoff of 380 eV was used for all calculations. The Brillouin zones of the (1 $\times$ 1)-surface unit cells of  $\text{Mo}_2\text{C}$  (0001) and MoN (0001) were sampled with  $6 \times 6$  Monkhorst–Pack  $k$ -point meshes. The surfaces were modelled with unsymmetric seven-layer slabs, where the lowest two layers were fixed at the bulk crystal structure. The geometries of the remaining layers were optimized to  $< 0.03 \text{ eV}/\text{Å}$ .

## References

1. Tessonnier, J.-P., et al., *Selective Deposition of Metal Nanoparticles Inside or Outside Multiwalled Carbon Nanotubes*. ACS Nano, 2009. **3**(8): p. 2081-2089.
2. Ebbesen, T.W., *Wetting, filling and decorating carbon nanotubes*. Journal of Physics and Chemistry of Solids. **57**(6-8): p. 951-955.
3. Cotter, T.P., *Activation of propane over Mo/V carbide*, in *Inorganic Chemistry*. 2011, Fritz-Haber-Institut der Max-Planck Gesellschaft: Berlin.
4. Brunauer, S., P.H. Emmett, and E. Teller, *Adsorption of Gases in Multimolecular Layers*. Journal of the American Chemical Society, 1938. **60**(2): p. 309-319.
5. Barrett, E.P., L.G. Joyner, and P.P. Halenda, *The Determination of Pore Volume and Area Distributions in Porous Substances. I. Computations from Nitrogen Isotherms*. Journal of the American Chemical Society, 1951. **73**(1): p. 373-380.
6. Tuinstra, F. and J.L. Koenig, *Raman Spectrum of Graphite*. The Journal of Chemical Physics, 1970. **53**(3): p. 1126-1130.
7. Dillon, R.O., J.A. Woollam, and V. Katkanant, *Use of Raman scattering to investigate disorder and crystallite formation in as-deposited and annealed carbon films*. Physical Review B, 1984. **29**(6): p. 3482.
8. Sadezky, A., et al., *Raman micro spectroscopy of soot and related carbonaceous materials: Spectral analysis and structural information*. Carbon, 2005. **43**(8): p. 1731-1742.
9. Williams, D.B. and C.B. Carter, *The Transmission Electron Microscope*, in *Transmission Electron Microscopy*. 2009, Springer US. p. 3-22.
10. Somorjai, G.A.L., Yimin, *Introduction to Surface Chemistry and Catalysis*. 2010, New York: Wiley.
11. Segall, M.D. and et al., *First-principles simulation: ideas, illustrations and the CASTEP code*. Journal of Physics: Condensed Matter, 2002. **14**(11): p. 2717.
12. Vanderbilt, D., *Soft self-consistent pseudopotentials in a generalized eigenvalue formalism*. Physical Review B, 1990. **41**(11): p. 7892.
13. Perdew, J.P., K. Burke, and M. Ernzerhof, *Generalized Gradient Approximation Made Simple*. Physical Review Letters, 1996. **77**(18): p. 3865.



## **Chapter 3:**

# **Ruthenium Nanoparticles on Carbon**

In this chapter, the metal-support interaction has been focused with the aim to find the correlation between the structure and function of Ru-carbon in ammonia decomposition. Carbon materials were chosen as supports for ruthenium nanoparticles, as they can exist in different forms that exhibit various functionalities, i. e. graphene, fullerene, graphite, carbon nanotubes, activated carbon, carbon black, etc. This chapter will be separated into two parts referred to the stacking geometry of graphene layers, those are one-dimension stacking graphene layers (graphite), and two-dimensional packed graphene sheets (multi-wall CNTs).

### **3.1 Structure-function correlations for Ru/CNT**

As elucidated in Chapter 1, Ru-based catalysts exhibit promising catalytic performance for both ammonia decomposition and synthesis.<sup>[1, 2]</sup> It was reported that using CNTs as supports for ruthenium nanoparticles can achieve the highest dispersion of ruthenium and the highest conversion in the decomposition of ammonia.<sup>[3]</sup> Li et al. found a (semi-quantitative) correlation between the ruthenium activity and the graphitic degree of the carbon support.<sup>[4]</sup> They found that the catalytic activity of ruthenium catalysts scales with the graphitization degree of carbon supports. Unfortunately, the morphology of ruthenium particles deposited on different carbon was not further investigated.

Recently, an effect of different locations originating from the tubular graphitic structure of CNTs supports was reported for some hydrogenation reactions, such as the conversion of cinnamaldehyde,<sup>[5, 6]</sup> the Fischer-Tropsch reaction,<sup>[7]</sup> and the conversion of syngas to ethanol.<sup>[8]</sup> Selective hydrogenation reactions always involve a specific interaction of one unsaturated bond

of the substrate with the active sites. Other hydrogenations suffer from insufficient contact times. The spatial restriction of the reaction inside nanometer-scale channels may steer the adsorption geometry substrates, thereby prolonging the contact time with the active domain and, thus, benefiting slow transformations. In the first section of this chapter, it will present a fundamental study on the structural effects of CNTs when used as supports for ruthenium nanoparticles, and on the localization of ruthenium nanoparticles for ammonia decomposition.

<b>Table 3-1. Physical and chemical properties of all samples</b>								
<b>Support</b>	<b>Diameter</b> (nm)	<b>BET surface area (m<sup>2</sup>/g)</b>			<b>Average particle size (nm)<sup>b</sup></b>		<b>Graphitization</b>	
		Support	Ru-in <sup>a</sup>	Ru-out <sup>a</sup>	Ru-in	Ru-out	Raman (I <sub>D</sub> /I <sub>G</sub> )	EELS (F <sub>sp2</sub> )
<b>C450</b>	10.2	363	348	410	2.0	2.5	1.463	83.1%
<b>C900</b>	9.8	381	309	338	2.3	2.8	1.390	89.9%
<b>C1500</b>	10.0	323	271	356	2.6	3.7	1.130	97.6%
a samples were collected after reaction;								
b Calculated from TEM images with 300 particles of every samples collected after reaction.								

### ***3.1.1 Surface modification of CNTs***

The starting material for this study is the commercial multiwalled CNTs produced by Bayer, Germany. The product known simply as Baytubes CNTs has 95wt% carbon purity and average outer diameter of 10nm. The impurities of this sample composed mainly of Co and Mn from the catalyst. These metal particles are encapsulated with graphitic carbon either at the tip or in the channel of the CNTs. Previous study in our group showed that the residual particles have the possibility to produce H<sub>2</sub> from NH<sub>3</sub> cracking.<sup>[9]</sup> Further, a detail TEM investigation of commercial CNTs showed that there is a broad distribution of defects over an individual CNT.<sup>[10]</sup> Some CNTs show there is a broad distribution of straight graphene layers while some show curly textures with defective graphene stacking. Most of the CNTs surface is coated with thin layers of pyrolytic carbon, ranging from one to several layers of amorphous carbon. Numerous studies have devoted to the purification of CNTs with the aim to remove single or multi layers of pyrolytic carbons. The abundant curvature present in pyrolytic carbons allow for their removal

with selective oxidation<sup>[11]</sup> approach by variety of oxidants such as CO<sub>2</sub><sup>[12-14]</sup>, air<sup>[15-19]</sup>, HNO<sub>3</sub><sup>[20-24]</sup> and H<sub>2</sub>O<sub>2</sub><sup>[25, 26]</sup>. The chosen purification method influences the chemical and physical properties of CNTs, i.e. they may open CNT caps, induce CNT fragmentation, and functionalize the inner and/or outer walls. It has been reported that the high temperature annealing procedures can remove some defects on the surface of CNT,<sup>[27]</sup> since the nanocrystalline graphene precursors attached on CNT can be graphitized to parallel alignment of the larger graphene layers at around 2800°C.<sup>[28]</sup> A two steps pre-treatments of commercial CNTs were used to vary the surface properties of CNTs, which will be used as support for Ru nanoparticles.

The experiments for surface modification of CNTs were details in Chapter 2. N<sub>2</sub>-physiosorption, Raman, TEM, EELS and XPS techniques were used to characterize the chemicophysical properties of CNTs samples.

### 3.1.1.1 Textural properties of CNTs

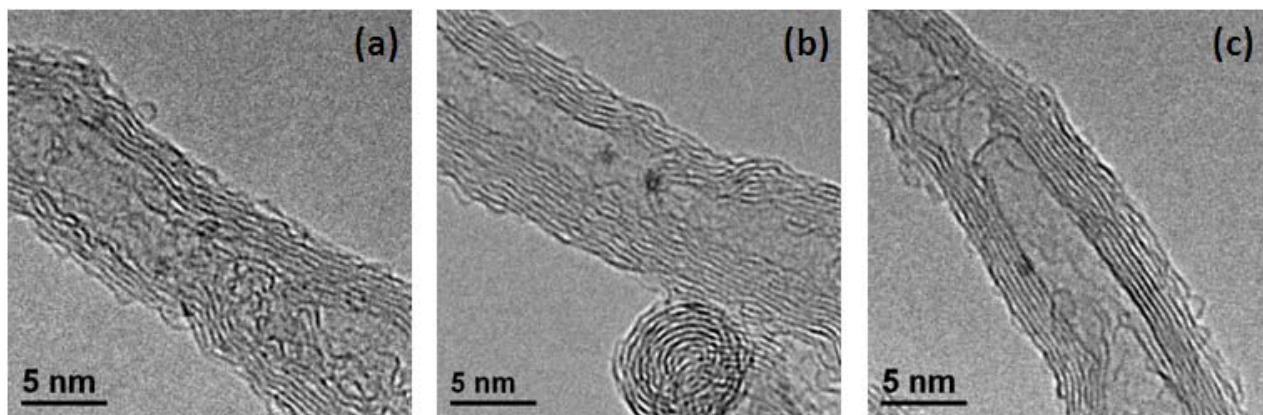


Figure 3-1. Representative TEM images of nitric acid functionalized commercial CNTs calcined at different temperatures. (a) C450; (b) C900; (c) C1500.

Figure 3-1 shows the representative TEM images of CNTs samples, which were nitric acid functionalized and calcined in inert gas at 450, 900 and 1500 °C respectively. Apparently, the pyrolytic carbon attached on CNTs surface could be (partly) removed, and the rough surface of CNTs could be graphitized again by high temperature annealing procedure.

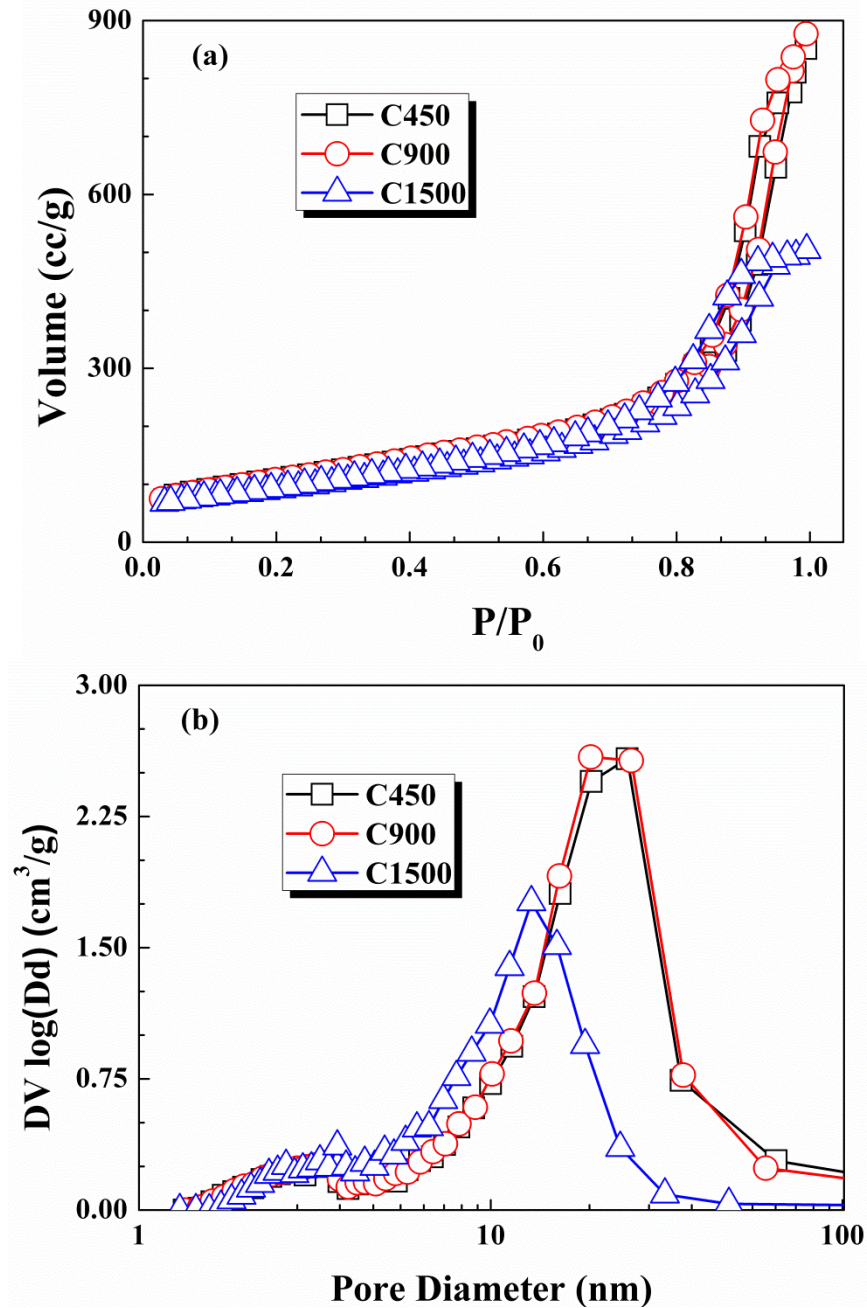


Figure 3-2. BET analysis of C450, C900 and C1500 CNTs supports. (a) isotherms; (b) BJH-desorption pores distributions.

The physical properties of the CNT supports were summarized in Table 3-1. The effects of the calcinations temperature on the textural characteristics of CNT supports were studied by  $\text{N}_2$  physisorption measurements. As shown in Figure 3-2, all samples exhibited type V isotherms

with H3 hysteresis loops indicating that the capillary pore structures of the samples. The Brunauer-Emmett-Teller (BET) surface area of C1500 was lower than those of C900 and C450, which is due to the elimination of structural defects or amorphous fragments roughening the CNTs.

### 3.1.1.2 Graphitization characterization of CNTs

Raman spectroscopy is a common method to characterize the order of carbon materials.<sup>[29-33]</sup> Raman bands of the samples and the quantitative results are summarized in Figure 3-3 and Table 3-1. The D band centered at  $\sim 1350\text{ cm}^{-1}$  is usually attributed to defects and pyrolytic carbon impurities in the CNT samples; the peak at around  $1580\text{ cm}^{-1}$  is assigned to in-plane vibrations of graphite (sp<sup>2</sup>-bonded carbon).<sup>[19, 30, 34]</sup> The second-order peak at  $2700\text{ cm}^{-1}$  is associated with 2D vibrations of carbon atoms, and its increase with heating temperature is related to the ordering of the graphitic structure (G' band).<sup>[35]</sup> The intensity ratio of the D and G bands (ID/IG) decreased with increasing calcinations temperature, indicating an increased structural ordering of the CNTs when treated at higher temperatures.

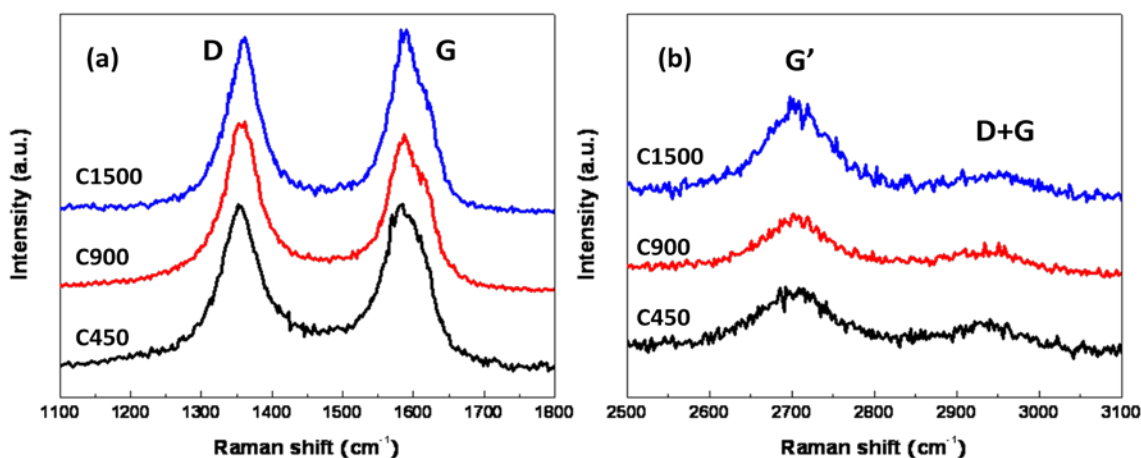


Figure 3-3. First- and second-order Raman spectra of the CNTs calcined at different temperature.

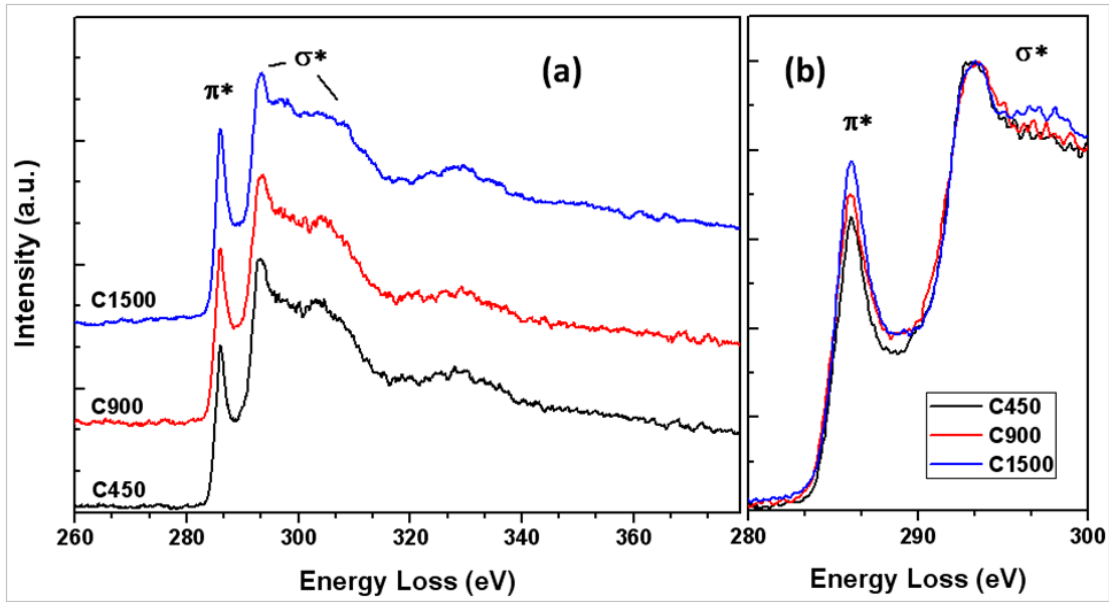


Figure 3-4. EELS analysis of CNTs calcined at different temperatures. (a) ELNES spectra of C450, C900 and C1500 samples; (b) normalized EELS spectra.

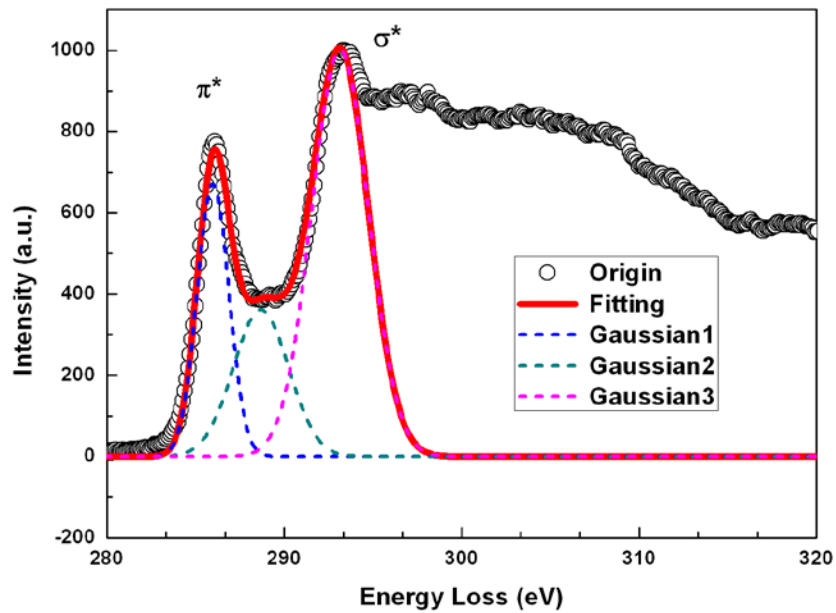


Figure 3-5. Gaussian deconvolution of EELS spectra for C1500 CNT support.

Energy-loss near-edge structure (ELNES) spectroscopy measurements of the C450, C900 and C1500 samples are presented in Figure 3-4. Spectra were obtained from a circular region with 100 nm diameter including several CNTs perpendicular to the electron beam. The carbon K-edge

shows clearly two energy loss features. The first narrow peak at around 285 eV corresponds to an electronic transition from carbon 1s to antibonding  $\pi^*$  states ( $\pi^*$ ), characteristic of the sp<sup>2</sup>-bonded carbon, while the broader structure at 290-310 eV indicates transitions to antibonding  $\sigma$  states ( $\sigma^*$ ).<sup>[36, 37]</sup> To estimate the relative sp<sup>2</sup> hybridization ratio, it is assumed that the ratio of integrated areas under  $\pi^*$  and  $\sigma^*$  peaks is proportional to the ratio of  $\pi$  and  $\sigma$  states. This ratio is normalized with respect to the value determined for highly ordered pyrolytic graphite (HOPG); a material consisting of only sp<sup>2</sup> hybridized carbon. The hybridization ratio was acquired by applying a Gauss fit to the spectra (Figure 3-5) and comparing the different areas of the respective Gauss curves.<sup>[36, 37]</sup> This gave the sp<sup>2</sup> ratios of the CNT samples in Table 1. As shown in Figure 3-4-b (spectra were normalized with the intensities of first  $\sigma^*$  peak), the intensity of  $\pi^*$  peaks increased in the order of C450 < C900 < C1500, thus, the degree of the carbon ordering increased with the calcinations temperature, which is consistent with Raman results.

$$F_{sp^2} = \frac{\left[ \frac{area(\pi^*)}{area(\pi^* + \sigma^*)} \right]_{sample}}{\left[ \frac{area(\pi^*)}{area(\pi^* + \sigma^*)} \right]_{HOPG}} \times 100\% \quad \text{Equation 3-1}$$

### 3.1.1.3 Surface characterization of CNTs

Surface functional groups of the Ru/CNT catalysts were analyzed by X-ray photoelectron spectroscopy (XPS) with Ru-out-C450 and Ru-out-1500 samples (details of assigning C1s data are summarized in Figure 3-6. All sp<sup>2</sup> and sp<sup>3</sup> C-C and C-H bonds were assigned to the C1s signal at 285 eV. The Gaussian peak at  $284.8 \pm 0.2$  eV (sp<sup>3</sup> C-C bond) was only observed in Ru-out-C450 sample, indicating the high temperature pretreatment can improve the CNTs surface ordering. The peaks at  $286.3 \pm 0.2$  eV,  $287.4 \pm 0.2$  eV and  $288.7 \pm 0.2$  eV were attributed by C-OH, C=O and O-C-OH groups on CNTs surface respectively, which corresponds within an error bar of 30% with the O1s spectra (Figure 3-5-c) at  $532.45 \pm 0.2$  eV,  $531.2 \pm 0.2$  eV and  $533.6 \pm 0.2$  eV. The approximate O molar quantities are 4.3% and 2.7% of Ru-out-C450 and Ru-out-C1500 respectively indicating that parts of CNTs surface functional groups introduced by HNO<sub>3</sub> refluxing could be removed by high temperature pretreatment.

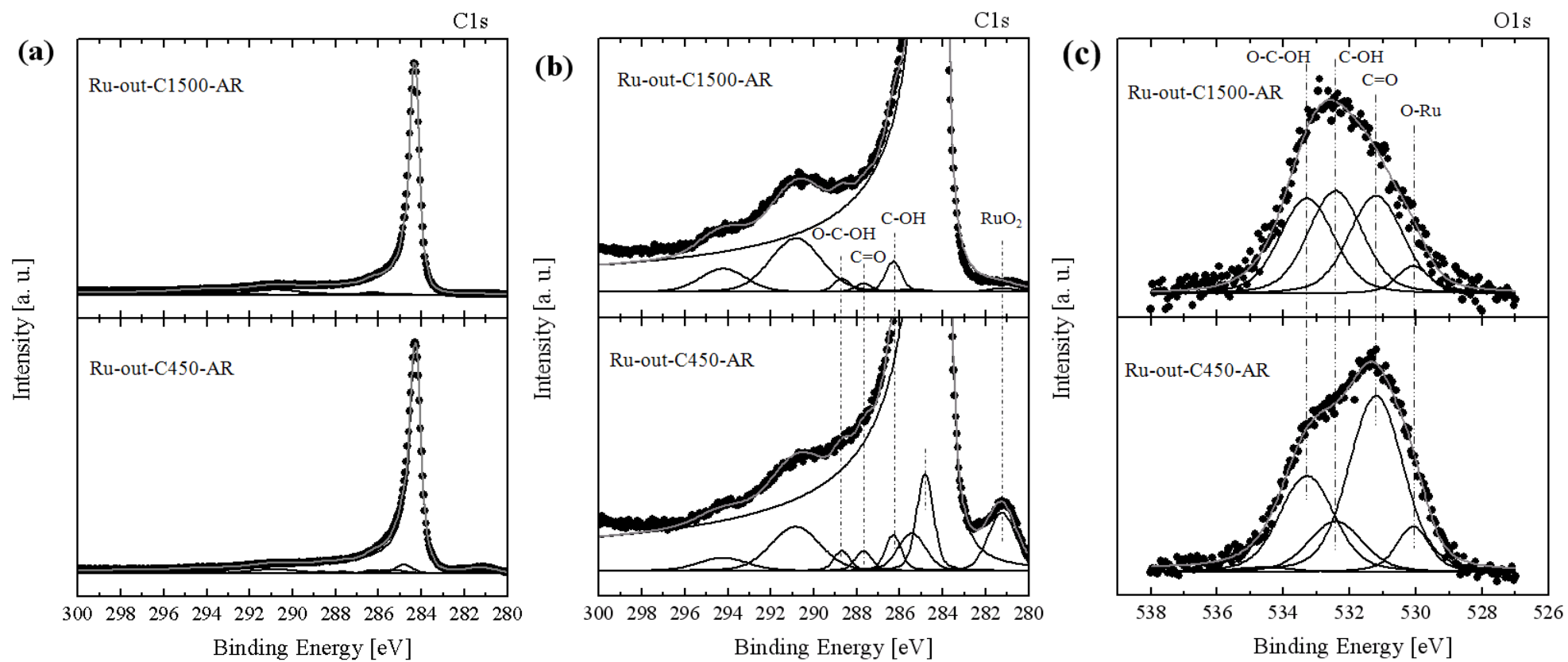


Figure 3-6. XPS analysis of Ru-out-C450 and Ru-out-C1500. (a) carbon 1s; (b) Ru 3d; (c) oxygen 1s

### ***3.1.2 Selective deposition of Ru nanoparticles on CNTs***

A two-step impregnation method<sup>[38]</sup> was used to prepare the inside supported Ru catalysts for this study. Incipient wetness impregnation is well-known technique used for catalyst preparation.<sup>[39, 40]</sup> A solid catalyst support is brought in contact with a solution containing the metal precursor. This technique usually leads to a homogeneous metal deposition with a good dispersion and narrow particle size distribution.<sup>[41]</sup> The synthesis procedure<sup>[38]</sup> was based on the ideas that (1) the CNT has a better affinity for organic solvents; (2) a solvent with a low surface tension will easily wet and penetrate inside the CNT; (3) a second, metal-free, solvent will remain outside of the nanotube and protect its outer surface from metal deposition if the liquid/solid interface energy is higher than the first solvent. The representative TEM images of Ru nanoparticles inside CNTs are shown in Figure 3-6 a-c, typical ruthenium nanoparticles are labeled with red and blue circles, representing the different locations on CNTs. As shown in the figure, most Ru particles were encapsulated inside the channels of the CNTs, except for a small amount of Ru on the outer surfaces. Our previous study found that by using this deposition technique a significant improvement is achieved compared to the classical incipient wetness impregnation method,<sup>[38, 42]</sup> that is, a 75% filling of nanoparticles located inside the CNT channels instead of 50%. Particle size distributions for each sample were calculated from TEM images, counting 300 individual particles each while the mean sizes of Ru are summarized in Table 3-1.

Decoration of the outer surface of closed CNTs is an easy task. However, decorating selectively only outer surface of opened CNTs is far more challenging.<sup>[38]</sup> A two-step impregnation method was used to prepare the samples outside supported ruthenium catalysts. An incipient wetness impregnation was first performed with benzene, which has a low surface tension and consequently wets and fills the tubes easily. An aqueous solution which contains Ru precursor is then added. Because of its higher liquid/solid interface energy, this solution cannot penetrate the CNTs. Thus, the channel remains protected and decoration only happens on the outer surface. In previous work,<sup>[38]</sup> our colleagues tested the solvents with different boiling points and miscibility with water, and used 3D-TEM to investigate location of the nanoparticles and their size, as well as distinguishing between the inner and outer parts of CNTs in order to estimate the ratio of the nanoparticles inserted the tubes.

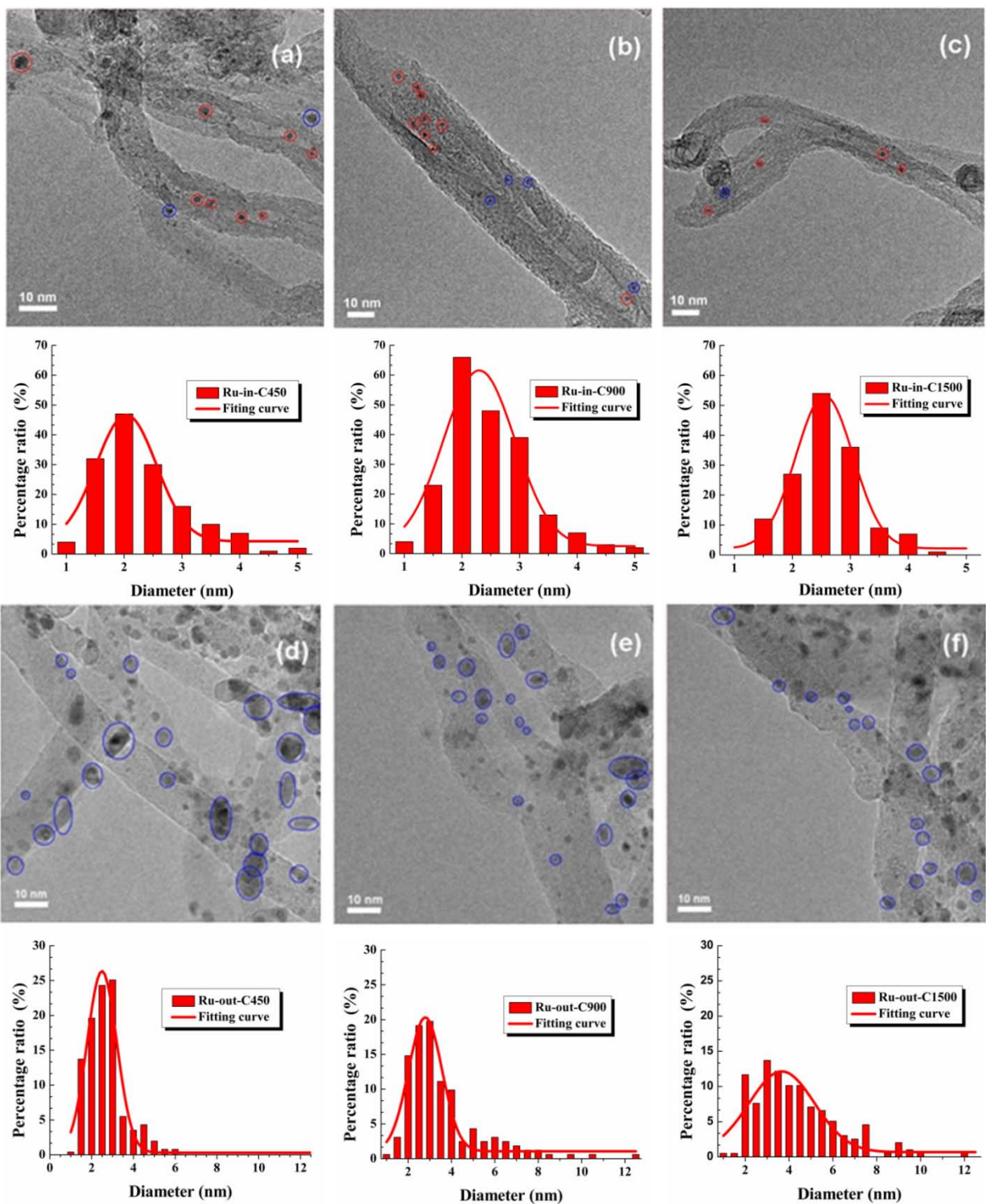


Figure 3-6. TEM images of 2wt% Ru/CNTs catalysts after reaction. (a-c) Ru-in supported on C450, C900 and C1500; (d-f) Ru-out supported on C450, C900 and C1500. The red and blue circles indicates Ru particles located inside and outside of the CNTs, respectively. All images inserted with particle size distributions of Ru nanoparticles calculated from 300 individual Ru particles in TEM images.

In this work, we tried to identify the location of the selected particles by tilting the angle of the sample holder. The representative TEM images of Ru nanoparticles inside CNTs are shown in Figure 3-6 e-f, typical ruthenium nanoparticles are labeled with red and blue circles, representing the different locations on CNTs. For the outside supported ruthenium catalysts, nearly no ruthenium were found inside the channels, indicating a successful preferential localization (more than 90% of the Ru nanoparticles were located outside the CNT walls).

As shown in Table 3-1, the ruthenium particle size increased with the calcinations temperature of the supporting CNTs for both Ru-in and Ru-out samples, indicating a lower site density for strong Ru-C interactions with increasing perfection of the support surface. Prior to the impregnation stage, the pristine CNTs were functionalized with concentrated nitric acid, introducing oxygen species on the surface of the CNTs.<sup>[43]</sup> Parts of these surface functional groups could act as “anchors” for the ruthenium precursor. Compared to Ru-in samples, the exterior ruthenium nanoparticles are even more sensitive to the thermally pretreated CNT surface.

The morphology of the ruthenium nanoparticles on the inner and outer walls of the CNTs could be identified to a certain extent by high-resolution TEM images. In Figure 3-7 and 3-8 we show representative ruthenium nanoparticles supported on the inner and outer walls of C450, C900 and C1500 samples, respectively. As shown in the images, the lattice distance were 0.20, 0.21 and 0.23 nm, which can be attributed to the characteristic values of Ru (101), (002) and (100) planes, respectively. The ruthenium particles outside the CNTs were mostly faceted and had a large size, while the ruthenium particles inside the CNTs were smaller, less well ordered, and exhibited specifically more defects. The average site of metal-support interactions differs in structure for the Ru-in and Ru-out samples. For the Ru-in samples, ruthenium tends to sit on local disorder sites in the graphene walls whereas in Ru-out samples ruthenium is located in pockets of the surface, occurring due to intersections of packets of graphene stacks. This was observed earlier with Ru catalysts supported on fullerene black exhibiting a similar local morphology.<sup>[44, 45]</sup>

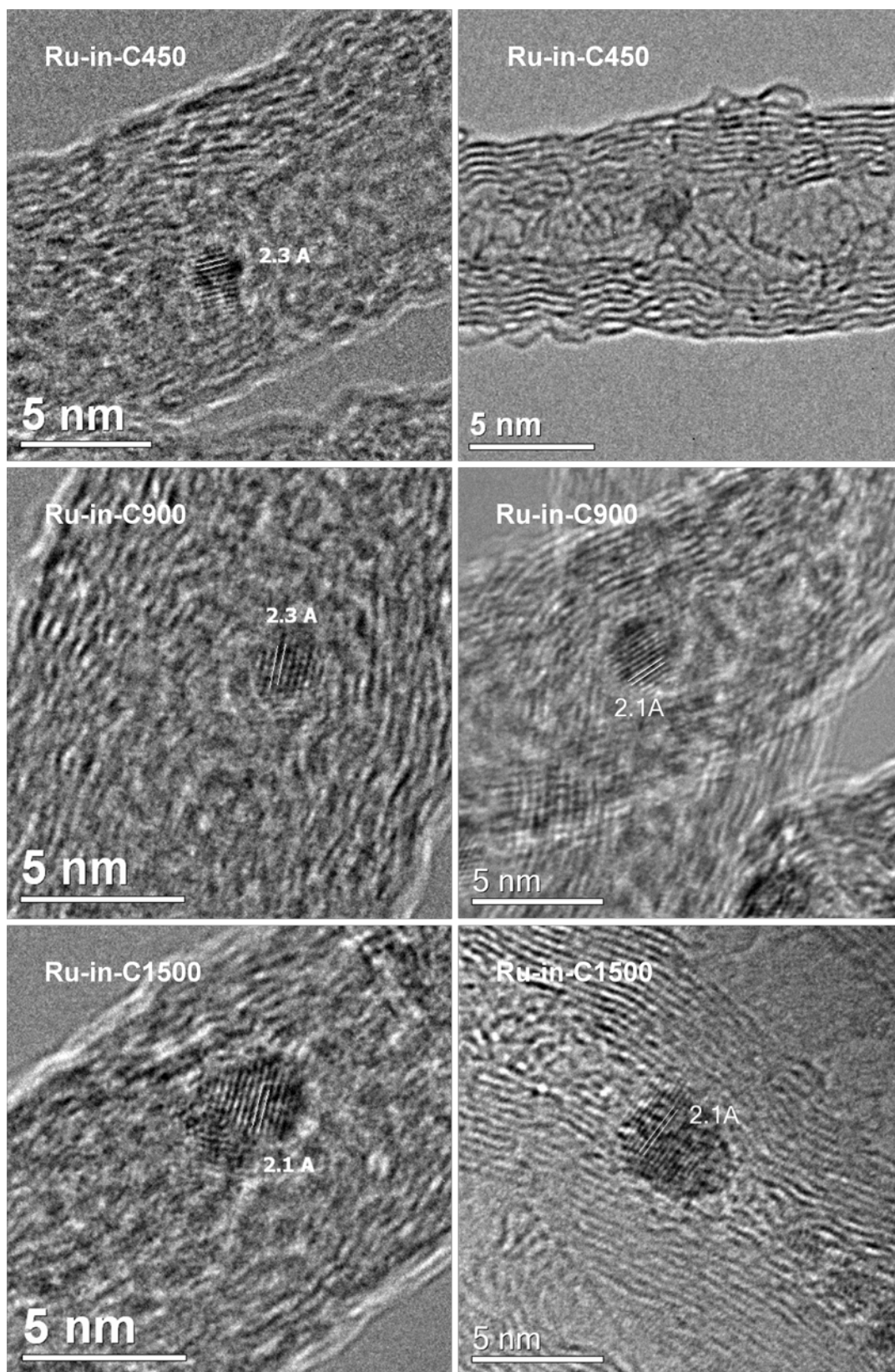


Figure 3-7. High resolution TEM images of Ru-in samples.

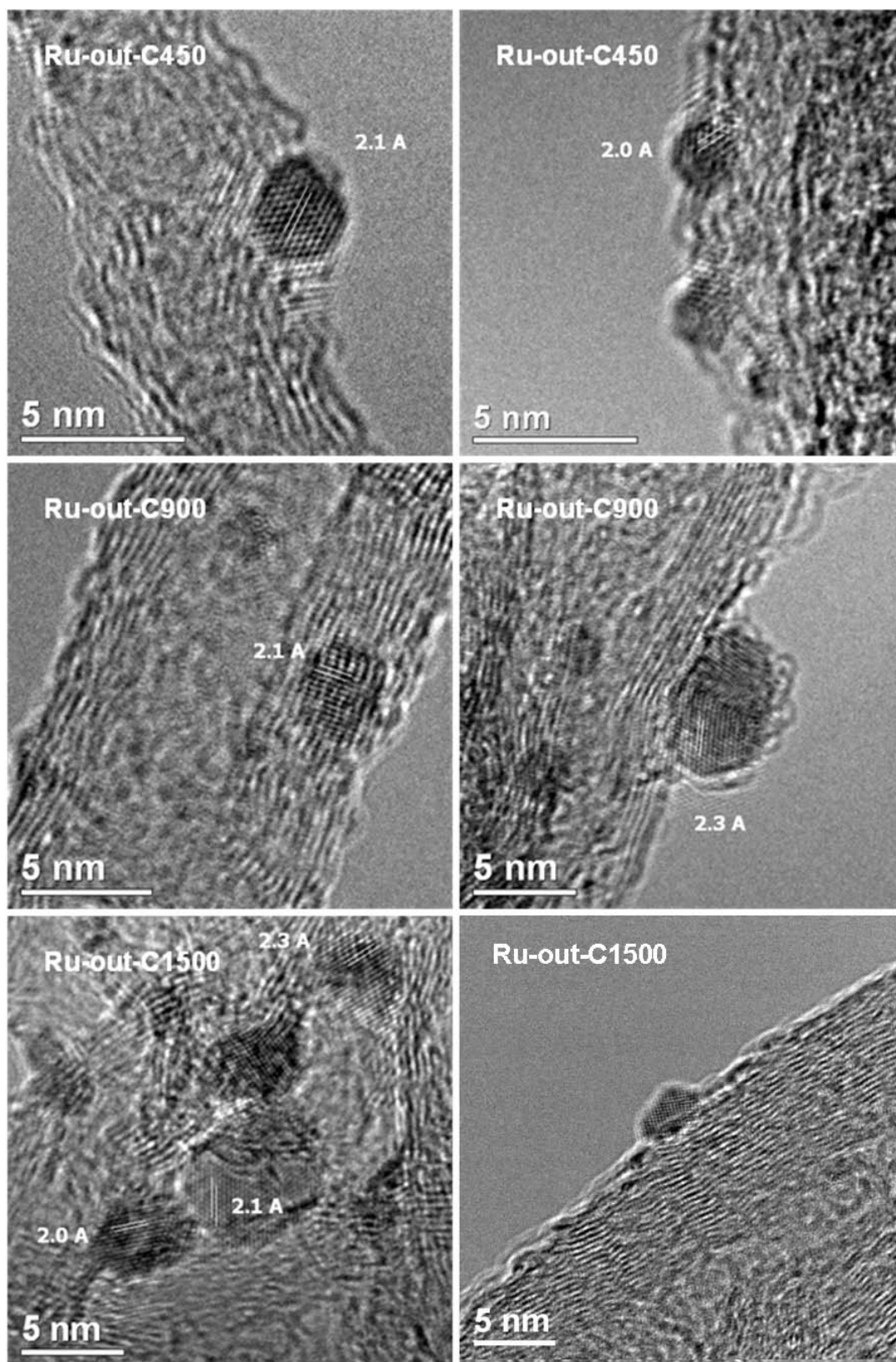


Figure 3-8. High resolution TEM images of Ru-out samples.

### 3.1.3 Catalytic $\text{NH}_3$ decomposition

Catalytic  $\text{NH}_3$  decomposition was performed according to the procedure detailed in the experimental section in chapter 2. All the Ru-CNTs samples were evaluated at the same reaction conditions (Figure 3-9).

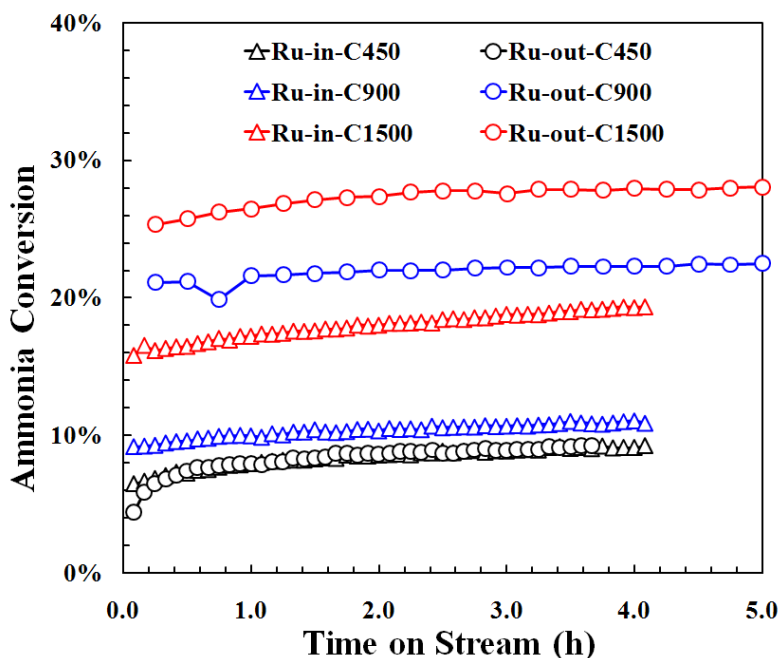


Figure 3-9. Catalytic performances of all samples. Reaction conditions: 50 mg catalyst, 30 ml/min pure  $\text{NH}_3$ ,  $36000 \text{ h}^{-1}$  space velocity, at  $450 \text{ }^\circ\text{C}$ .

Figure 3-10 summarizes the catalytic performance (hydrogen production rate at steady state) correlated with structural descriptors. The catalytic activity of Ru nanoparticles scales with their size; larger particles exhibit more active sites per particle than small particles, suggesting that no relationship between exposed surface and active site density exists for this reaction. Extrapolating from ammonia synthesis, being the reverse reaction, this finding is in line with the known fact<sup>[46]</sup> that the reaction is totally dominated by surface steps.<sup>[47]</sup> The observation that large particles are more active in ammonia decomposition was also made earlier.<sup>[48, 49]</sup> It was further argued that special surface sites should occur with high abundance on ruthenium particles with sizes between 3 and 5 nm and that support effects may control the Ru particle sizes at

constant loading.<sup>[50]</sup> The present findings support this notion: a higher degree of graphitization leads to a weaker metal carbon interaction and hence to larger particles, as also seen in the TEM data of figures. Ru-in particles are inherently smaller than Ru-out particles and therefore no positive confinement effect is observed in this reaction. It seems, however, that Ru-in particles are inherently less well ordered and exhibit specifically more defects, which is in line with the trend seen in Fig. 3-10 that Ru-in particles of the same size are more active than Ru-out particles. Most Ru-out particles exhibit a shape with faces and, hence, are probably pure metallic; the Ru-in particles exhibit many internal effects that are likely stabilized by heteroatoms originating either from synthesis or from the support (carbon).

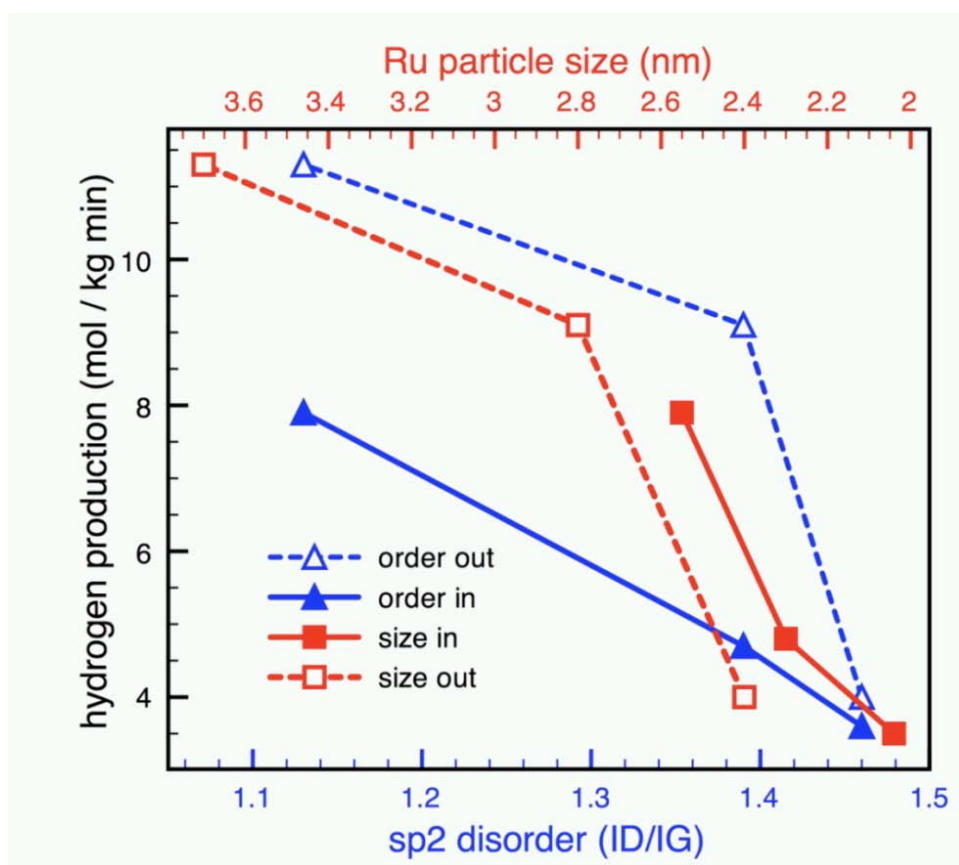


Figure 3-10. Correlation of steady catalytic performance with structural descriptors for the support and for the active mass.

At high conversions and on large surface facets inhibition of activity occurs by adsorbed hydrogen,<sup>[51]</sup> as also indicated by the leveling off in the particle-size-activity curve of Ru-out in

Fig. 3-10. This adverse effect is in line with the faceted shape seen in the TEM images, producing many large flat terraces with a low density of high-energy sites. An explanation of the clear finding from Fig. 3-10 that high support ordering and large particles of Ru offer the best performance stems from the requirement that the most active site unites high electron density and high under-coordination; in the small particles of Ru-in, which are rough and therefore offer high under-coordination, the stabilizing heteroatoms limit the electron density and hence deactivate the rough sites. The different local geometry of the support is also not beneficial for Ru-in as for those particles the accessibility to the  $\pi$  electron system of graphene units is inhibited most due to the local disorder of the carbon. It is speculative that the local disorder of support induces also covalent interaction or in directly through delivery of stabilizing carbon atoms dissolving into the ruthenium particle grain boundaries. The Ru-in system may benefit from alkali promotion<sup>[51, 52]</sup> and then offer not only better long-term stability but also better utilization of the active mass. Ammonia decomposition requires the difficult step of N-N recombination through surface diffusion from two sites of ammonia cleavage on weakly adsorbing sites (terraces).<sup>[53]</sup> This dictates that an active site for ammonia decomposition is a larger ensemble than that for the forward reaction of ammonia synthesis, which can occur on a single step site as required hydrogen is populating on all Ru sites in highly mobile form.

### **3.2 Structure-function correlations for Ru/graphite**

In this section, a detail investigation of Ru-carbon interactions was studied by using combinational characterization methods including high-resolution TEM and in-situ XPS measurements.

As mentioned in last section, Ru-based catalysts exhibit promising catalytic properties both in the ammonia decomposition and synthesis.<sup>[1, 2]</sup> By acknowledging the findings in ammonia synthesis, the active sites for this reaction are the step atoms of ruthenium particle.<sup>[53, 54]</sup> According to the DFT calculations, this reaction is primarily happening on B5-type sites on Ru (shown in Fig. 1-3 in Chapter 1),<sup>[55]</sup> whose density could be determined by the morphology (size and shape) of Ru particles.<sup>[56]</sup> Single crystal studies and DFT calculations revealed that the maximum probability for B5-type appeared for particles of 1.5 – 2.5 nm.<sup>[56, 57]</sup> Aside from

theoretical estimates, there have been several experimental studies on the effect of Ru particle size on catalytic performance in ammonia synthesis and decomposition.<sup>[58]</sup> Our study of Ru on CNTs showed that the catalytic activity of ammonia decomposition scales with the particle size of ruthenium nanoparticles supported on either outside or inside wall of carbon nanotubes. This observation that large particles are more active in ammonia decomposition was also made earlier.<sup>[48, 49]</sup> It was further argued that special surface sites should occur with high abundance on ruthenium particles with sizes between 3 and 5 nm and that support effects may control the Ru particle sizes at constant loading.<sup>[50]</sup> A.M. Karim et al. investigated the shape and polydispersity of Ru particles supported on  $\gamma$ -Al<sub>2</sub>O<sub>3</sub>. They found the Ru activity for ammonia decomposition increased by almost 2 times as the particle size increased from 0.8 nm to over 7 nm. In spite of the different crystallinities and metal-support interactions, authors attributed the low activity of small particles to the polydispersity rather than activity on terraces. “only when a series of chemically identically and completely monodisperse Ru particles on the same support, and with the same number density were be compared, might one be expected to find a clear structure sensitivity as expression of the site density as function of particle morphology”.<sup>[53]</sup> “It is remarkable that the theoretical concept,<sup>[59]</sup> which does not take into account the practically most relevant mesoscopic structuring of metastable forms of the elements, arrives at experimentally correct predictions. It can only be concluded that it is not the mesoscopic structure by itself but rather a local electronic property arising from the nanostructure that constitutes the tuning factor for the few active site atoms that form part of the complex surface of a promoted catalyst with many local geometries and substantial chemical variability.”<sup>[53]</sup>

In present study, we will report a fundamental study on the structural effects of graphite when used as supports for ruthenium nanoparticles, especially focus on the local geometry of ruthenium nanoparticles, which could probably influence the subsurface N-species. In addition to questions about the elementary steps of the reaction and the importance of the real structure and subnitrides for the catalyst.

### ***3.2.1 Characterizations of the supports***

#### ***3.2.1.1 Textural properties of graphite samples***

Table 3-2. Physical properties of samples						
Support	Scale of graphitic unit <sup>a</sup>		BET <sup>b</sup> (m <sup>2</sup> g <sup>-1</sup> )	I <sub>D</sub> /I <sub>G</sub> <sup>c</sup>	Catalyst	H <sub>2</sub> production rate <sup>d</sup> mmol <sub>H2</sub> /(g <sub>Ru</sub> ·min)
	Diameter	Thickness				
High-surface area graphite	30-200 nm	20-50 nm	348.66	0.43	Ru-HSAG	217
Graphite	4-20 μm	0.3-3 μm	11.04	0.27	Ru-G	422
Exfoliated graphite	4-20 μm	5-20 nm	15.07	0.39	Ru-EG	159

a Measured from SEM images.  
b N<sub>2</sub> physisorption.  
c Intensity ratios of D- and G-band measured from Raman.  
d steady states at 450 °C, with 36000 h<sup>-1</sup> space velocity.

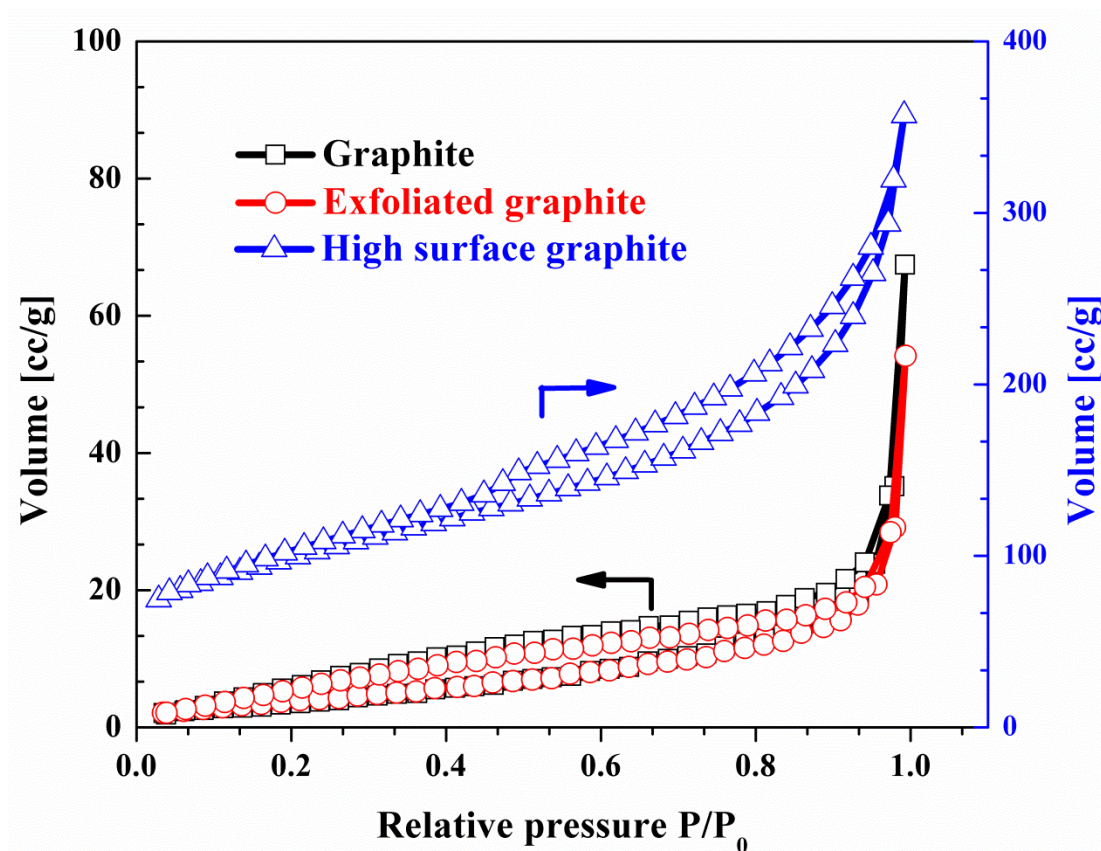


Figure 3-11. N<sub>2</sub>-adsorption/desorption isotherms of different graphite samples.

The physical properties of the graphite supports were summarized in Table 3-2. The specific surfaces of graphite with different scale of unit were measured from N<sub>2</sub>-physisorption technique. The diameters and thicknesses of graphite were estimated based on SEM and TEM analysis. The “high-surface-area graphite” (HSAG-300) exhibited the highest BET surface area, which is around 350 m<sup>2</sup>/g. The isotherms of the support samples were shown in Fig. 3-11, with a similar adsorption isotherm of type III, suggesting the strong cohesion force between adsorbate N<sub>2</sub> molecular and graphite.

### ***3.2.1.2 Graphitization characterization of graphite samples***

The graphitic structures of different graphite were studied by Raman spectroscopy, which is a common method to characterize the order of carbon materials.<sup>[29-33]</sup> The Raman spectra of the samples and the quantitative results are summarized in Fig. 3-12 and Table 3-2. The D band centered at ~1350 cm<sup>-1</sup> is usually attributed to defects and pyrolytic carbon impurities in carbon material; the peak at around 1580 cm<sup>-1</sup> is assigned to in-plane vibrations of graphite (sp<sup>2</sup>-bonded carbon).<sup>[19, 30, 34]</sup>

In order to quantify the disorder of carbon materials, the intensity ration of D- and G-bands (ID/IG) was calculated based on the mathematical fitting procedures for the Raman spectra.<sup>[33, 60]</sup> In this study, we used a mathematical fitting procedure to fit the carbon band combinations for the Raman spectra.<sup>[29]</sup> In principle, the Raman spectra of carbon could be attributed to five different bands: G, around 1580 cm<sup>-1</sup> is the ideal graphitic lattice (E<sub>2g</sub>-symmetry); D1, around 1350 cm<sup>-1</sup> is disordered graphitic lattice (graphene layer edges, A<sub>1g</sub>-symmetry); D2, around 1620 cm<sup>-1</sup> is the disordered graphitic lattice (surface graphene layers, E<sub>2g</sub>-symmetry); D3, around 1500 cm<sup>-1</sup> is amorphous carbon; D4, around 1200 cm<sup>-1</sup> is disordered graphitic lattice (A<sub>1g</sub>-symmetry), polyenes and ionic impurities. As shown in Fig. 3-12, the D3 and D4 bands could not be observed in graphite and exfoliated graphite samples indicates that the amorphous carbons are absent on the surface of G and EG samples. The increased ID/IG ratio of exfoliated graphite is due to the increasing density of graphene edges. This phenomenon could also be ascribed to the rough surface of exfoliated graphite caused by the strong acidic pretreatment and oxidation processes. The Raman spectra of HSAG sample showed all 5 bands of carbon combinations,

indicates the disorder structure of carbon. The TEM analysis showed the morphology of high-surface-area graphite, which has bend graphene layers stacking as same as soot but with some disorder or dislocated graphene layers.

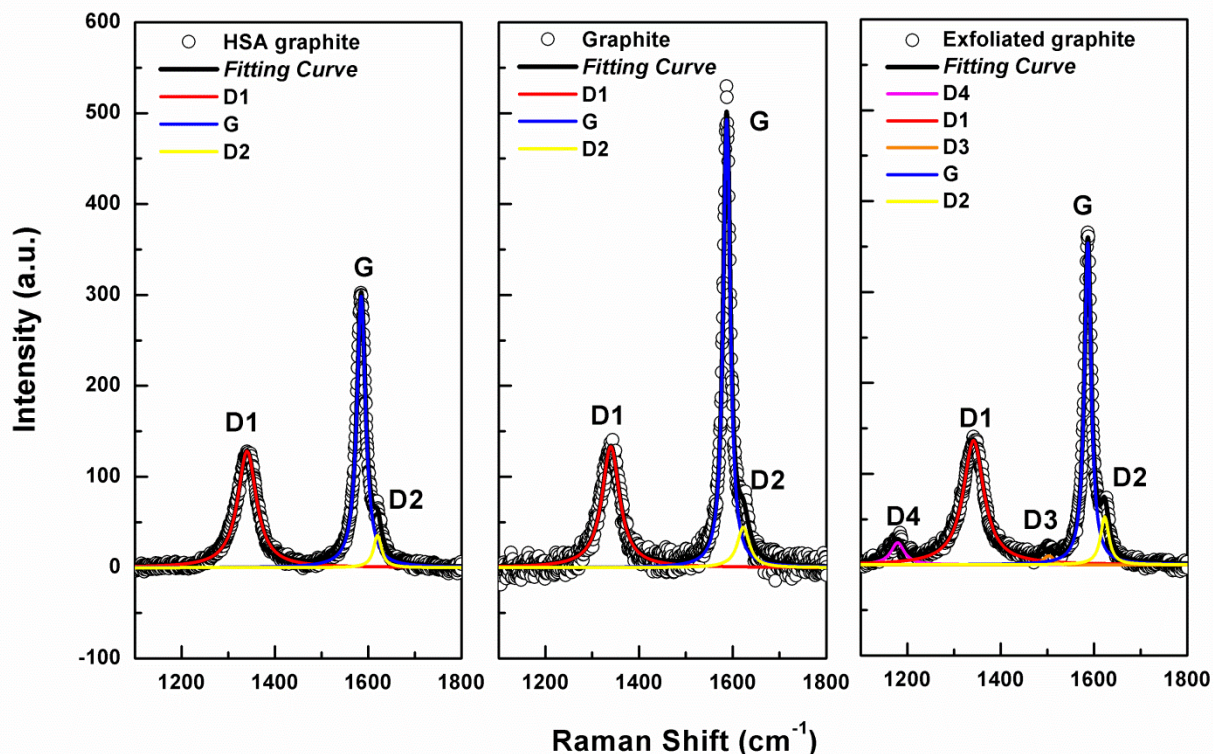


Figure 3-12. Raman spectra of different graphite. All spectra were fitted following the procedure in literature. Ref. [29]

### 3.2.1.3 Surface analysis of graphite

The surface properties of different graphite samples were analysed by X-ray photoelectron spectroscopy, which could identify the chemical configuration on the surface of carbon materials. Figure 3-13 summarized the C1s and O1s XPS spectra of Ru-G, Ru-EG and Ru-HSAG catalysts obtained at 400 °C in vacuum including the details of assigning C1s and O1s features. All sp<sup>2</sup> and sp<sup>3</sup> C-C and C-H bonds were assigned to the C1s signal at 285 eV. The Gaussian peak at 284.8 ± 0.2 eV (sp<sup>3</sup> C-C bond) was only observed in high surface area graphite. The only visible functional group on graphite sample is at 288.95 ± 0.2 eV, which is

probably carboxyl, anhydride, ester, etc. These findings indicate the high graphitic structure and relative clean surface on graphite sample.

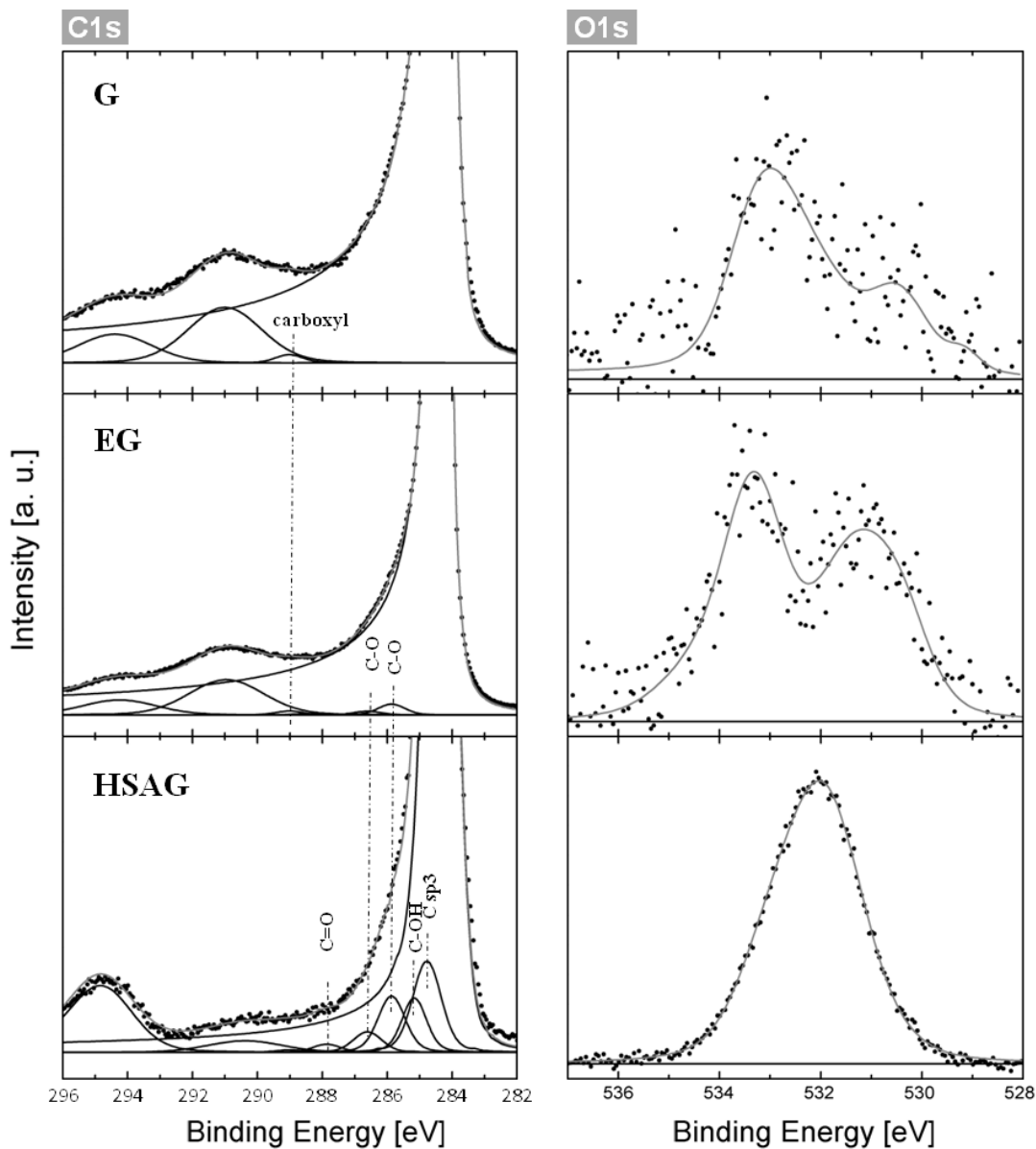


Figure 3-13. XPS analysis of different samples operated at 400 °C in vacuum.

It can be seen that the functional group with C-O bonds are appearing on exfoliated graphite sample, which were formed during the chemical exfoliation procedure. Due to the low amount of those groups on both graphite and exfoliated graphite samples, it is difficult to deconvolute all

the peaks of O1s spectra, but the two peaks corresponding to singly and doubly bound oxygen can be observed at  $531.2 \pm 0.2$  eV and  $533.6 \pm 0.2$  eV. Similar results were found over oxidized carbon nanotubes samples.<sup>[61]</sup> Both the C1s and O1s spectra of high surface area graphite sample show the much more oxygen containing groups compared to the other two graphite. The approximate O molar quantities scale with the order of HSAG > EG > G. It was reported that the dispersed oxidized vacancies on the surface of carbon materials can be used in bonding nanoparticles.<sup>[62]</sup> Thus the different metal-support interactions will be expected when depositing ruthenium nanoparticles on these three types of graphite.

### 3.2.2 Catalytic performance of ruthenium samples

Figure 3-14 shows the ammonia conversion of Ru-G sample as function of reaction time. At 450 °C, the steady  $H_2$  production rates of Ru-G, Ru-EG and Ru-HSAG catalysts are 422, 159 and 217  $mmol_{H_2}/(g_{Ru} \cdot min)$  which are listed in Tab. 3-2. The highest reactivity was observed on ruthenium particles supported on a clean and highly graphitic graphite.

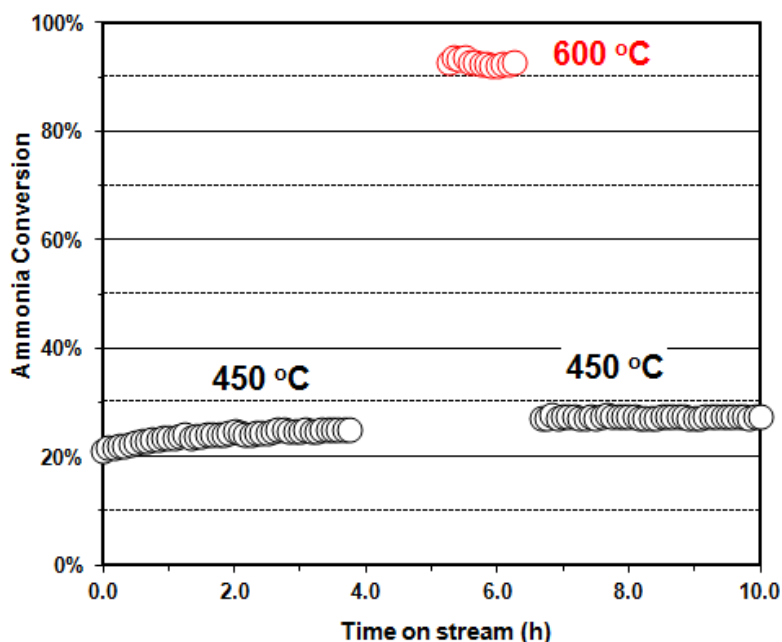


Figure 3-14. Catalytic performance of Ru-G (2wt% Ru supported on graphite) sample at 450 and 600 °C. Reaction condition: 50 mg sample, pure  $NH_3$  with space velocity of  $36000 h^{-1}$ .

### 3.2.3 Morphology of Ru nanoparticles on different graphite

The depositions of Ru nanoparticles on different graphite samples were operated with incipient wetness impregnation method, which detailed in Chapter 2. The prepared catalysts were dried at 110 °C overnight, and pretreated with NH<sub>3</sub> in the catalytic bed of the reactor at 450 °C. After catalytic performance measurements, samples were collected under inert gas, and transferred into a sealed bottle for further characterizations (due to technical problem, samples could not be 100% oxygen-proof).

The morphology of ruthenium nanoparticles supported on different graphite samples was studied by transmission electron microscopy (TEM). The lattice distance of observing ruthenium particles in all images of all catalysts are 0.20, 0.21 and 0.23 nm, which can be attributed to the characteristic values of Ru (101), (002) and (100) planes, respectively.

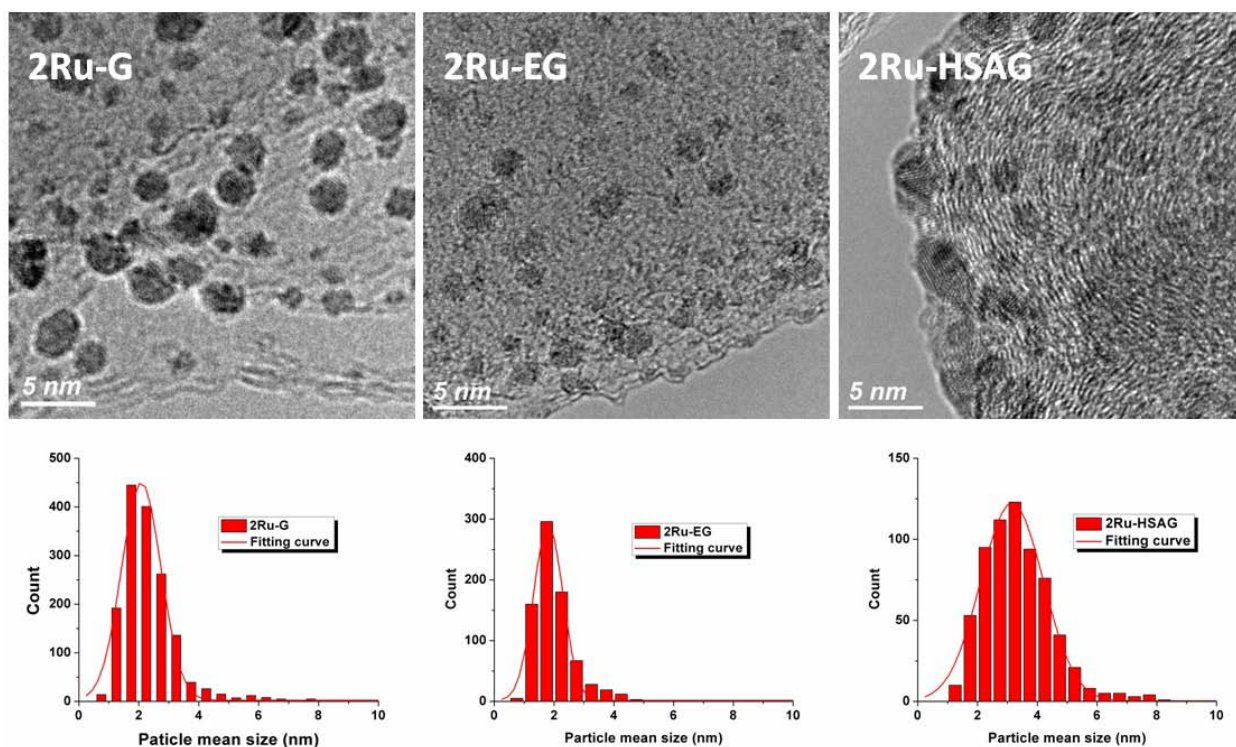


Figure 3-15. Representative TEM images of Ru nanoparticles supported on different graphite (samples were collected after reaction). The particle mean size distributions were calculated with more than 500 individual counting particles.

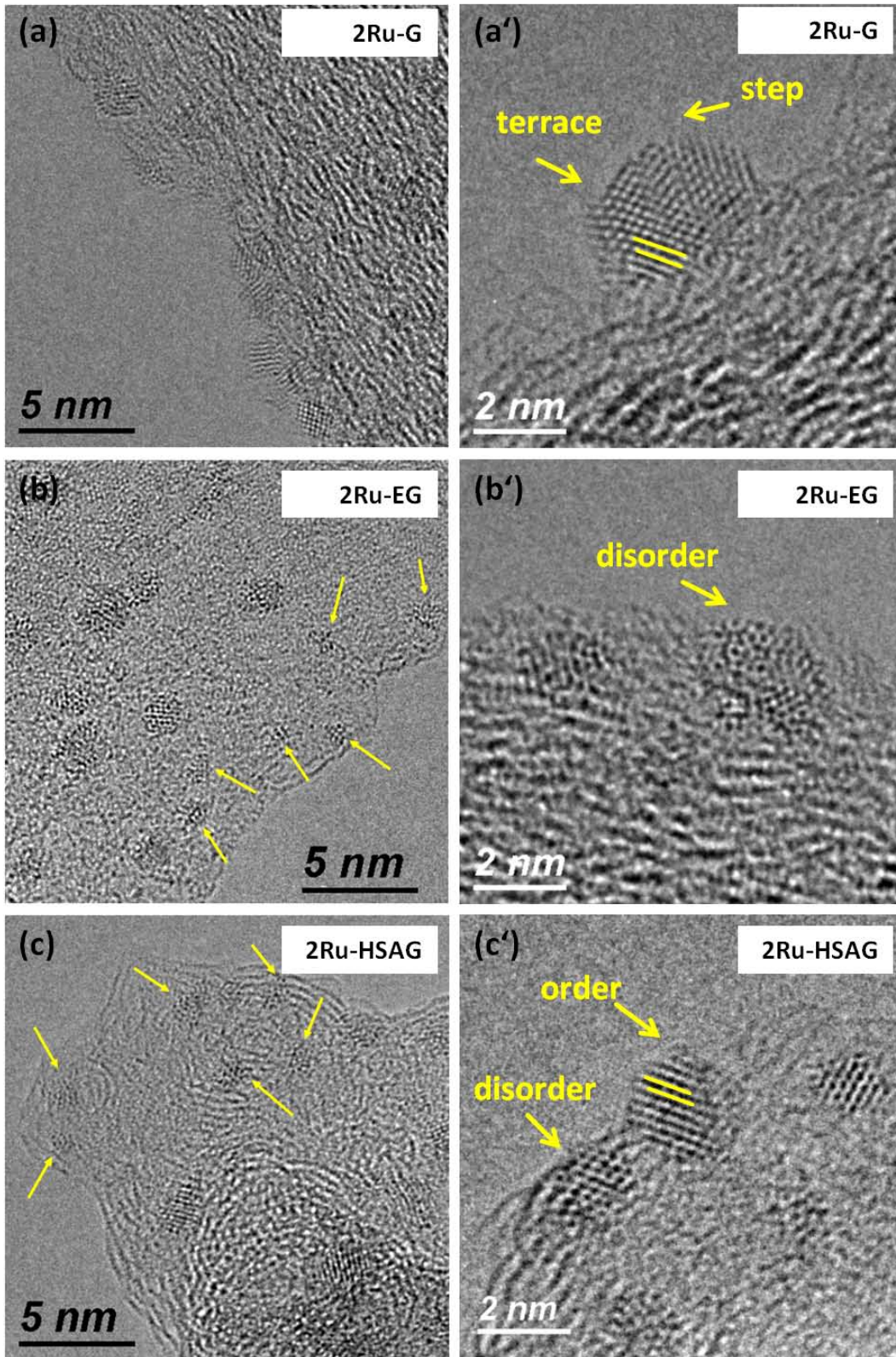
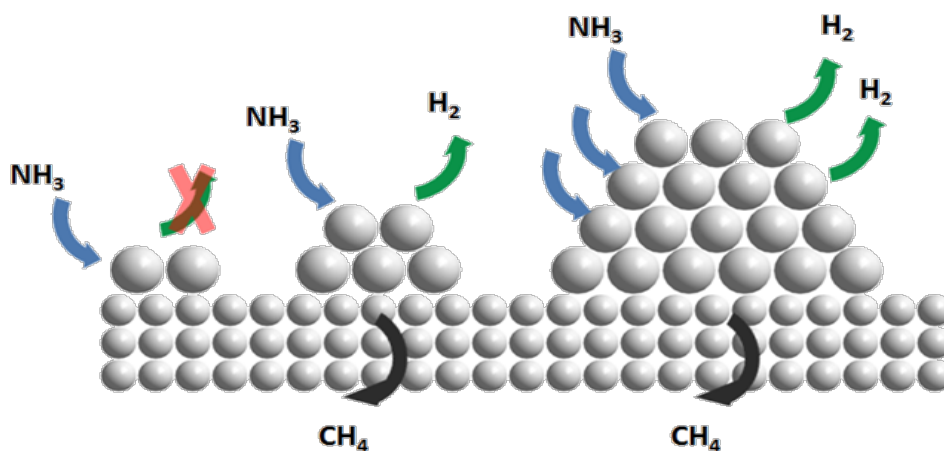


Figure 3-16. Representative high resolution TEM images of Ru nanoparticles supported on different graphite (samples were collected after reaction).

The representative TEM images (inserted with particle mean size distributions calculated with more than 500 individual counting particles) and high resolution TEM (HRTEM) images of three catalysts are shown in Figure 3-15 and 3-16. The ruthenium particles on a clean graphite surface were mostly faceted and had a large size (2.5 nm), while the Ru particles on relative rough graphite surface (exfoliated graphite) were smaller (2.0 nm), less well ordered, and exhibited specifically more defects. This finding is in good agreement with our previous study of ruthenium particles on CNTs<sup>[63]</sup>, that high support ordering leads to a weaker metal-carbon interaction and hence to larger particles. Ammonia decomposition requires the difficult step of N-N recombination through surface diffusion from two sites of ammonia cleavage on weakly adsorbing sites (terraces)<sup>[53]</sup>. This dictates that an active site for ammonia decomposition is a larger ensemble than that for the reverse reaction of ammonia synthesis, which can occur on a single step site as required hydrogen is populating on all ruthenium sites in highly mobile form. At high conversions and on large surface facets inhibition of activity occurs by adsorbed hydrogen<sup>[51]</sup>, as also indicated by the adverse relationship between ruthenium particle size and catalytic conversion of Ru-G and Ru-EG catalysts. These results are in line with the faceted shape seen in the HRTEM images (Fig. 3-16), producing many large flat terraces with a low density of high-energy sites.



Scheme 3-1.  $\text{NH}_3$  decomposition over different size of Ru nanoparticles supported on carbon material.

Compared to Ru-G catalyst, Ru-HSAG exhibited larger size (3.3 nm) with broader distribution of Ru particles, and lower reactivity of ammonia decomposition. The high density of oxygen

species on the surface (XPS O1s in Fig 3-13), the low degree of graphitization (Raman spectra in Fig. 3-12) and the local geometry of the curved graphene layers lead to the broad distribution of ruthenium particles deposited on high surface area graphite. Rinaldi et al. reported the disordering structure of supporting metal particles originates from the local disordering structure of carbon support.<sup>[64]</sup> They presented the HRTEM images of different nickel particles supported on disordering and ordering carbon supports (as shown in Fig. 1-8 in Chapter 1). Unfortunately, due to the “knock on” effect and beam damage during the observation with TEM at 300 kV, it is difficult to investigate the interface on the boundary of carbon material and nanosized ruthenium particles, which is most likely the direct proof to explain the differences in catalytic activity observed for metals supported on various carbons.<sup>[64]</sup>

In Fig. 3-16 (a) to (c), a series of ruthenium atomic clusters with size lower than 2 nm could be observed in Ru-EG and Ru-HSAG catalysts but invisible in Ru-G catalyst. These atomic ruthenium clusters anchored by the dispersed oxidized vacancies on carbon surface has much higher density of high energy sites (defects), but the turnover frequency of NH<sub>3</sub> molecule should be extremely low owing to the strong interaction of Ru-N bond and the shortage of sites for H atoms. This process could be described as Scheme 3-1. Ruthenium atoms are immobilized on the dispersed oxidized vacancies on the surface of graphite, and tend to sit on local disorder sites in the graphene layers. Similar results were also observed earlier with Ru catalysts supported on fullerene black<sup>[44, 45]</sup>. The disordering carbon where ruthenium sits on has tendency to be dissolved in ruthenium particles to form carbides at the boundary. This incorporation of carbon from the support could lead the disordering structure of ruthenium particles, and further influence the catalytic performance for ammonia decomposition as consequence. It is known that, Ru can catalyze the methanation of carbon in a H<sub>2</sub> rich environment, which could inhibit the formation of hydrogen under the reaction condition for ammonia decomposition. On a clean and high graphitic carbon surface, due to the low interaction between ruthenium particle and carbon, ruthenium particles trend to keep the well-ordered structure and lead to the formation of large flat of terraces, which are beneficial for the re-combinative desorption of N and H atoms. An explanation of the clear finding from the HRTEM images and catalytic conversion, that the high performance of ruthenium nanoparticles supported on carbon materials must stem from either the large size or the well ordering structure of Ru originated from the high ordering structure of carbon supports.

### 3.2.4 In-situ XPS measurements of the working system

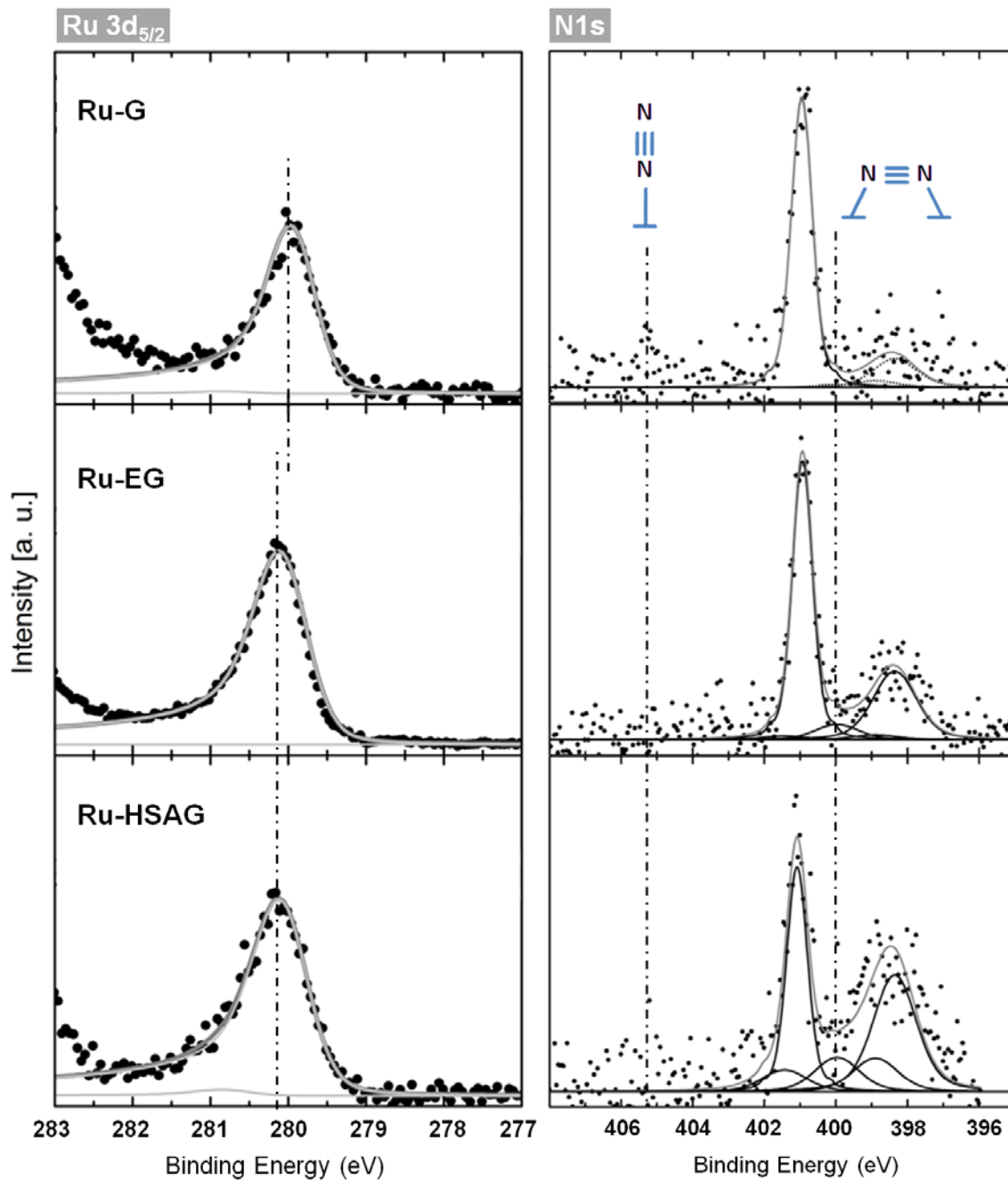


Figure 3-17. Core-level photoelectron spectrum of Ru3d<sub>5/2</sub> and N1s of all catalysts measured in 0.5 mbar NH<sub>3</sub> at 400 °C on an in situ XPS instrument performed at the ISIS beamline located at the BESSY II synchrotron.

To investigate the reactants' behavior on different ruthenium surfaces, three catalysts were characterized by means of in situ X-ray photoelectron spectroscopy (XPS) measured at 400 °C and 0.5 mbar NH<sub>3</sub>, which is close to the practical reaction condition of ammonia decomposition. The Ru3d5/2 spectra in Fig. 3-17 show that the ruthenium is mainly in the metallic states at the working conditions. The formation of ruthenium nitride or subnitride on the three samples could not be observed by this highly sensitive in situ technique, which is probably due to the low density of these species. The binding energy of Ru3d5/2 peak over Ru-G sample is 0.1 eV smaller compared to the other two spectra of Ru-EG and Ru-HSAG catalysts, indicates that at the reaction condition the electron density on ruthenium surface could be alternated by Ru-carbon interaction. The high performance of ammonia decomposition on Ru benefits from the high electron density on ruthenium surface, which could accelerate the recombinative desorption of N-atoms (the rate determining step),<sup>[53]</sup> and increase the forward turnover frequency.

After normalization of C1s peak, the intensity of ruthenium peak increased with the increasing disorder structure of graphite support. The high intensity of ruthenium on disordered graphite support should be attributed to the small atomic clusters anchored on the disordered graphite. These findings suggest that not all the ruthenium atoms exposed on the surface should be ascribed to the active sites for ammonia decomposition, which is in good agreement with the HRTEM analysis.

The core-level photoelectron N1s spectra (Fig. 3-17-right) of all samples operated at 400 °C in 0.5 mbar NH<sub>3</sub> show a mixture of N states. The sharp and narrow peak at 400.9 eV is the gas phase peak of ammonia. The strongest component is found at 398.4 eV, which in this case is most likely the adsorbed NH<sub>3</sub> and some N-C species. It was reported earlier that the adsorption of N<sub>2</sub> on iron surface could be assigned to a molecularly adsorbed N<sub>2</sub> (400.2 eV), linear N<sub>2</sub> (405.3 eV) species,<sup>[65]</sup> and the atomic N (397 eV).<sup>[66]</sup> These observations were further energetically corresponded very well to the experiment on a pretreated ruthenium crystal in 10<sup>-6</sup> mbar N<sub>2</sub> at 300 K (shown in Figure 3-18).<sup>[54]</sup> As mentioned before, the recombinative desorption of N atoms from the surface of catalyst is the rate determining step of ammonia decomposition. This suggests that the desorption of N<sub>2</sub> from the catalysts surface plays the important role to the reaction of ammonia decomposition. In Fig. 3-17-right, the N1s peak at 400 eV of Ru-G sample is nearly invisible, indicates a low coverage of N<sub>2</sub> molecular on the large and ordering Ru

nanoparticles, which should be responsible for the high turnover frequency of ammonia decomposition. The high intensities of this dinitrogen peak on the small (Ru-EG) or disorder (Ru-HSAG) ruthenium nanoparticles indicate the high coverage of  $N_2$  molecular, which should be ascribed to either the high energy density of small ruthenium clusters or the disordered ruthenium surface. The difficulties of  $N_2$  desorption from the small/disordering ruthenium particles lead to the low turnover frequency of  $NH_3$  molecular and low catalytic conversion as consequence.

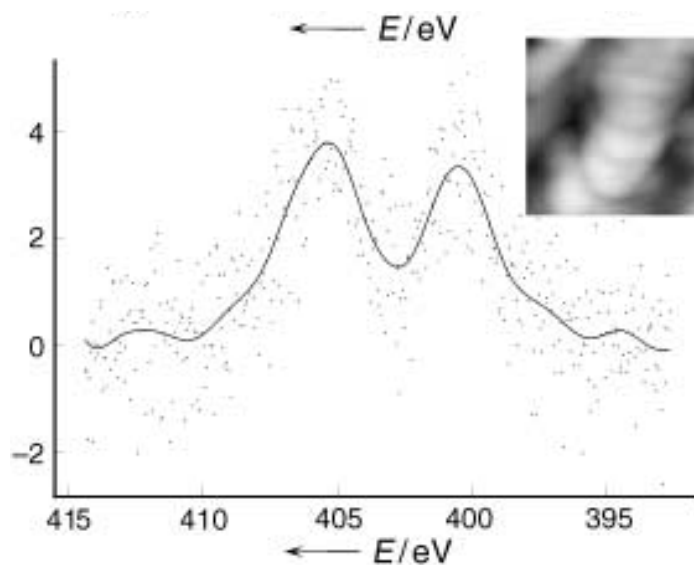


Figure 3-18. Core-level photoelectron spectrum of the N1s level of molecular adsorbed nitrogen. The measurement was taken with  $Mg_{k\alpha}$  excitation and with a sample temperature of 300 K and a background pressure of  $10^{-6}$  mbar  $N_2$ . The inset shows an atomic force microscopy (AFM) image of the microstructure of the sample surface in air. (Figure taken from Ref.[54].)

### **3.3 Chapter conclusions**

#### ***3.3.1 Ru-CNTs***

In this section, we reported a structure-function correlation for ruthenium nanoparticles on CNTs. The observed trend is counter-intuitive to the general notion about a beneficial effect of reduced particle size for better activity in a nonselective reaction. The fact that the support offers different sites for Ru-in and Ru-out masks the possible beneficial effect of the enhanced electron density of thermally annealed CNTs. The size of ruthenium particles can be controlled effectively by a combination of modifying the site density of defects on the support and by localization of the active metal inside or outside of the mesopores of the CNT. At the inside of the CNTs it was not possible to sufficiently enhance the electron density of the support to strongly activate the rough and small metal particles. It remains to be seen if the intrinsic difference in curvature between convex (outer) and concave (inner) has an effect on the metal-support interaction.

#### ***3.3.2 Ru-graphite***

These work leads to the following major conclusions. First, it is clear that the catalytic activity of metals supported on carbon materials can be partially explained by the metal-carbon interaction originating from the local order of carbons (carbon incorporation). Similar conclusions were observed from carbons growth on Ni supported on carbon with different graphitization structure,<sup>[64]</sup> and hydrogenation reaction on Pd-Ga intermetallic nanoparticle supported on CNTs.<sup>[62]</sup> Second, with the help of high resolution transmission electron microscopy, the detail morphology of small Ru atomic particles could be observed and correlated to the reaction performance with the particle size and shape (ordering structure). Third, the highly sensitive in situ surface characterization technique could offer the direct crucial information of the nanoparticles in practically relevant catalysts at the working state. In summary, the combinative characterizations can lead to a direct conclusion, that the different catalytic performances of carbon supported ruthenium catalysts for the reaction of ammonia decomposition is dependent on the local graphitic order of carbon supports. The high graphitic carbon support can benefit for

the formation of well ordered Ru nanoparticles with large terraces for H<sub>2</sub> desorption and steps as active sites for NH<sub>3</sub> molecular. It remains to be seen the direct evidence of the formation of metal surface nitrides or subsurface nitrides play the most important factor in this reaction.

## References

1. Choudhary, T.V., C. Sivadinarayana, and D.W. Goodman, *Catalytic Ammonia Decomposition: CO<sub>x</sub>-free Hydrogen Production for Fuel Cell Applications*. *Catalysis Letters*, 2001. **72**(3-4): p. 197-201.
2. Yin, S.F., et al., *A Mini-Review on Ammonia Decomposition Catalysts for On-Site Generation of Hydrogen for Fuel Cell Applications*. *Applied Catalysis a-General*, 2004. **277**(1-2): p. 1-9.
3. Yin, S.F., et al., *Investigation on the Catalysis of CO<sub>x</sub>-free Hydrogen Generation from Ammonia*. *Journal of Catalysis*, 2004. **224**(2): p. 384-396.
4. Li, L., et al., *Catalytic Ammonia Decomposition over Ru/carbon Catalysts: The Importance of the Structure of Carbon Support*. *Applied Catalysis A: General*, 2007. **320**: p. 166-172.
5. Castillejos, E., et al., *An Efficient Strategy to Drive Nanoparticles into Carbon Nanotubes and the Remarkable Effect of Confinement on Their Catalytic Performance*. *Angewandte Chemie International Edition*, 2009. **48**(14): p. 2529-2533.
6. Ma, H., et al., *Pt nanoparticles Deposited over Carbon Nanotubes for Selective Hydrogenation of Cinnamaldehyde*. *Catalysis Communications*, 2007. **8**(3): p. 452-456.
7. Chen, W., et al., *Effect of Confinement in Carbon Nanotubes on the Activity of Fischer-Tropsch Iron Catalyst*. *Journal of the American Chemical Society*, 2008. **130**(29): p. 9414-9419.
8. Pan, X., et al., *Enhanced Ethanol Production Inside Carbon-NanotubeReactors Containing Catalytic Particles*. *Nature Materials*, 2007. **6**(7): p. 507-511.
9. Zhang, J., et al., *Commercial Fe- or Co-containing Carbon Nanotubes as Catalysts for NH<sub>3</sub> Decomposition*. *Chemical Communications*, 2007(19): p. 1916.
10. Rinaldi, A., *Synthesis of Carbon Nanotubes on Carbon Supports and the Purification of Carbon Nanotubes*, in *Inorganic Chemistry*. 2010, Fritz-Haber-Institut der Max-Planck Gesellschaft: Berlin. p. 1-228.
11. Brukh, R. and S. Mitra, *Kinetics of carbon nanotube oxidation*. *Journal of Materials Chemistry*, 2007. **17**(7): p. 619.
12. Smith, M.R., et al., *Selective oxidation of single-walled carbon nanotubes using carbon dioxide*. *Carbon*, 2003. **41**(6): p. 1221-1230.
13. Delpeux, S., et al., *An efficient two-step process for producing opened multi-walled carbon nanotubes of high purity*. *Chemical Physics Letters*, 2005. **404**(4-6): p. 374-378.
14. Ajayan, P.M., et al., *Opening carbon nanotubes with oxygen and implications for filling*. *Nature*, 1993. **362**(6420): p. 522-525.
15. Li, C., *Oxidation of multiwalled carbon nanotubes by air: benefits for electric double layer capacitors*. *Powder Technology*, 2004. **142**(2-3): p. 175-179.
16. Park, Y.S., et al., *High yield purification of multiwalled carbon nanotubes by selective oxidation during thermal annealing*. *Carbon*, 2001. **39**(5): p. 655-661.
17. Shaffer, M.S.P., X. Fan, and A.H. Windle, *Dispersion and packing of carbon nanotubes*. *Carbon*, 1998. **36**(11): p. 1603-1612.
18. Ando, Y., X. Zhao, and H. Shimoyama, *Structure analysis of purified multiwalled carbon nanotubes*. *Carbon*, 2001. **39**(4): p. 569-574.
19. Osswald, S., et al., *Elimination of D-band in Raman spectra of double-wall carbon nanotubes by oxidation*. *Chemical Physics Letters*, 2005. **402**(4-6): p. 422-427.
20. Hu, H., et al., *Nitric Acid Purification of Single-Walled Carbon Nanotubes*. *The Journal of Physical Chemistry B*, 2003. **107**(50): p. 13838-13842.
21. Rinzler, A.G., et al., *Large-scale purification of single-wall carbon nanotubes: process, product, and characterization*. *Applied Physics A: Materials Science & Processing*, 1998. **67**(1): p. 29-37.

22. Jia, Z., et al., *Production of short multi-walled carbon nanotubes*. Carbon, 1999. **37**(6): p. 903-906.
23. Shao, L., et al., *Removal of amorphous carbon for the efficient sidewall functionalisation of single-walled carbon nanotubes*. Chemical Communications, 2007(47): p. 5090-5092.
24. Fogden, S., et al., *Purification of single walled carbon nanotubes: The problem with oxidation debris*. Chemical Physics Letters, 2008. **460**(1-3): p. 162-167.
25. Hernadi, K., et al., *Reactivity of different kinds of carbon during oxidative purification of catalytically prepared carbon nanotubes*. Solid State Ionics, 2001. **141-142**: p. 203-209.
26. Suzuki, T., et al., *Purification of single-wall carbon nanotubes produced by arc plasma jet method*. Diamond and Related Materials, 2007. **16**(4-7): p. 1116-1120.
27. Kosaka, M., et al., *Annealing effect on carbon nanotubes. An ESR study*. Chemical Physics Letters, 1995. **233**(1-2): p. 47-51.
28. Nysten, B., et al., *AFM and STM studies of the carbonization and graphitization of polyimide films*. Physical Review B, 1993. **48**(17): p. 12527.
29. Sadezky, A., et al., *Raman micro spectroscopy of soot and related carbonaceous materials: Spectral analysis and structural information*. Carbon, 2005. **43**(8): p. 1731-1742.
30. Osswald, S., M. Havel, and Y. Gogotsi, *Monitoring oxidation of multiwalled carbon nanotubes by Raman spectroscopy*. Journal of Raman Spectroscopy, 2007. **38**(6): p. 728-736.
31. Tuinstra, F. and J.L. Koenig, *Raman Spectrum of Graphite*. The Journal of Chemical Physics, 1970. **53**(3): p. 1126-1130.
32. Sato, K., et al., *D-band Raman intensity of graphitic materials as a function of laser energy and crystallite size*. Chemical Physics Letters, 2006. **427**(1-3): p. 117-121.
33. Nakamura, K., M. Fujitsuka, and M. Kitajima, *Disorder-induced line broadening in first-order Raman scattering from graphite*. Physical Review B, 1990. **41**(17): p. 12260.
34. Osswald, S., E. Flahaut, and Y. Gogotsi, *In Situ Raman Spectroscopy Study of Oxidation of Double- and Single-Wall Carbon Nanotubes*. Chemistry of Materials, 2006. **18**(6): p. 1525-1533.
35. Ferrari, A.C. and J. Robertson, *Interpretation of Raman spectra of disordered and amorphous carbon*. Physical Review B, 2000. **61**(20): p. 14095.
36. Ferrari, A.C., et al., *Density,  $sp^3$  fraction, and cross-sectional structure of amorphous carbon films determined by x-ray reflectivity and electron energy-loss spectroscopy*. Physical Review B, 2000. **62**(16): p. 11089.
37. Papworth, A.J., et al., *Electron-energy-loss spectroscopy characterization of the  $sp^2$  bonding fraction within carbon thin films*. Physical Review B, 2000. **62**(19): p. 12628.
38. Tessonier, J.-P., et al., *Selective Deposition of Metal Nanoparticles Inside or Outside Multiwalled Carbon Nanotubes*. ACS Nano, 2009. **3**(8): p. 2081-2089.
39. Gates, B.C., *Supported Metal Cluster Catalysts*. Handbook of Heterogeneous Catalysis. 2008: Wiley-VCH Verlag GmbH & Co. KGaA.
40. Geus, J.W. and A.J. van Dillen, *Preparation of Supported Catalysts by Deposition–Precipitation*. Handbook of Heterogeneous Catalysis. 2008: Wiley-VCH Verlag GmbH & Co. KGaA.
41. Serp, P., M. Corrias, and P. Kalck, *Carbon nanotubes and nanofibers in catalysis*. Applied Catalysis A: General, 2003. **253**(2): p. 337-358.
42. Zhang, J., et al., *Individual Fe–Co Alloy Nanoparticles on Carbon Nanotubes: Structural and Catalytic Properties*. Nano Letters, 2008. **8**(9): p. 2738-2743.
43. Zhang, J., et al., *Surface-Modified Carbon Nanotubes Catalyze Oxidative Dehydrogenation of n-Butane*. Science, 2008. **322**(5898): p. 73-77.
44. Braun, T., et al., *Fullerene-based ruthenium catalysts: a novel approach for anchoring metal to carbonaceous supports. I. Structure*. Catalysis Letters, 1997. **43**(3): p. 167-173.

45. Braun, T., et al., *Fullerene-based ruthenium catalysts: a novel approach for anchoring metal to carbonaceous supports. II. Hydrogenation activity*. Catalysis Letters, 1997. **43**(3): p. 175-180.
46. Hellman, A., et al., *Ammonia synthesis and decomposition on a Ru-based catalyst modeled by first-principles*. Surface Science, 2009. **603**(10-12): p. 1731-1739.
47. Dahl, S., et al., *Electronic factors in catalysis: the volcano curve and the effect of promotion in catalytic ammonia synthesis*. Applied Catalysis A: General, 2001. **222**(1-2): p. 19-29.
48. Murata, S. and K.-I. Aika, *Preparation and characterization of chlorine-free ruthenium catalysts and the promoter effect in ammonia synthesis. : 1. An alumina-supported ruthenium catalyst*. Journal of Catalysis, 1992. **136**(1): p. 110-117.
49. Liang, C., et al., *Ammonia synthesis over Ru/C catalysts with different carbon supports promoted by barium and potassium compounds*. Applied Catalysis A: General, 2001. **208**(1-2): p. 193-201.
50. García-García, F., A. Guerrero-Ruiz, and I. Rodríguez-Ramos, *Role of B5-Type Sites in Ru Catalysts Used for the NH<sub>3</sub> Decomposition Reaction*. Topics in Catalysis, 2009. **52**(6): p. 758-764.
51. Aika, K., et al., *Support and promoter effect of ruthenium catalyst : I. Characterization of alkali-promoted ruthenium/alumina catalysts for ammonia synthesis*. Journal of Catalysis, 1985. **92**(2): p. 296-304.
52. Klerke, A., S.K. Klitgaard, and R. Fehrmann, *Catalytic Ammonia Decomposition Over Ruthenium Nanoparticles Supported on Nano-Titanates*. Catalysis Letters, 2009. **130**(3-4): p. 541-546.
53. Schlögl, R., *Ammonia Synthesis*. Handbook of Heterogeneous Catalysis. 2008: Wiley-VCH Verlag GmbH & Co. KGaA.
54. Schlögl, R., *Catalytic Synthesis of Ammonia—A “Never-Ending Story”?* Angewandte Chemie International Edition, 2003. **42**(18): p. 2004-2008.
55. Honkala, K., *Ammonia Synthesis from First-Principles Calculations*. Science, 2005. **307**(5709): p. 555-558.
56. Jacobsen, C.J.H., et al., *Structure sensitivity of supported ruthenium catalysts for ammonia synthesis*. Journal of Molecular Catalysis A: Chemical, 2000. **163**(1-2): p. 19-26.
57. Gavnholt, J., et al., *Structure and reactivity of ruthenium nanoparticles*. Physical Review B, 2008. **77**(3): p. 035404.
58. Raróg-Pilecka, W., et al., *Structure sensitivity of ammonia synthesis over promoted ruthenium catalysts supported on graphitised carbon*. Journal of Catalysis, 2005. **231**(1): p. 11-19.
59. Jacobsen, C.J.H., et al., *Optimal Catalyst Curves: Connecting Density Functional Theory Calculations with Industrial Reactor Design and Catalyst Selection*. Journal of Catalysis, 2002. **205**(2): p. 382-387.
60. Wang, Y., D.C. Alsmeyer, and R.L. McCreery, *Raman spectroscopy of carbon materials: structural basis of observed spectra*. Chemistry of Materials, 1990. **2**(5): p. 557-563.
61. Kundu, S., et al., *Thermal Stability and Reducibility of Oxygen-Containing Functional Groups on Multiwalled Carbon Nanotube Surfaces: A Quantitative High-Resolution XPS and TPD/TPR Study*. The Journal of Physical Chemistry C, 2008. **112**(43): p. 16869-16878.
62. Shao, L., et al., *Nanosizing Intermetallic Compounds Onto Carbon Nanotubes: Active and Selective Hydrogenation Catalysts*. Angewandte Chemie International Edition, 2011: p. n/a-n/a.
63. Zheng, W., et al., *Structure-Function Correlations for Ru/CNT in the Catalytic Decomposition of Ammonia*. ChemSusChem, 2010. **3**(2): p. 226-230.
64. Rinaldi, A., et al., *Dissolved Carbon Controls the Initial Stages of Nanocarbon Growth*. Angewandte Chemie International Edition, 2011. **50**(14): p. 3313-3317.
65. Kishi, K. and M.W. Roberts, *Adsorption of nitrogen and ammonia by polycrystalline iron surfaces in the temperature range 80-290 K studied by electron spectroscopy*. Surface Science, 1977. **62**(1): p. 252-266.

66. Grunze, M., et al., *pi*-Bonded N<sub>2</sub> on Fe(111): The Precursor for Dissociation. Physical Review Letters, 1984. **53**(8): p. 850.



## Chapter 4:

### Alloying transition metal nanoparticles on CNTs

Carbon nanotubes supported transition metal nanoparticles have attracted intensive interests in several important interdisciplinary research fields. CNTs have a hollow tubular channel and provide an extremely high mechanical strength of carbon walls to encapsulate magnetic nanowires or nanorods<sup>[1]</sup> up to micrometers in length. The graphitic wall as protective shell is expected to prevent the sintering of nanoparticles during the shaping process and to avoid the dipolar relaxation between two neighboring magnetic centres, which are major drawbacks of traditional spinel nanoparticles.<sup>[1]</sup> As a novel carbon material, CNTs have been employed as supports for active metals in heterogeneous catalysis. Compared with traditional oxide supports, CNTs have high thermal and electronic conductivities, good resistance to acidic/basic chemicals at high temperature, controllable porosity, and tuneable surface properties.<sup>[2]</sup>

Alloys (or bimetals) are proved to have superior catalytic properties with respect to the reactivity as compared with pure metals.<sup>[3]</sup> Mixtures of transition metals are particular interest in a number of reactions, including the Fischer-Tropsch reaction,<sup>[4]</sup> carbon nanotube growth,<sup>[5]</sup> water gas shift reaction,<sup>[6]</sup> NH<sub>3</sub> synthesis<sup>[7]</sup>, etc. Synergic improvement of the catalytic activity is expected for ammonia synthesis by alloying two active metals (Fe, Co, Ni, Mo, etc.).<sup>[8, 9]</sup> Because of the similarity in limiting factors of rate-determining steps, that is, dissociative adsorption of the N<sub>2</sub> molecule and combinative desorption of surface N\* atoms for synthesis and decomposition respectively, bimetallic or alloy catalysts have been thought to be the main stream trend to optimal solution of decomposition catalysts. However, previous experimental attempts have been restricted in using the metal oxides as support.<sup>[10]</sup> During the thermal pretreatment or reaction at high temperature, the oxidic support can partially transform the metallic alloy into the less reducible ternary oxide with spinel structure (e.g., Ni-Al, Co-Al, Fe-Al and Co-Si). The observed

variance in activity probably arises from the change in reducibility and thus active sites over the surface. In literature, the enhanced performance is often ascribed to the special electronic and/or structural effects of the alloying process. However, it is not convincing to conclude this since there is always a lack of direct evaluations of the alloying status in individual nanoparticles. In this work, we investigated the  $\text{NH}_3$  decomposition reaction over Fe-Co and Fe-Ni bimetallic nanoparticles and employed CNTs to support metallic clusters.

#### 4.1 Textural property of support CNTs

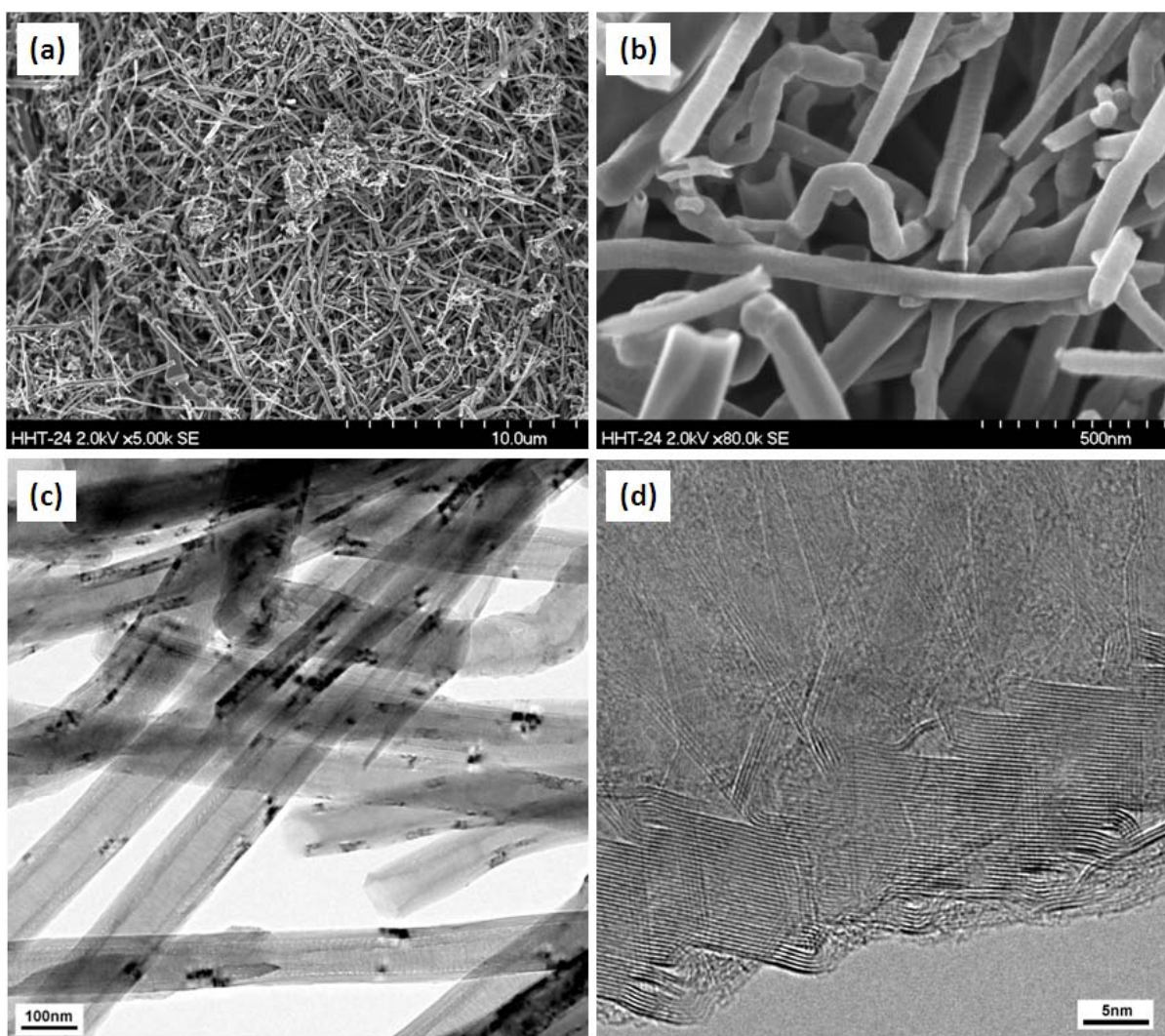


Figure 4-1. SEM and TEM images of The CNTs sample. (a) and (b) overview and high-resolution SEM images; (c) and (d) overview and high-resolution TEM images.

The textural properties of CNTs used as support were investigated by N<sub>2</sub> physisorption and electron microscopy. The specific surface area of the support CNTs is 31.77 m<sup>2</sup>/g, which is much smaller than the one of Baytubes (in Chapter 3). This observation is in agreement with previous work of Peigney et al. who showed the correlation between the specific surface area, the carbon nanotube diameter and number of walls.<sup>[11]</sup> The isotherm of the CNTs showed almost no hysteresis indicating that it is mainly macroporous with pores larger than 50 nm.

The low magnification SEM image (Fig. 4-1-a) shows the agglomerate size is generally 10 to 100 μm indicating densely packed CNTs originated from the post-synthesis debulking method used by Pyrograf products. The debulking process results in decreasing the diameter of the fiber clumps.<sup>[12]</sup> Under high magnification SEM image (Fig. 4-1-b) mainly fibers with polygonal cross sections can be observed, owing to the high temperature treated procedure during the synthesis (3000 °C). It appears that after graphitization above 2800 °C the graphene sheets parallel to the fiber axis get reorganized and the overall structure recrystallizes to form a fiber made of conically stacked highly graphitic crystallites.<sup>[12]</sup>

The representative TEM and HRTEM images of the CNTs are shown in Fig. 4-1. Both the inner and the outer core are well graphitized. Each graphene sheet can easily be followed from the central tubule to the interface between the two wall layers. Oberlin studied the graphitization process of carbon,<sup>[13]</sup> and reported that in the range of 1000-2000°C, small graphitic domains appear that connect to form large wrinkled graphene layers when raising the temperature. These layers untwist and straighten out at temperatures above 2000°C, when carbon atoms start to become mobile. This straightening of the graphene sheets has been clearly observed for the CNTs, which have been post-treated at 3000°C. The carbon atoms are mobile enough to reorganize completely around the core of the fiber. The graphene layers then form large conical structure that stack along the main axis of the fiber. The edges of these cones are separated enough to be seen in the SEM images as small lines perpendicular to the main axis of the CNTs (CNFs). These cones eventually sinter further and recrystallize into large prismatic domains.

## 4.2 Characterizations of metal alloy nanoparticles on CNTs/CNFs

CNTs encapsulated metal alloy nanoparticles were produced on the basis of the capillary phenomenon in the channel of CNTs, as depicted in chapter 2.1.2. In order to investigate the effect of the addition of secondary transition metal (cobalt or nickel) to iron catalyst, Co/Ni nitrates were added into Fe nitrate precursor solution with M(Co,Ni)/Fe ratios of 1, 0.5 and 0.2 respectively.

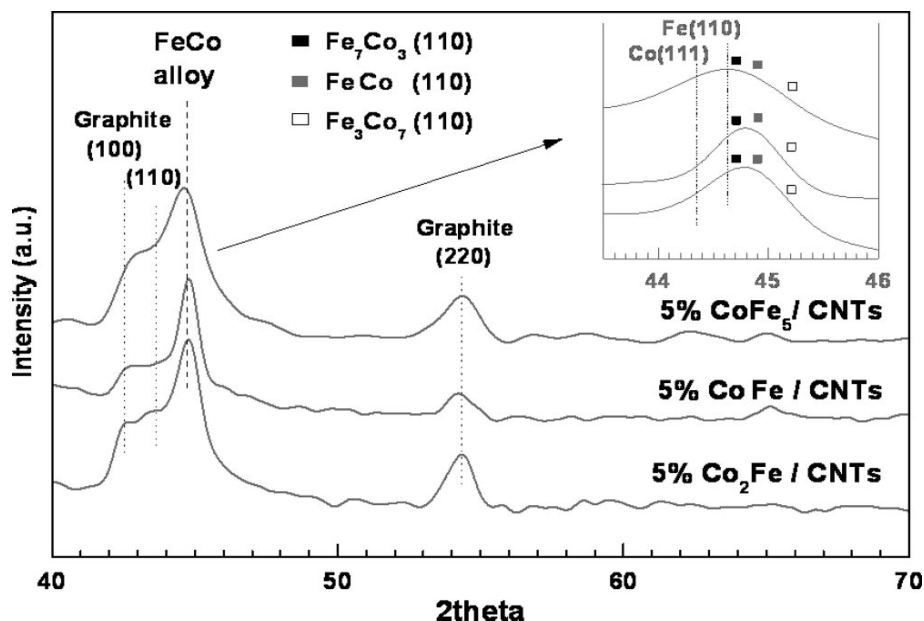


Figure 4-2. XRD patterns of fresh CNTs/CNFs supported Fe-Co catalysts.

Powder X-ray diffraction (XRD) data of the fresh Fe-Co samples were shown in Figure 4-2, in which no signals corresponding to single metallic or metal oxide phases were observed. All characteristic patterns could be ascribed to graphite and metallic Fe-Co alloy phases. As the Co/Fe ratio decreased, the peak of the alloy gradually shifted from 44.7 to 45.1°. Deconvolution of each peak revealed the coexistence of several typical alloy phases with different Fe/Co ratio, for example,  $\text{Fe}_3\text{Co}_7$ , FeCo and  $\text{Fe}_7\text{Co}_3$ , regardless of the nominal composition, which is essentially related to the intrinsic properties of Fe and Co metals to form continuous solid-solution series.

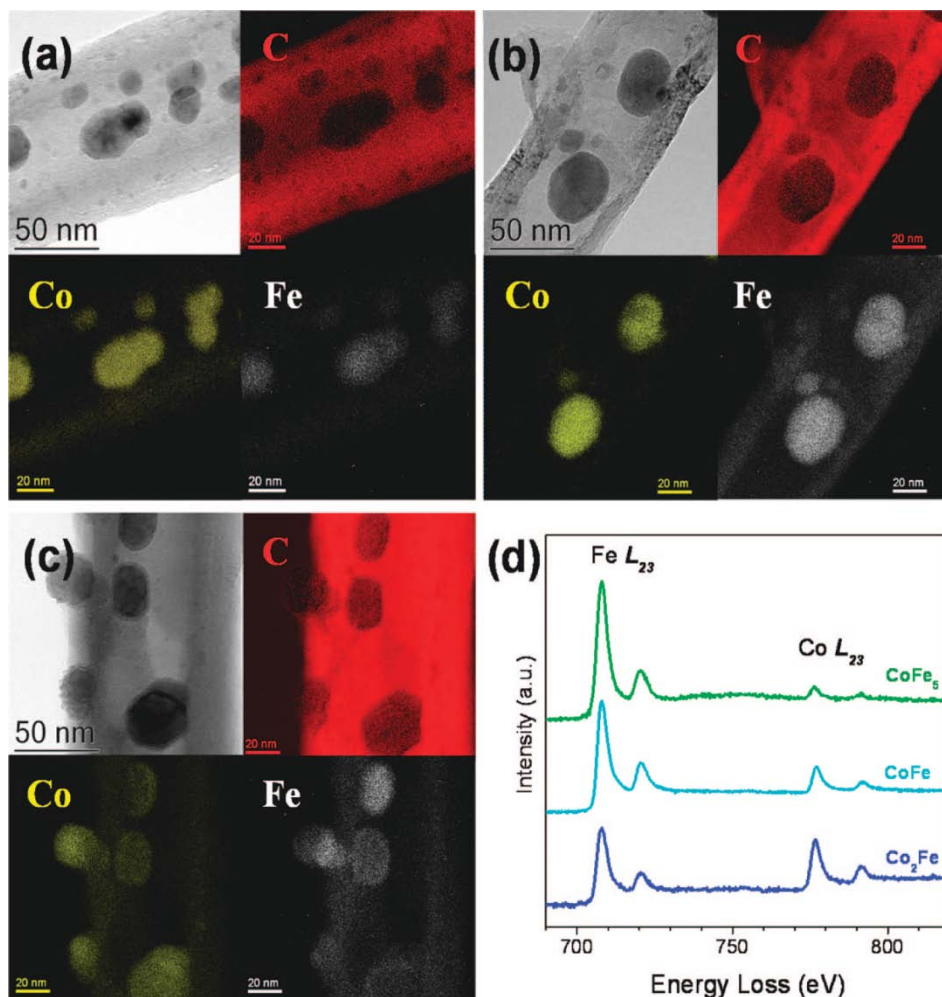


Figure 4-3. TEM characterization results of CNTs supported Fe-Co catalysts. EELS elemental mapping of fresh samples. (a) 5%  $\text{Co}_2\text{Fe}/\text{CNTs}$ ; (b) 5%  $\text{CoFe}/\text{CNTs}$ ; (c) 5%  $\text{CoFe}_5/\text{CNTs}$ ; (d) EELS spectra of fresh samples. (Images taken by Dr. J.-O. Müller. Ref. [14].)

Elemental maps obtained by the energy filtered transmission electron microscopy (EFTEM) of the fresh Fe-Co samples were presented in Fig. 4-3. It can be seen, that every metal particle contains both Fe and Co atoms with homogeneous distributions, suggesting a high alloying extent throughout the nanoparticles. The used samples after the  $\text{NH}_3$  decomposition reaction maintained their well mixed structure. As shown in Fig. 4-3, Co-K and Fe-K profiles as a function of the distance along the line scans revealed the homogeneous distributions of Co and Fe in each individual nanoparticle. Fig. 4-3-d showed the Fe- $L_{23}$  ionization edge at 708 eV and the Co- $L_{23}$  ionization edge at 779 eV. With reduction of the Co/Fe ratio from 2.0 to 0.2, the Co

signal decreased while the Fe signal increased. A significant signal from oxygen (O-K ionization edge around 530 eV) was also recorded by EELS, which mainly arose from the surface oxidation due to air exposure.

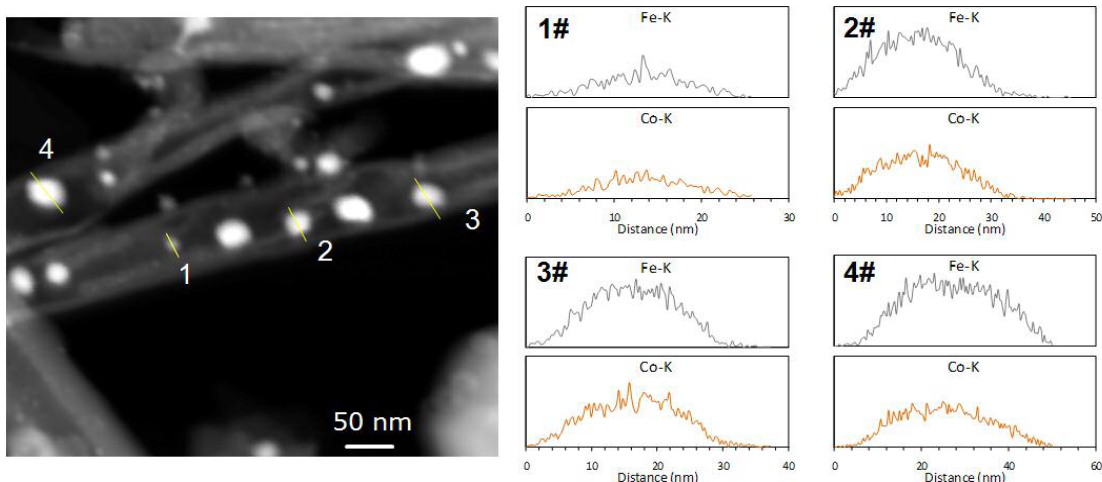


Figure 4-3. Elemental composition of nanoparticles inside the used 5%CoFe/CNTs. (left) dark-field STEM image; (right) line scan EDX spectra of typical nanoparticles. (Images taken by Dr. J.-O. Müller. Ref. [14].)

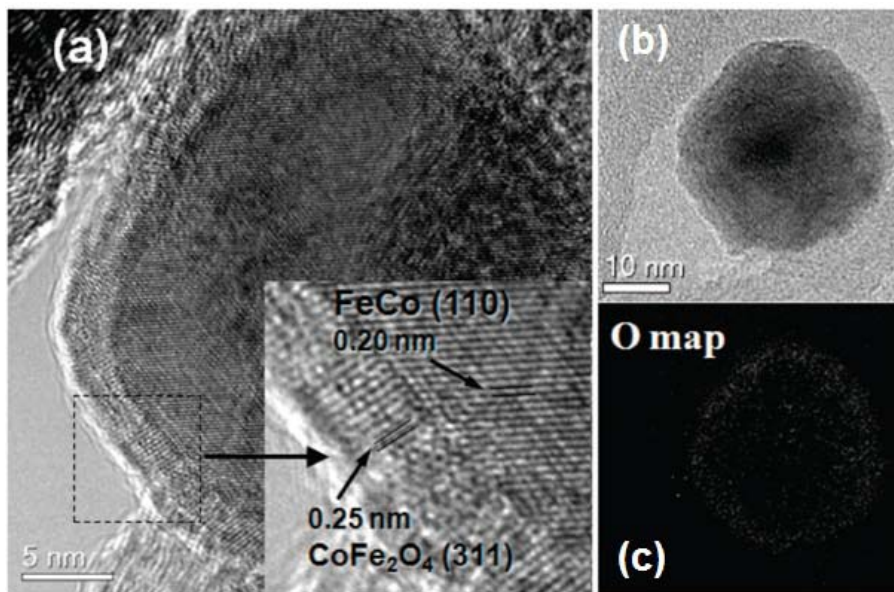


Figure 4-4. TEM analysis of a representative Fe-Co nanoparticle. (a) HRTEM image of the used 5%CoFe/CNTs; (b) the observing Co-Fe particle; (c) oxygen map of the corresponding image of (b). (Images taken by Dr. J.-O. Müller. Ref. [14].)

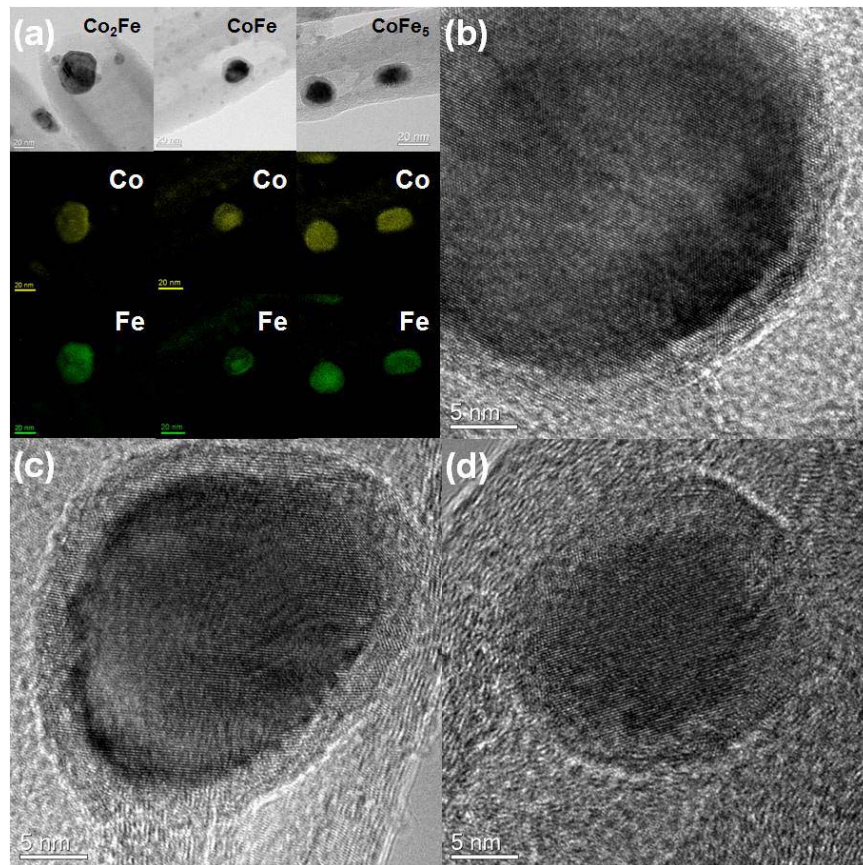


Figure 4-5. Microscopic characterizations of the catalysts after reaction. (a) elemental mapping of Fe and Co in used catalysts; (b) HRTEM image of 5%Co<sub>2</sub>Fe/CNTs; (c) HRTEM image of 5%CoFe/CNTs; (d) HRTEM image of 5%CoFe<sub>5</sub>/CNTs. (Images taken by Dr. J.-O. Müller. Ref. [14].)

The metallic-oxide core-shell structure could be identified by high-resolution TEM image and oxygen mapping of representative alloy particles in the used samples, shown in Fig. 4-4. The lattice distance of core and shell were 0.20 and 0.25 nm, respectively, which could be attributed to the characteristic of Fe-Co alloy (110) and CoFe<sub>2</sub>O<sub>4</sub> (311) planes. This evidence agreed with the measurements of EFTEM and EELS. As shown in the insert of Fig. 4-4-a, the thickness of the oxide shell was close to 10 atomic layers, being thus too thin to be detected by the XRD technique. The existence of such an oxide shell was always observed and independent of the location of the particles. Statistic evaluation of 150 particles for each sample revealed a similar

average particle size of  $13 \pm 2$  nm. It was confirmed, that after reaction, no change in the alloying extent between Fe and Co could be found (in Fig. 4-5). This is different from the pure Fe catalyst, in which an iron nitride phase was formed as active sites during the reaction,<sup>[15]</sup> no nitrogen signal could be identified in the Fe-Co samples, indicating the active phase is the metallic alloy.

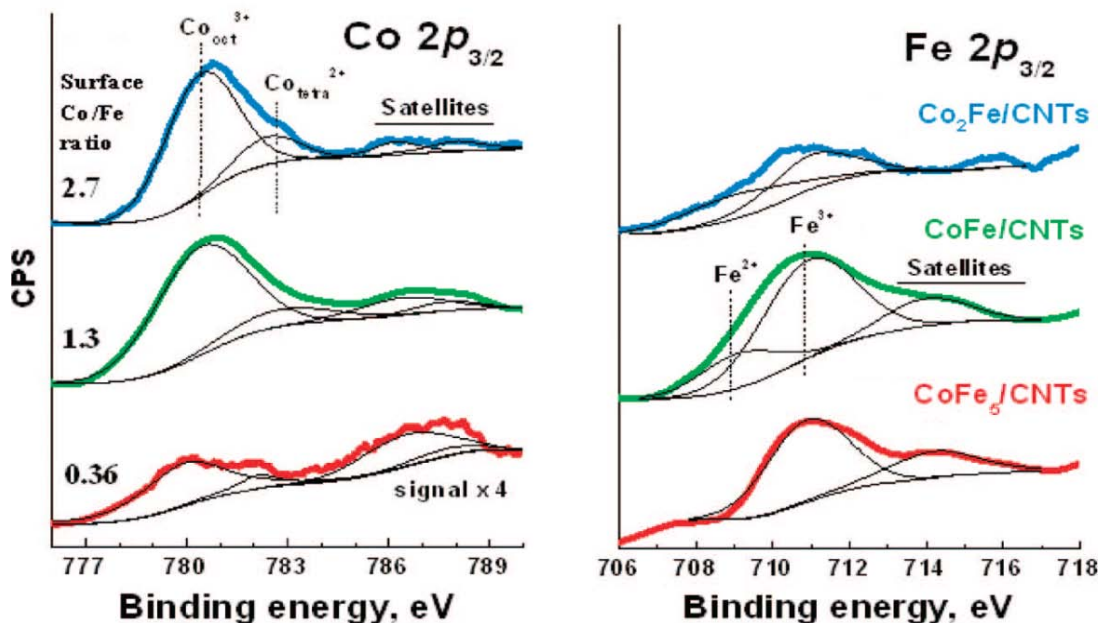


Figure 4-6. Co2p and Fe2p XPS spectra of used catalysts. Samples were exposed to air during the transportation and preparation of pellet for XPS measurements.

The chemical state and relative abundance of Co and/or Fe were determined by X-ray photon spectroscopy analysis. As shown in Fig. 4-6, the signal corresponding to Co can be resolved into two components, that is, Co<sup>3+</sup> ions in an octahedral environment ( $E_{\beta} = 780.0-780.4$  eV) and Co<sup>2+</sup> ions in tetrahedral sites ( $E_{\beta} = 782.3-782.6$  eV). The XPS spectra of Fe 2p<sub>3/2</sub> displayed two components, that is, Fe<sup>3+</sup> (Fe<sub>2</sub>O<sub>3</sub>, 710.6-710.8 eV) and Fe<sup>2+</sup> (FeO, 708.8 eV).<sup>[16, 17]</sup> With increasing Co/Fe ratio, part of the Co shifted from lower oxidation state to higher oxidation state ( $I_{Co^{3+}}/I_{Co^{2+}}$  increased), while Fe signal shifted from higher oxidation state to lower oxidation state ( $I_{Fe^{3+}}/I_{Fe^{2+}}$  decreased). This indicates an electron transfer between Co and Fe and the near-distance interaction between the two metal atoms, indicating the Fe-Co alloy phase might

form on the surface during reaction. The stability of the Fe-Co alloy phase over the surface can be related to their negative segregation energy and positive mixing energy.<sup>[18]</sup> Quantitative analysis of the XPS data showed the accordance in Fe/Co ratios between surface and bulk of each sample, which agreed with the good homogeneity in each individual nanoparticle determined by the microscopic techniques. It should be noted that the derived concentration of surface metals from XPS spectra ranged at  $1.3 \pm 0.5$  wt%, which was less than the bulk concentration, that is, 5wt%. Signals were contributed from particles (1) at the tip of tubes, (2) inside CNTs which were parallel to the beam line, and (3) outside CNTs/CNFs with the amount around 0.2wt% of nanoparticles.

### **4.3 Catalytic decomposition of NH<sub>3</sub> on CNT-supported metal alloy nanoparticles**

Catalytic NH<sub>3</sub> decomposition was conducted according to the experimental procedures in Chapter 2. For each reaction run, the outlet gas mixture only comprised N<sub>2</sub>, H<sub>2</sub> and NH<sub>3</sub>, without CH<sub>4</sub> that might form in the methanation of the carbon support.<sup>[19]</sup> Fig. 4-7-a compared the steady-state H<sub>2</sub> productivity and the activation energies of Fe-Co alloy samples. At 550°C, the conversion over pure Co was 2.7 times that of pure Fe. However, the high activity of Co was kept over Fe-Co alloys with the Co/Fe ratio widely ranging from 0.2 to 2.0. Substituting Co by Fe resulted in an increase in the overall activation energy of NH<sub>3</sub> decomposition from 79 to 105-109 kJ/mol, which is still lower than that over pure Fe, that is, 147 kJ/mol. The highest barrier of Fe can be related with the high coverage of nitrogen over the reconstructed surface due to the very strong binding of nitrogen species on Fe.<sup>[20, 21]</sup> Since the recombinative desorption of surface nitrogen atoms acts as the rate-limiting step,<sup>[21, 22]</sup> one would expect the lowest activity of pure Fe for NH<sub>3</sub> decomposition. Co has one more d band electron than Fe, and thus the electron density of Fe might benefit from the formation of a surface Fe-Co bond. The modified electronic properties of Fe are expected to assist the absorbed nitrogen atoms to desorb from surface, thus leading to a decrease in the activation barrier. As compared with such a pronounced electron donating from Co and Fe in the near distance, the electronic charge from a domain of one alkali metal oxide (e.g. K<sub>2</sub>O) to a Fe particle seems to be far inefficient, which can well explain the absence of the promotion effect of K on a fused Fe catalyst in previous studies.<sup>[23]</sup>

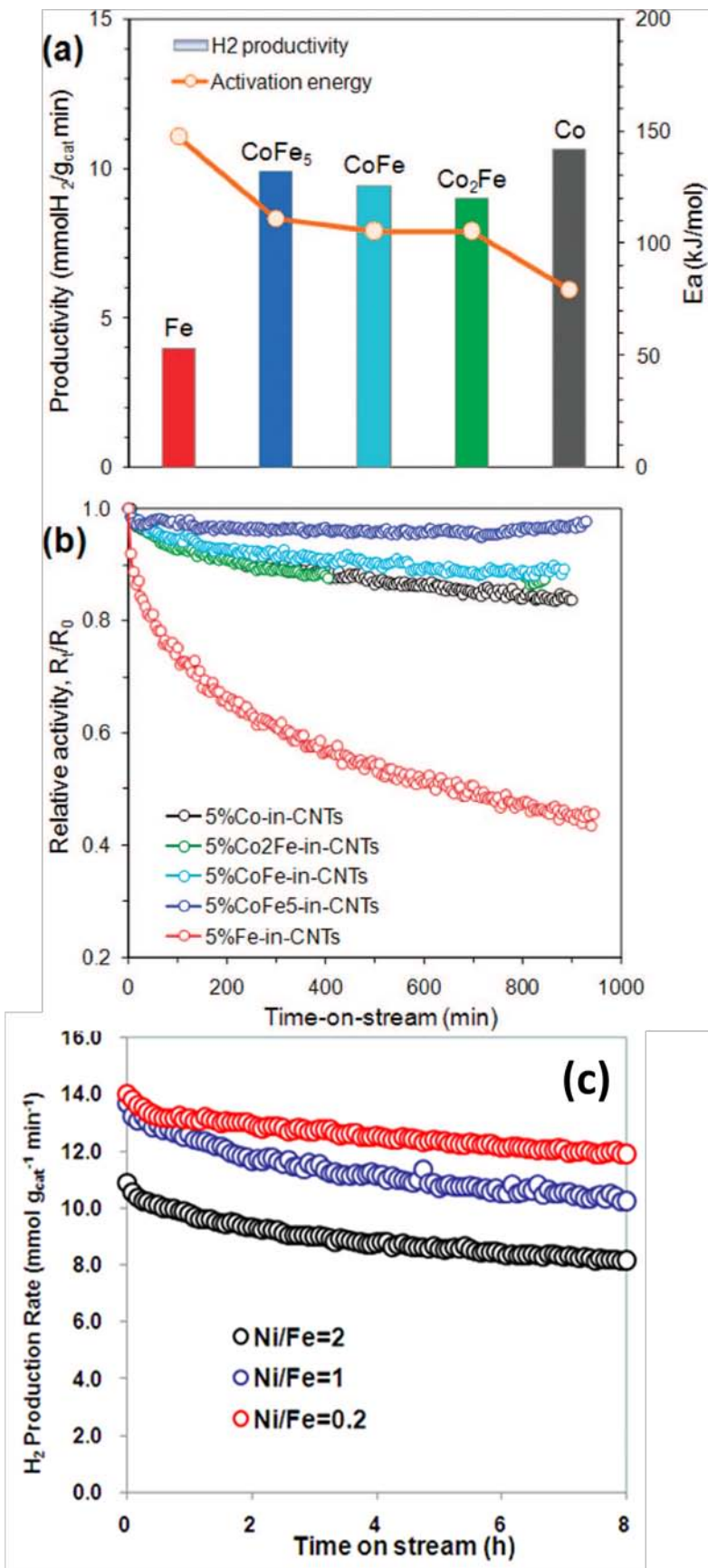


Figure 4-7. Catalytic performance CNT-supported metal alloy catalysts for NH<sub>3</sub> decomposition. (a) Steady-state activities of Fe-Co catalysts at 550°C and activation energy (450-550°C, 36000 mL<sub>NH<sub>3</sub></sub>/(g·h)); (b) normalized catalytic stabilities of Fe-Co catalysts (600°C, 36000 mL<sub>NH<sub>3</sub></sub>/(g·h)); (c) catalytic stabilities of Fe-Ni catalysts (600°C, 36000 mL<sub>NH<sub>3</sub></sub>/(g·h)).

Fig. 4-7-b showed the relative activity of each catalyst with the same weight loading of metal along with reaction time. Significant deactivation was clearly seen over Co and Fe monometallic catalysts. Especially for Fe, only 45% of the initial activity remained after reaction after 1000 min. All tested bimetallic catalysts were much more stable than monometallic ones, and the stability increased with increasing fraction of Fe in alloys. Considering the absence of a bulk metal carbide or nitride phase, one can attribute the loss in activity mainly to the sintering of nanoparticles. It is therefore concluded that the significantly enhanced stability originated from the suppressing agglomeration and coalescence via atomic and/or crystallite migration by alloy formation. The tendencies on activity and stability agreed well with the morphological analysis.

#### 4.4 Selective deposition of metal alloy nanoparticles on CNTs/CNFs

Selective deposition of metal alloy nanoparticles on different locations of CNTs was also investigated in this study. A CoFe<sub>5</sub>-out-CNT sample was synthesized as described in Chapter 2. The location of nanoparticles on CNTs was confirmed by tilting the sample holder in TEM, as shown in Figure 4-8. Morphological analyses of fresh CoFe<sub>5</sub>-out-CNT and CoFe<sub>5</sub>-in-CNT samples did not reveal any observable differences, as evidenced by the similar size distribution in Fig. 4-9. CoFe<sub>5</sub>-out-CNT approached the steady state after 400 min and finally displayed a NH<sub>3</sub> conversion of 24%, which was less than that over CoFe<sub>5</sub>-in-CNT, that is, 48%. Significant sintering of outside particles was observed on CoFe<sub>5</sub>-out-CNT, and the mean size increased from 14.8 to 29.6 nm, resulting in a sharp decrease in the ratio of exposed metal atoms according to its reciprocal proportion to the mean particle size. On the contrary, the mean size in CoFe<sub>5</sub>-in-CNT remained almost unchanged, that is, 13.7-14.7 nm. The calculated metal dispersion of CoFe<sub>5</sub>-in-CNT was 6.8%, which was twice that of CoFe<sub>5</sub>-out-CNT. By normalization of the conversion to metal dispersion it can be concluded that both catalysts displayed nearly the same turnover rate,

that is,  $5.4 \pm 0.1 \text{ mol}_{\text{H}_2}/(\text{site} \cdot \text{s})$ . The activation energy,  $116 \pm 5 \text{ kJ/mol}$ , was also not influenced by the location of alloy particles. Therefore, we can expect that the higher conversion over inside particles may originate from their thermal stability. To confirm this, we compared the sintering behaviors of particles inside and outside of CNTs by heating the samples in a TEM chamber in vacuum. Fig. 4-9-a showed the overview images of nanoparticles outside of CNTs at room temperature. The location of the selected particles was confirmed by tilting the sample from  $-20^\circ$  to  $25^\circ$ . There was no observable change as the temperature was increased to  $550^\circ\text{C}$  (Fig. 4-9-b-d). However, when the temperature approached  $600^\circ\text{C}$ , the outside particles immediately aggregated into bigger entities, which explains the inferior performance of  $\text{CoFe}_5$ -out-CNT from the beginning of the reaction.

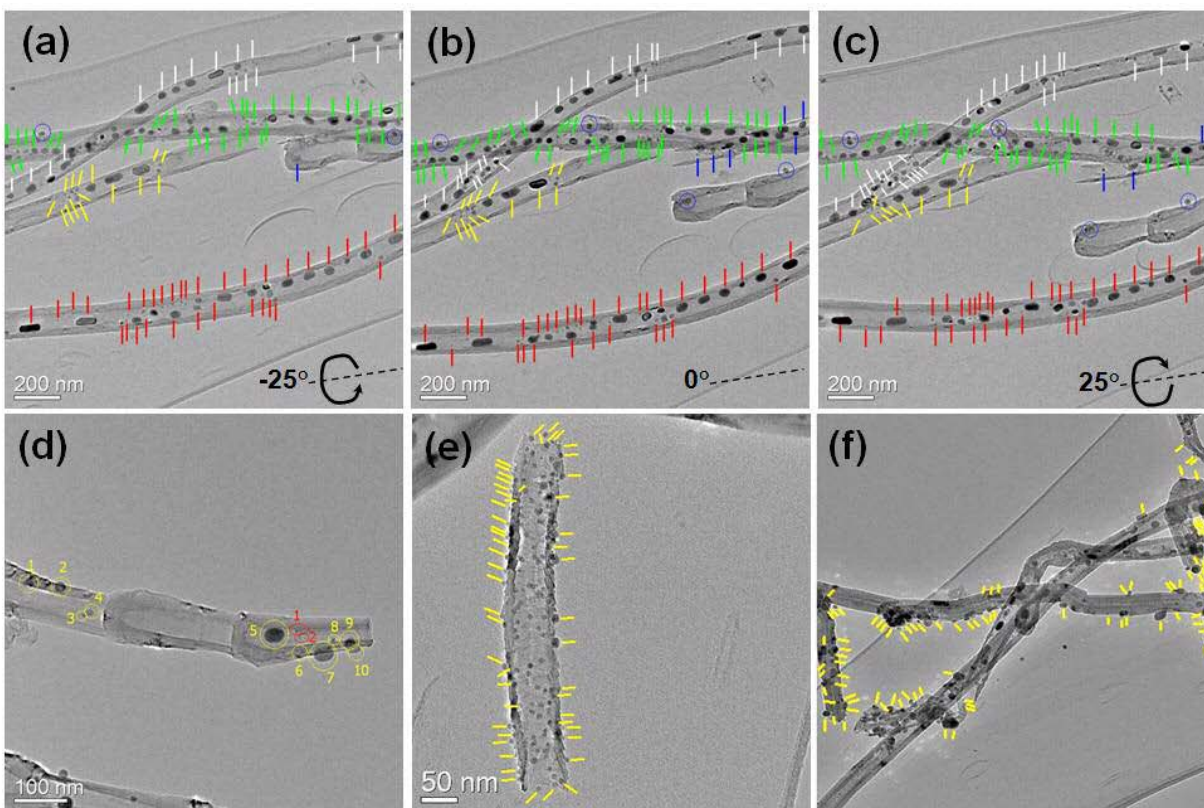


Figure 4-8. TEM images of  $\text{CoFe}_5$ -in-CNT and  $\text{CoFe}_5$ -out-CNT samples. (a-c) tilting the sample holder of  $\text{CoFe}_5$ -in-CNT with the angles of  $\pm 25^\circ$ . Sticks: particles inside; circles: particles outside. (d-f) representative images of the  $\text{CoFe}_5$ -out-CNT sample in tilting experiments. Yellow: particles outside; red: particles inside.

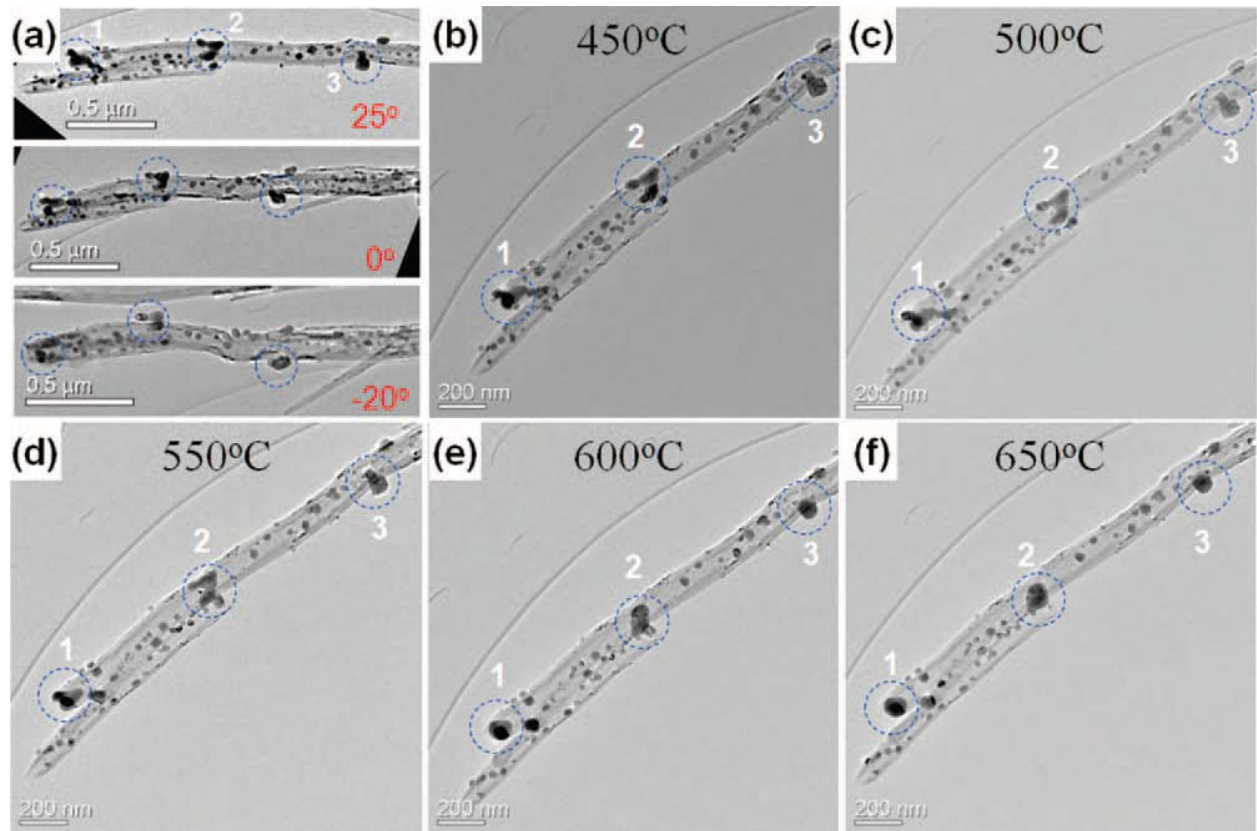


Figure 4-9. Characterization of the thermal stability of CoFe<sub>5</sub>/CNT. (a) TEM images observed by tilting the sample holder from -20° to 25°; (b-f) representative images of the sample observed at different temperatures.

#### 4.5 Chapter conclusions

In summary, this chapter reported the combinative characterization of transition metal alloy nanoparticles located within CNTs. The high-extent alloying of Fe and Co was confirmed by elemental analysis, XRD and XPS measurements. In ammonia decomposition, a high catalytic activity can be achieved by alloying iron with little amount of cobalt or nickel. The resulting nanoparticles benefit from the thermal stability. The effect of CNTs supports was found to be an improvement of the thermal stability of the alloy particles encapsulated inside channel, rather than a change in the turnover rate of the catalytic components.

## References

1. Pham-Huu, C., et al., *Synthesis of CoFe<sub>2</sub>O<sub>4</sub> nanowire in carbon nanotubes. A new use of the confinement effect*. Chemical Communications, 2002(17): p. 1882-1883.
2. Serp, P., M. Corrias, and P. Kalck, *Carbon nanotubes and nanofibers in catalysis*. Applied Catalysis A: General, 2003. **253**(2): p. 337-358.
3. Rodriguez, J., *Physical and chemical properties of bimetallic surfaces*. Surface Science Reports, 1996. **24**(7-8): p. 223-287.
4. Gucci, L., et al., *CO hydrogenation over cobalt and iron catalysts supported over multiwall carbon nanotubes: Effect of preparation*. Journal of Catalysis, 2006. **244**(1): p. 24-32.
5. Corrias, M., et al., *CVD from ethylene on cobalt ferrite catalysts: The effect of the support*. Carbon, 2005. **43**(13): p. 2820-2823.
6. L.C. Pereira, A., et al., *Effect of cobalt on the activity of iron-based catalysts in water gas shift reaction*, in *Studies in Surface Science and Catalysis*, M.S. Fábio Bellot Noronha and S.-A. Eduardo Falabella, Editors. 2007, Elsevier. p. 225-230.
7. Rarogpilecka, W., et al., *Carbon-supported cobalt-iron catalysts for ammonia synthesis*. Applied Catalysis A: General, 2006. **300**(2): p. 181-185.
8. Boisen, A., et al., *Why the optimal ammonia synthesis catalyst is not the optimal ammonia decomposition catalyst*. Journal of Catalysis, 2005. **230**(2): p. 309-312.
9. Jacobsen, C.J.H., et al., *Catalyst Design by Interpolation in the Periodic Table: Bimetallic Ammonia Synthesis Catalysts*. Journal of the American Chemical Society, 2001. **123**(34): p. 8404-8405.
10. Mirzaei, A., et al., *Characterization of iron-cobalt oxide catalysts: Effect of different supports and promoters upon the structure and morphology of precursors and catalysts*. Applied Catalysis A: General, 2006. **301**(2): p. 272-283.
11. Peigney, A., et al., *Specific surface area of carbon nanotubes and bundles of carbon nanotubes*. Carbon, 2001. **39**(4): p. 507-514.
12. Tibbetts, G.G., et al., *A review of the fabrication and properties of vapor-grown carbon nanofiber/polymer composites*. Composites Science and Technology, 2007. **67**(7-8): p. 1709-1718.
13. Oberlin, A., *Carbonization and graphitization*. Carbon, 1984. **22**(6): p. 521-541.
14. Zhang, J., et al., *Individual Fe-Co Alloy Nanoparticles on Carbon Nanotubes: Structural and Catalytic Properties*. Nano Letters, 2008. **8**(9): p. 2738-2743.
15. Zhang, J., et al., *Commercial Fe- or Co-containing Carbon Nanotubes as Catalysts for NH<sub>3</sub> Decomposition*. Chemical Communications, 2007(19): p. 1916.
16. de la Peña O'Shea, V.A., et al., *Surface and Structural Features of Co-Fe Oxide Nanoparticles Deposited on a Silica Substrate*. European Journal of Inorganic Chemistry, 2006. **2006**(24): p. 5057-5068.
17. Zhang, J., H. Wang, and A. Dalai, *Development of stable bimetallic catalysts for carbon dioxide reforming of methane*. Journal of Catalysis, 2007. **249**(2): p. 300-310.
18. H. Larsen, J. and I. Chorkendorff, *From fundamental studies of reactivity on single crystals to the design of catalysts*. Surface Science Reports, 1999. **35**(5-8): p. 163-222.
19. Tomita, A. and Y. Tamai, *Hydrogenation of carbons catalyzed by transition metals*. Journal of Catalysis, 1972. **27**(2): p. 293-300.
20. Mortensen, J.J., et al., *Nitrogen adsorption on Fe(111), (100), and (110) surfaces*. Surface Science, 1999. **422**(1-3): p. 8-16.
21. Schlögl, R., *Ammonia Synthesis*. Handbook of Heterogeneous Catalysis. 2008: Wiley-VCH Verlag GmbH & Co. KGaA.
22. Ertl, G. and J. Rüstig, *Decomposition of NH<sub>3</sub> on Nickel: Absence of a Magneto-Catalytic Effect*. Surface Science, 1982. **119**(1): p. L314-L318.

23. Jedynak, A., et al., *Ammonia decomposition over the carbon-based iron catalyst promoted with potassium*. Applied Catalysis A: General, 2002. **237**(1-2): p. 223-226.



## Chapter 5:

# Molybdenum Carbides and Nitrides

Carbides and nitrides of early transition metals have been the focus of much attention following the pioneering work of Levy and Boudart,<sup>[1]</sup> who showed that tungsten carbides display Pt-like behavior in several catalytic reactions. It has been subsequently demonstrated that transition metal carbides and nitrides that typically utilized group VIII noble metals as catalysts, including hydrogenation,<sup>[2]</sup> dehydrogenation,<sup>[3]</sup> hydrogenolysis,<sup>[4]</sup> isomerization<sup>[1, 5, 6]</sup> and methane to syngas,<sup>[7]</sup> in which the catalytic activities approached or surpassed those of noble metals.

As described in previous chapters, the metal nitrogen interactions play important role in both synthesis and decomposition of ammonia, since the adsorption and desorption of nitrogen are reaction determining steps of ammonia synthesis and decomposition respectively.<sup>[8, 9]</sup> Considering that the catalytic efficiency of the elements for synthesis and decomposition of ammonia has been correlated with the chemisorption energy of nitrogen, transition metal carbides and nitrides have been applied in both the catalytic synthesis and decomposition of NH<sub>3</sub>.<sup>[10]</sup> Oyama showed a number of interstitial alloys (molybdenum carbide and nitride), that were more active than ruthenium but less active than the doubly-promoted iron catalyst for ammonia synthesis.<sup>[11]</sup> He also reported similar rate parameters for vanadium nitride to those of iron and platinum in ammonia decomposition.<sup>[12]</sup> Choi investigated vanadium carbide<sup>[13]</sup> and molybdenum carbide,<sup>[14]</sup> and Pansare et al. studied tungsten carbide<sup>[15]</sup> for ammonia decomposition. Those materials reported in the literature showed interesting performance for ammonia decomposition, unfortunately, none of the catalysts could achieve more than 3 mmol/(g<sub>cat</sub>·min) H<sub>2</sub> formation rate, which is likely due to the low surface area of the reported materials.

In this study, both bulk and nanostructured molybdenum carbide/nitride materials will be investigated as catalysts for ammonia decomposition.

## 5.1 Bulk system of Mo carbides and nitrides

One of the most facile routes to high surface area transition metal carbides can be attributed to Lee et al.<sup>[16]</sup> who developed a temperature-programmed reduction method which allows the formation of carbide materials from precursor oxides under a wide range of conditions. In this study, we prepared high surface area molybdenum carbide (labeled as Mo<sub>2</sub>C, #7484 in AC database) from *h*-MoO<sub>3</sub> metal oxide precursor using a temperature-programmed reduction-carburisation under a flowing atmosphere of H<sub>2</sub> and CH<sub>4</sub>.<sup>[17]</sup> This was applied in the catalytic decomposition of ammonia and exhibited high performance in H<sub>2</sub> production.

### 5.1.1 Catalytic performance of high surface area Mo carbide

Catalytic ammonia decomposition was conducted according to the procedure detailed in experimental section. The performance of high surface area molybdenum carbide (Mo<sub>2</sub>C) over 100h on stream at 600 °C is shown in Fig. 5-1. Here the NH<sub>3</sub> conversion of Mo<sub>2</sub>C decreases from 85% to 71% over 15 hours, and subsequently stabilizes at a constant H<sub>2</sub> formation rate about 30 mmol/(g<sub>cat</sub>·min). The catalytic activity of 2wt%Ru/graphite is also shown in Fig. 5-1 for comparison, showing an H<sub>2</sub> formation rate of about 37 mmol/(g<sub>cat</sub>·min) under the same conditions. The apparent activation energy over Mo<sub>2</sub>C sample is about 89 kJ/mol, which is close to 2wt%Ru supported on different carbon materials (75-85 kJ/mol). These findings imply that the high surface area transition metal carbides have potential to replace noble metal in the application for CO<sub>x</sub>-free H<sub>2</sub> production from ammonia.

In the following sections, we will focus on the characterization information of the fresh, 4-hour used (labeled as Mo<sub>2</sub>C-NH<sub>3</sub>-4h, #7825 in AC database), and 100-hour used (labeled as Mo<sub>2</sub>C-NH<sub>3</sub>-100h, #7824 in AC database) samples.

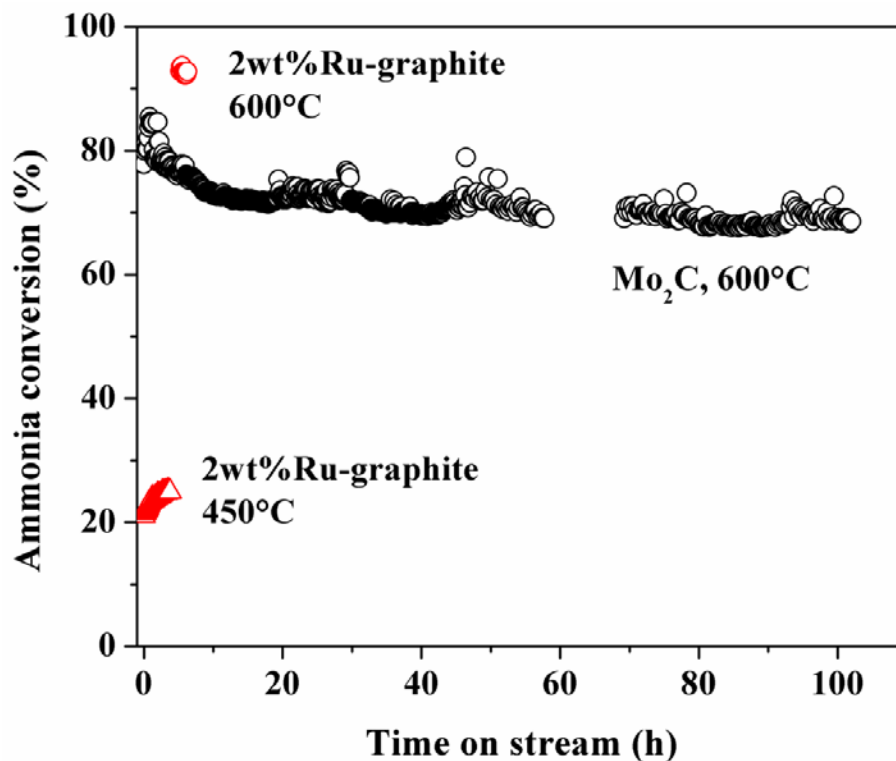


Figure 5-1. Catalytic activity and stability of Mo carbide for NH<sub>3</sub> decomposition. Reaction condition: 50 mg sample, NH<sub>3</sub> space velocity is 36,000 ml/(g<sub>cat</sub>·min), reaction temperature 600°C. Triangle: catalytic performance of 2wt% Ru/graphite with same condition at 600°C and 450°C respectively.

### 5.1.2 Textural properties of fresh and used Mo carbides

Table 5-1. Physical properties of samples			
Sample	BET surface area <sup>a</sup> (m <sup>2</sup> /g)	Pore Volume <sup>b</sup> (cm <sup>3</sup> /g)	Phase structure <sup>c</sup>
Mo <sub>2</sub> C	47.72	8.923 E-2	Hexagonal Mo <sub>2</sub> C
Mo <sub>2</sub> C-NH <sub>3</sub> -4h	6.00	4.634 E-2	Hexagonal Mo <sub>2</sub> C and MoN
Mo <sub>2</sub> C-NH <sub>3</sub> -100h	4.83	2.604 E-2	Hexagonal MoN

a calculated from N<sub>2</sub> adsorption and desorption analysis  
b total pore Volume  
c determined from XRD and TEM analysis

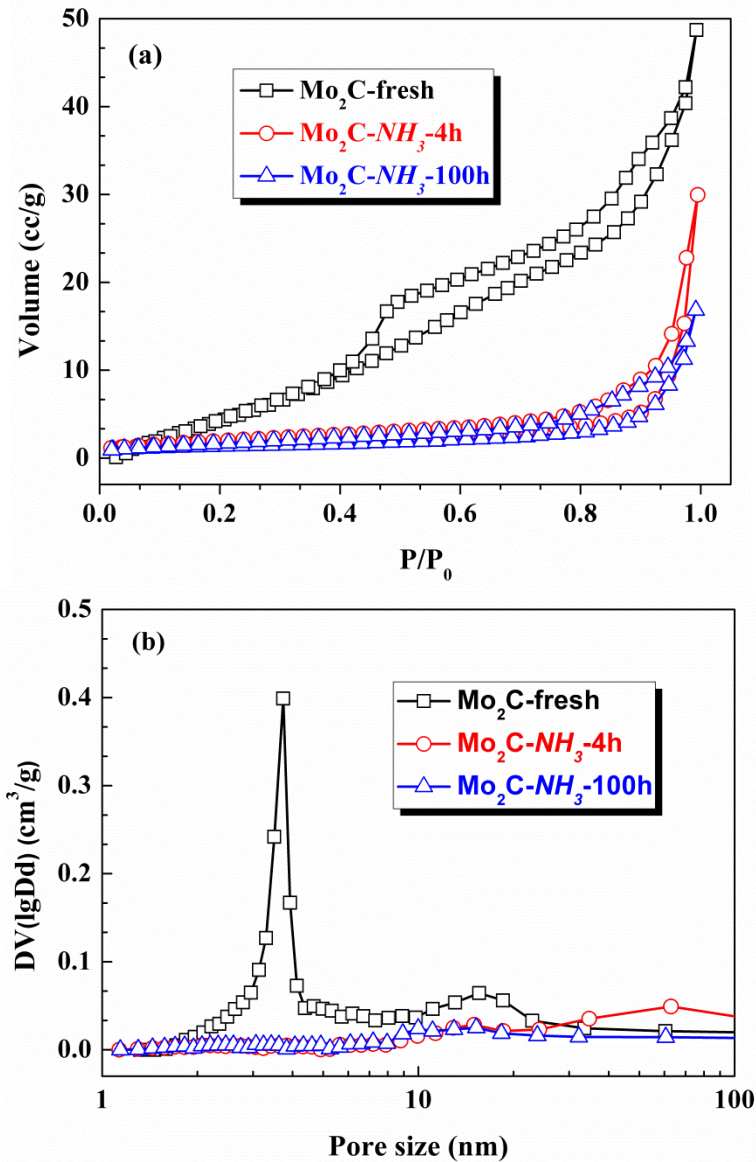


Figure 5-2. N<sub>2</sub>-adsorption/desorption analysis. (a) isotherms; (b) pore size distribution form BJH desorption.

The results of the physicostructural characterizations of the fresh and used catalysts are summarized in Table 5-1. Figure 5-2 shows the N<sub>2</sub>-physisorption isotherms<sup>[18]</sup> and BJH pore size distributions<sup>[19]</sup> for the desorption branch of all samples. The isotherm of fresh molybdenum carbide sample is intermediate between type II and type IV with an H-3 hysteresis loop indicating slit-like mesopore structure. As shown in Fig. 5-2-b, two different pore-size distributions (2-4 nm and 10-11 nm) were observed on the fresh Mo<sub>2</sub>C sample. Following ammonia decomposition for 4 hours at 600 °C, the mesopores between 2-4 nm were not

observed, and the isotherm changed to a typical type II shape indicating the disappearance of mesopore structure. This resulted in a considerable drop of surface area from 50 to 6 m<sup>2</sup>/g. The surface area and mesopore structures further decreased with time-on-stream (TOS). After 100 hours of reaction, there was about 90% loss of surface area. However, the loss of catalytic activity was only about 15%. Therefore, in order to find an agreement between the solid materials and catalytic performance, further characterization of the fresh Mo<sub>2</sub>C, Mo<sub>2</sub>C-NH<sub>3</sub>-4h and Mo<sub>2</sub>C-NH<sub>3</sub>-100h samples were carried out.

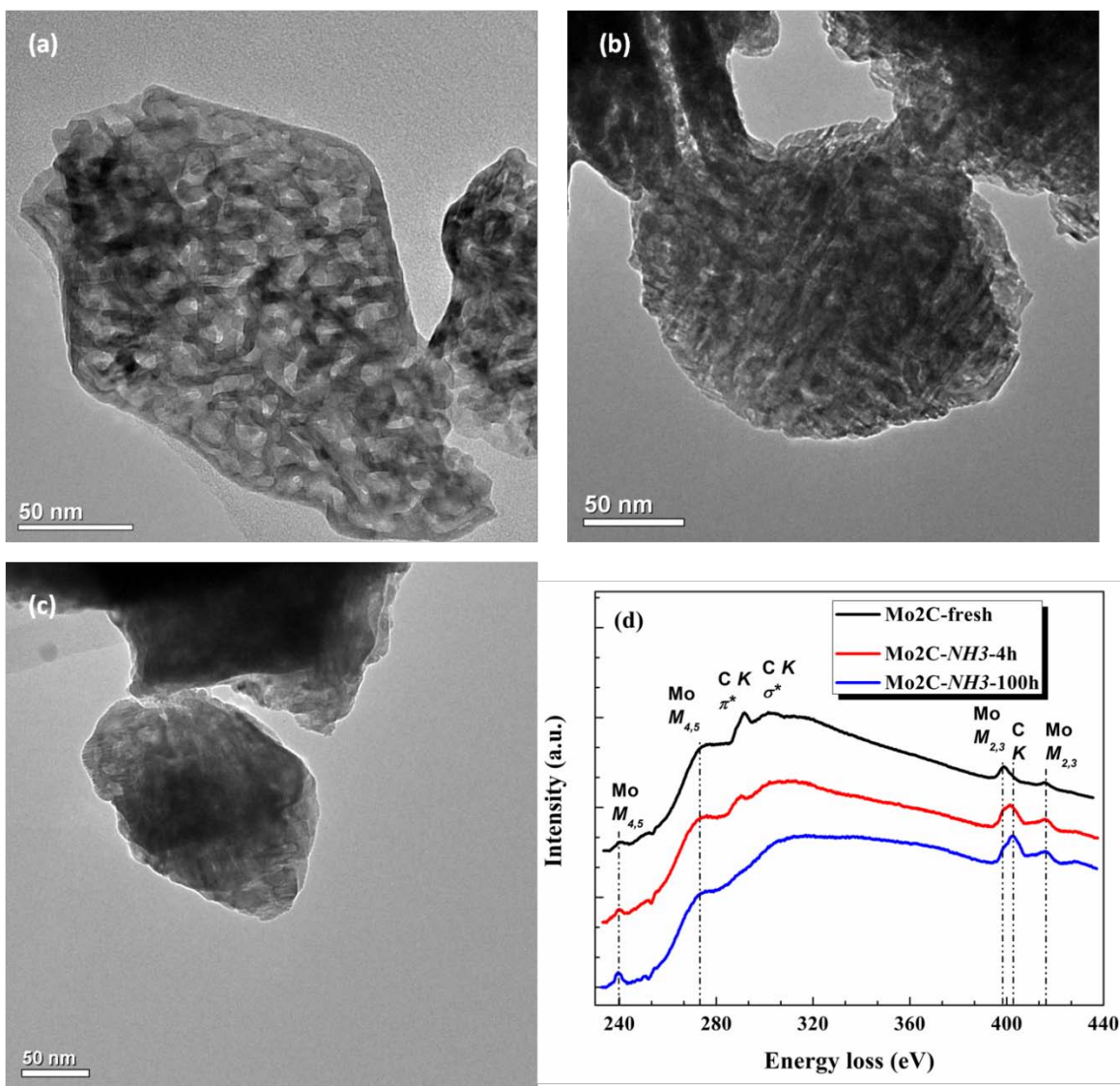


Figure 5-3. TEM images and EELS spectra of fresh and 4-h and 100-h used Mo carbide/nitride samples. (a) Mo<sub>2</sub>C-fresh; (b) Mo<sub>2</sub>C-NH<sub>3</sub>-4h; (c) Mo<sub>2</sub>C-NH<sub>3</sub>-100h; (d) Mo M-edge, C and N K-edge EELS spectra of the samples.

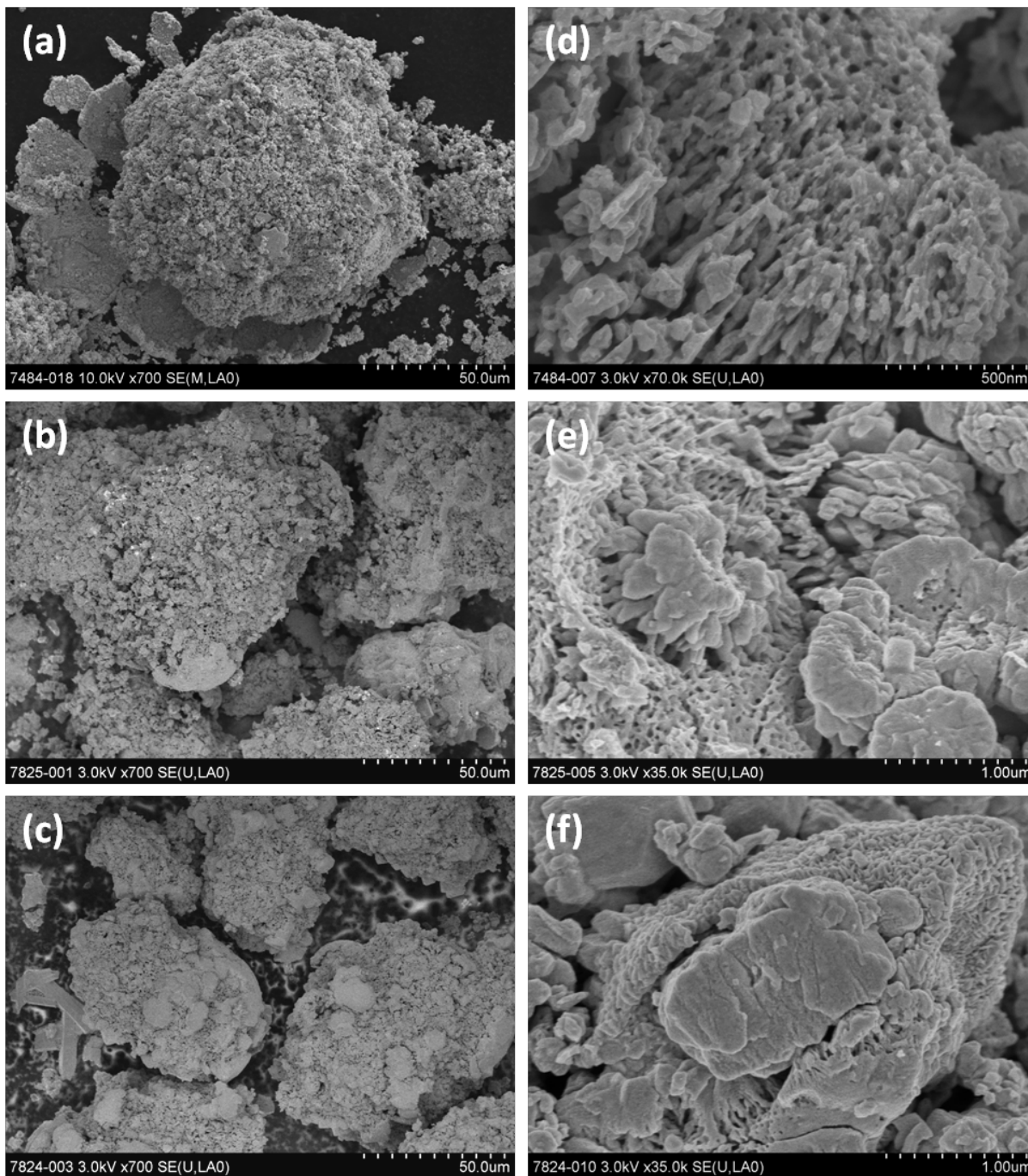


Figure 5-4. SEM images of Mo carbide samples. (a) and (d)  $\text{Mo}_2\text{C}$ -fresh; (b) and (e)  $\text{Mo}_2\text{C-NH}_3$ -4h; (c) and (f)  $\text{Mo}_2\text{C-NH}_3$ -100h.

The morphologies of all the samples were investigated by transmission/scanning electron microscopy (SEM/TEM). Figure 5-3 shows the representative TEM images of the three samples.

As shown in Fig. 5-3-a, the fresh Mo<sub>2</sub>C sample has a homogeneous mesopore structure giving the uniform distribution of the bright regions in the TEM image. After reaction for 4 hours, the catalyst appears to lose the porosity (TEM image of Fig. 5-3-b). Further, very few mesopores can be observed in the sample of Mo<sub>2</sub>C-NH<sub>3</sub>-100h (in Fig. 5-3-c), which has increased in apparent density by comparison with the fresh sample. These observations are in good agreement with the results obtained from N<sub>2</sub>-physisorption. The representative SEM images with different magnifications of all samples shown in Fig. 5-4. also agree with the findings that after reaction of ammonia decomposition, the catalyst became more compact solid structure with lower specific surface area.

### ***5.1.3 Phase identifications of fresh and used Mo carbides***

Before correlated the textural properties of fresh and used molybdenum carbide with the catalytic performances it must be noted that the majority of published literature with these materials deals with the synthesis and characterization of molybdenum carbides and nitrides, which regards to the various phases of them. For molybdenum carbide, they are  $\alpha$ -Mo<sub>2</sub>C (orthorhombic),  $\beta$ -Mo<sub>2</sub>C (hexagonal),  $\eta$ -MoC<sub>1-x</sub> (hexagonal),  $\delta$ -MoC<sub>1-x</sub> (cubic),  $\gamma$ -MoC (hexagonal) and  $\gamma'$ -MoC<sub>1-x</sub> (hexagonal);<sup>[20]</sup> for molybdenum nitride, they are  $\beta$ -Mo<sub>2</sub>N (tetragonal),  $\gamma$ -Mo<sub>2</sub>N (cubic),  $\delta$ -MoN (hexagonal), and  $\zeta$ -MoN (cubic).<sup>[21]</sup> In this study, both powder XRD and high resolution TEM techniques were used to identify the phase of the fresh and used materials. Figure 5-5 shows the XRD patterns of the fresh and used samples. The XRD pattern of fresh Mo<sub>2</sub>C sample indicates a hexagonal closed packed structure ( $\beta$ -Mo<sub>2</sub>C), which was compared the reference pattern of JCPD-00-035-0787 Mo<sub>2</sub>C (34.4° (100), 38.0°(002), 39.4°(101), 61.5° (103) and 74.6° (112)). The XRD pattern of used molybdenum carbide collected after 100 hours indicated a hexagonal MoN structure by comparing with JCPD-01-089-5024 MoN (31.8° (002), 36.1° (200), 48.8° (202), 64.9° (220), 78.0° (204) and 85.3° (402)). Both  $\beta$ -Mo<sub>2</sub>C and  $\delta$ -MoN diffraction peaks can be observed in pattern of Mo<sub>2</sub>C-NH<sub>3</sub>-4h, which indicates nitridation of Mo<sub>2</sub>C during the ammonia decomposition reaction. The XRD pattern of Mo<sub>2</sub>C-NH<sub>3</sub>-4h exhibited broader and lower intensity compared to Mo<sub>2</sub>C-fresh and Mo<sub>2</sub>C-NH<sub>3</sub>-100h, indicates smaller volume crystallites and that the nitridation of the carbide involves the formation of dislocation structures in the primary carbide crystallites.

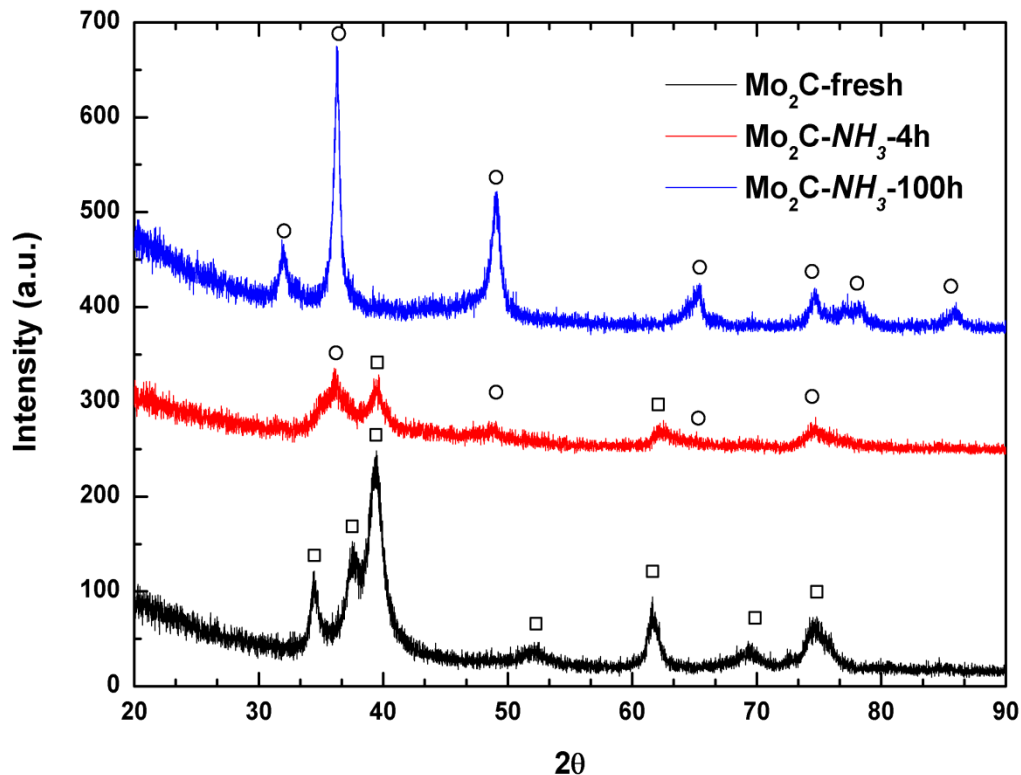


Figure 5-5. XRD patterns of fresh, 4h- and 100h- used Mo carbide samples. square: JCPD-00-035-0787  $\text{Mo}_2\text{C}$ ; circle: JCPD-01-089-5024  $\text{MoN}$ . All used samples were collected after ammonia decomposition reaction and sealed under the protection of inert gas (it could not be prevented against exposing to air when prepared the samples for characterizations).

Figure 5-6 shows the high resolution TEM images of the fresh and used catalysts revealing the polycrystalline structures of all samples. Lattice fringe analysis confirmed that, there is only one phase in either fresh or 100h used sample, that is  $\beta\text{-Mo}_2\text{C}$  (in fresh  $\text{Mo}_2\text{C}$  sample) and  $\delta\text{-MoN}$  (in  $\text{Mo}_2\text{C-NH}_3\text{-100h}$  sample) respectively; both of these two structures can be observed co-existing in  $\text{Mo}_2\text{C-NH}_3\text{-4h}$  sample (Fig. 5-6-b). In addition, a large number of twin-boundaries, stacking faults, steps, and defects could be observed among the high-resolution images of all the observing samples, which can be recognized as highly energetic sites in these samples.<sup>[22]</sup>

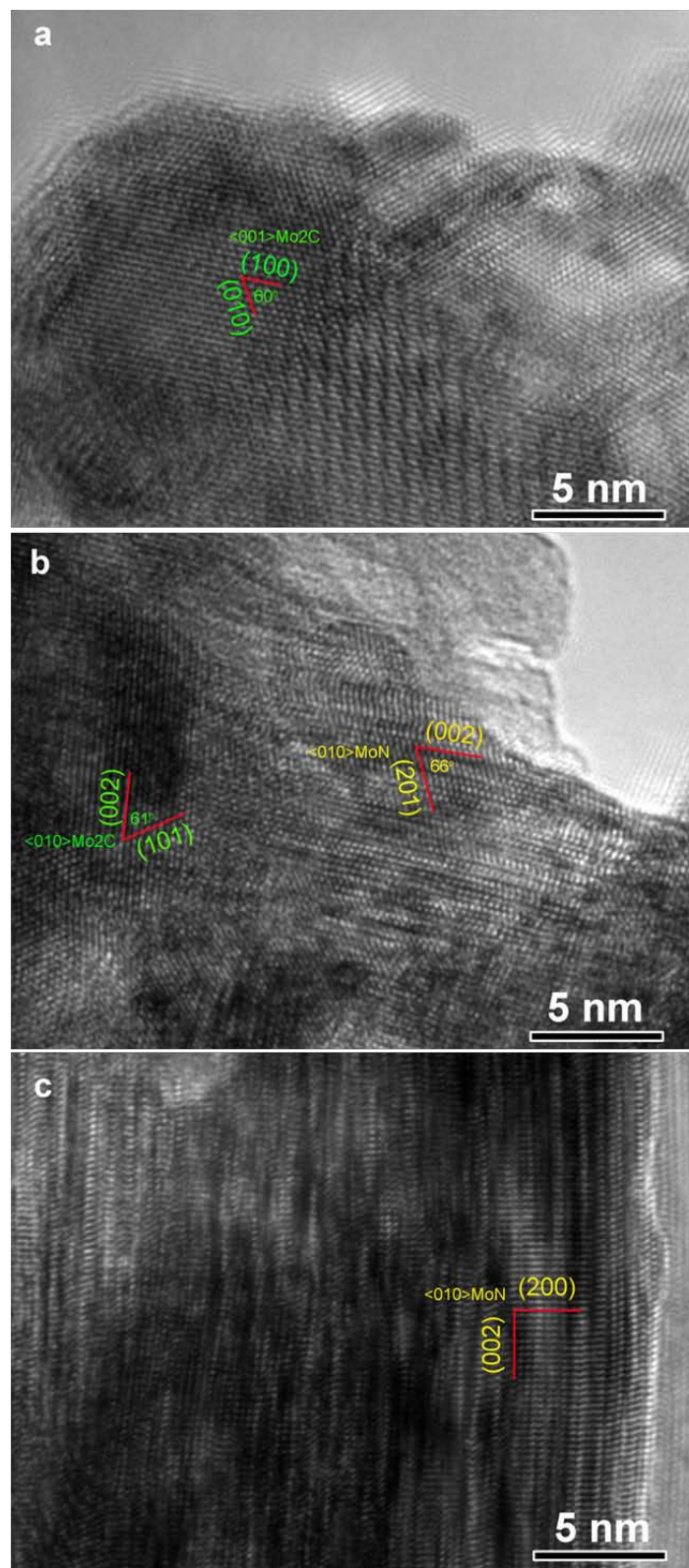


Figure 5-6. High resolution images of fresh and used molybdenum carbide samples indexing with different lattice orientations. (a)  $\text{Mo}_2\text{C}$ -fresh; (b)  $\text{Mo}_2\text{C-NH}_3$ -4h; (c)  $\text{Mo}_2\text{C-NH}_3$ -100h.

In a catalytic cycle which involves several elementary steps, the step which is not in thermodynamic equilibrium, is the rate-determining step. In ammonia synthesis this step is the adsorption of nitrogen.<sup>[23]</sup> In the reverse reaction, ammonia decomposition, this step is the recombinative desorption of di-nitrogen atoms from the surface. It was reported [9], that in ammonia synthesis the active site might occur on a single step edge, as the required hydrogen populates on metal particles all sites in highly mobile form. The active site for the reverse reaction, ammonia decomposition, is a larger ensemble than that for synthesis. As a bulk solid system, the carbide and nitride in this study are not as same as the supported nanoparticles of metals, which have much more specific surface area, by which to provide surface sites exposed to the reactants. Nor is the model catalyst or single crystal for surface science, which could only offer one or several coordination structures. We believe that the observed high energy sites related to dislocation defects and crystal twinning which are observed in these carbide and nitride samples could be the active sites for ammonia decomposition in this case. This may explain why the significant drop of the specific surface area did not cause a dramatic decrease in catalytic performance. Unfortunately, the density of these high energy sites could not be measured from the electron microscopy technique.

#### ***5.1.4 Electronic properties of fresh and used Mo carbide and nitride samples***

The electronic property of catalyst is the one of the most important factors in heterogeneous catalytic reaction.<sup>[22]</sup> Electron energy-loss spectroscopy (EELS) is the favored technique for the chemical analysis of transition metal carbides and nitrides.<sup>[24]</sup> Unfortunately, however the Mo  $M_{4,5}$ -edge (at ca. 227 eV) and  $M_{2,3}$ -edge (doublet peaks at ca. 410 eV and 392 eV respectively) overlap with the C K-edge (at ca. 284 eV) and N K-edge (at ca. 401 eV), causing difficulty in the standard procedure for EELS analysis.<sup>[25]</sup> Figure 5-3-d summarized the EELS spectra of all samples. In the spectra of  $Mo_2C$ -fresh, the Mo M-edge is broad and has small feature at ca. 227, 393 and 410 eV respectively. A large peak was observed for the C K-edge which is indicative of the presence of  $sp^2$ -bonded carbon.

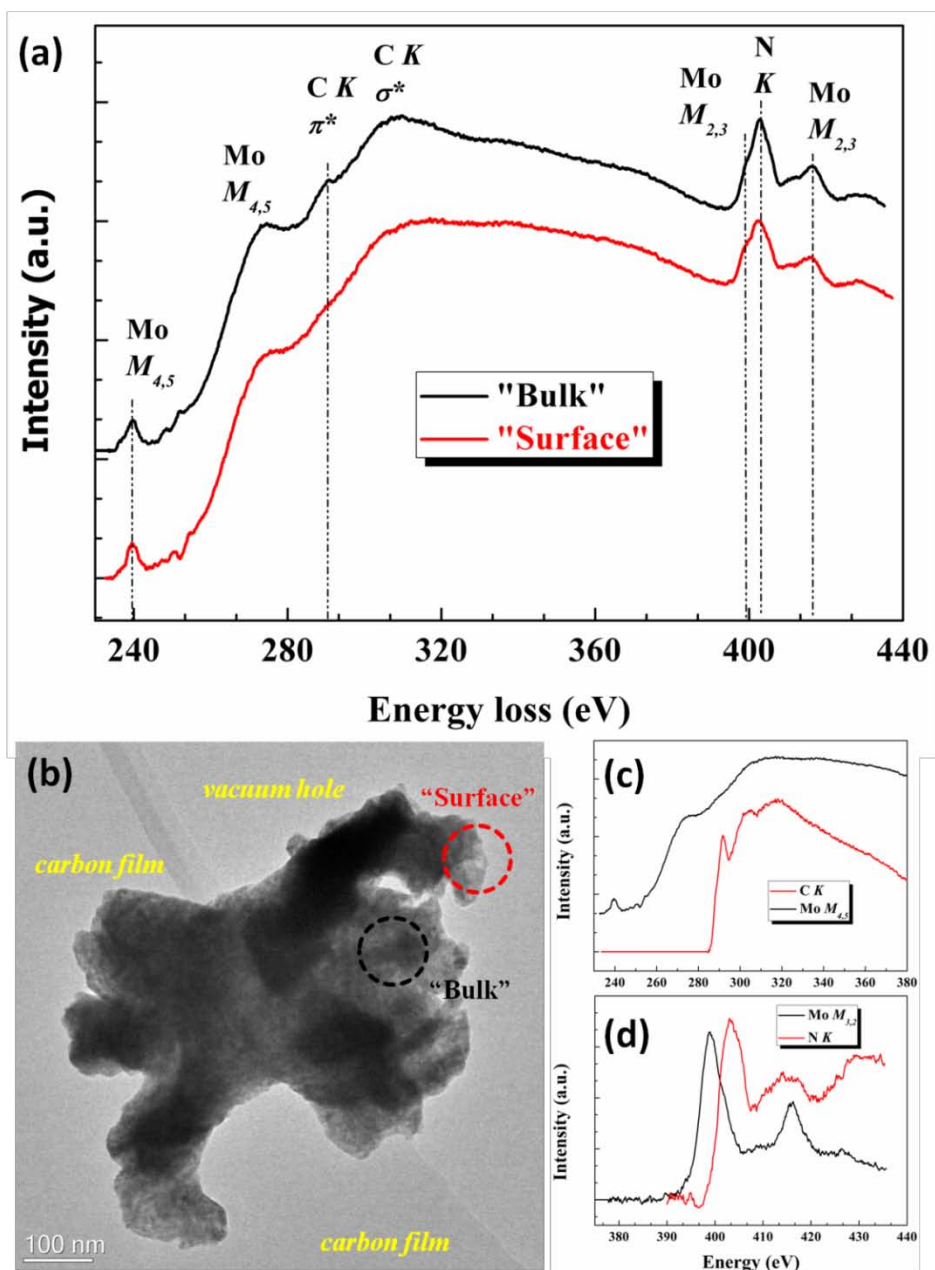


Figure 5-7. EELS spectra of Mo<sub>2</sub>C-NH<sub>3</sub>-4h sample with two different selective areas (a); (b) TEM image of Mo<sub>2</sub>C-NH<sub>3</sub>-4h sample labeled with two probe areas for EELS measurements; (c) and (d) reference spectra of carbon K-edge and molybdenum M<sub>4,5</sub>-edge, nitrogen K-edge and molybdenum M<sub>3,2</sub>-edge respectively.

After 4 hours reaction, the intensity of carbon peak decreases while the formation of N K-edge at ca. 401 eV is observed, consistent with the formation of molybdenum nitride. After 100 hours, nearly no carbon edge is observed indicating the complete nitridation of molybdenum carbide. In

ammonia synthesis, the dissociative adsorption of nitrogen on metallic surfaces leads to a state of adsorbed nitrogen atoms sometimes referred to as “nitride”, the dissolved nitrogen can not only recombine and desorb but also be dissolved in subsurface and form a solid solution.<sup>[9]</sup> In ammonia decomposition, after cleavage of N-H bond, the adsorbed N atoms may also undergo the same phenomena as seen in ammonia synthesis to form the “surface” and “subsurface” nitride and further form the bulk nitride. At the same time, the adsorbed H atoms can not only recombine and desorb but also react with carbon atoms in solid solution to form C-H bonds and eventually desorb from the surface as CH<sub>4</sub>. In Fig. 5-7-a, the EELS spectra of Mo<sub>2</sub>C-NH<sub>3</sub>-4h sample is shown, which has both Mo<sub>2</sub>C and MoN structures confirmed by XRD and TEM analysis. Two representative areas were selected to measure the EELS spectra. One is on the outer region of the selected particle, which more or less could be regarded as the “surface” of the sample; the other is in the centre of the selected particle, which is close to “bulk” region. The intensity of carbon features of the “bulk” area is much more pronounced than the “surface” part, which contains nearly no C signal. These results indicated the nitridation of Mo<sub>2</sub>C during ammonia decomposition starting from the surface to the bulk, which is in good agreement with previous characterizations and also with the literature.<sup>[9]</sup>

### ***5.1.5 Density functional theory calculations***

We first determined the heats of formation of different Mo-C-N bulk compounds. Besides the experimentally known hexa-Mo<sub>2</sub>C [space group: P6<sub>3</sub>/mmc (194)]<sup>[26]</sup> and δ<sub>1</sub>-MoN (space group: P-6m2 (187))<sup>[27]</sup> structures we constructed Mo<sub>2</sub>C<sub>2</sub>, Mo<sub>2</sub>CN, and Mo<sub>2</sub>N<sub>2</sub> by adding C and N atoms to interstitial sites of hexa-Mo<sub>2</sub>C. As can be seen in Figure 5-8, both molybdenum carbide/nitride and molybdenum nitride are more stable than Molybdenum carbide structures by roughly 0.2 eV per unitcell, showing that there is a driving force for molybdenum carbide to convert into a nitride in a nitrogen atmosphere. Although we find that a mixed Mo<sub>2</sub>CN crystal phase should even be more stable than Mo<sub>2</sub>N<sub>2</sub> and MoN, its formation might be kinetically hindered since it would involve a substantial atomic rearrangement within the crystal.

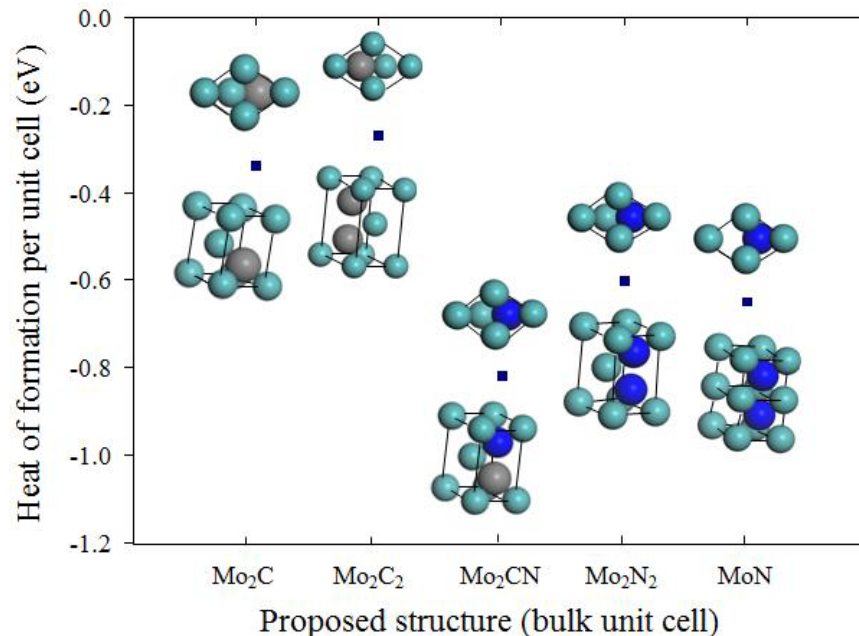


Figure 5-8. Calculated heat formation of different unit cells of proposed molybdenum carbide and nitride structures. (DFT Calculations were done by Dr. P. Kaghadzchi and Dr. T. Jacob, Universität Ulm)

As discussed former section, both the rate-limiting steps for the synthesis ( $N_2$  dissociation) and decomposition (recombinative desorption of N atoms) of ammonia are related to the interaction between N and active surface sites of the catalyst. Also, it was reported that, the computed TOFs of ammonia synthesis could be perfectly correlated with the computed relative heats of chemisorptions of activated nitrogen by the link between the kinetic parameters of a reaction with the thermodynamic parameters of bond strengths of adsorbates.<sup>[9, 28, 29]</sup> Therefore, we concentrated on the bond strength between N and the catalyst surface, which should play the dominant role in both the synthesis and decomposition of ammonia. We conducted a series of calculations for nitrogen adsorption on stepped hexa-Mo<sub>2</sub>C (0001) and  $\delta_1$ -MoN (0001), which are comparable to the catalysts' structures proposed by the experimental findings. Both surfaces were modelled as stepped surfaces with six atom-wide terraces of (0001) orientation, separated by double-atomic steps in case of Mo<sub>2</sub>C (0001) and mono-atomic steps in case of  $\delta_1$ -MoN(0001). Non-equivalent bridge (b-) and hollow (h-) sites near the step edge (yellow circles in Fig. 5-9) or on the terrace (red circles in Fig. 5-9) are considered. The surface layers was relaxed and converged to obtain the total energy.

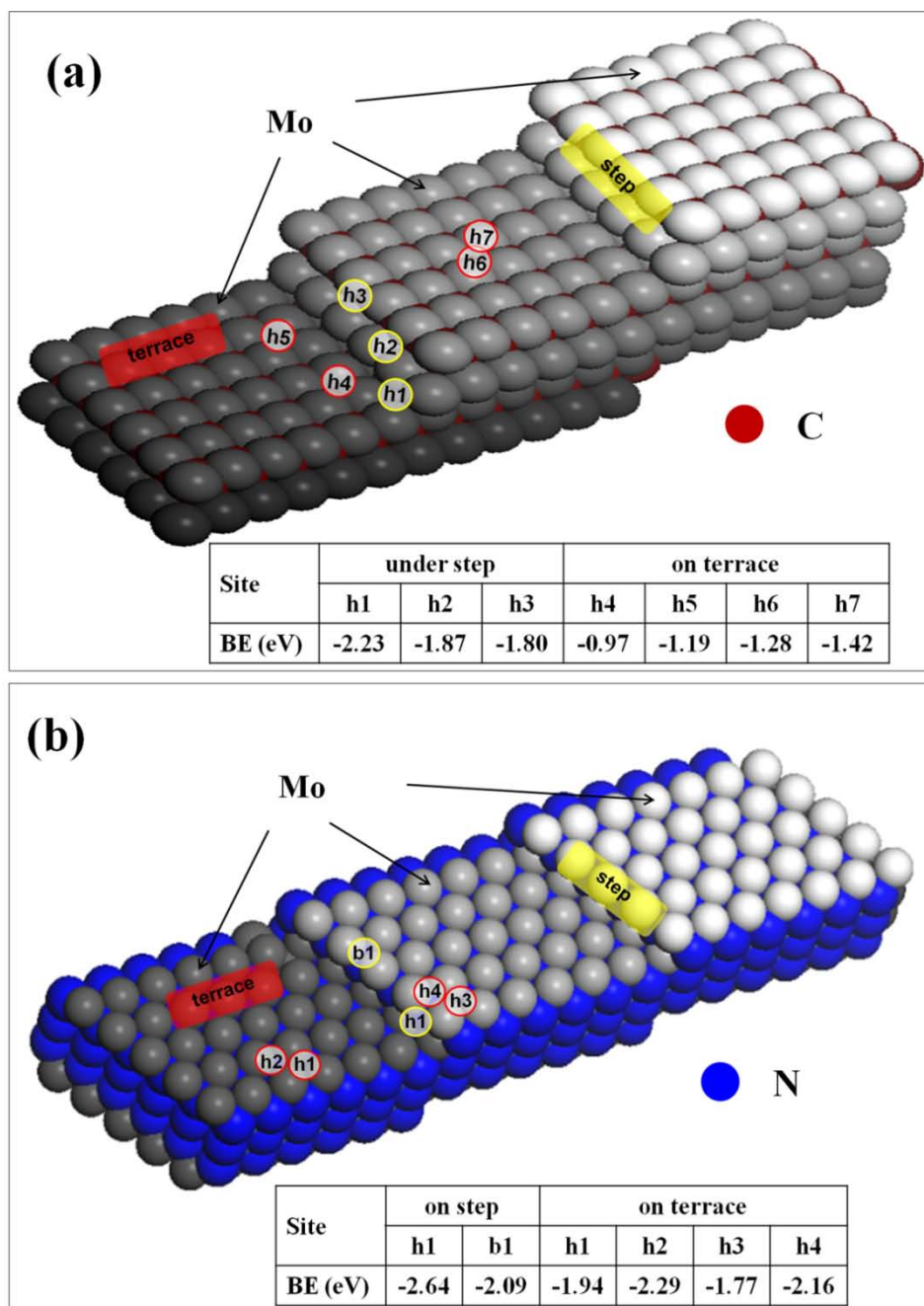


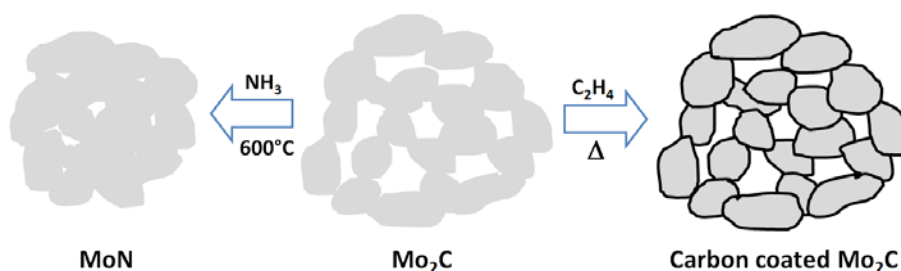
Figure 5-9. Calculated nitrogen adsorption energies (binding energy (eV) referenced to  $\frac{1}{2}$   $N_2$  molecule) at hollow/bridge sites on the proposed step and terrace surface of  $Mo_2C$  (0001) and  $MoN$  (0001). (DFT Calculations were done by Dr. P. Kaghazchi and Dr. T. Jacob, Universität Ulm)

The binding energies were calculated by subtracting the total energy of the clean surface and half of the  $N_2$  in gas phase from the total energy of the surface with nitrogen and compared in Fig. 5-

9. On both stepped surfaces, N prefers binding at the step edges, where the calculated binding energies are 0.81 and 0.35eV larger on Mo<sub>2</sub>C (0001) and  $\delta$ -MoN (0001) as compared to terrace sites. This can be understood by the fact that nitrogen atoms have three unpaired electrons and prefer high coordination sites. Following the previous discussion on the role of the binding energies, the higher heats of chemisorption of N at steps may thus indicate an increased activity for ammonia decomposition. Moreover, the binding energy at the step edge of MoN(0001) is ~0.4 eV higher (more strongly bound) than at the edge of Mo<sub>2</sub>C (0001), indicating an even higher activity on Molybdenum nitride surfaces. While the previous studies already show the general activity trend, it will be the aim of future work to elucidate the full reaction mechanism on the different surfaces to allow for quantitative conclusions of their activities.

### 5.1.6 Carbon coating on high surface area molybdenum carbide

In last section, we showed that the observed deactivation of the high surface area Mo<sub>2</sub>C was related to the considerable drop of the specific surface area with the ammonia decomposition reaction. The inner mesopores were destroyed due to the nitridation of Mo<sub>2</sub>C with adsorbed ammonia. In this section, we will attempt to stabilize the mesopores structure of high surface area Mo<sub>2</sub>C catalyst against collapse by a mechanical force from coating molecular layers on the surface of Mo<sub>2</sub>C catalyst.



Scheme 5-1. Catalysts design to keep molybdenum stable for ammonia decomposition.

Molybdenum carbide was believed have the similar chemio-physio properties as noble metals.<sup>[1]</sup> In literature, the reactions of alkane substrates over molybdenum carbides have been studied for methane activation,<sup>[7, 30]</sup> dehydrogenation of propane<sup>[31]</sup>/ butane<sup>[4]</sup> and isomerisation of

pentane/hexane/heptanes. Among these reactions related with hydrocarbon reactants, the coke of carbon on the surface of catalyst is one of the important deactivation factors influences the stability of carbide and the further applications. On the other hand, as an inert reactant to the reaction of ammonia decomposition, graphitic carbon could be a perfect sketch for molybdenum carbide to stabilize the mesopores structure. It has been reported that the graphitic carbon coating has been used in lithium batteries and other electron chemistry.<sup>[32, 33]</sup> In this study, we used ethylene ( $C_2H_4$ ) as carbon resource for coating high surface area  $Mo_2C$ .

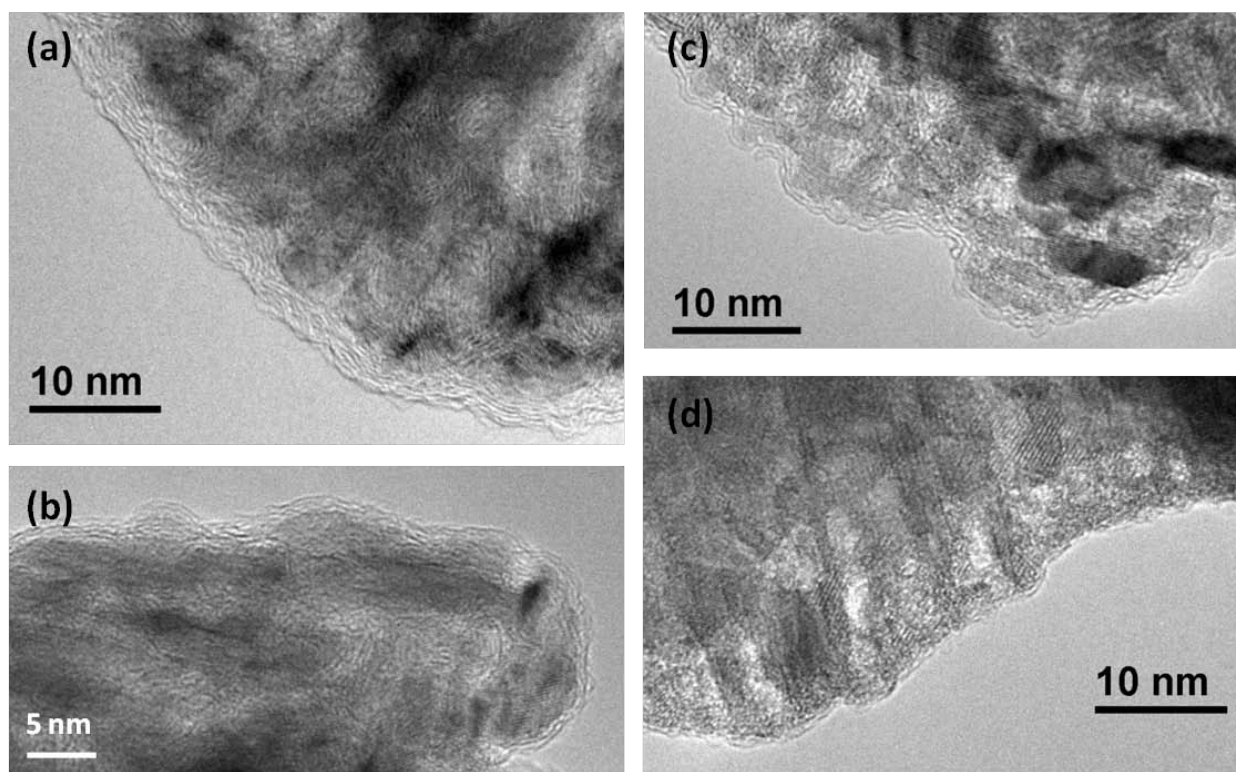


Figure 5-10. TEM images of high-surface-area  $Mo_2C$  coated with carbon layers at different conditions. (a) pure  $C_2H_4$  at  $600^\circ C$ ; (b)  $15\% C_2H_4$ -Ar at  $600^\circ C$ ; (c) pure  $C_2H_4$  at  $500^\circ C$ ; (d) pure  $C_2H_4$  at  $400^\circ C$ .

Fig. 5-10 showed the representative TEM images of coated  $Mo_2C$  with different reaction conditions. 5 to 10 graphitic carbon layers were observed in Fig. 5-10-a, which was pretreated with pure ethylene at  $600^\circ C$  for 3 hrs. Although the mesopores were still available as denoted in

the bright and dark region in the figure, the mesopores were almost fully filled with deposited carbon, which can not only block the mesopores, but also block the active sites for ammonia decomposition. In order to optimize the coating layers of carbon, we varied the reaction temperatures and reactant concentrations. Fig. 5-10-b shows the TEM image of high surface area  $\text{Mo}_2\text{C}$  reacted with 15%  $\text{C}_2\text{H}_4$ -Ar mixture at  $600^\circ\text{C}$  for 3 hrs. Fig. 5-10-b&c shows the TEM images of high surface area  $\text{Mo}_2\text{C}$  pretreated with pure  $\text{C}_2\text{H}_4$  at  $500^\circ\text{C}$  and  $400^\circ\text{C}$  respectively. One or two layers of graphene layers could be coated on the high surface area  $\text{Mo}_2\text{C}$  by reaction at a low temperature.

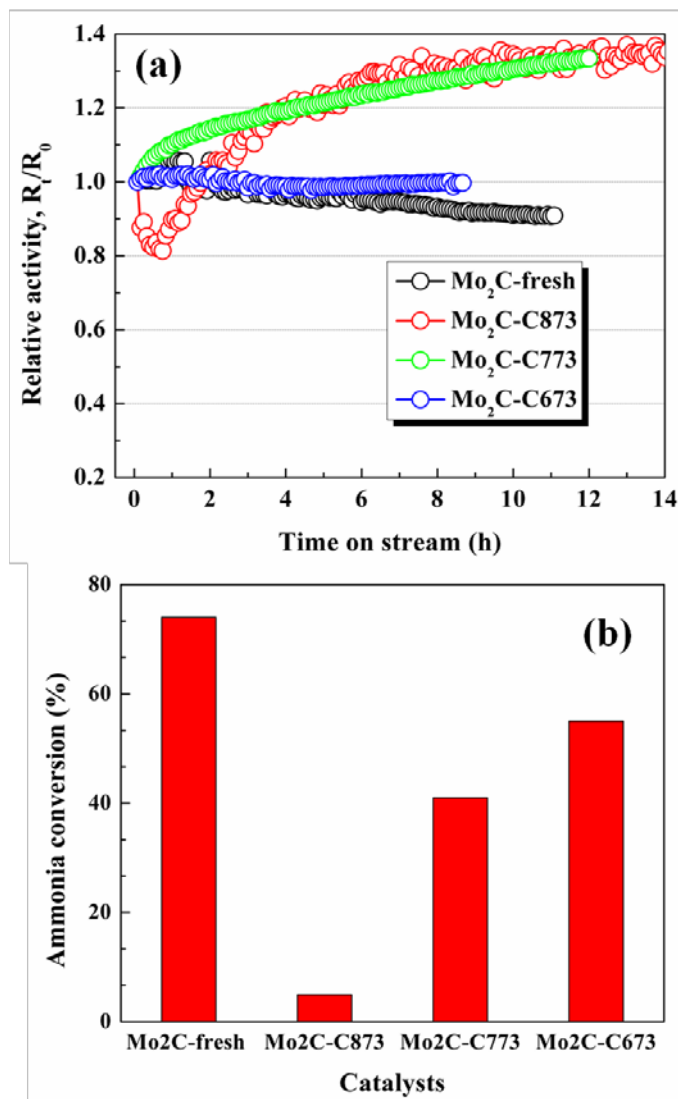


Figure 5-11. Catalytic performances of all catalysts. Reaction condition: 50 mg sample,  $\text{NH}_3$  space velocity is  $36,000 \text{ h}^{-1}$ , reaction temperature  $600^\circ\text{C}$ .

The catalytic performances (steady state reactivity and stability) of carbon coated catalysts were summarized in Fig. 5-11. Although the stability (Fig. 5-11-a) was improved by introducing carbon layers coated on the surface of molybdenum carbide, the activities of dropped significantly (Fig. 5-11-b) with the increasing graphitic carbon layers, which is due to the block of active sites by graphene layers.

## 5.2 Nanostructured molybdenum nitride

### 5.2.1 CNT/CNFs supported molybdenum carbide

In order to synthesis the nanoparticles of molybdenum carbide, we have employed hollow vapor-grown nanotubes and nanofibers (CNT/CNFs) as support material for molybdenum carbide species used as catalysts for the reaction of ammonia decomposition. As mentioned in Chapter 4, carbon nanotubes and nanofibers are progressively employed as catalyst support for many reactions. Compared to other supports, they are chemically stable in most aggressive media, they show a high thermal conductivity and offer the possibility to chemically modify their surface.<sup>[34]</sup> The thermal stability of metal nanoparticles encapsulated in CNTs channel, which was observed in Chapter 4, could also work for carbide nanoparticles for the same reaction.

High dispersion of  $\text{MoO}_x$  on common supports such as alumina, silica or even activated carbon is typically achieved by impregnation with an aqueous solution of ammonium heptamolybdate at a pH below the point of zero charge of the support (PZC).<sup>[35, 36]</sup> In this case, the surface of the support becomes positively charged and attracts the metal oxide anions. Nitric acid functionalized CNT/CNFs contain oxygen species that enhance their interaction with water and help to disperse and anchor transition metal ions.<sup>[37, 38]</sup> However, the important amount of carboxyl groups renders the support acidic and thus negatively charged when in contact with an aqueous solution. Zeta potential measurement showed that the isoelectric point of functionalized CNT/CNFs is around pH 5. In this study, the functionalized CNFs were impregnated using the incipient wetness technique via an aqueous solution of ammonium heptamolybdate ( $(\text{NH}_3)_6\text{Mo}_7\text{O}_{24}\cdot 4\text{H}_2\text{O}$ ) with the acidity adjusted to PH=3 with nitric acid. After deposition, the sample was slowly dried at room temperature for 10 hrs. During drying, the proton concentration ( $\text{H}^+$ ) slowly increased and condensation of  $\text{Mo}_7\text{O}_{24}^{6-}$  is expected to take place in the liquid film,

near the surface of the CNT/CNFs, thus leads to a high dispersion of molybdenum precursors. Then, the sample was dried at 100°C for 5 hrs and subsequently calcined at 350°C for 2 h.

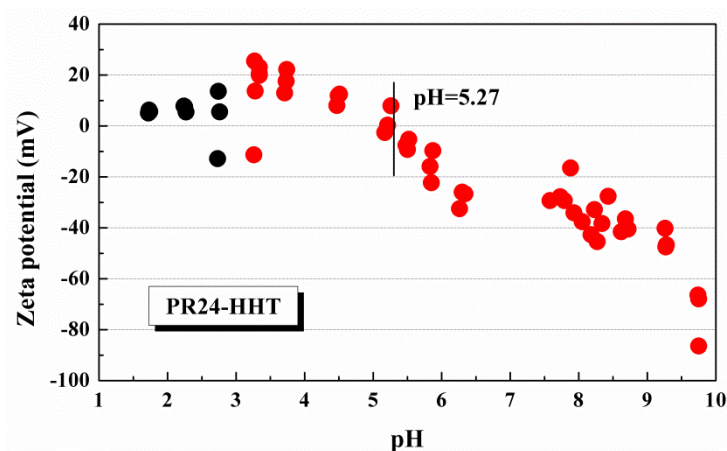


Figure 5-12. Zeta potential measurement of nitric acid functionalized CNFs/CNTs

The further carburisation procedure is similar to the preparation of high surface area molybdenum carbide.<sup>[17]</sup> Fig. 5-13 showed the TEM image of fresh Mo<sub>2</sub>C-CNF catalyst at a selected region (on the tip of one single CNF). In this region molybdenum carbide nanoparticles were well dispersed on the surface of CNF with homogeneous size distribution. As shown in Fig. 5-13-b, the lattice distance of molybdenum carbide could be observed and confirm the hexagonal structure of Mo<sub>2</sub>C nanoparticles.

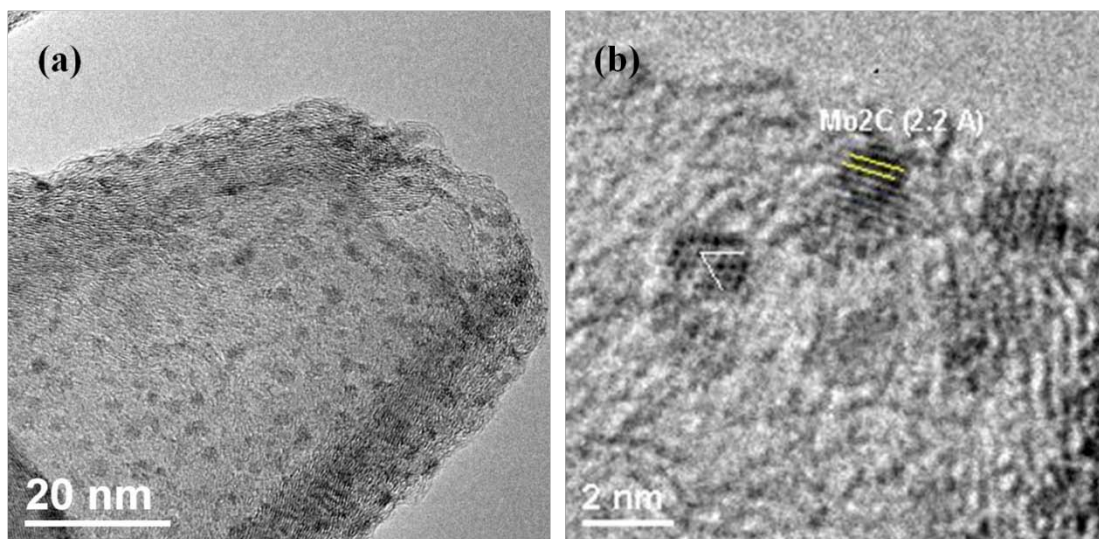


Figure 5-13. TEM image of fresh Mo<sub>2</sub>C-CNFs catalyst at a selected region. (a) tip of one single CNF; (b) high resolution TEM image indexing with lattice distance of hexagonal Mo<sub>2</sub>C.

Unfortunately, this kind of  $\text{Mo}_2\text{C}$  nanoparticles is not the only part of the catalyst, large particles were also observed inside CNT/CNFs channel (in Fig. 5-14). The large molybdenum carbide particles inside CNF (Fig. 5-14-a) exhibited similar morphology as the high surface area  $\text{Mo}_2\text{C}$  bulk system in this chapter. The typical mesopores structures could also be observed on the large  $\text{Mo}_2\text{C}$  particles inside the CNFs channel (Fig. 5-14-c). The  $\text{N}_2$  physisorption isotherms of functionalized CNFs,  $\text{Mo}_2\text{C}$ -CNF-fresh and  $\text{Mo}_2\text{C}$ -CNF-used are shown in Fig. 5-15. All isotherms of the samples exhibited type III shape and almost no hysteresis, indicates that they are mainly macroporous with pores larger than 50nm, which is probably due to the contribution of CNFs.

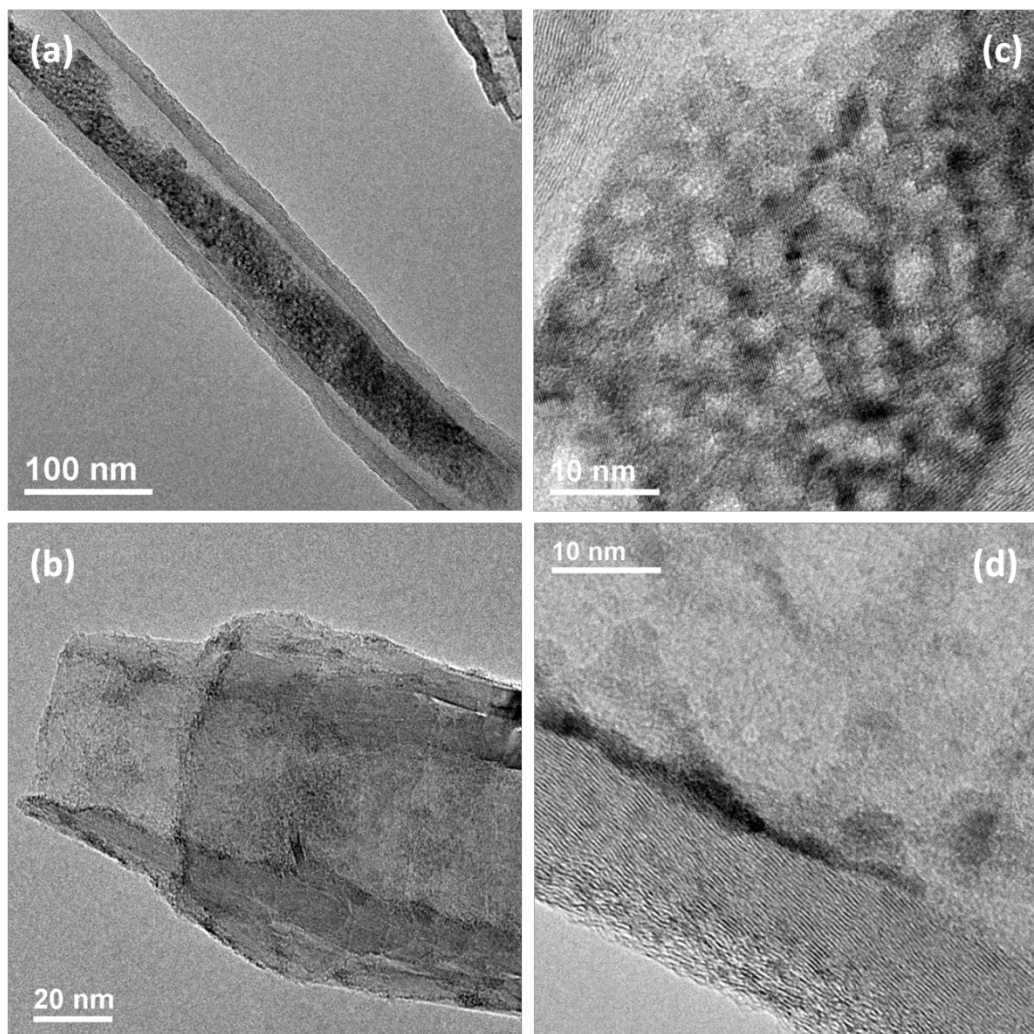


Figure 5-14. TEM images of fresh  $\text{Mo}_2\text{C}$ -CNF catalyst.

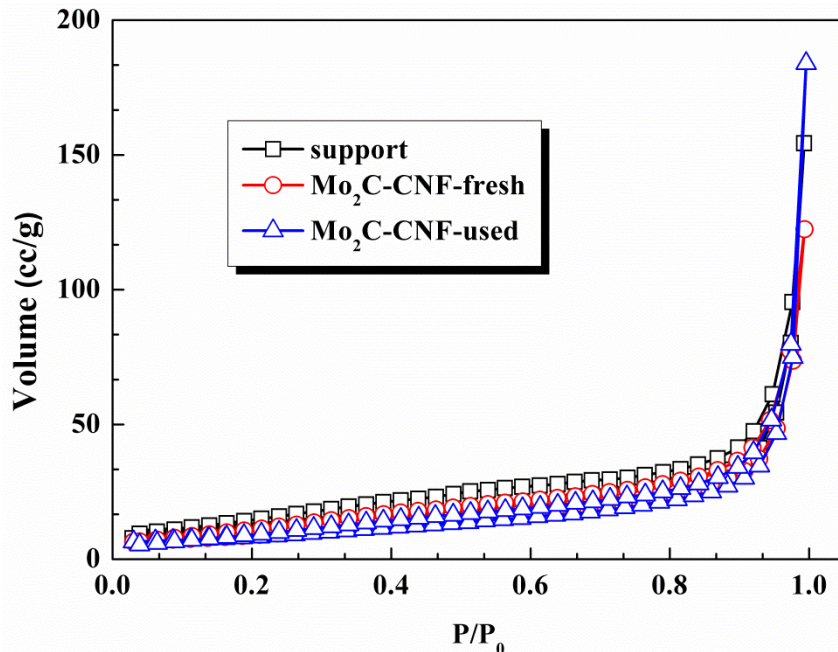


Figure 5-15.  $N_2$  adsorption/desorption isotherms of support and  $Mo_2C$  supported on CNTs/CNFs before and after reaction.

Although the morphology and crystallographic structure of molybdenum carbide could be identified by TEM techniques, the short of average information could be supplied by the powder X-ray diffraction technique. Fig. 5-16 showed the XRD patterns of samples before and after carbonization and after reaction of ammonia decomposition. The diffraction peaks of carbon (observed over all samples) is owing to the thick and high graphitic layers of stacking graphene sheets. For  $Mo_2C$ -CNF-fresh sample, very weak diffraction patterns of hexagonal structure ( $Mo_2C$ ) were observed (similar assignment as bulk molybdenum carbide, JCPD-00-035-0787  $Mo_2C$  ( $34.4^\circ$  (100),  $38.0^\circ$ (002),  $39.4^\circ$ (101),  $61.5^\circ$  (103) and  $74.6^\circ$  (112))), indicates either the low crystallinity of  $Mo_2C$  particles or the thick graphene layers of CNFs block the signal of  $Mo_2C$ . For  $Mo_2C$ -CNF-used sample, the diffraction patterns of hexagonal MoN were observed (JCPD-01-089-5024 MoN ( $31.8^\circ$  (002),  $36.1^\circ$  (200),  $48.8^\circ$  (202),  $64.9^\circ$  (220),  $78.0^\circ$  (204) and  $85.3^\circ$  (402))). The intensity of MoN diffraction patterns in  $Mo_2C$ -CNF-used catalyst is relative stronger than those of  $Mo_2C$ -CNF-fresh, indicated the better crystallinity of MoN nanoparticles. The  $Mo_2C$  diffraction peaks could not be observed in the catalyst collected after reaction. This finding agrees with the result of bulk  $Mo_2C$ , which is due to the nitridation of  $Mo_2C$  under the reaction of ammonia decomposition.

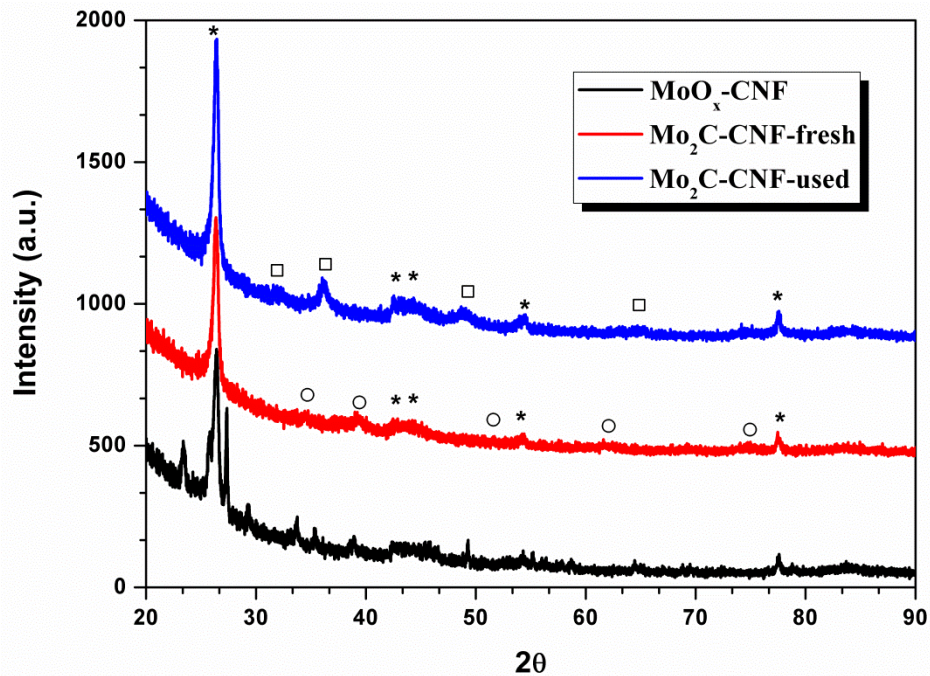


Figure 5-16. XRD pattern of  $\text{MoO}_3\text{-CNF}$ ,  $\text{Mo}_2\text{C-CNF-fresh}$  and  $\text{Mo}_2\text{C-CNF-used}$  samples. star: diffraction peaks of carbon; circle: diffraction peaks of hexagonal  $\text{Mo}_2\text{C}$ ; square: diffraction peaks of hexagonal  $\text{MoN}$ .

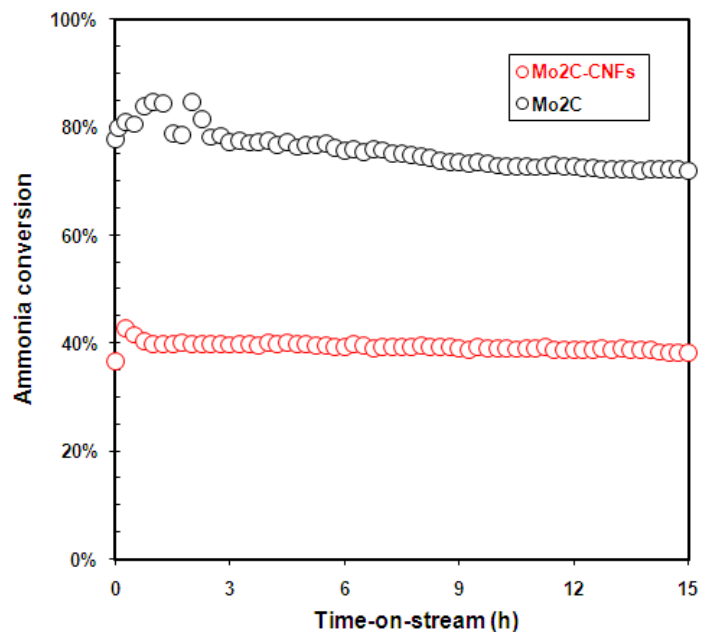


Figure 5-17. Catalytic performance of  $\text{Mo}_2\text{C}$  and supported  $\text{Mo}_2\text{C}$  (10wt%). Reaction condition: 50 mg sample,  $\text{NH}_3$  space velocity is  $36000 \text{ h}^{-1}$ , reaction temperature  $600^\circ\text{C}$ .

The catalytic performance of CNT/CNFs supported Mo<sub>2</sub>C (10wt%) sample were shown in Figure 5-17. There is no significant enhancement of stability on Mo<sub>2</sub>C supported on CNT/CNFs compared with the bulk system of molybdenum carbide, which is due to the poor distribution of Mo<sub>2</sub>C clusters located on the inner and outer surfaces of CNT/CNFs

### ***5.2.2 Hydrothermal carbonization preparing nanostructured molybdenum nitride***

The two methods we tried to maintain the mesopores structure of Mo<sub>2</sub>C during ammonia decomposition were not successfully working. The complex surface properties of CNT/CNFs could lead a low dispersion of molybdenum precursor on CNT/CNFs surface. The coating of carbon layers on the surface of Mo<sub>2</sub>C can stabilize the nanostructure, but block the active sites of the catalyst. We believe the mechanic force of second component (carbon) should be further considered but in an opposite way, that is, using carbon material to isolate molybdenum nanoparticles. The addition of carbon material should be operated before the nucleation of molybdenum precursor, otherwise the growth of large particles could not be prevented. In this case, a special fast carbonization method must be applied to introduce carbon material into the MoN system. Among the countless literature for carbon formation from carbohydrates with faster chemical processes, hydrothermal carbonization (HTC) seems to be especially promising.<sup>[39]</sup> Hydrothermal carbonization process can be operated at comparatively moderate condition (normally under 200°C<sup>[40, 41]</sup>). Under this condition, most carbohydrates could be carbonized into different forms of solid carbonaceous materials.<sup>[42]</sup> This technique is extremely valuable for preparing our designed catalyst. Before carbonization, carbonaceous and molybdenum precursors could be mixed with high homogeneity. The details of the preparation were summarized in Chapter 2. After hydrothermal carbonisation, samples were washed and dried at 110°C overnight, and further calcined in ammonia at 650°C for 24 hrs. The prepared samples were labeled as MoN-HTC-I and MoN-HTC-II with 2:15 and 1:15 ratios of Mo:C.

#### ***5.2.2.1 Characterizations of nanosized Mo-based particles***

Figure 5-19 shows the X-ray diffraction patterns of MoN-HTC-I and MoN-HTC-II samples with Mo:C ratio of 2:15 and 1:15 respectively. Both hexagonal  $\beta$ -Mo<sub>2</sub>C (JCPD-00-035-0787) and  $\delta$ -MoN (JCPD-01-089-5024) diffraction patterns could be clearly observed on MoN-HTC-I sample (less loading of carbon precursor) indicates the high crystallinity of the molybdenum carbide/nitride nanoparticles. The formation of molybdenum carbide can occur in the process of either HTC or the ammolyis, since it was reported that the presence of metal ions can effectively accelerate the hydrothermal carbonization.<sup>[43]</sup> In the process of ammolyis at 650 °C, the molybdenum species (nitrate or oxide) might be reduced by the H atoms from the dissociation of ammonia molecule. At the same time, the molecular or amorphous carbon could dissolve<sup>[44]</sup> into the metallic molybdenum lead the formation of carbide. There is no diffraction information of molybdenum carbide/nitride was observed in MoN-HTC-II sample (higher loading of carbon precursor), suggesting either the poor crystallinity of molybdenum-based particles, or the narrow distribution of well dispersed Mo<sub>2</sub>C/MoN nano-particles.

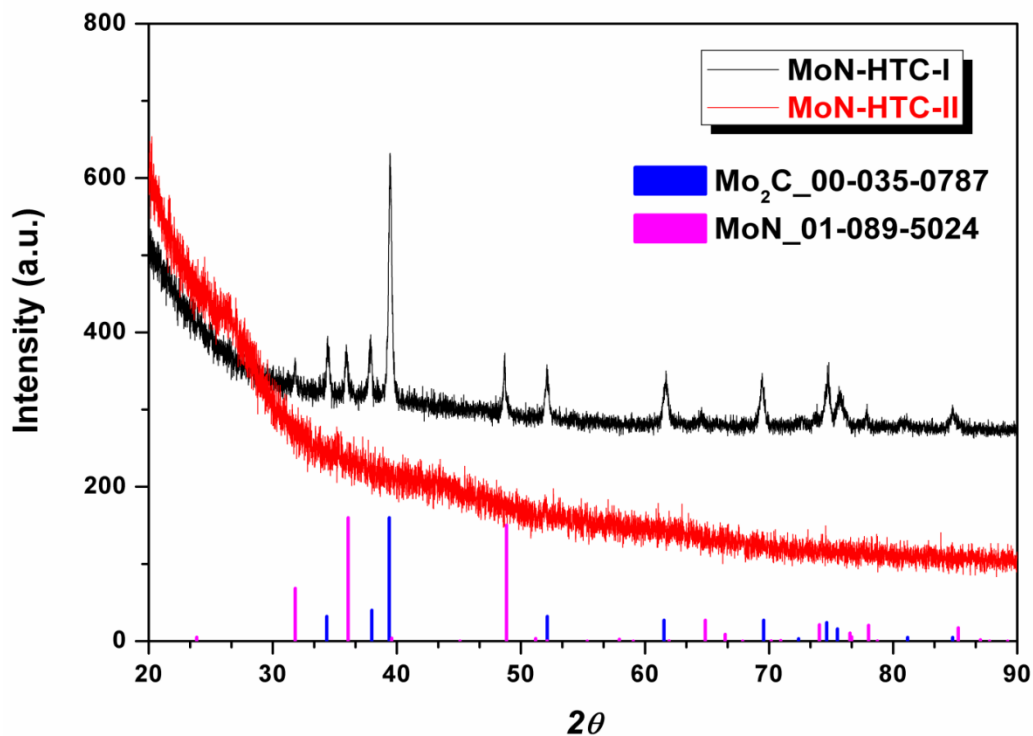


Figure 5-19. XRD patterns of MoN-HTC-I and MoN-HTC-II samples. Blue and pink bars present JCPD-00-035-0787 Mo<sub>2</sub>C and JCPD-01-089-5024 MoN respectively.

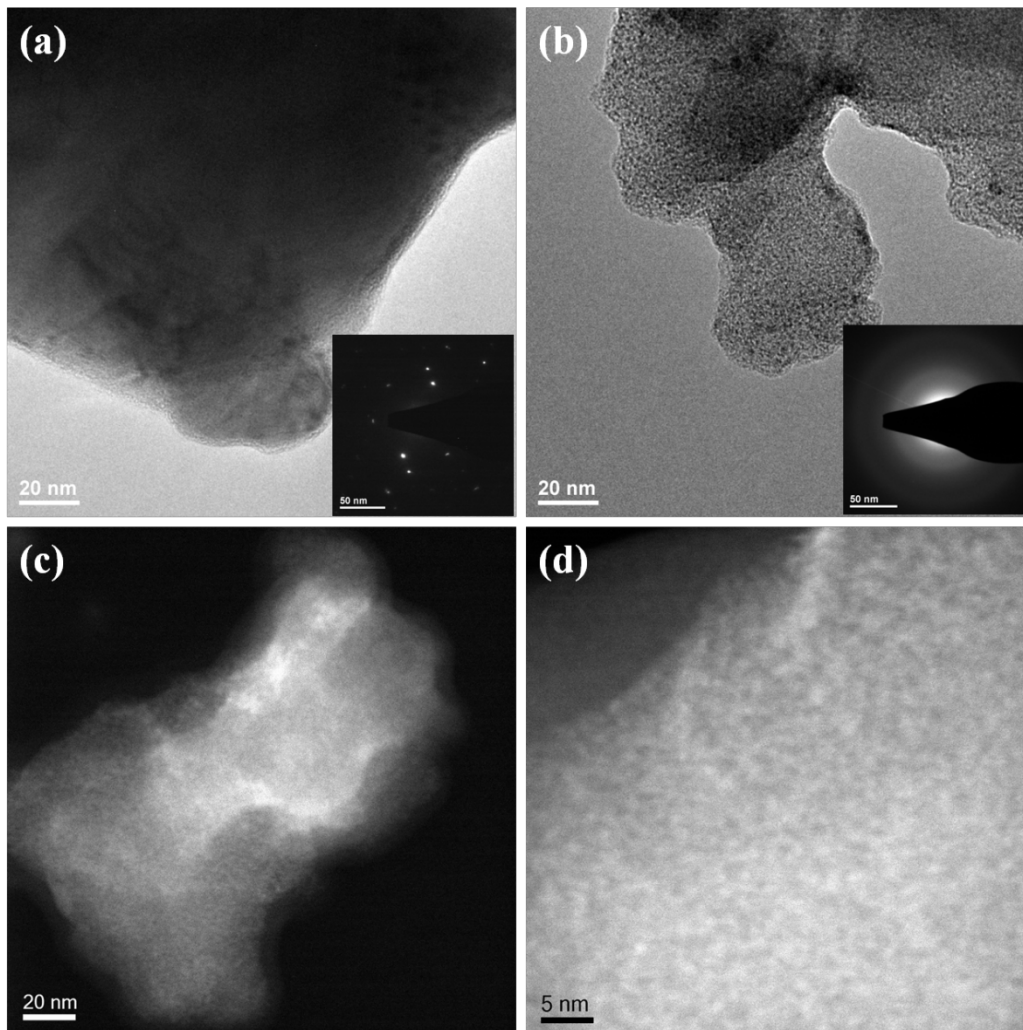


Figure 5-20. TEM analysis of prepared molybdenum nitride samples. (a) and (b) are the representative TEM images MoN-HTC-I and MoN-HTC-II samples, inserted with SAED images. (c) and (d) HADDF images of MoN-HTC-II sample.

Figure 5-20 (a) and (b) show the representative overview TEM images of the prepared catalysts. The particles (molybdenum-based materials) of MoN-HTC-I sample are in the range of micrometers without porous structures. This is probably due to the high loading amount of molybdenum, which had much more chance to sinter or aggregate into large particles. As shown in the selected area electron diffraction (SAED) image of Fig. 5-20–a, the spots of diffraction patterns of molybdenum carbide/nitride indicated the high crystallinity of high molybdenum loading sample, which is in agreement with XRD result. On the opposite, when increasing the

addition of carbon precursor (D-glucose), the carbonaceous species would dominate in the system, the molybdenum precursors were separated by the carbonaceous species and do not aggregate into large particles. The representative overview TEM image (Fig. 5-20-b) revealed a different morphology compared with that of MoN-HTC-I sample, that is, the material exhibits similar structure as solid carbon but with homogeneously dispersed dark dots, which are probably Mo-based components. The SAED image of MoN-HTC-II sample inserted in Fig. 5-20-b shows only the diffraction ring of carbon indicates the amorphous structures of carbon. In accordance with XRD result, the missing of SAED information of MoN-HTC-II sample might be ascribed to the small or amorphous structure of Mo-based particles with poor crystallinity.

High-angle annular dark-field image in the scanning transmission electron microscope (HAADF-STEM) is possible to directly image the atomic configuration of small nanoparticles. The contrast of HAADF images is strongly dependent on the average atomic number of the scatterer encountered by the incident probe. Fig. 5-20-c&d show the HAADF images of MoN-HTC-II sample. The size range of bright dots (present the heavier Mo atoms compared with C and N atoms) is not in accordance with the size range of black dots observing in TEM image, which is due to the mixture distribution of N and C atoms in both of Mo-based clusters and carbon materials from the hydrothermal carbonization of glucose. Since it is known that,<sup>[45]</sup> carbide and nitride materials have the typical binary “interstitial alloy” structures with carbon or nitrogen atoms dissolved in metal replacing metal atoms with different metal:C/N stoichiometries.

Representative high resolution TEM (HRTEM) images of the catalysts are shown in Figure 5-21. The large Mo<sub>2</sub>C/MoN particles with high crystallinity could be clearly identified in the sample with high Mo:C ratio. As shown in Fig. 5-21-a, two square areas were indexed with lattice distances of MoN (002) and (202) planes, which were further confirmed by the analysis of Fast Fourier Transform (FFT) of the selected area. The HRTEM image in Fig. 5-21-b shows a representative area of MoN-HTC-II sample. On the edge of the observing sample, several layers with disordering stacks, bend curvature and defects, probably are the solid carbon materials formed either in the hydrothermal carbonization process or in the ammonolysis at high temperature. In the middle of the observing area dispersed several dark spots with the homogeneous distribution of radius, which are probably the Mo-based components, since the TEM image is a 2-dimensional projection of a 3-dimensional material,<sup>[46]</sup> the contrast of the

image can present either the thickness difference of the observing sample or the mixture of different components with different transparent intensities. The dark spots were further identified by high resolution images indexing with  $\text{Mo}_2\text{C}$  and  $\text{MoN}$  lattice distances shown in the inserted images of Fig. 5-21-b.

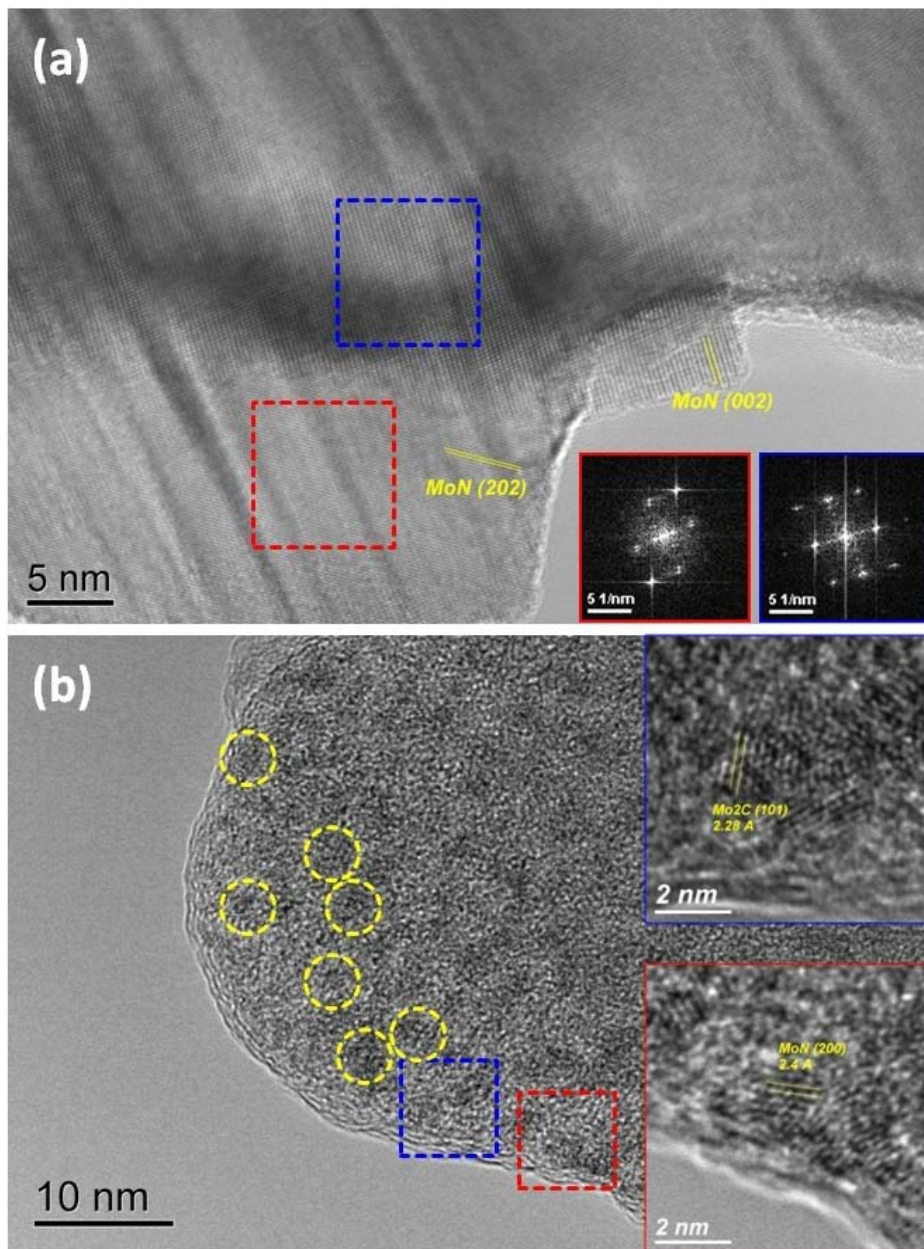


Figure 5-21. High resolution TEM images of the catalysts. (a) MoN-HTC-I, red and blue squares were chosen to acquire Fast Fourier Transform (FFT); (b) MoN-HTC-II, red and blue squares were chosen to acquire HRTEM images out of focus, yellow circles labeled the area which are probably the molybdenum carbide/nitride nanoparticles.

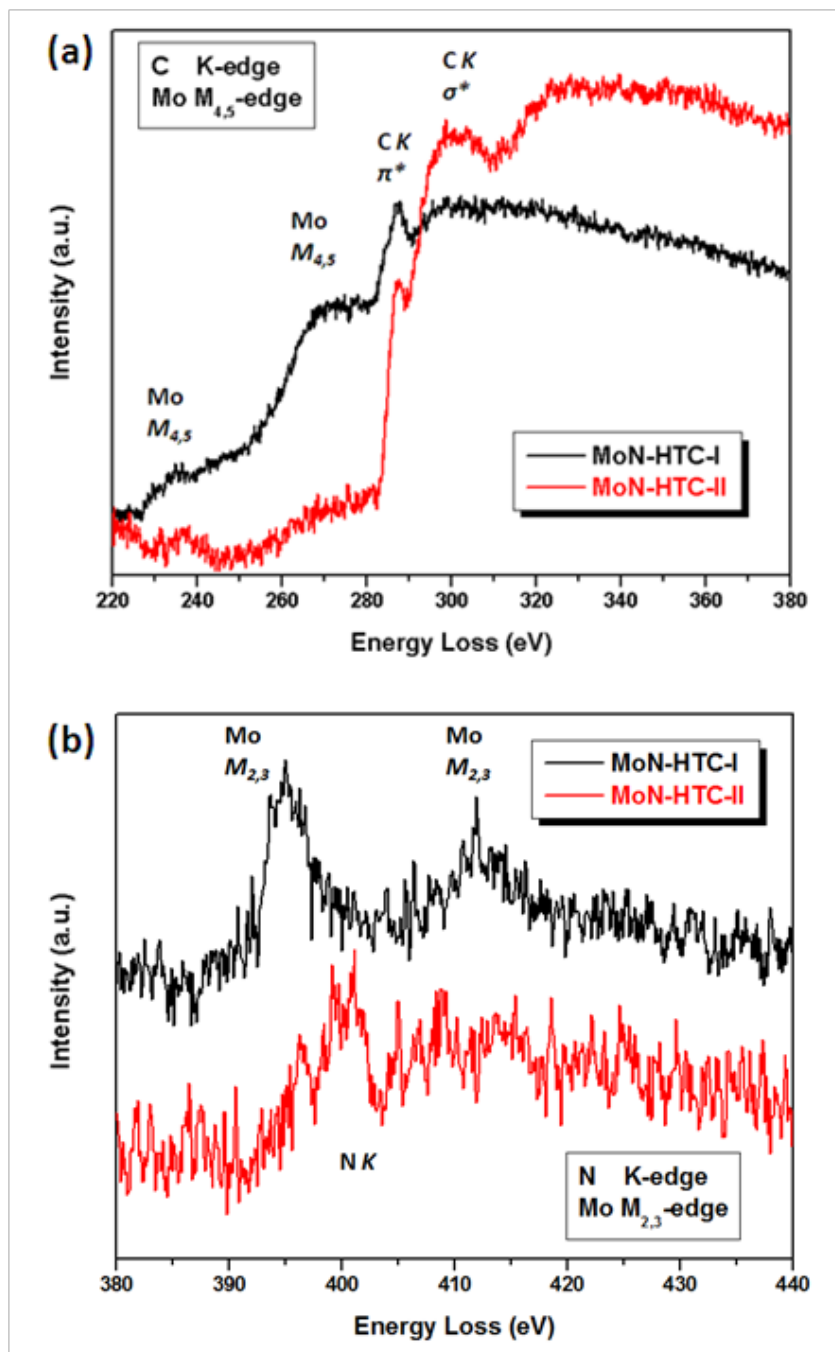


Figure 5-22. EELS spectra of MoN-HTC-I and MoN-HTC-II catalysts . (a) carbon K-edge and molybdenum  $M_{4,5}$ -edge; (b) nitrogen K-edge and molybdenum  $M_{2,3}$ -edge.

Electron energy-loss spectroscopy (EELS) is the favored technique for the chemical analysis of carbide/nitride properties.<sup>[24]</sup> Unfortunately, the Mo  $M_{4,5}$ -edge (at ca. 227 eV) and  $M_{2,3}$ -edge

(doublet peaks at around 400 eV) overlap with the C K-edge (at around 285-310 eV) and N K-edge (at ca. 401 eV), causing difficulty in the standard procedure for EELS analysis.<sup>[25]</sup> Figure 5-22 shows Mo 3*d*, C 1*s* and N 1*s* energy-loss near edge structure (ELNES) spectra of the two prepared samples. The peak at around 286 eV corresponds to an electronic transition from C 1*s* to the anti-bonding  $\pi^*$  states, indicating the existence of sp<sup>2</sup>-bonded carbon in both MoN-HTC-I and MoN-HTC-II samples. The broader structure at 290-310 eV indicates transitions to anti-bonding  $\sigma^*$  states.<sup>[47]</sup>

Fig. 5-22-b shows the Mo M<sub>2,3</sub>-edge and N K-edge spectra of the two catalysts. The doublet peaks of molybdenum around 400 eV (transition of Mo 3*p* electrons to the unoccupied 4*d* states) can be clearly observed on MoN-HTC-I sample with higher ratio of Mo:C during hydrothermal carbonization process. The EELS spectrum of MoN-HTC-II with higher carbon loading shows a dominant peak at about 403 eV with a tiny shoulder peak at 397 eV, which were assigned to N K-edge and Mo M<sub>3</sub>-edge respectively according to the EELS spectra. These findings revealed that the catalyst MoN-HTC-II with smaller particle size of molybdenum carbide/nitride is nitrogen-rich compared with the large carbide/nitride particle of MoN-HTC-I sample. This suggests that the small Mo-based particles are much easier to be nitrated compared with large particles. It was reported that the adsorbed nitrogen atoms, from the dissociative adsorption of either nitrogen or ammonia, sometime referred to as “nitride”, the dissolved nitrogen can not only recombine and desorb, but also be dissolved into subsurface and form a solid solution.<sup>[48]</sup> In the process of ammonia nitridation, the dissociated NH<sub>3</sub> molecule will probably follow the similar pathway to form the nitride from surface, subsurface and deeper down into the core of the material. It should be noticed that, the N information observed from EELS analysis could also be attributed to the N species on the surface of carbon, which were introduced by amination of carbon with NH<sub>3</sub> at high temperature.<sup>[49]</sup>

### ***5.2.2.2 Catalytic measurements of nanosized Mo-based particles***

Catalytic performances of NH<sub>3</sub> decomposition over the two prepared catalysts with different Mo-carbide/nitride domain size were conducted according to the procedure detailed in experimental section. The catalytic performances (in form of ammonia conversions) of MoN-HTC-I and

MoN-HTC-II catalysts in Figure 5-23 show the stable activities of both catalysts in 20 hrs reaction at 600 °C. The steady-state hydrogen production rates of catalysts were summarized in Table 5-2 with the catalytic data of carbide and nitride catalysts reported in literature.

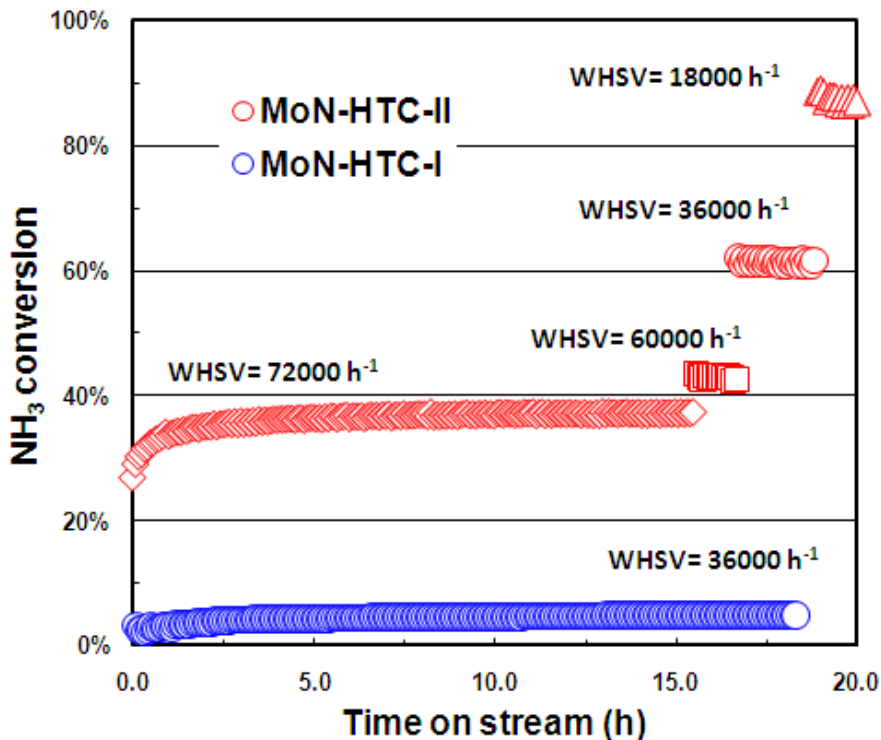


Figure 5-23. Catalytic stability measurements of MoN-HTC-I and MoN-HTC-II catalysts at 600 °C, via different weight hourly space velocities (diamond: 72000 h<sup>-1</sup>, square: 60000 h<sup>-1</sup>, cycle: 36000 h<sup>-1</sup> and triangle 18000 h<sup>-1</sup>).

At 600 °C, MoN-HTC-I sample offered about 3 mmol/(g<sub>cat</sub>·min) hydrogen production rate in 20 hrs, which is in the range of H<sub>2</sub> producibility of molybdenum carbide reported in the literature (the comparison of steady-state H<sub>2</sub> production rate in Tab. 5-2).<sup>[14]</sup> The representative overview TEM image in Figure 5-21-a shows the relative huge Mo-based crystals, which exhibits nearly no pore-structure indicating the extremely low porosity (The specific surface area of MoN-HTC-I sample could not be measured by N<sub>2</sub>-adsorption/desorption technique). It should be noticed that, some core-shell structures (Mo-based particles covered by solid carbon with thickness around 5-10 nm) are existing in MoN-HTC-I sample (Fig. 5-20-a), which could also lead to the low catalytic activity due to the blockage of catalytic component. The catalytic activity of MoN-

HTC-II catalyst is about 10 times higher (23 mmol/(g<sub>cat</sub>·min) hydrogen production rate in 20 hours) than MoN-HTC-I catalyst operated at the same reaction condition. This reactivity is close to the performance of bulk material of high surface area molybdenum carbide (reported in this chapter). The high performance of MoN-HTC-II catalyst benefits from the relative small nanosize molybdenum carbide/nitride particles. In MoN-HTC-II catalyst, the carbon materials could act as the “spacers”, which can isolate the individual molybdenum carbide and nitride particles, and stabilize them during the long-term ammonia decomposition at 600 °C as consequence.

<b>Table 5-2. Catalytic NH<sub>3</sub> decomposition: comparison with literature data in terms of steady-state H<sub>2</sub> production rate.</b>					
Catalyst	Structure <sup>a</sup>	BET (m <sup>2</sup> /g)	Reaction Temp. (°C)	H <sub>2</sub> production rate (mmol/gcat/min)	Reference
MoN-HTC-I	β-Mo <sub>2</sub> C & δ-MoN	- <sup>b</sup>	600	~ 3	This work
MoN-HTC-II	β-Mo <sub>2</sub> C & δ-MoN	- <sup>b</sup>	600	23	This work
MoC	Mo <sub>2</sub> C (β)	16	550	~ 4	[14]
MoN <sub>x</sub> /α-Al <sub>2</sub> O <sub>3</sub>	-	-	650	1.4	[50]
WC	α-WC	1.5	500	~ 0.2	[15]
FeC <sub>x</sub>	Fe <sub>3</sub> C	415	600	9.2	[51]
a based on XRD					
b could not be measured by N <sub>2</sub> adsorption/desorption.					

## 5.3 Chapter conclusions

### 5.3.1 Bulk system of Mo carbide and nitride

In this section, we reported a high performance ammonia decomposition catalyst of high surface area molybdenum carbide, which could achieve about 30 mmol/(g<sub>cat</sub>·min) constant H<sub>2</sub> production rate. The comprehensive characterization of fresh and used samples showed that the high surface area Mo<sub>2</sub>C can not only crack the NH<sub>3</sub> molecule, but also has a tendency to form MoN under pure ammonia atmosphere at high temperature (600 °C), causing a significant drop of specific surface area (from about 50 m<sup>2</sup>/g to about 5 m<sup>2</sup>/g). Theoretical calculation showed that under pure ammonia atmosphere, N-atoms tend to diffuse to the subsurface positions of Mo<sub>2</sub>C and the molybdenum nitride is progressively formed. This result is in agreement with the EELS analysis over the sample collected after 4 hrs reaction, that is, MoN is dominant on the surface compared to the bulk.

In 100 hours of catalytic measurement the activity was observed to drop by about 15% over the first 15 hrs before stabilizing. This drop in activity is not proportional to the drop in specific surface area, indicating that the molybdenum nitride may be more active for ammonia decomposition compared to molybdenum carbide. The opposite order was observed by S. Oyama over β-Mo<sub>2</sub>C and γ-Mo<sub>2</sub>N for ammonia synthesis at 400 °C.<sup>[11]</sup> We believe that the abundance of high energy sites (twin-boundaries, stacking faults, steps and defects) observed on molybdenum nitride should be the sites for cracking ammonia, since this reaction requires high electron density as well as under-coordinated sites to proceed. The observation of N-catalyst interactions over the terrace and step locations of Mo<sub>2</sub>C and MoN showed the importance of high energy sites for ammonia decomposition, in agreement with earlier studies in the literature.<sup>[52]</sup> N atoms tend to more strongly bound (0.4 eV higher) to the step edge on MoN (0001) than Mo<sub>2</sub>C (0001), which likely benefits for the difficult step of N-N recombination through surface diffusion from two sites of ammonia cleavage on weakly adsorbing sites (terraces).<sup>[9]</sup>

Further, we tried to stabilize the mesopore structure of high surface area Mo<sub>2</sub>C catalyst against collapse by a mechanical force from coating molecular layers on the surface of Mo<sub>2</sub>C catalyst. The carbon layers introduced by reacted with C<sub>2</sub>H<sub>4</sub> at high temperatures can mechanical improve the thermal stabilities of Mo<sub>2</sub>C catalysts in the reaction of ammonia decomposition at

600 °C, unfortunately, the catalytic activities are not promising due to the blockage of active site on the catalysts surface.

### ***5.3.2 Nanosizing Mo carbide and nitride catalysts***

The hollow vapor-grown carbon nanotubes and nanofibers have been used as supports for Mo-based carbide and nitride catalysts. Unfortunately, due to the complicated surface properties of CNT/CNFs, the dispersion of Mo carbide and nitride are far away from the homogeneous nanosized particles. Although the slight enhancement of the catalytic stabilities over the supported catalysts was observed, it is difficult to distinguish the contribution from the nanosized particles or the improvement of thermal stability encapsulated inside CNT/CNFs channel. Further work should be focused on the optimization of modification of CNT/CNFs surface, which will be beneficial for the homogeneous dispersion of metals, metal oxides and carbide/nitrides on the different locations of CNT/CNFs.

In the last part of this chapter, we reported a simple preparation method to prepare homogeneous molybdenum carbide/nitride nanoparticles dispersed in carbon, which benefits from the relative mild carbonization process of hydrothermal carbonization<sup>[39, 42, 43]</sup> of glucose and ammonium heptamolybdate with proper Mo:C mole ratio. The characterization results of XRD and electron microscopy (TEM/HRTEM/SAED/HAADF/EELS) techniques identify the existences of molybdenum carbide and nitride in the prepared catalysts. With the help of “spacers”, carbon, the individual MoN nanoparticles could survive throughout the long-term catalytic decomposition of ammonia at high temperature and offer a constant H<sub>2</sub> formation rate (about 23 mmol/(g<sub>cat</sub>·min)), which is comparable with the high performance bulk material of high surface area molybdenum carbide, and even with the noble metal, Ru-based catalysts for clean hydrogen production. Future works might focus on the considerations concerning the mechanism of the formation of metal carbide and nitride during the whole procedure including hydrothermal carbonization and ammolyis, which could lead to the optimization of catalysts for the beneficial applications in not only the hydrogen production from ammonia decomposition, but also in other heterogeneous catalytic reactions.

## References

1. Levy, R.B. and M. Boudart, *Platinum-Like Behavior of Tungsten Carbide in Surface Catalysis*. Science, 1973. **181**(4099): p. 547-549.
2. Patterson, P.M., T.K. Das, and B.H. Davis, *Carbon monoxide hydrogenation over molybdenum and tungsten carbides*. Applied Catalysis A: General, 2003. **251**(2): p. 449-455.
3. Leclercq, L., et al., *Catalytic properties of transition metal carbides : II. Activity of bulk mixed carbides of molybdenum and tungsten in hydrocarbon conversion*. Journal of Catalysis, 1989. **117**(2): p. 384-395.
4. Neylon, M.K., et al., *Catalytic properties of early transition metal nitrides and carbides: n-butane hydrogenolysis, dehydrogenation and isomerization*. Applied Catalysis A: General, 1999. **183**(2): p. 253-263.
5. Ribeiro, F.H., et al., *Reactions of neopentane, methylcyclohexane, and 3,3-dimethylpentane on tungsten carbides: The effect of surface oxygen on reaction pathways*. Journal of Catalysis, 1991. **130**(1): p. 86-105.
6. Bouchy, C., et al., *Microstructure and Characterization of a Highly Selective Catalyst for the Isomerization of Alkanes: A Molybdenum Oxycarbide*. Journal of Catalysis, 2000. **190**(1): p. 92-103.
7. Claridge, J.B., et al., *New Catalysts for the Conversion of Methane to Synthesis Gas: Molybdenum and Tungsten Carbide*. Journal of Catalysis, 1998. **180**(1): p. 85-100.
8. Schlögl, R., *Catalytic Synthesis of Ammonia—A “Never-Ending Story”?* Angewandte Chemie International Edition, 2003. **42**(18): p. 2004-2008.
9. Schlögl, R., *Ammonia Synthesis*, in *Handbook of Heterogeneous Catalysis*, G. Ertl, et al., Editors. 2008, Wiley-VCH Verlag GmbH & Co. KGaA.
10. Kojima, R. and K.-i. Aika, *Molybdenum Nitride and Carbide Catalysts for Ammonia Synthesis*. Applied Catalysis A: General, 2001. **219**(1-2): p. 141-147.
11. Oyama, S.T., *Preparation and Catalytic Properties of Transition Metal Carbides and Nitrides*. Catalysis Today, 1992. **15**(2): p. 179-200.
12. Oyama, S.T., *Kinetics of Ammonia Decomposition on Vanadium Nitride*. Journal of Catalysis, 1992. **133**(2): p. 358-369.
13. Choi, J.-G., *Ammonia Decomposition over Vanadium Carbide Catalysts*. Journal of Catalysis, 1999. **182**(1): p. 104-116.
14. Choi, J.-G., *Ammonia Decomposition over Mo Carbides*. Journal of Industrial and Engineering Chemistry, 2004. **10**(6): p. 967-971.
15. Pansare, S., W. Torres, and J. Goodwinjr, *Ammonia Decomposition on Tungsten Carbide*. Catalysis Communications, 2007. **8**(4): p. 649-654.
16. Lee, J.S., S.T. Oyama, and M. Boudart, *Molybdenum carbide catalysts : I. Synthesis of unsupported powders*. Journal of Catalysis, 1987. **106**(1): p. 125-133.
17. Cotter, T.P., *Activation of propane over Mo/V carbide*, in *Inorganic Chemistry*. 2011, Fritz-Haber-Institut der Max-Planck Gesellschaft: Berlin.
18. Brunauer, S., P.H. Emmett, and E. Teller, *Adsorption of Gases in Multimolecular Layers*. Journal of the American Chemical Society, 1938. **60**(2): p. 309-319.
19. Barrett, E.P., L.G. Joyner, and P.P. Halenda, *The Determination of Pore Volume and Area Distributions in Porous Substances. I. Computations from Nitrogen Isotherms*. Journal of the American Chemical Society, 1951. **73**(1): p. 373-380.
20. Hugosson, H.W., et al., *Theory of phase stabilities and bonding mechanisms in stoichiometric and substoichiometric molybdenum carbide*. Journal of Applied Physics, 1999. **86**(7): p. 3758-3767.
21. Perry, A.J., et al., *Crystal structure of molybdenum nitride films made by reactive cathodic arc evaporation*. Surface and Coatings Technology, 1992. **54-55**(Part 1): p. 261-265.

22. Somorjai, G.A.L., Yimin, *Introduction to Surface Chemistry and Catalysis*. 2010, New York: Wiley.
23. Ertl, G., *Catalytic Ammonia Synthesis*. Fundamental and Applied Catalysis, ed. J.R. Jennings. 1991, New York: Springer. 476.
24. Kuimalee, S., et al., *Quantitative analysis of a complex metal carbide formed during furnace cooling of cast duplex stainless steel using EELS and EDS in the TEM*. *Micron*, 2010. **41**(5): p. 423-429.
25. Egerton, R.F., *Electron Energy-Loss Spectroscopy in the Electron Microscope*. 2nd ed. 1996, New York. 500.
26. Clougherty, E.V., K.H. Lothrop, and J.A. Kafalas, *A New Phase formed by High-Pressure Treatment : Face-centred Cubic Molybdenum Monocarbide*. *Nature*, 1961. **191**(4794): p. 1194-1194.
27. Kanoun, M.B., S. Goumri-Said, and M. Jaouen, *Structure and mechanical stability of molybdenum nitrides: A first-principles study*. *Physical Review B*, 2007. **76**(13): p. 134109.
28. Logadottir, A., et al., *The Brønsted-Evans-Polanyi Relation and the Volcano Plot for Ammonia Synthesis over Transition Metal Catalysts*. *Journal of Catalysis*, 2001. **197**(2): p. 229-231.
29. Jacobsen, C.J.H., et al., *Catalyst Design by Interpolation in the Periodic Table: Bimetallic Ammonia Synthesis Catalysts*. *Journal of the American Chemical Society*, 2001. **123**(34): p. 8404-8405.
30. P. E. York, A., et al., *Molybdenum and tungsten carbides as catalysts for the conversion of methane to synthesis gas using stoichiometric feedstocks*. *Chemical Communications*, 1997(1): p. 39-40.
31. Solymosi, F., et al., *Reactions of Propane on Supported Mo<sub>2</sub>C Catalysts*. *Journal of Catalysis*, 2000. **195**(2): p. 316-325.
32. Wilcox, J.D., et al., *Factors Influencing the Quality of Carbon Coatings on LiFePO<sub>4</sub>*. *Journal of The Electrochemical Society*, 2007. **154**(5): p. A389.
33. Hu, Y.-S., et al., *Superior Storage Performance of a Si@SiO<sub>x</sub>/C Nanocomposite as Anode Material for Lithium-Ion Batteries*. *Angewandte Chemie International Edition*, 2008. **47**(9): p. 1645-1649.
34. Serp, P., M. Corrias, and P. Kalck, *Carbon nanotubes and nanofibers in catalysis*. *Applied Catalysis A: General*, 2003. **253**(2): p. 337-358.
35. Wachs, I., *Recent conceptual advances in the catalysis science of mixed metal oxide catalytic materials*. *Catalysis Today*, 2005. **100**(1-2): p. 79-94.
36. Chen, K., et al., *Structure and Properties of Oxidative Dehydrogenation Catalysts Based on MoO<sub>3</sub>/Al<sub>2</sub>O<sub>3</sub>*. *Journal of Catalysis*, 2001. **198**(2): p. 232-242.
37. Rosca, I., et al., *Oxidation of multiwalled carbon nanotubes by nitric acid*. *Carbon*, 2005. **43**(15): p. 3124-3131.
38. Hull, R.V., et al., *Pt Nanoparticle Binding on Functionalized Multiwalled Carbon Nanotubes*. *Chemistry of Materials*, 2006. **18**(7): p. 1780-1788.
39. Titirici, M.-M. and M. Antonietti, *Chemistry and materials options of sustainable carbon materials made by hydrothermal carbonization*. *Chemical Society Reviews*, 2010. **39**(1): p. 103.
40. Wang, Q., et al., *Monodispersed hard carbon spherules with uniform nanopores*. *Carbon*, 2001. **39**(14): p. 2211-2214.
41. Sun, X. and Y. Li, *Colloidal Carbon Spheres and Their Core/Shell Structures with Noble-Metal Nanoparticles*. *Angewandte Chemie International Edition*, 2004. **43**(5): p. 597-601.
42. Titirici, M.-M., M. Antonietti, and N. Baccile, *Hydrothermal carbon from biomass: a comparison of the local structure from poly- to monosaccharides and pentoses/hexoses*. *Green Chemistry*, 2008. **10**(11): p. 1204-1212.
43. Cui, X., M. Antonietti, and S.-H. Yu, *Structural Effects of Iron Oxide Nanoparticles and Iron Ions on the Hydrothermal Carbonization of Starch and Rice Carbohydrates*. *Small*, 2006. **2**(6): p. 756-759.

44. Rinaldi, A., et al., *Dissolved Carbon Controls the Initial Stages of Nanocarbon Growth*. Angewandte Chemie International Edition, 2011. **50**(14): p. 3313-3317.
45. Oyama, S.T., *Transition Metal Carbides, Nitrides, and Phosphides*, in *Handbook of Heterogeneous Catalysis*. 2008, Wiley-VCH Verlag GmbH & Co. KGaA.
46. Williams, D.B. and C.B. Carter, *The Transmission Electron Microscope*, in *Transmission Electron Microscopy*. 2009, Springer US. p. 3-22.
47. Ferrari, A.C., et al., *Density,  $sp^3$  fraction, and cross-sectional structure of amorphous carbon films determined by x-ray reflectivity and electron energy-loss spectroscopy*. Physical Review B, 2000. **62**(16): p. 11089.
48. Schlögl, R., *Ammonia Synthesis*. Handbook of Heterogeneous Catalysis. 2008: Wiley-VCH Verlag GmbH & Co. KGaA.
49. Arrigo, R., et al., *Tuning the Acid/Base Properties of Nanocarbons by Functionalization via Amination*. Journal of the American Chemical Society, 2010. **132**(28): p. 9616-9630.
50. Liang, C., et al., *Catalytic Decomposition of Ammonia over Nitrided  $MoNx/\alpha-Al_2O_3$  and  $NiMoNy/\alpha-Al_2O_3$  Catalysts*. Industrial & Engineering Chemistry Research, 2000. **39**(10): p. 3694-3697.
51. Kraupner, A., et al., *Mesoporous  $Fe_3C$  Sponges as Magnetic Supports and as Heterogeneous Catalyst*. Journal of Materials Chemistry, 2010. **20**(29): p. 6019-6022.
52. Dahl, S., et al., *Electronic factors in catalysis: the volcano curve and the effect of promotion in catalytic ammonia synthesis*. Applied Catalysis A: General, 2001. **222**(1-2): p. 19-29.

## Chapter 6:

### Preliminary kinetic study of ammonia decomposition over molybdenum nitrides and metal nanoparticles

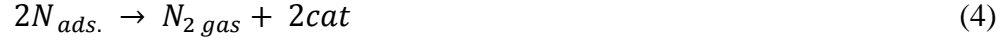
The kinetic study of ammonia decomposition was first investigated with the interest of understanding its reverse reaction, ammonia synthesis <sup>[1, 2]</sup>. The ammonia decomposition reaction is endothermic:



The Gibbs free energy  $\Delta G^0$  for the reaction is  $+16.4 \text{ kJ mol}^{-1}$ , indicates the reaction benefits from the high temperature and low pressure. With these data including the data of its reversal reaction, the equilibrium for the “reforming” of ammonia can be estimated, which were summarized in Table 1-1 (Chapter 1).

At the beginning of last century, after the establishment of the Haber-Bosch process (high-pressure, high-temperature synthesis of ammonia) people were trying to understand the reaction mechanism for both the synthesis and decomposition of ammonia. First experiments were performed over iron catalysts in static system with pure ammonia.<sup>[3, 4]</sup> Later, Winter <sup>[5]</sup> reported the kinetic experiments over alumina supported iron catalysts, and he found the rate of ammonia decomposition was proportional to  $P_{NH_3}/(P_{H_2})^{1.5}$ . He suggested the following reactions to express the kinetics of ammonia decomposition:





The equilibrium constant for reaction (3) is:

$$K = \frac{[N_{ads.}][H_{ads.}]^3}{[NH_3_{ads.}]}$$

and, consequently

$$[N_{ads.}] = K' \frac{[NH_3_{gas}]}{[H_2_{gas}]^{1.5}}$$

With the assumption that the slow step in the decomposition of ammonia is the reaction (4), the rate of ammonia decomposition can be expected to be proportional to  $P_{NH_3}/(P_{H_2})^{1.5}$ .

It was further studied by Temkin and Pyzhev,<sup>[2]</sup> who suggested that the “rate of escape of nitrogen molecules from the surface of the catalyst depends very strongly on the fraction of the surface covered by adsorbed nitrogen”. The two important assumptions applied by them are: (1) the adsorption of nitrogen on iron in the presence of an NH<sub>3</sub>-H<sub>2</sub> mixture will be the same as it would be at equilibrium with the partial pressure of nitrogen equivalent to the existing partial pressure of NH<sub>3</sub> and H<sub>2</sub> in the gas mixture; (2) the slow step in the decomposition is the rate of escape of nitrogen molecules from the surface of the catalysts. As the consequence, the rate of ammonia decomposition can be expressed as:

$$r = k \left( \frac{P_{NH_3}^2}{P_{H_2}^3} \right)^\beta \quad (6)$$

Later, these assumptions and equation were applied in most kinetic studies for ammonia decomposition. For example, Love and Emmett<sup>[6]</sup> investigated the kinetics of ammonia decomposition over three Fe-based catalysts. Their data was re-investigated by Takezawa and Mezaki using Langmuir-Temkin-Pyzhev model, which was proved to be reliable for the description of reaction rate data.<sup>[7]</sup>

It was further argued with the reaction rate determining step for ammonia decomposition, which should be both of the adsorption of ammonia and the desorption of dinitrogen.<sup>[8-11]</sup> These kinetic

measurements were taken over polycrystalline Pt wires<sup>[9]</sup>, iron wires<sup>[8]</sup>, molybdenum foil<sup>[11]</sup>, and tungsten foil<sup>[10]</sup>, which exhibit relative low surface area and are far away from the practical catalysts. Takezawa and Toyoshima reported the temperature dependent rate determining steps of ammonia decomposition over an ammonia synthetic catalyst, those are the desorption of adsorbed nitrogen at low temperature and dehydrogenation of the adsorbed amino radical at high temperature. It was further proposed a relative new mechanism<sup>[12]</sup> by Shindo et al.,<sup>[10]</sup> who investigated the mechanism of ammonia decomposition on a “clean” tungsten surface ( $5.3 \times 83 \times 0.025 \text{ mm}^3$  tungsten foil) in the temperature range of 500-1200 °C under ammonia pressure of  $10^{-6}$ - $10^{-3}$  Pa. They found that the order of ammonia changed with temperature from first order to fractional at 1200 and 500 °C. The hydrogen partial pressure had no effect on either the reaction rate or on the amount of surface nitrogen. Thus, they proposed that there is a “dynamic balance” between two rate-determining steps, which are reaction (3) and (4), that is corresponding to the supply and desorption of chemisorbed nitrogen. It should be noticed that the surface of metal foil might not be “clean”, the roughness on the surface might be even worse when treated with ammonia at high temperature. This Tamaru mechanism, or so called “W-type mechanism” was applied over a vanadium nitride catalyst by Oyama.<sup>[13]</sup> As shown in Figure 1-6 (in Chapter 1), the rate of ammonia decomposition on vanadium nitride is zero order in ammonia partial pressure at low temperature and first order at high temperature. The reaction rate was independent with the partial pressures of hydrogen and nitrogen indicated the Tamaru mechanism.

Egawa et al. investigated on stepped Ru(1110) and flat Ru(001) surfaces for ammonia decomposition.<sup>[14]</sup> They found that the rate of  $\text{N}_2$  formation on Ru(1110) is one order of magnitude faster than that on Ru(001) for which edge effects have been eliminated. A much more open structure of Ru( $11\bar{2}1$ ) surface was also proved to be more reactive than Ru(0001) surface, which were reported by Dietrich et al.<sup>[15]</sup> A detail study of kinetic of ammonia dissociation over Ru (001) plane was reported by Tsai and Weiberg,<sup>[16]</sup> who suggested the rate-determining step changed with temperature and established a reaction expression under the hypothesis that both recombinative desorption of N atoms as the most abundant reactive intermediate and the initial N-H bond cleavage are slow elementary steps. Since the end of last century, due to the renewed interest of hydrogen production from ammonia, several kinetic studies of supported ruthenium catalysts for ammonia decomposition were reported. Bradford et

al. studied the ruthenium particles supported on carbon and reported that the decomposition of  $\text{NH}_3$  is around 0.7 order in  $\text{NH}_3$  and -2 order in  $\text{H}_2$ , and both the initial N-H cleavage and recombinative nitrogen desorption are slow kinetic steps.<sup>[17]</sup> Their results could apparently explain the  $\text{H}_2$  inhibition effect at low reaction temperature (less than 400 °C) on the small (1-2 nm) Ru crystallites. The later investigations were focused to correlate the particle size and shape of ruthenium supported system following the propose that both synthesis and decomposition of ammonia should be structure sensitive reactions, that the reactivity benefits from the abundance of the particular step sites allowing the fivefold coordination of nitrogen (B-5 site).<sup>[18, 19]</sup> The density of active sites (B-5 site) of Ru particles calculated by Wulff construction shows the maximum abundance at about 2.5 nm, which is favorable compared to the experimental particle size distribution of practical Ru-based catalyst for ammonia synthesis. Garcí'a-Garcí'a et al.<sup>[20]</sup>, Zhang et al.<sup>[21]</sup> and Zheng et al.<sup>[22]</sup> reported the similar result that the optimum Ru particle size for ammonia decomposition is between 3 and 5 nm, which are in agreement with the maximum concentration of B-5 site on the Ru particle. It was further argued that larger particles are more active in this reaction.<sup>[23]</sup> Karim et al.<sup>[23]</sup> attributed the high activity on large Ru particle (about 7 nm) to elongated planar structure compared to the small Ru particle (1.8-3 nm) with hemispherical morphology.

The findings in this work (Chapter 3) shows that the larger ruthenium particles supported on clean and ordering carbon surface can offer a better performance for ammonia decomposition. The local disorder of the carbon support introduces the local disorder to the metal particle, and leads to a strong interaction between metal and reaction intermediates observing by in-situ XPS measurement. We believe that there might be not enough evidence to correlate the morphology to the performance either with the B-5 site abundances on small particles or with the “elongated planar structure” on large particles.

In this chapter, the preliminary study will start from kinetic measurements of three types of molybdenum nitrides, that are  $\text{MoN-Mo}_2\text{C}$  (“ $\text{Mo}_2\text{C}$ -fresh” sample in Chapter 5),  $\text{MoN-MoO}_3$  (prepared from  $\text{MoO}_3$ ) and  $\text{MoN-HTC}$  (“ $\text{MoN-HTC-II}$ ” sample in Chapter 5), which were in-situ activated in ammonia at 600 °C overnight.

## 6.1 Kinetics results of molybdenum nitrides

### 6.1.1 Kinetic results of MoN-Mo<sub>2</sub>C

Reactivity measurements were carried out at different temperatures shown in Figure 6-1. The activation energy was calculated using the Arrhenius equation:

$$Ea = -R \left[ \frac{\partial \ln k}{\partial \left( \frac{1}{T} \right)} \right]_P \quad (7)$$

in the temperature region of 400 to 525 °C. The apparent activation energy of MoN-Mo<sub>2</sub>C sample is about 183 kJ/mol, which is close to the vanadium nitride catalysts reported by McGill et al. [24] and Oyama [13].

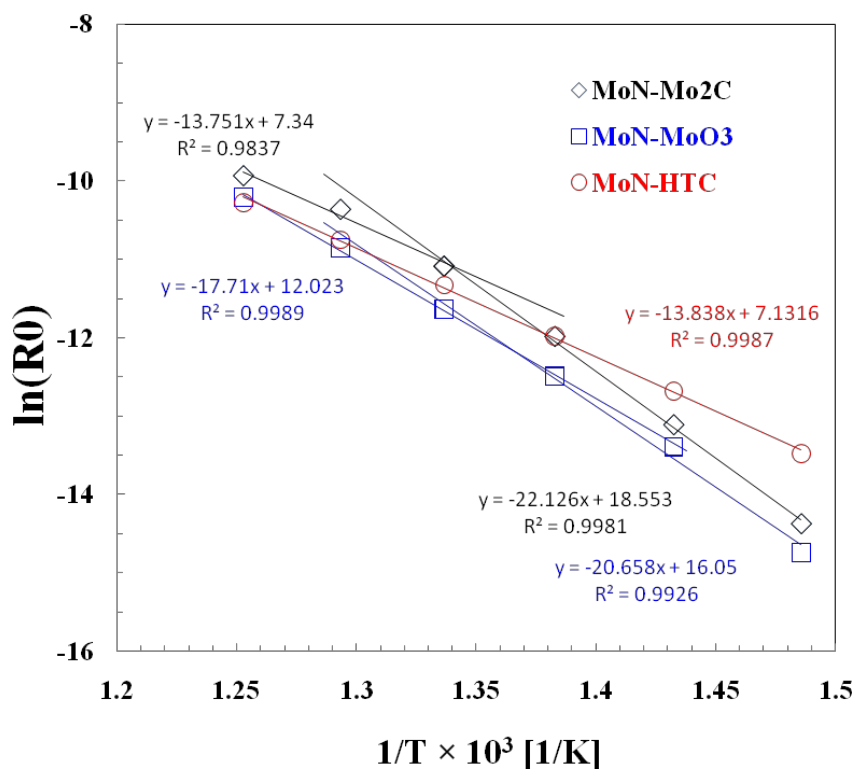


Figure 6-1. Arrhenius plots of the rate of ammonia decomposition at atmospheric pressure over three molybdenum nitrides catalysts.

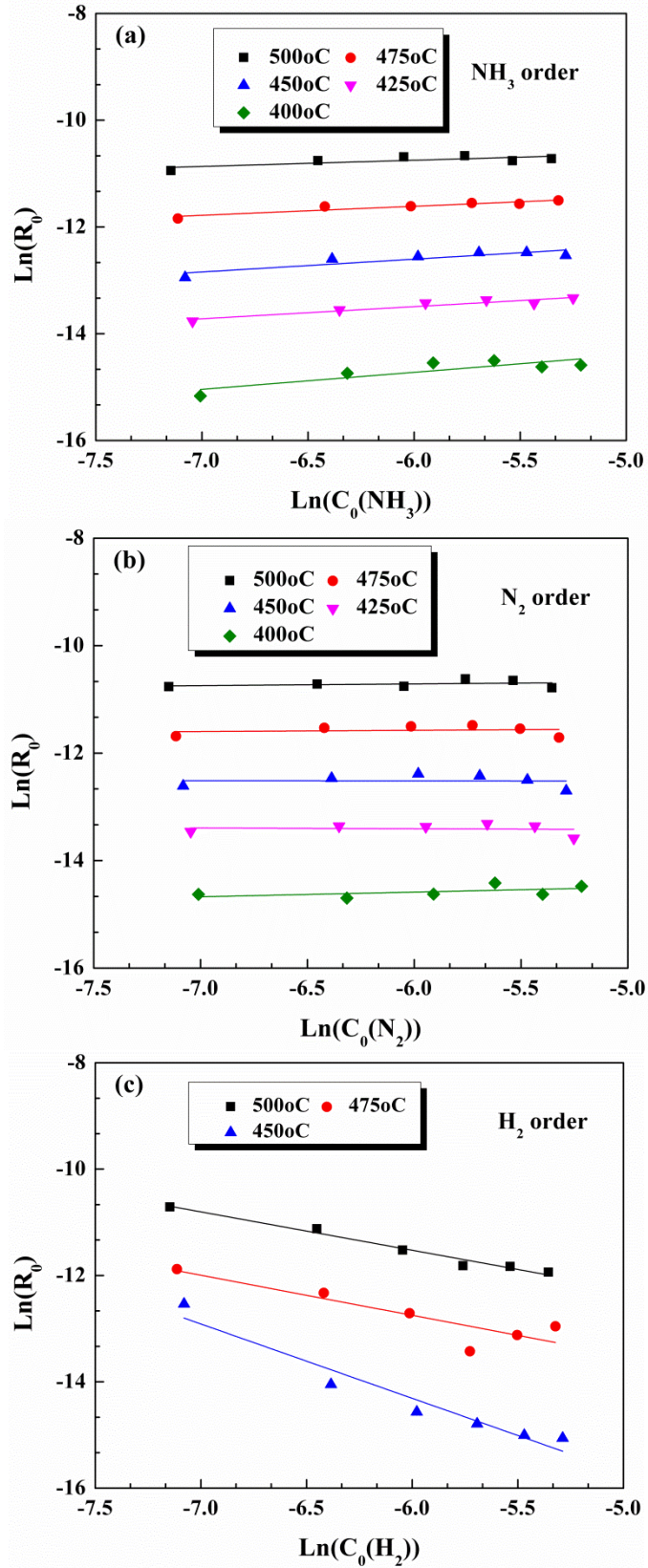


Figure 6-2. Variations of  $\text{NH}_3$ ,  $\text{N}_2$  and  $\text{H}_2$  partial pressures using argon as balance.

The reaction orders for NH<sub>3</sub>, H<sub>2</sub> and N<sub>2</sub> were determined from a fit of the experimental data to a power law equation:

$$r = kP_{NH_3}^\alpha P_{H_2}^\beta P_{N_2}^\gamma \quad (8)$$

the variations of partial pressure of NH<sub>3</sub>, H<sub>2</sub>, and N<sub>2</sub> were measured at different temperatures (400, 425, 450, 475, and 500 °C) with at least five different residence times, which were shown in figure 6-2.

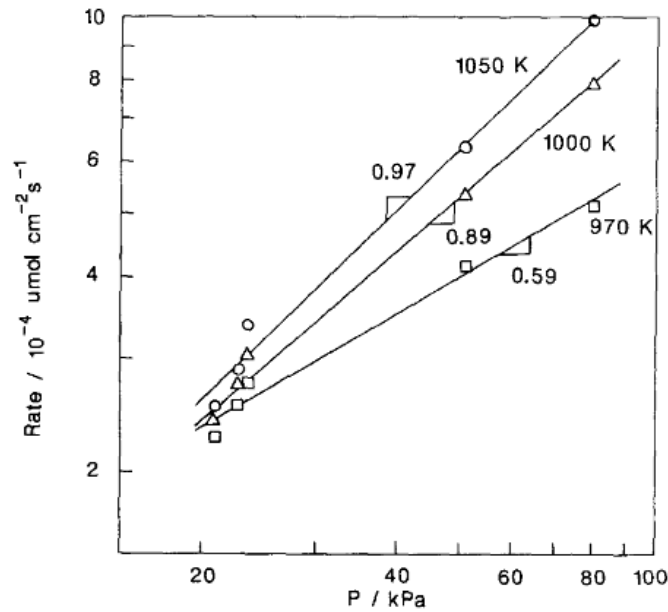


Figure 6-3. Ammonia reaction order as function of temperature. Reaction temperature: (circle) 1050 K, (triangle) 1000 K, (square) 970 K. (Figure taken from Ref. [13].)

The values of  $\gamma$  (Fig. 6-2-b) are close to zero at five working temperatures (400 to 500 °C) indicates that the rate of ammonia decomposition does not depend on the partial pressures of nitrogen. Thus, the power law equation for the rate expression can be written as:

$$r = k'P_{NH_3}^\alpha P_{H_2}^\beta \quad (9)$$

At the operating conditions, the value of  $\alpha$  was found to be slightly sensitive to temperature; i.e., it was 0.38 at 400 °C, 0.2~0.3 at 425 and 450 °C, and around 0.15 at 475 and 500 °C. These

relative low values of  $\text{NH}_3$  order, compared with those of vanadium nitrides reported by McGill et al.<sup>[24]</sup> and Oyama<sup>[13]</sup> (0.5 and close to 1, respectively) indicates the low influence of ammonia partial pressure to the reaction rate probably originates from the smaller crystalline and abundance of high energetic sites (steps, defects, stacking faults and twin-boundaries) on the surface of molybdenum nitrides (observed by HRTEM and shown in Chapter 5). Oyama found that at low temperatures the rate is zero order in ammonia partial pressure, while at high temperatures the rate approaches 1 order, as shown in Figure 6-3. The findings in this study showing the reverse tendency of the ammonia orders as the function of temperature.

The values of the  $\text{H}_2$  order ( $\beta$ ) for MoN- $\text{Mo}_2\text{C}$  sample were negative, indicates the existence of the inhibition effect of hydrogen to ammonia decomposition over molybdenum nitride catalyst. This behavior differs from the results of Oyama<sup>[13]</sup> who found that the rate of ammonia decomposition does not depend on the partial pressure of hydrogen, and hydrogen is not chemisorbed on vanadium nitride at about 500 to 900 °C. It is generally accepted that  $\text{H}_2$  has an inhibitive effect on the  $\text{NH}_3$  decomposition rate while  $\text{H}_2$  was co-fed along with  $\text{NH}_3$ , particularly at high  $\text{H}_2$  partial pressure and low temperature on noble metal ruthenium catalysts.<sup>[14, 15, 17, 22, 24]</sup> As shown in Fig. 6-2-c and Table 6-1, the values of  $\beta$  are about -0.75 at 500 and 475 °C, -1.4 at 450 °C, and -1.6 at 400 °C. This indicates the similarity of reaction behaviors between molybdenum nitride and ruthenium for the reaction of ammonia decomposition.

We believe that the different reaction behaviors between molybdenum nitride in this study and the vanadium nitrides reported by McGill et al. and Oyama should be ascribed to the different structural properties of these nitride materials. As elucidated in their papers, the vanadium nitrides were prepared from ammonium vanadate and vanadium(V) oxide with pure ammonia at 1100 and 1000 °C. The high temperature of nitridation process could lead to the sintering of crystalline, and lose the density of high energetic sites on the surface of catalysts. Volpe and Boudart reported the “topotactic transformation” of the oxide precursor in the nitride production in ammonia was reasonable to form high surface area molybdenum nitride.<sup>[25]</sup> It was further reported by Jagers et al. that using ammonium molybdate as precursors could prepare even higher surface area of molybdenum nitride owing to the high mobility of ammonia in these precursor leads to a homogeneously nitridation.<sup>[26]</sup> These findings suggest that the different

reaction behaviors of vanadium nitrides between McGill et al. and Oyama might be owing to the different crystalline size of their materials. The absence of hydrogen inhibition effect should be ascribed to the large crystalline of their vanadium nitride catalyst, which can offer enough weak sites (terraces) for the desorption of hydrogen from the surface of nitride.

### 6.1.2 Kinetic results of MoN-MoO<sub>3</sub> and MoN-HTC

In order to investigate the correlation between the reaction behavior and the structural properties of catalytic units, we measured two more types of molybdenum nitrides with different crystalline size. MoN-MoO<sub>3</sub> sample was prepared from *h*-MoO<sub>3</sub> (the same precursor as MoN-Mo<sub>2</sub>C), and used the same thermal pretreatment, but in the mixture of ammonia and hydrogen instead of the carburization condition. Similar phase structure of MoN-MoO<sub>3</sub> was observed from XRD and TEM analysis compared with MoN-Mo<sub>2</sub>C catalyst, in spite of a little bit larger crystalline size (XRD information) and particle size (TEM information). MoN-HTC stands for the “MoN-HTC-II” sample reported in Chapter 5, which prepared by the combination of hydrothermal carbonization and ammonia nitridation. The nanostructured molybdenum nitride particles are around 2-5 nm and isolated by carbon materials.

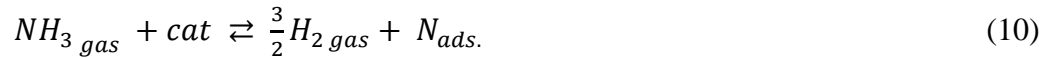
<b>Table 6-1. Reaction parameters estimated from the power law equation for ammonia cracking</b>						
Temp. °C	MoN-Mo <sub>2</sub> C		MoN-MoO <sub>3</sub>		MoN-HTC	
	NH <sub>3</sub>	H <sub>2</sub>	NH <sub>3</sub>	H <sub>2</sub>	NH <sub>3</sub>	H <sub>2</sub>
425	0.23	-1.7	0.64	-0.38	-0.03	-2.12
450	0.29	-1.4	0.72	-0.46	-0.09	-1.25
475	0.17	-0.75	0.40	-0.45	-0.11	-0.98
500	0.14	-0.72	n	n	n	n

(n) stands for not measured.

The Arrhenius plots of the two catalysts are shown in Fig. 6-1. The activation energy of MoN-MoO<sub>3</sub> is about 172 kJ/mol, close to the value of MoN-Mo<sub>2</sub>C catalyst. A lower energy barrier was

observed on the nanosized molybdenum nitride catalyst (MoN-*HTC*), which is 120 kJ/mol. It is known that the nanostructured particles would be more active than the same material in the form of bulk system, which is owing to the abundance of active surface.

The variations of partial pressures of NH<sub>3</sub>, N<sub>2</sub> and H<sub>2</sub> over MoN-*MoO*<sub>3</sub> and MoN-*HTC* catalysts were also investigated as the same procedure for MoN-*Mo*<sub>2</sub>C. There was also no influence of nitrogen partial pressure to the rate of ammonia decomposition for these two catalysts. Both values of  $\alpha$  and  $\beta$  at different temperatures were summarized in Table 6-1. The  $\alpha$  values of MoN-*MoO*<sub>3</sub> are larger than those of MoN-*Mo*<sub>2</sub>C, and more than half order at low temperature closing the values reported by McGill et al.<sup>[24]</sup> and Oyama.<sup>[13]</sup> The values of H<sub>2</sub> orders are still negative, and higher than the ones of MoN-*Mo*<sub>2</sub>C sample indicates the less inhibition effect of hydrogen. Since the existence of the inhibition of hydrogen, and there is no influence of nitrogen partial pressure, the following 2-step model can represent the reaction of ammonia decomposition assuming the adsorbed N is the most abundant reactive intermediate:



The reaction (10) is a single quasi-equilibrated reaction combining the steps (1)-(3) and (5). After dissociative adsorption of ammonia, the adsorbed hydrogen would retard the overall rate by driving the equilibrium for the formation of adsorbed nitrogen backward, while the gas-phase dinitrogen could not retard the rate of step (4), which is an irreversible elemental step.

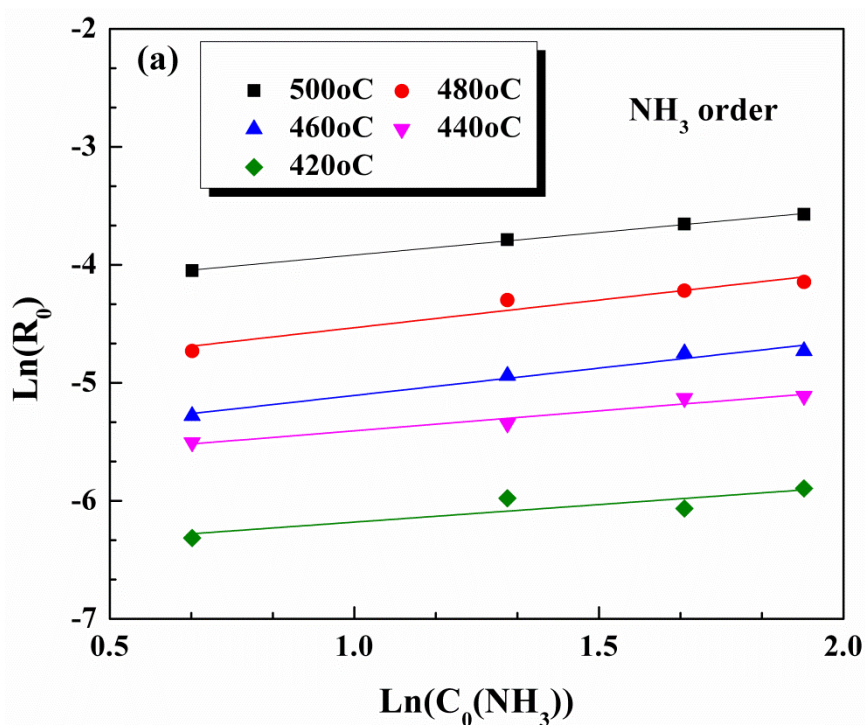
In table 6-1, the  $\alpha$  values of MoN-*HTC* are closing to zero, indicates nearly no effect of ammonia partial pressure to the reaction rate. It is impossible that ammonia cannot adsorb on the surface of the catalyst. It is also impossible that the surface of the catalyst is saturated by the adsorbed ammonia molecules. On the opposite, ammonia can easily adsorb on the surface of nanostructured molybdenum nitride particles, and the N-H bonds would be cracked as soon as possible. Thus the partial pressure of ammonia has slight influence to the overall rate of ammonia decomposition. It should be further noticed that the much more negative values of hydrogen orders indicates a much stronger influence of hydrogen on the nanostructured nitride particles compared with bulk systems.

## 6.2 Kinetics results of ruthenium and iron-cobalt alloy catalysts

The kinetic study of ammonia decomposition was also investigated over the other catalytic components, i. e. 2wt%Ru supported on graphite (Ru-G sample in Chapter 3), and 5wt%FeCo encapsulated inside CNTs channel (CoFe<sub>5</sub>-in-CNT in Chapter 4).

### 6.2.1 Kinetic results of FeCo-CNTs

The post characterization of FeCo-CNTs (CoFe<sub>5</sub>-in-CNTs) was reported in Chapter 4. The average mean size of iron-cobalt alloy particles encapsulated in CNTs channel is about 15 nm after the reaction of ammonia decomposition at 600 °C. The kinetic measurement was carried out at a steady state after the pretreatment of pure ammonia at 600 °C overnight.



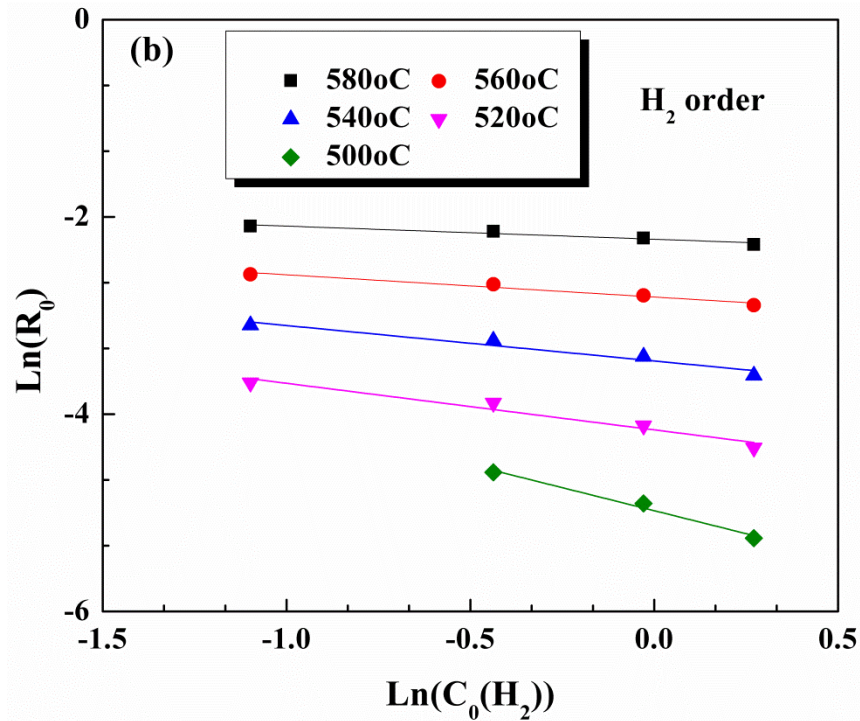


Figure 6-4. Variation of  $\text{NH}_3$  partial pressure to the rate of ammonia decomposition (argon as balance).

Table 6-2. Reaction parameters of FeCo-CNTs catalyst estimated from the power law equation							
Temp. °C	$\text{NH}_3$		Temp. °C	$\text{N}_2$		Temp. °C	$\text{H}_2$
500	0.38		475	-0.23		580	-0.13
480	0.47		450	-0.16		560	-0.23
460	0.46		425	-0.30		540	-0.36
440	0.33					520	-0.47
420	0.29					500	-0.93

The apparent activation energy of FeCo-CNTs calculated from Arrhenius equation is about 140 kJ/mol. The variations of  $\text{NH}_3$ ,  $\text{N}_2$  and  $\text{H}_2$  partial pressures were measured at different temperatures. Not like molybdenum nitrides catalysts, the  $\text{N}_2$  orders are negative, which are around -0.2 at the temperature region from 425 to 475 °C. This might be due to the formation of

surface iron nitride species under the relative low temperature reaction condition, which relates to the much stronger interaction of Fe-N compared to ruthenium and other metals or carbides/nitrides.<sup>[27]</sup> In fact, the formation of metal subnitrides and their efficacy as inhibitors for the decomposition of ammonia was described before.<sup>[27, 28]</sup> Kraupner et al. investigated bulk iron carbide for ammonia decomposition, and found the fully nitridation of iron carbide after 16-h reaction.<sup>[29]</sup> Unfortunately, we did not observe the formation of nitride on the surface of iron or iron-cobalt particles (in Chapter 4). Since the post characterization could not prevent the oxidation of iron nitride, which is highly pyrolytic to air. It is also possible that the formation of nitride would only occur on the surface or subsurface of the metal particles, which could not be observed by TEM and XRD techniques. The positive orders of ammonia on FeCo-CNTs catalyst (in Figure 6-4) are nearly insensitive to temperature and around half order. This behavior differs from the low pressure results of Tsai et al.<sup>[16]</sup> and Egawa et al.<sup>[14]</sup> whose ammonia order increased and approached unity with increased temperature over ruthenium single crystals. This might be also due to the formation of iron nitride species, which were formed between metallic iron and adsorbed nitrogen atoms after cleavage of ammonia.

The inhibitive influence of hydrogen on the reaction rate was also observed on FeCo-CNTs catalyst, but less effective compared to the nanostructured molybdenum nitride and ruthenium particles. This is due to the lower interaction between Fe and H atoms compared to Ru-H.

### ***6.2.2 Kinetic results of Ru-graphite***

The post characterization of Ru-graphite (Ru-G) was reported in Chapter 3. The average mean size of ruthenium nanoparticles supported on the clean and highly graphitic graphite is about 2.5 nm, which has well ordering ruthenium crystallite with steps and terraces (HRTEM image in Fig. 3-16-a', Chapter 3). The kinetic measurement was carried out at a steady state after the pretreatment of pure ammonia at 450 °C overnight.

The activation energy of Ru-graphite sample estimated from the Arrhenius plot is about 113 kJ/mol, which is close to the values of supported ruthenium catalysts reported in literature.<sup>[17, 21-23]</sup> This lowest apparent  $E_a$  observed in this study confirms that ruthenium is the most active element for the decomposition of ammonia, even over the relative low loading (2 wt%) of

ruthenium. Thus, the kinetic measurements on Ru-graphite catalyst were carried out at lower temperature compared to the other catalysts.

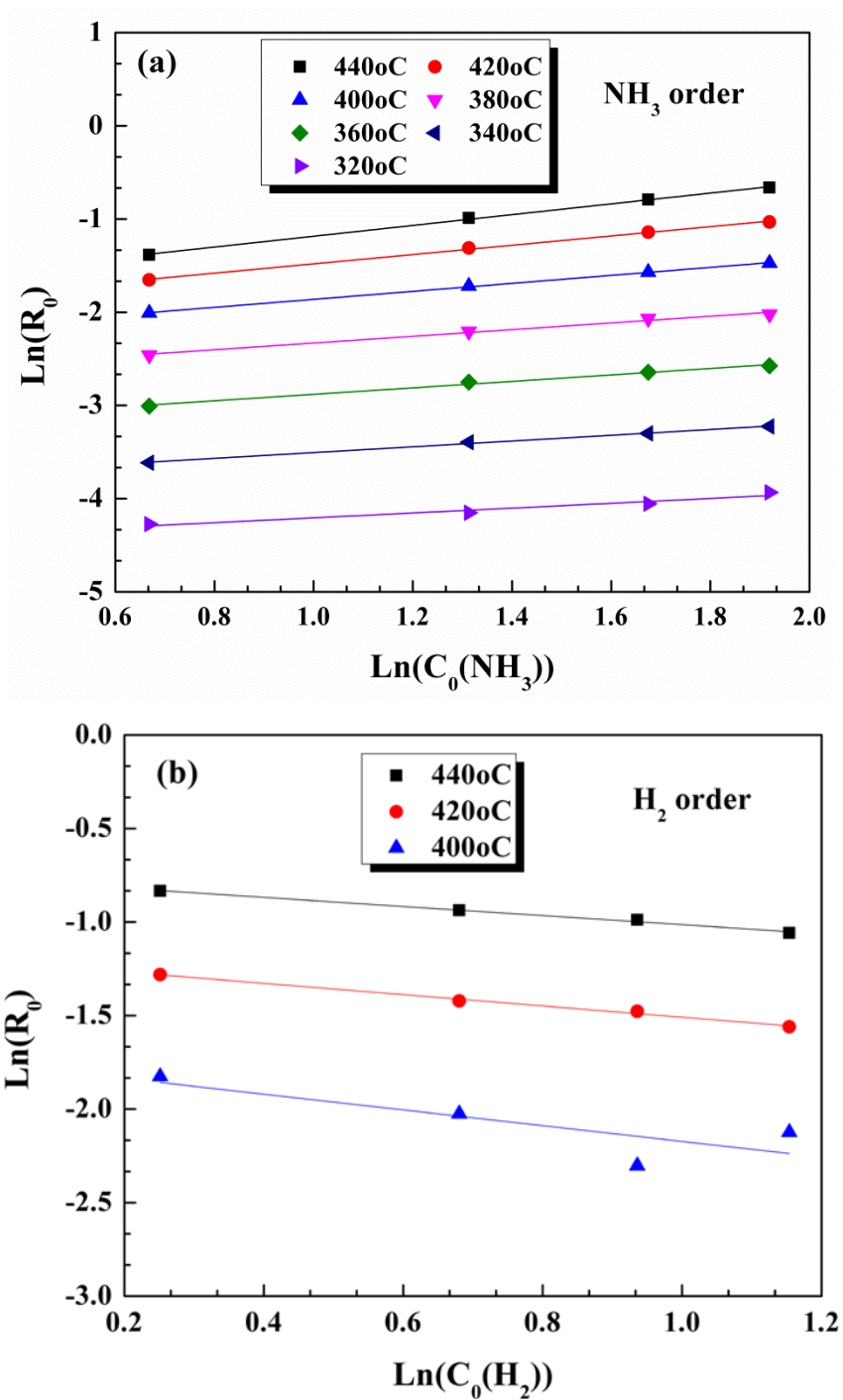


Figure 6-5. Variations of NH<sub>3</sub> and H<sub>2</sub> partial pressures to the rate of ammonia decomposition (argon as balance).

There is no partial pressure dependence on nitrogen to the reaction rate of ammonia decomposition. Both  $\text{NH}_3$  and  $\text{H}_2$  partial pressure variations at different temperature were summarized in Figure 6-5. Clearly, the dependence of temperature on both  $\text{NH}_3$  and  $\text{H}_2$  orders were found similar to the findings of Tsai et al. [16] and Egawa et al. [14] on ruthenium single crystals, and the vanadium nitride reported by Oyama (Fig.6-2). [13]

<b>Table 6-3. Reaction parameters of Ru-graphite catalyst estimated from the power law equation</b>							
<b>Reaction orders</b>	<b>Reaction temperature (°C)</b>						
	440	420	400	380	360	340	320
<b><math>\text{NH}_3</math></b>	0.58	0.50	0.43	0.36	0.35	0.31	0.26
<b><math>\text{H}_2</math></b>	-0.24	-0.30	-0.42	n	n	n	n

(n) stands for not measured.

The inhibitive influence of hydrogen to the reaction rate on Ru-graphite catalyst was not as strong as expected, and was intermediate between the values of nanostructured molybdenum nitride and iron-cobalt-alloy particles. As elucidated in Chapter 3, the ruthenium particles supported on the clean and highly graphitic graphite exhibit well ordering structure, which contain abundant high energetic sites (steps) and low energetic sites (terraces). The cooperation of these two-type sites benefits for the desorptions both of nitrogen and hydrogen. Since the most difficult step of ammonia cracking is desorption of nitrogen, which need a larger ensemble steps. While the adsorption of ammonia and the desorption of hydrogen take place on the weak sites in a relative flat terrace. The inhibitive effect of hydrogen might be much more pronounced on a small (less than 2 nm) or a disordering ruthenium nanoparticle, owing to the low density of the terraces. Bradord et al. reported a strong hydrogen inhibition effect on the ruthenium particles supported on carbon black, but structural characterizations were not presented. [17] The larger ruthenium particles could offer a better ammonia decomposition reactivity were reported earlier, i. e. Karim et al. reported the optimal mean size of ruthenium particle supported on alumina for ammonia decomposition should be around 7 nm. [23] They emphasized the importance of B-5 sites

and the structural shape on ruthenium clusters. In Chapter 3, we found that the morphology (size, shape/ordering) of ruthenium particles indeed differs in the reactivity of ammonia decomposition. Direct information from HRTEM and in-situ XPS confirm that the disordering and small particles could lead to the strong interaction with adsorbed reactants (observations of reaction intermediate of adsorbed nitrogen), as shown in Fig. 3-18. The kinetic results based on the simple power law model are in agreement with the characterization information of Ru-graphite.

### 6.3 Comparison of kinetic measurements

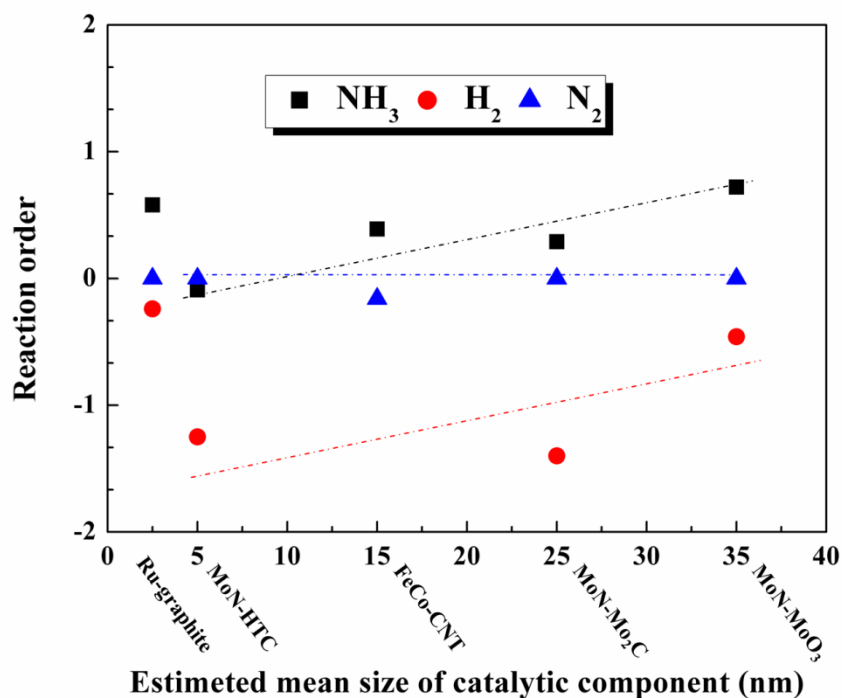


Figure 6-6. Reaction orders (around 450 °C) of NH<sub>3</sub>, H<sub>2</sub> and N<sub>2</sub> as function of estimated mean size of catalytic component.

Figure 6-6 shows the preliminary comparison of reaction behaviors of ammonia decomposition (at around 450 °C) between different catalytic components. The mean size of catalytic unit was estimated from TEM and XRD results. For iron and molybdenum nitride catalyst, with the increasing mean size of catalytic unit, the reaction rate of

ammonia decomposition is more dependent on the partial pressure of ammonia and less effective by the partial pressure of hydrogen. The high energetic sites (steps) are probably deficient on the surface of a large crystal with high crystallinity, leading to the shortage of active sites for the desorption of dinitrogen. On the other hand, the abundance of low energy sites (terrace) on the large crystal will benefit for the desorption of hydrogen. The nanostructured ruthenium catalyst is not in line with the preliminary relationship over the other catalysts. The high efficiency of cracking  $\text{NH}_3$  molecule, the mediate interaction with N atom, and the ordering structure of ruthenium particles can be correlated to the high turnover frequency and the less inhibitive effect of hydrogen in the reaction of ammonia decomposition.

## 6.4 Chapter conclusions and outlook

### 6.4.1 Chapter conclusions

In summary, this chapter investigated the kinetic reaction behaviors of three catalytic systems reported in this thesis for the reaction of ammonia decomposition. The preliminary kinetic results following the simple power-law mode could draw the conclusions as follows:

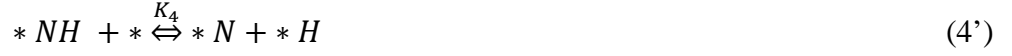
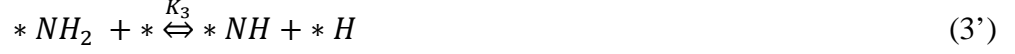
For molybdenum nitride catalysts, the reaction behaviors are controlled by the domain crystalline size of molybdenum nitride. Compared with bulk molybdenum nitride (MoN- $Mo_2C$  and MoN- $MoO_3$ ) lower activation energy and stronger hydrogen inhibitive effect were observed on the nanostructured molybdenum nitride catalyst (MoN-*HTC*). These can be ascribed to the abundance of high density of high energetic sites of catalytic unit, and the low density of “weak” sites (terraces) on the nanostructured molybdenum particles. Both of the activation energy and reaction orders of nanostructured molybdenum are close the ones of ruthenium catalyst indicates the similar chemophysical properties between metal nitride and noble metal.

For nanostructured ruthenium catalyst, the strong inhibition of hydrogen was not observed in this study. This is probably due to the well ordered and relative large ruthenium facets, which can offer high energetic sites of step facilitating the desorption of nitrogen and low energetic sites of terrace for the adsorption of ammonia and the desorption of hydrogen.

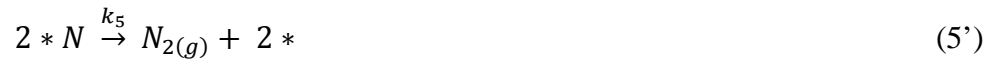
For iron-cobalt alloy catalyst, the negative nitrogen orders observed in this study indicates the nitridation of iron metal should be the inhibitors for ammonia decomposition. The relative less hydrogen inhibitive effect is due to the lower interaction between hydrogen and iron compared with nanostructured ruthenium and molybdenum nitride catalysts.

### 6.4.2 Outlook

The simple power law model could always facilitate the investigation of the effects of the different operation variables on the reactions. However, it is insufficient to investigate the intrinsic reaction mechanism of ammonia decomposition. In order to give a relative precise rate expression, the elemental steps of ammonia decomposition will be re-written as follow:



where  $k_i$  is the reaction rate constant;  $K_i$  stands for the equilibrium constant of individual elemental step; \* is denoted as single active site on the surface of catalyst. Considering the results from fitting the power law model, we will use Temkin-Pyzhev mechanism to integrate all the data of kinetic measurements. The Temkin-Pyzhev mechanism, which supposes the associative desorption of N atoms (step 5') as the rate-determining step, and adsorbed N is the most abundant reaction intermediate.<sup>[30]</sup> Since steps (1')-(4') and (6') are all in equilibrium, the reaction of ammonia decomposition could be written as:



following the Langmuir-Hinshelwood mechanism, the ammonia decomposition rate can be expressed as:

$$r_{NH_3} = \frac{k_5[CS]^2 K_7^2 P_{NH_3}^2}{P_{H_2}^3 \left(1 + \frac{K_7 P_{NH_3}}{P_{H_2}^{3/2}}\right)^2} = \frac{k' P_{NH_3}^2}{(P_{H_2}^{3/2} + K_7 P_{NH_3})^2} \quad (11)$$

in which [CS] ([CS]=[\*]+ [\*N]) stands for the total number of active sites per gram in the catalyst;  $K_7=K_1K_2K_3K_4K_6^{3/2}$ .

To estimate the equilibrium and rate constants, the differential equations of NH<sub>3</sub> consumption and H<sub>2</sub> formation are established and numerically solved via “Berkeley Madonna” using equation:

$$\frac{d(P_{NH_3})}{d(\tau^*)} = -2r_{NH_3} \frac{d(P_{H_2})}{d(\tau^*)} = 3r_{NH_3} \quad (12)$$

The modified residence time  $\tau^*$  is obtained by the inverse volume flow multiplied with a temperature coefficient and the catalyst weight.

In order to integrate all the experimental data to the proposed model, the surface sites of the catalysts should be quantified, which are unfortunately still missing in this work. In the future, the quantitative surface sites of catalytic components over all catalysts in this study will be measured by a temperature programmed desorption of ammonia (NH<sub>3</sub>-TPD). The turn-over frequency will be modified by the density of surface sites assuming the surface is uniform, that all the sites which could chemisorb ammonia will be regarded as active sites. Although the early findings in this study indicates that the decomposition of ammonia on the nanostructured catalyst is probably nonuniform reaction, that is the recombinative dissociative desorption of nitrogen occurs on the steps while the cleavage of ammonia and desorption of hydrogen will happen on weakly adsorbing sites (terraces). Unfortunately, there is no method so far could sufficiently and simply measure the density of steps or terraces on the nanostructured metal or carbide/nitride particles.

## References

1. Emmett, P.H. and S. Brunauer, *The Adsorption of Nitrogen by Iron Synthetic Ammonia Catalysts*. Journal of the American Chemical Society, 1934. **56**(1): p. 35-41.
2. Temkin, M. and V. Pyzhev, *Kinetic of ammonia synthesis on promoted iron catalysts*. Acta Physicochimica Urss, 1940. **12**(3): p. 327-356.
3. Kunsman, C.H., E.S. Lamar, and W.E. Deming, *XCIII. Rates and temperature coefficients of the catalytic decomposition of ammonia over molybdenum, tungsten, and promoted iron*. Philosophical Magazine Series 7, 1930. **10**(67): p. 1015-1037.
4. Kunsman, C.H., *The Decomposition of Ammonia on Iron Catalysts*. Science, 1927. **65**(1691): p. 527-528.
5. Winter, E., *Der Katalytische Ammoniakzerfall an Eisen*. Z. physikal. Chem. , 1931. **B13**: p. 401-424.
6. Love, K.S. and P.H. Emmett, *The Catalytic Decomposition of Ammonia over Iron Synthetic Ammonia Catalysts*. Journal of the American Chemical Society, 1941. **63**(12): p. 3297-3308.
7. Takezawa, N. and R. Mezaki, *Langmuir-temkin-pyzhev rate models for ammonia decomposition reaction*. The Canadian Journal of Chemical Engineering, 1970. **48**(4): p. 428-431.
8. Löffler, D.G. and L.D. Schmidt, *Kinetics of NH<sub>3</sub> Decomposition on Iron at High Temperatures*. Journal of Catalysis, 1976. **44**(2): p. 244-258.
9. Löffler, D.G. and L.D. Schmidt, *Kinetics of NH<sub>3</sub> Decomposition on Polycrystalline Pt*. Journal of Catalysis, 1976. **41**(3): p. 440-454.
10. Shindo, H., et al., *Reaction Mechanism of Ammonia Decomposition on Tungsten*. Journal of the Chemical Society, Faraday Transactions 1: Physical Chemistry in Condensed Phases, 1980. **76**: p. 280-290.
11. Boudart, M., et al., *Nitrogen Adsorption and Ammonia Decomposition on Polycrystalline Molybdenum*. Journal de Chimie Physique et de Physico-Chimie Biologique, 1981. **78**(11-12).
12. Tamaru, K., *A "New" General Mechanism of Ammonia Synthesis and Decomposition on Transition Metals*. Accounts of Chemical Research, 1988. **21**(2): p. 88-94.
13. Oyama, S.T., *Kinetics of Ammonia Decomposition on Vanadium Nitride*. Journal of Catalysis, 1992. **133**(2): p. 358-369.
14. Egawa, C., et al., *Ammonia Decomposition on (1 1 10) and (0 0 1) Surfaces of Ruthenium*. Journal of the Chemical Society, Faraday Transactions 1: Physical Chemistry in Condensed Phases, 1984. **80**(6): p. 1595-1604.
15. Dietrich, H., K. Jacobi, and G. Ertl, *Decomposition of NH<sub>3</sub> on Ru(111)*. Surface Science, 1996. **352-354**: p. 138-141.
16. Tsai, W. and W.H. Weinberg, *Steady-State Decomposition of Ammonia on the Ruthenium(001) Surface*. The Journal of Physical Chemistry, 1987. **91**(20): p. 5302-5307.
17. Bradford, M.C.J., P.E. Fanning, and M.A. Vannice, *Kinetics of NH<sub>3</sub> Decomposition Over Well Dispersed Ru*. Journal of Catalysis, 1997. **172**(2): p. 479-484.
18. Honkala, K., *Ammonia Synthesis from First-Principles Calculations*. Science, 2005. **307**(5709): p. 555-558.
19. Jacobsen, C.J.H., et al., *Structure sensitivity of supported ruthenium catalysts for ammonia synthesis*. Journal of Molecular Catalysis A: Chemical, 2000. **163**(1-2): p. 19-26.
20. García-García, F., A. Guerrero-Ruiz, and I. Rodríguez-Ramos, *Role of B5-Type Sites in Ru Catalysts Used for the NH<sub>3</sub> Decomposition Reaction*. Topics in Catalysis, 2009. **52**(6): p. 758-764.
21. Zhang, J., et al., *Highly Efficient Ru/MgO Catalysts for NH<sub>3</sub> Decomposition: Synthesis, Characterization and Promoter Effect*. Catalysis Communications, 2006. **7**(3): p. 148-152.

22. Zheng, W., et al., *NH<sub>3</sub> Decomposition Kinetics on Supported Ru Clusters: Morphology and Particle Size Effect*. *Catalysis Letters*, 2007. **119**(3-4): p. 311-318.
23. Karim, A.M., et al., *Correlating Particle Size and Shape of Supported Ru/ $\gamma$ -Al<sub>2</sub>O<sub>3</sub> Catalysts with NH<sub>3</sub> Decomposition Activity*. *Journal of the American Chemical Society*, 2009. **131**(34): p. 12230-12239.
24. McGill, W.J. and F. Sebba, *The Kinetics of Ammonia Decomposition over Vanadium Nitride*. *Journal of Catalysis*, 1963. **2**(2): p. 104-108.
25. Volpe, L. and M. Boudart, *Compounds of molybdenum and tungsten with high specific surface area : I. Nitrides*. *Journal of Solid State Chemistry*, 1985. **59**(3): p. 332-347.
26. Jagers, C.H., J.N. Michaels, and A.M. Stacy, *Preparation of high-surface-area transition-metal nitrides: molybdenum nitrides, Mo<sub>2</sub>N and MoN*. *Chemistry of Materials*, 1990. **2**(2): p. 150-157.
27. Schlögl, R., *Ammonia Synthesis*, in *Handbook of Heterogeneous Catalysis*, G. Ertl, et al., Editors. 2008, Wiley-VCH Verlag GmbH & Co. KGaA.
28. Mittasch, A. and W. Frankenburg, *Early Studies of Multicomponent Catalysts*, in *Advances in Catalysis*, V.I.K. W.G. Frankenburg and E.K. Rideal, Editors. 1950, Academic Press. p. 81-104.
29. Kraupner, A., et al., *Mesoporous Fe<sub>3</sub>C Sponges as Magnetic Supports and as Heterogeneous Catalyst*. *Journal of Materials Chemistry*, 2010. **20**(29): p. 6019-6022.
30. Temkin, M. and V. Pyzhev, *Kinetics of Ammonia Synthesis on Promoted Iron Catalysts*. *Acta Physicochimica Urss*, 1940. **12**(3): p. 327-356.

## Personal Information

Family name: Zheng  
First name: Weiqing  
Date of birth: 18<sup>th</sup> May 1980  
Place of birth: Dalian, China  
Marriage: Married in May 2006  
with Xiaolin Zhang

## Education

- 02.2008 ~ present      **Doctoral Thesis**  
*Fritz-Haber-Institut der Max-Planck-Gesellschaft*  
*Department of Inorganic Chemistry*  
*Faradayweg 4-6, 14195, Berlin, Deutschland*  
**Supervisor:** Prof. Dr. Robert Schlögl  
**Subject:** Heterogeneous Catalysis, Chemical Engineering  
**Thesis:** “Nanomaterials for Ammonia Decomposition”
- 09.2004 ~ 11.2007      **Master’s Degree**
- 09.2004 ~ 08.2005      *Graduate University of the Chinese Academy of Sciences*  
*College of Chemistry and Chemical Engineering*  
*19A Yuquanlu, 100049, Beijing, China*
- 09.2005 ~ 11.2007      *Dalian Institute of Chemical Physics, CAS*  
*Laboratory of Applied Catalysis*  
*457 Zhongshan Road, 116023, Dalian, China*  
**Supervisor:** Prof. Dr. Hengyong Xu  
**Subject:** Heterogeneous Catalysis, Chemical Engineering  
**Thesis:** “The Study of Ni-based Catalyst and Its Catalytic Performance for Ammonia Decomposition”
- 09.1999 ~ 07.2003      **Bachelor’s Degree**
- 09.1999 ~ 08.2001      *Dalian University of Technology*  
*School of Chemical Engineering*
- 09.2001 ~ 08.2003      *Dalian University of Technology*  
*State Key Laboratory of Fine Chemicals*  
*158 Zhongshan Road, 116012, Dalian, China*  
**Supervisor:** Prof. Dr. Zongshi Li  
**Subject:** Applied Chemistry, Fine Chemical Engineering  
**Thesis:** “The Synthesis and Properties of Alkyl Methyl-naphthalene Sulfonate Surfactant for Tertiary Recovery”



## Acknowledgements

The work presented in this thesis was carried out at the Department of Inorganic Chemistry at the Fritz Haber Institute of Max Planck Society in Berlin. Herein I would like to give thanks to numerous people who helped me to make it possible in my studies.

First and foremost I would like to thank Professor Dr. Robert Schlögl for giving me the opportunity to carry out my study and for sharing his vision and great knowledge in the field of catalysis. I would also like to thank my supervisor, Professor Dr. Dang Sheng Su, for his continuing support for my work and life. Their excellent supervision and enthusiasm have helped in building my practical and intellectual skills.

I would like also to thank the thesis committee Prof. Reinhard Schomäcker, Prof. Klaus Rademann and Prof. Thorsten Ressler for their inputs and patience.

I would like thank to Professor Dr. Jian Zhang who has immensely contributed to development of my scientific journey in the Fritz Haber Institute.

I would like to thank all my collaborators, Prof. Ferdi Schüth and Klaus Schlichte in MPI-Mülheim, Otremba Torsten in TU-Berlin Dr. Payam Kaghazchi and Dr. Timo Jacob in Ulm University for the measurements and fruitful discussions.

My sincere gratitude is also extended to all the researchers, lab technicians in and fellow students in Inorganic Chemistry of The Fritz-Haber Institute. I would like to acknowledge the following people for the technical assistance: Raoul Blume, Lide Yao, Gisela Weinberg, Wei Zhang, Bingsen Zhang, Yonglai Zhang, Gisela Lorenz, Edith Kitzelmann, Frank Girgsdies, Olaf Timpe. Special thanks for Tom Cotter who offered his fancy materials and helped me to a deep understand of carbide and nitride.

I would like to acknowledge the members of the old carbon group for their kindness help; Rosa Arrigo, Manfred Schuster, Benjamin Frank, Lidong Shao, Bo Zhu, Aihua Zhang, Wiebke Frandsen, Achim Klein-Hoffmann, Norbert Pfänder, Julian Tornow, Yuchen Du, Alberto Villa, Qiang Zhang, Xiaochen Zhao and Chengmeng Chen. Special thanks to my officemates, Sylvia Reiche and Jean-Phillippe Tessonier, and to my roommates, Di Wang and Ali Rinaldi.

I would like to thank my wife, Xiaolin, without her support and sacrifice that I could not manage to survive through my stay in Berlin.

Finally I would like to thank my parents, who raised me, supported me, and always believed in me.